Delft University of Technology & Norwegian University of Science and Technology

Dynamic Analysis of a Monopile Offshore Wind Support Structure Subjected to Earthquakes

OE 54030 Thesis & TMR 5950 Thesis Project

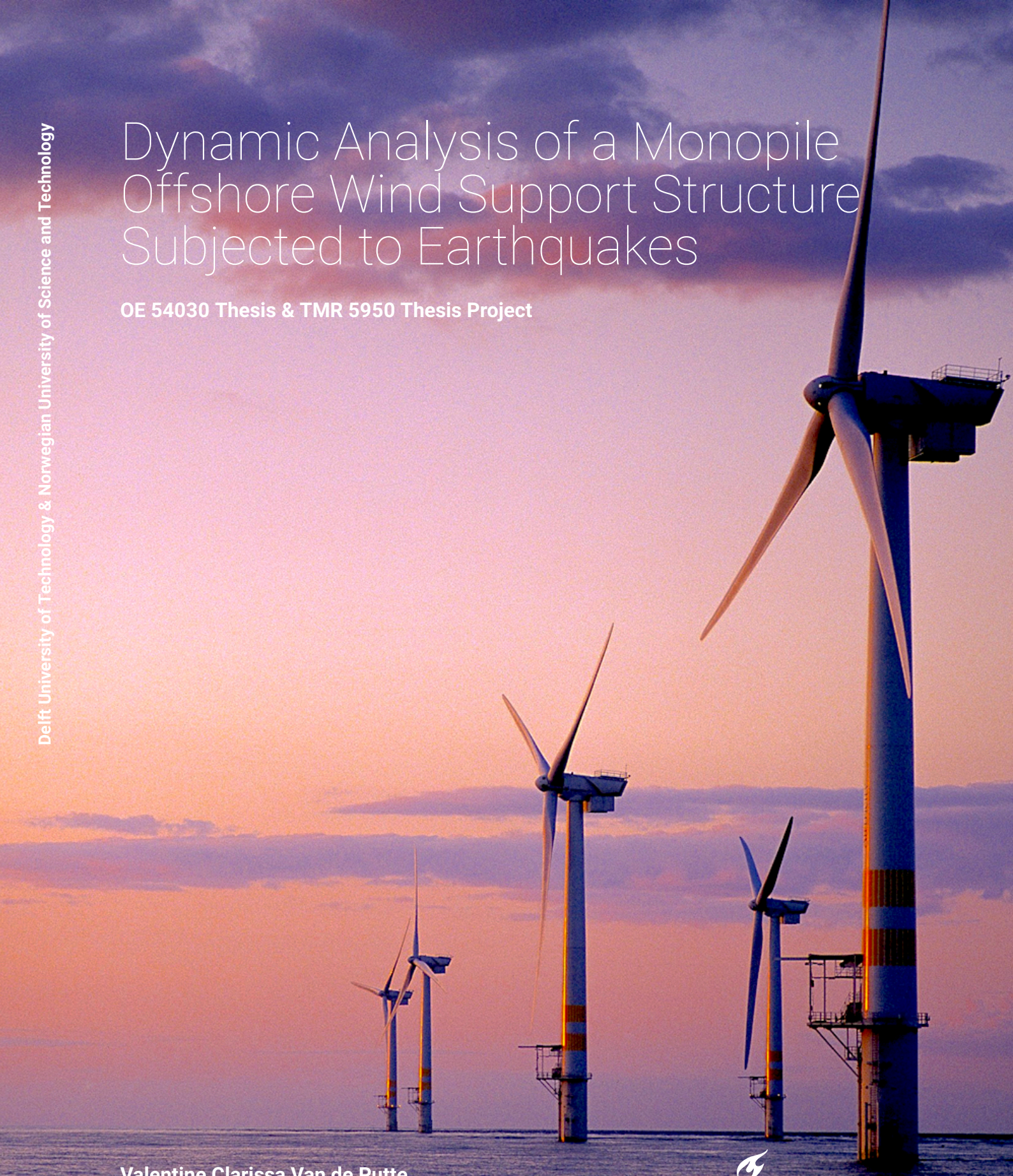

Valentine Clarissa Van de Putte

Graduating supervisor: Prof. A. Metrikine

Supervisor TU Delft: Prof. F. Pisanó
Ir. P. van der Male

Supervisor NTNU: Prof. G.R. Eiksund

Supervisor GeoSea N.V.: Ir. D. Rabaut
Ir. W. Haring

TUDelft

NTNU

DEME

The cover image was copied from an article by Utility Weekly
"UK still top for offshore wind but China dominates onshore":
utilityweek.co.uk/uk-still-top-for-offshore-wind-but-china-dominates-onshore/.

Dynamic Analysis of a Monopile Offshore Wind Support Structure Subjected to Earthquakes

A Comparative Study Between the Responses of an Elastic and an Inelastic Soil-Structure Interaction Model Through Incremental Dynamic Analysis

by

Valentine Clarissa Van de Putte

to obtain the degree of Master of Science in Offshore Engineering and Dredging
at the Delft University of Technology,

and to obtain the degree of Master of Science in Technology - Wind Energy
at the Norwegian University of Science and Technology.

Student number:	4206649 (TU Delft) and 471813 (NTNU)
Course code:	OE 54030 (TU Delft) and TMR 5950 (NTNU)
Project duration:	March 1, 2017 – November 9, 2018

Thesis committee:	Prof. A. Metrikine,	TU Delft, graduating professor
	Prof. F. Pisanó ,	TU Delft, supervisor
	Ir. P. van der Male ,	TU Delft, supervisor
	Prof. G. Eiksund ,	NTNU Trondheim, supervisor
	Ir. D. Rabaut ,	GeoSea N.V., supervisor
	Ir. W. Haring ,	GeoSea N.V., supervisor

An electronic version of this thesis is available at `http://repository.tudelft.nl/`.

NTNU
Norwegian University of Science and Technology

TU Delft
Delft University of Technology

GeoSea
Geotechnical & Offshore Solutions

Of the many sources of external load that must be considered in the design of fixed structures, the most important by far in terms of its potential for disastrous consequences is the earthquake.

Clough & Penzien, *Dynamics of Structures*, 2003

Earthquakes systematically bring out the mistakes made in design and construction – even the most minute mistakes; it is this aspect of earthquake engineering that makes it challenging and fascinating, and gives it an educational value far beyond its immediate objectives.

Newmark & Rosenblueth, *Fundamentals of Earthquake Engineering*, 1971

Acknowledgements

First and foremost, I would like to thank my parents Carine and Franklijn for their eternal support and love. You both taught me that hard work always pays off in the end; the bumps in the road are a mere count of one's perseverance. *Bedankt, voor alles.*

To Emmeline, I apologize for being an insufferable sister these past few months (although you will argue it is not only when a master study is in the making). Thank you for bearing with me, and for being as caring as you are.

To Michel, thank you for always challenging me to be my next best. It is with great love that I look back on these past six years, and with excitement to the years to come. I am looking forward to what the future has in store for us.

I am grateful for the valuable friendships I got to make along the way, with a special mention to Marijn, Dries, Matthieu, Irene, Joris and Cody. To the people I met during my academic career and gave colour to my student life: although your name is not mentioned here, I will never forget you.

Special gratitude goes out to prof. Gudmund Reidar Eiksund and Ir. Pim van der Male for their valuable feedback and guidance throughout the project, and to prof. Federico Pisanò and prof. Andrei Metrikine. I would like to thank Wouter Haring and Dieter Rabaut of DEME GeoSea for believing in the value of my research topic. Lastly, I thank BMT Argoss in the Netherlands and the CWB in Taiwan for sharing respectively metocean data and earthquake data free of charge.

Thank you to all the people who have inspired and encouraged me along the way!

Abstract

Wind energy is getting foothold in Asia. After the success story of wind as an eco-friendly secure supply of energy in Europe, countries in Asia that aim to phase out their (import) dependency on fossil fuels and nuclear power seek their avail in renewables. Taiwan, a country poor on natural resources, has set the goal to phase out nuclear energy by 2025; 20 % of power generation is planned to come from renewable energy of which the target for offshore wind is set at 21.6 % [71]. But of the 1.35 GW capacity that represents, a mere 8 MW was installed in 2017 [23]. For countries such as Taiwan, with a vast wind energy potential but with limited land area, offshore wind energy seems to be both the answer and the challenge. Unlike in its northern European home, facilities developed along the Taiwan Strait should be able to withstand strong earthquakes, something the European industry is unfamiliar with from its experience of deploying offshore wind in the North Sea. More insight in the seismic design of bottom founded offshore wind turbines is paramount, this to verify if the current design recommendations founded on European best-practice are transferable to Asian offshore environments.

This thesis project has set out to investigate the response in fore-aft direction of a monopile wind foundation supporting an NREL 5 MW turbine, offshore the coast of Taiwan, which is affected by weak to strong earthquake ground motion in combination with normal sea state conditions. The soil at the location of the monopile is layered, with sand overlying clay, mud-, sandstone and gravel. Liquefaction, although of great concern in seismic design of piled structures, is not investigated.

Two soil-structure interaction models' responses are compared in this study, one denoted as an *elastic* and one as an *inelastic* beam on a nonlinear Winkler spring foundation. The goal of using two different soil definitions was threefold:

1. quantify the effect of inelastic soil-structure behavior on the system's response, by comparing a nonlinear elastic SSI model with a nonlinear inelastic series hysteretic-viscous damping SSI model,
2. analyze the earthquake intensity level at which nonlinear inelastic effects become dominant,
3. verify whether the elastic response assumption made in design standards is valid and leads to a safe design.

Incremental dynamic time-series analysis of the response of a Timoshenko beam finite-element model was conducted, where this model is exposed to co-directional steady wind, regular waves and an as-recorded earthquake signal of increasing intensity. This earthquake record is scaled to different magnitudes, including the Extreme Level Earthquake and Abnormal Level Earthquake as defined by ISO19901-2.

It was shown that the response of the structure is highly sensitive to the amplitude of the earthquake, following a nonlinear increase in response with increasing PGD. Even at the recorded moderate earthquake level, nonlinear effects occurred in the soil-structure system. As such, it is not recommended to assume linear elastic soil-structure response of a monopile for earthquake loads below the Extreme Earthquake Level (i.e. the level generally assumed up to which the structure responds elastically). Because of the presence of nonlinear inelastic behavior in the soil-structure response under moderate seismic loads, using time history analysis is recommended over spectral analysis as nonlinear effects depend not only on the amplitude but also on the duration and frequency of loading.

Against expectations, the responses of the two soil-structure interaction models were not similar for the as-recorded free-field motion, which was far below the Extreme or Abnormal Earthquake Level and where nonlinear inelastic effects were not expected to introduce dissimilarities between the elastic and inelastic model. This indicated that the ground displacement due to the earthquake motion could no longer be classified as small, and the soil-structure response no longer as linear elastic. This is in disagreement with experiments on slender piles, where observations and experiments in other fields of earthquake research learn that elastic behavior can be expected for small to moderate ground displacements [31] [13] [14] [1].

For all earthquake acceleration levels considered in this study, – 0.25 g , 0.75 g and 1.17 g –, the structure did not meet its ultimate, nor its serviceability requirements when assuming a nonlinear elastic response of the soil. Ignoring the effect of hysteresis and radiation damping proved to lead to a serious overestimation of the loads, response and structural capacity utilization of the structure, especially below mudline. Energy dissipation should be included in seismic soil-structure interaction modeling, as an elastic assumption puts an excessive demand on the structure.

Load simulations on the nonlinear inelastic model predicted much smaller responses and capacity use of the structure, as radiation damping proved to have an important load-reducing effect. However, it was assessed that radiation damping should only be active during low amplitude loading, when the response of the soil-structure is linear elastic, as otherwise the viscous radiation damper introduced nonphysical excessive dashpot forces that led to unrealistically small pile displacements above mudline. Hysteresis damping should be included to model energy dissipation of the seismic shear waves during large amplitude motion, and the radiation damper should be adapted to only have significant influence during low amplitude motion.

As such, it is recommended to apply either more complex finite-element modelling of the soil-structure interaction, that can incorporate gapping/cyclic softening/liquefaction/hysteresis and radiation damping, or to use a p-y curve approximation that incorporates these nonlinear inelastic effects to a realistic degree. Standardized p-y curves [2],– such as the curves used in the nonlinear elastic SSI –, were not validated for the use in highly dynamic environments such as earthquake loading, and are hence not recommended to be used in earthquake-resistance design of monopiles based on the results of this study.

Contents

List of Figures

List of Tables

Nomenclature

Constant

g	Gravitational constant	[9.81 m/s^2]

Greek

α_r	Strength reduction factor	[%]
ϵ	Strain	[%]
η	Viscous damping	[Ns/m]
γ	Bulk unit weight	[N/m^3]
γ	Shear strain	[-]
γ'	Effective unit weight	[N/m^3]
λ	Eigenvalue	[rad^2/s^2]
ν	Poisson ratio	[-]
Ω	Rotational rotor speed	[rpm]
Φ	Shear deformation parameter-]	[
ϕ	Internal friction angle	[°]
ϕ	Shear rotation	[°]
ρ	Density	[kg/m^3]
ρ'	Effective density	[kg/m^3]
σ	Normal stress	[N/m^2]
σ	Shear strength	[N/m^2]
τ	Shear stress	[N/m^2]
τ	Shear stress	[N/m^2]
θ	Rotation	[°]

Roman

$\underline{\underline{\mathbf{M}}}$	Mass matrix	
$\underline{q}$	Overall displacement vector	
A	Area	[m^2]
a	Axial induction factor	[-]
a'	Tangential induction factor	[-]
B	Number of rotor blades	[-]
c	Chord length	[m]

c	Tangent modulus constant plastic p-y equation	[-]
C_c	Closure spring tuning constant	[-]
C_d	Drag coefficient	[-]
C_d	Drag spring expected drag participation constant	[-]
C_r	Constant ratio yield to ultimate soil resistance per unit length	[-]
c_v	Radiation damper constant per unit length	[Ns/m^2]
C_{AD}	Aerodynamic damping	[Ns/m]
D	Diameter	[m]
d	Depth	[m]
E	Elastic modulus	[N/m^2]
E	Number of elements	[-]
E	Total number of elements	[-]
E_s	Initial modulus of subgrade reaction	[N/m^3]
F	Force	[N]
f	Force per unit length	[N/m]
G	Shear modulus	[N/m^2]
k	Shear correction coefficient	[-]
k	Soil spring stiffness	[N/m^2]
$\underline{\underline{\mathbf{K}}}$	Stiffness matrix	
l	Element length	[m]
l	Element length	[m]
N	Total number of nodes	[-]
n	Sharpness constant plastic p-y equation	[-]
p	Soil resistance load per unit length	[N/m]
q	Compressive strength	[N/m^2]
R	Radius	[m]
r_g	Radius of gyration	[m]
V	Velocity	[m/s]
W	Weight	[N]
y	Pile displacement (lateral)	[m]
z	Axial displacement	[m]

Subscripts

$_0$	Initial
$_{eqv}$	Equivalent

EQ	Earthquake
ult	Ultimate
yield	Yield
b	Bending
c	Closure
d	Drag
e	Elastic
f	Foundation or soil
g	Gap
g	Geometric
i	Inner
o	Outer
p	Plastic
r	Rotational
s	Shear
t	Translational
u	Undrained
y	Lateral axis direction
z	Vertical axis direction
50	50 %

Superscripts

$^{+}$	Positive direction
$^{-}$	Negative direction
^{e}	Element

Abbreviations

1P	Rotational frequency of the wind turbine rotor
3P	Blade passing frequency of the wind turbine rotor
ALE	Abnormal Level Earthquake
API	American Petroleum Institute
BEM	Blade Element Momentum
BNWF	Beam on Nonlinear Winkler Foundation
BR	Buckling Ratio
CWB	Central Weather Bureau
DART	Downhole Accelerometer Arrays Taipei Basin
DNV-GL	Det Norske Veritas-Germanischer Lloyd
EERA	Equivalent-linear Earthquake site Response Analsyis
ELE	Extreme Level Earthquake
EOM	Equations of Motion
ESS	Extreme Sea State
ETM	Extreme Turbulence Model
FE	Finite Element
FEM	Finite Element Model
FLS	Fatigue Limit State
GDMS	Geophysical Database Management System
GPS	Global Positioning System
HSE	Health, Safety and Environmental
IDA	Incremental Dynamic Analysis
IEC	International Electrotechnical Commission
IES	Institute of Earthquake Sciences
ISO	International Organization for Standardization
K-NET	Kyoshin Network for strong ground motion
MCE	Maximum Considered Earthquake
MP	Mono-Pile
MSL	Mean Sea Level
MTN	Taiwan Mountain Seismic Network
MWL	Maximum Water Level
NERA	Nonlinear Earthquake site Response Analysis
NREL	National Renewable Energy Laboratory
NSS	Normal Sea State
OpenSees	Open System for Earthquake Engineering Simulation

P	Primary normal stress wave
PEER	Pacific Earthquake Engineering Research Center
PGA	Peak Ground Acceleration
PGD	Peak Ground Displacement
PGV	Peak Ground Velocity
RNA	Rotor-nacelle assembly
RQD	Rock Quality Designation
S	Secondary shear wave
SLS	Serviceability Limit State
SMART2	Strong-Motion Array Taiwan Phase II
SRA	Site Response Analysis
SSE	Squared Sum of Errors
SSI	Soil-structure interaction
SSI1	Nonlinear Elastic Seismic Soil-Structure Interaction Model
SSI2	Nonlinear Inelastic Series Hysteretic-Viscous Damping Seismic Soil-Structure Interaction Model
SWL	Still Water Level
TP	Transition piece
TSMIP	Taiwanese Strong Motion Instrumentation Program
ULS	Ultimate Limit State
UR	Utilization Ratio (yield limit criterion)

1 Introduction

Wind energy is getting foothold in Asia. After the success story of wind as an eco-friendly secure supply of energy in Europe, and after the dreadful incident at the Fukushima nuclear power plant in Japan, countries in Asia that aim to phase out their (import) dependency on fossil fuels and nuclear power seek their avail in renewable energy sources.

Case in point is Taiwan. This country, poor on natural resources, has set the ambitious goal to phase out nuclear energy by 2025 and to invest heavily in renewable energy projects; 20 % of the power generation should be from renewable energy, of which offshore wind is targeted to represent 21.6 % or 1.35 GW [71]. But today, a mere 8 MW of offshore wind capacity is installed [23]. For Asian countries such as Taiwan, with a vast wind energy potential but that find themselves limited in land area, offshore wind energy seems to be both the answer as well as the challenge. Unlike in its northern European home, facilities developed along the Pacific Belt (Figure 1.1) should be able to withstand strong earthquakes, something the European industry is unfamiliar with from its experience of deploying offshore wind in the North Sea. More insight into the seismic design of bottom founded offshore wind turbines is paramount for these countries to deploy their offshore wind energy potential.

In light of the recent developments in the offshore wind energy market in East Asia, and the subsequent push for seismic design of bottom-fixed offshore wind support structures, this thesis project aims to provide valuable insight into the seismic response behaviour of a monopile offshore wind support structure.

1.1. Motivation and Explanation of the Research

Due to the novelty of the demand for seismic design of offshore wind structures, little detailed guidelines exist nor is there a general consensus between design standards on how to conduct analyses in the design process. Often reference is made to local codes for buildings and other (onshore) structures, as industrial experience in designing seismically resistance bottom-founded wind structures is scarce. The question rises whether a structure based on the current editions of the design standards, which make use of guidelines for other types of structures, is likely to fulfill its 25 to 30 year serviceability requirement under (repetitive) strong ground motion.

The common thread in current seismic guidelines for monopile offshore wind structures is that one should assume the response to be elastic, and that this response should be investigated for a return period event of 475 years after which no structural damage should exist. The earthquake is to be treated as a separate environmental force, superimposed on other environmental influences such as waves and wind.

However, observations from geotechnical and earthquake research have learned that in areas of medium to high seismicity, with soft to medium soil conditions, a high degree of nonlinearity is expected in the soil. Consequently, inelastic responses of the foundation are to be expected, which contradict the elastic assumption of the design codes. These observations also advocate full time-history analysis of a nonlinear inelastic soil-structure interaction model, as spectral analysis might fail to catch these nonlinear inelastic responses.

Therefore, in this thesis project, a case study is performed of a monopile design conform the standards for a location offshore the coast of Taiwan. The time-history responses of two seismic SSI interaction models are compared, where the first model makes use of the elastic assumptions stated in the design codes, and the second model incorporates inelastic SSI interaction effects as observed during moderate to strong ground motion.

A monopile foundation is analyzed as this type of foundation represents 81.7 % of all wind support structures offshore according to the WindEurope statistics of 2017 [75]. These foundations are the most economically sound option for small to moderate waterdepths, as is the case at the selected offshore location in Taiwan. Additionally, their production process is less complex and well integrated. As such, considering the most used substructure worldwide is the monopile foundation for offshore wind, it is only straightforward to perform a first seismic soil-structure analysis study on this type of foundation.

In this author's opinion, it is worthwhile to investigate to what level of ground motion the responses of an elastic and an inelastic SSI model agree, and what factors lead to differences in response between the two models. It should be investigated whether current recommended practice leads to safe earthquake-resistant bottom-founded wind foundations.

1.2. Scope of the Thesis Project

The computational model of the monopile offshore wind foundation is inspired by an existing design for a specific location offshore the coast of Taiwan. The design of the structure is based on recommended practice by design standards and local design codes. The monopile foundation is supporting a transition piece, tower and NREL 5 MW rotor-nacelle assembly. The monopile, transition piece and tower are modeled as elastic finite Timoshenko beam elements, while the rotor-nacelle assembly is modeled as a point mass at hub height.

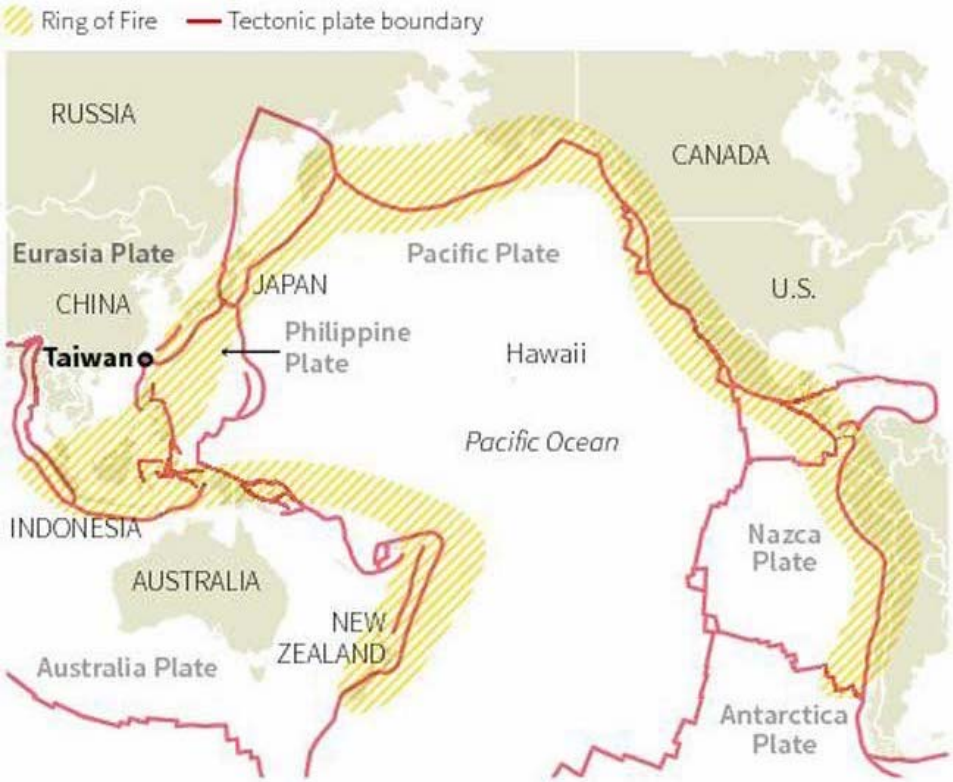

Figure 1.1: *Taiwan as it is located on the Ring of Fire [80].*

The finite-element beam model is resting on a nonlinear Winkler spring foundation. Depending on the SSI analysis conducted in this comparative study, the soil foundation is either a set of nonlinear elastic springs or a set of series hysteretic-viscous spring-dashpot elements. The latter elements can mimic inelastic effects such as yielding, gapping/cave-in, hysteretic and radiation damping. Liquefaction is not included in this study, although it is recognized to be of great concern in seismic pile design.

It should be remarked that only lateral seismic soil-structure interaction is investigated in this project, in a 2D plane. Vertical interaction and three-dimensional effects do not belong to the scope of this project. Only excitation of the structure in fore-aft direction is considered, with unidirectional rotor, wind, wave and earthquake loads.

Time-history analysis of the dynamic response of the full structure will be conducted. Environmental factors forcing the dynamic response are a steady wind, regular waves and a steady current. The wind and wave properties are conform met-ocean observations relating to a Normal Sea State at the location offshore the coast of Taiwan. The environmental loads are assumed to act in the same plane, and in the same direction.

On top of that, the structure is simulated to suffer from earthquake imposed loads. To model this, time series data of one strong ground motion recorded by a free-field station near the location is implemented in the model. Site response analysis of the seismic wave propagation through the local soil profile was conducted prior to any seismic SSI analysis, this to obtain the ground motion variation over depth. Corrections for distance effects suffered by the signal between the recording station and the monopile location were considered outside the scope of this project. Again, the earthquake load is assumed to act in the same plane and in the same direction as the other environmental loads. It is assumed to act in combination with Normal Sea State conditions as this situation has the highest likelihood of occurring in reality.

To account for the variability of earthquake ground motion when using only one earthquake recording, incremental dynamic analysis is implemented. By scaling the acceleration record of the ground to amplitudes that comply with probabilistic return period events, one can investigate the capacity behaviour of the structure for earthquakes that may or may not occur in the structure's lifetime, but of which yet no recordings exist.

1.3. Goal of the Research

The main research question in this thesis project is *"whether elastic response of a monopile offshore wind support structure may be assumed in seismic SSI analysis, when that structure is exposed to ground motion of different intensity"*. Therefore, in this project, it is investigated if and to what level of ground motion an elastic and an inelastic SSI interaction model agree.

Besides that, this research aims to investigate the capacity behaviour of the structure under increasing ground motion. The amplitudes of the ground motion in the incremental dynamic analysis compare to predicted levels of an extreme and abnormal earthquake.

For the elastic assumption in the design codes to be valid, the elastic and inelastic model responses should agree up to the design earthquake level, often referred to as the Extreme Level Earthquake, which has a return period of 475 years. Up to this level of ground excitation, the response of the structure is designed to be elastic; no inelastic effects should govern the response, causing both models to predict the same structural behaviour. For ground motions beyond that level, soil nonlinearities and inelastic responses of the structure are anticipated, causing the elastic and inelastic SSI model to no longer agree. The Abnormal Level Earthquake may lead to permanent deformations and tilt, but the foundation should maintain enough structural capacity to prevent a total collapse.

If the computed behaviour is not conform expectations, meaning that lower level earthquakes lead to inelastic responses sooner than ELE, then the elastic assumption in seismic design becomes invalid. Elastic assumptions may or may not be underestimating the actual inelastic response of the structure, and lead to a design with insufficient structural capacity to survive an ALE.

1.4. Outline of the Thesis Report

Chapter 2 provides a short summary of the literature study preceding this thesis project [95]. It covers the recommendations regarding seismic design according to the standards in more detail, and introduces the reader to earthquakes, to the effects they have on the structure and the soil, and to seismic soil-structure interaction modeling.

In Chapter 3 the approach to construct the two seismic soil-structure interaction models is explained. The structural and soil properties are listed, and the assumptions made in producing the finite element model and the soil interaction models are clarified. The mathematics to arrive at the equations of motion for both interaction models are presented.

Chapter 4 summarizes the load cases to be simulated. It also explains the method to compute the rotor, wind, wave and earthquake loads on the structure. For the earthquake load, incremental dynamic analysis and site response analysis is elucidated.

The results and a discussion of these results are presented in Chapter 5. The conclusions with regard to this research are listed in Chapter 6, while the subsequent Chapter 7 takes away some key recommendations and reflections with respect to seismic design of monopile offshore wind support structures.

2

Existing Literature

This chapter aims to give the reader some background on the recommendations made by design standards with respect to seismic design of offshore wind support structures. It also aims to provide deeper insight into the characteristics and dynamics of earthquakes, this to understand the complexity of the engineering problem. To conclude this chapter, a seismic soil-structure interaction model that has shown reasonable agreement with experimental observations is introduced. As this model seems to incorporate many of the nonlinear effects associated with strong ground motion in soft soils, it will serve as a verification model to a model developed according to design standard recommendations.

A more elaborate literature review on earthquakes, the effect they have on their surroundings, and seismic soil-structure analysis methods can be consulted in the *Specialization Project* [95], a literature study that was conducted prior to this thesis project.

2.1. Recommendations by Design Standards

Less details and guidelines exist for the seismic design of wind turbines and wind support structures than for buildings and other structures. The offshore wind industry, developed in northern European waters, never before had to consider designing earthquake-resistant structures prior to its expansion to Asia. Due to the novelty of the engineering problem, and the lack of industrial expertise, the design standards have been forced to rely on recommendations for other types of structures. Moreover, it becomes clear that there is no consensus yet on earthquake resistant design requirements. In the paragraphs hereafter, the recommendations made by well-known design standards are summarized and compared.

2.1.1. DNV-GL

According to the design standards published by DNV-GL:

- DNVGL-ST-0126: Support Structures for Wind Turbines (Ed. April 2016) [28],
- DNV-OS-J101: Design of Offshore Wind Turbine Structures (Ed. May 2014) [27],

the support structure should respond elastically to the environmental loads. The earthquake load is considered to act in combination with wind and wave loads during normal operation of the turbine. For parked conditions, the wind load is reduced to 80 % of its maximum. Three-dimensional spectral analysis is recommended, of the two horizontal and one vertical direction of propagation of the earthquake acceleration wave. The earthquake load should compare to the 475 year return period event.

For more detailed seismic analysis recommendations, DNV-GL refers to API and Eurocode 8, as well as local building codes.

2.1.2. Eurocode 8

Just as DNV-GL, Eurocode 8:

- EN 1998-5: Design of Structures for Earthquake Resistance - Part 5: Foundations, Retaining Structures and Geotechnical Aspects [32] (Ed. November 2004),

stipulates that the response of the structure should remain elastic, while on top of that there should be no structural collapse for a 10/50 event. A 10/50 year event means an earthquake occurrence for which the probability of being exceeded in 50 years time is 10 %. This corresponds to a return period of 475 years. The structure should hence be designed for an earthquake that is unlikely of being exceeded during the structure's lifetime. Based on historical data and recordings of past earthquake events, a probabilistic estimate can be made of the magnitude of a 10/50 event. For probabilistic estimation formulae, please see [95].

2.1.3. API

The design standard by the American Petroleum Institute:

- RP 2A-WSD: Recommended Practice for Planning, Designing and Constructing Fixed Offshore Platforms - Working Stress Design (Ed. December 2000) [2],

states that two levels of earthquakes should be considered in seismic design.

The first earthquake level should be of reasonable likelihood of not being exceeded during the structure's life, comparing to the 475 year return period event stated by DNV-GL and Eurocode 8. No significant structural damage should exist after this return period event, but no statement on whether or not the response should be elastic or can be (slightly) plastic is made, although the *"no significant damage"* requirement leans towards an elastic response assumptions.

The second earthquake level should be a rare, intense earthquake, with a return period of 1000 years. After such an event, irreparable damage may exist but the structure should hold enough reserve capacity to prevent a collapse. This recommendation is included in the API standard as it is focused on offshore platforms, which are not necessarily designed to respond elastically to environmental loads as monopile wind structures are. Insight into the deformational behaviour of these structures is therefore valuable.

2.1.4. The Taiwanese Building Code

This code is developed for onshore buildings:

- Seismic Design Code and Commentary for Buildings (Ed. 2011) [22],

but by lack of offshore wind recommendations may also be applied to the design of a monopile wind foundation offshore the coast of Taiwan.

This building code advocates the analysis of two level earthquakes, applying the same line of reasoning as the API codes. The design level earthquake should lead to no structural damage, and is defined as a 10/50 event as with Eurocode 8. The corresponding return period is 475 years (or 50 years divided by 10.5 %). In order to prevent structural collapse of the structure during an extremely large earthquake, a Maximum Considered Earthquake level was incorporated in the latest version of the design code. This MCE corresponds to a 2/50 event, which in turn reflects a 2475 return period event (calculated as 50 years divided by 2.02 %). These return periods and probabilities of exceedance are derived from an L-1 exposure level, for life-safety category S-1 (manned, non-evacuated structures).

The Taiwanese building code is the only code discussed in this chapter that includes dynamic as well as static analysis methods, and offers recommendations on when to use dynamic analysis; for buildings higher than 50 m, a height well below average hub height of a turbine, dynamic analysis is recommended. However, it does not specify under which circumstances to use spectral or time-history analysis, just as for the other design codes.

2.1.5. IEC

The design standards by the International Electrotechnical Commission:

- IEC 61400-1: Wind Turbines - Part 1: Design Requirements (Ed. 2014) [46],
- IEC 61400-3: Wind Turbines - Part 3: Design Requirements for Offshore Wind Turbines (Ed. 2009) [45],

state no earthquake resistance requirements except that the structure should respond elastically to a 475 year return period event. The earthquake environmental condition should be combined with the other environmental and operational loads under either normal power production or shutdown conditions. Dynamic analysis should be performed, but this can be either spectral or time-history analysis.

2.1.6. ISO

The International Organization for Standardization says in :

- ISO 19901-2: Petroleum and Natural Gas Industries - Specific Requirements for Offshore Structures - Part 2: Seismic Design Procedures and Criteria (Ed. 2014) [49],

that a designer should consider two level earthquakes. The Extreme Level Earthquake should lead to no structural damage and no interruptions of normal operations. The Abnormal Level Earthquake should hold no serious HSE consequences, although irreparable damage or a complete economic loss of the structure is possible. Considering the exposure level of an offshore wind turbine to be L-1, it being an unmanned (S-3) and high financial consequence structure (C-1), the return periods for an ELE and ALE event have been established as 500 year and 3000 year return events respectively. These return periods compare to the recommendations made by other design codes.

2.1.7. The Common Thread

In general, the design codes state that:

- the response of the structure to environmental action should be elastic,
- no damage to the structure should be done by an Extreme Level Earthquake, with return period 475 years,
- the earthquake motion should be applied as a separate environmental force, and the responses of the structure should be evaluated under normal operation and shutdown conditions,
- the dynamic analysis can be done by either spectral or time-history methods.

Only some codes, such as ISO 19901-2 and the Taiwanese Building Code, state that an Abnormal Level Earthquake event should be included in the design process; the structure may be damaged beyond repair, but should not collapse. This event is not included in most codes because only an elastic response of an offshore wind turbine foundation is allowed, and the structure is considered a loss from the point it no longer does. However, it may be interesting to know the extent of damage to the structure after such an abnormal event would have occurred.

Translating these recommendations in performance requirements, the structure:

- should show elastic behaviour and should suffer from no damage due to a 475 year return period ELE,
- should suffer from no collapse due to a 2475 year return period ALE but may suffer from permanent damage, although permanent tilt should stay within 0.5 °[53].

However, observations from geotechnical and earthquake engineering research have shown that in regions where moderate to strong ground motion may occur, and soft to medium soil conditions exist, a high degree of nonlinear inelasticity may be expected in the soil. As a consequence, the response of the foundation may as well be inelastic instead of the anticipated elastic behaviour. To illustrate the complexity of earthquake behaviour and strong ground motion characterization, the reader is shortly introduced to the dynamics of earthquakes in the subsequent section.

2.2. Earthquakes - An Introduction

An earthquake is the result of a sudden release of energy that had built up in the Earth's crust, and manifests itself by (violent) ground shaking. The origin of earthquakes can be *natural* or *artificial*, but most earthquakes are the result of inter-plate friction [68], referred to as *tectonic* earthquakes. A classification of earth tremors is shown in Figure 2.1.

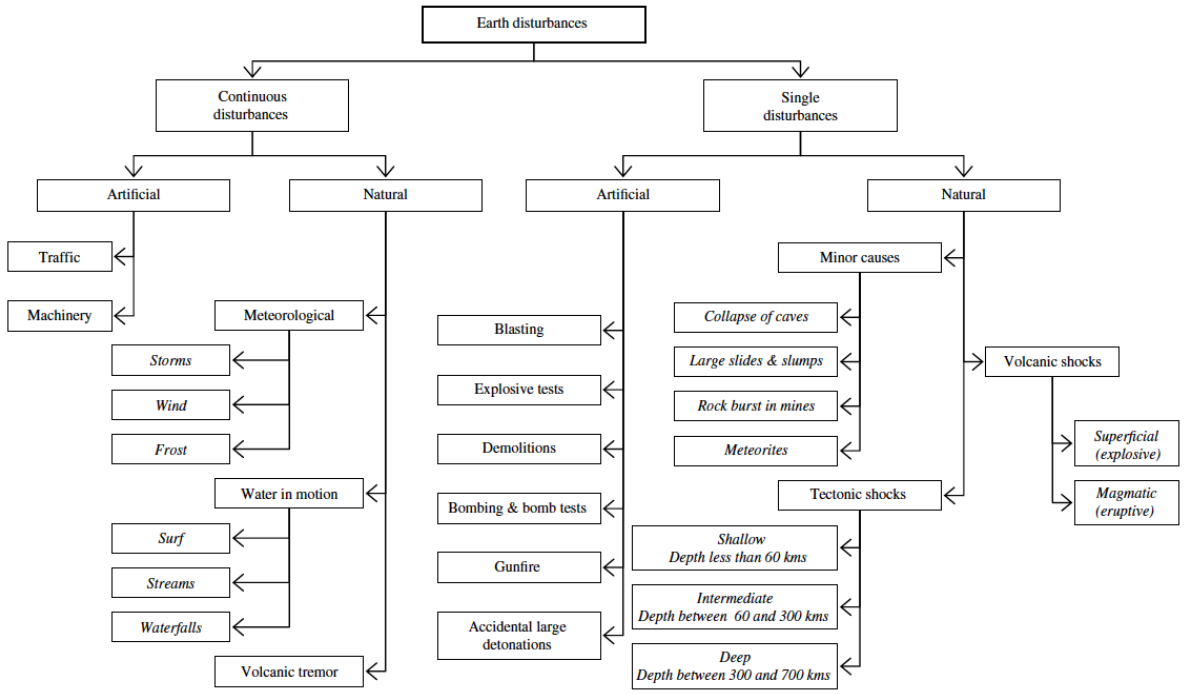

Figure 2.1: *Types of earthquakes based on their source (natural or artificial) and occurrence (continuous or single disturbance). Credit to [68] for the image.*

Tectonic earthquakes can be explained from the theory of large-scale plate tectonics. The Earth's outer structure consists of a solid lithosphere floating on a hot, highly viscous asthenosphere [95]. This lithosphere does not move as a single unit. In fact, it is divided into a pattern of different plates of various sizes [21]. The relative movement of these plates and their interaction at the plate boundaries is the main cause of earthquakes, with inter-plate[(1)] earthquakes amounting to 95 % of all recorded earthquakes in the world [68]. Evidence of the theory of plate tectonics is found in the high concentration of earthquakes along known plate boundaries, illustrated in Figure 2.3. Tectonic earthquakes are of particular interest to structural engineering, due to their large area of influence and their violent, unpredictable nature.

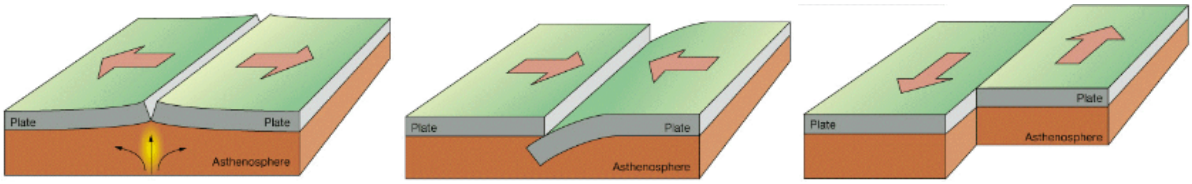

(a) *Divergent.* ***(b)*** *Convergent.* ***(c)*** *Transform.*

Figure 2.2: *Principal types of plate boundaries [76].*

[(1)] Next to inter-plate earthquakes, intra-plate earthquakes exist. These earthquakes occur at weak spots in the lithosphere plate, that were caused by internal fracture in the plate or by geological anomalies. Two types of intra-plate earthquakes exist: (1) plate-boundary related, where stress built up at the edges is transmitted through the plate and released at the weak spot; (2) mid-plate, which are unrelated to plate boundary activity [68].

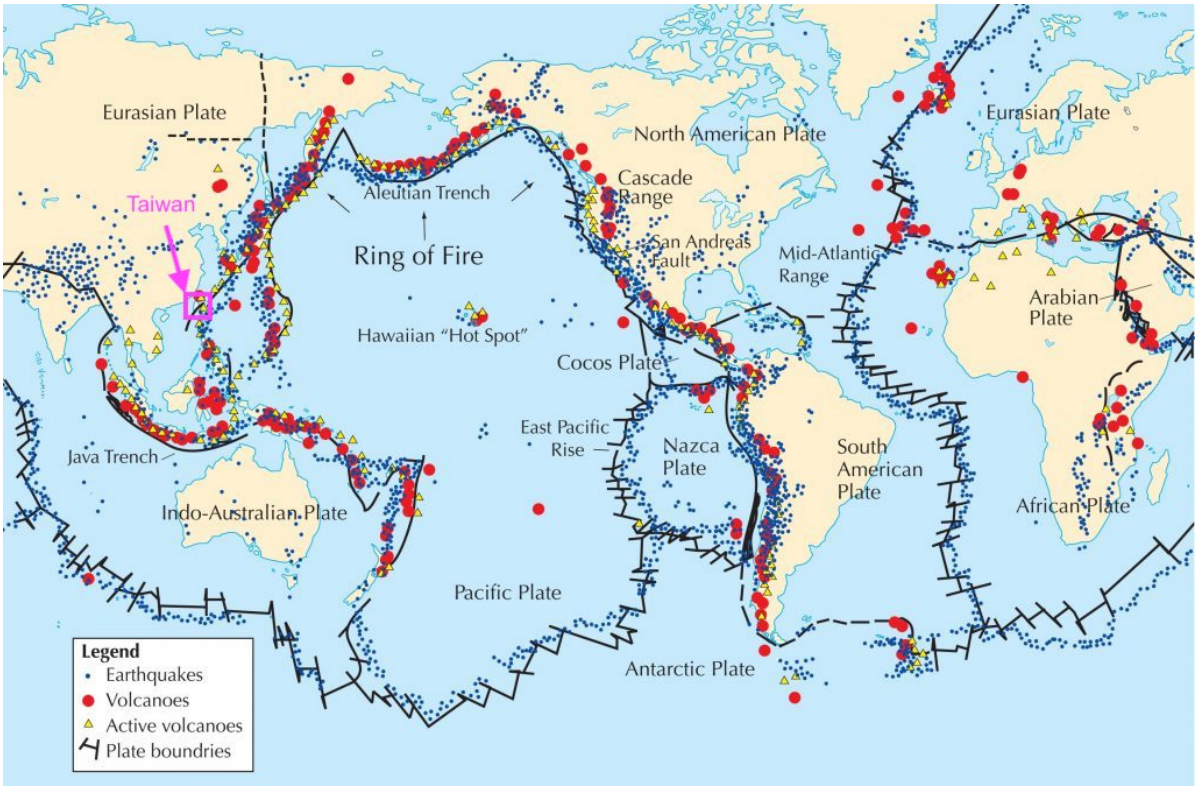

Figure 2.3: *Correlation between plate boundaries and the location of earthquakes, depicted on a world map [100].*

The principal types of plate boundaries are categorized according to their relative motion. Plates can either move towards each other (*convergent*), move away from each other (*divergent*), or slide past each other (*transform*), illustrated in Figure 2.2.

The type of plate boundary relates to the type of *fault*. The earthquake fault is the rupture in the Earth's crust where stresses and strains exceed the soil material's ultimate strength, from where built-up frictional energy is released as the ground cracks. The initial point of rupture is called the *focus* of the earthquake or *hypocenter*, the *epicenter* is the location of the focus as projected on the Earth's surface. As plates converge or diverge, the fault is classified as a *dip-slip* fault. For transform plates, the fault is classified as a *strike-slip*. A combination of these two types is called an *oblique* fault, where for example a convergent plate collides with two transform plates.

The depth of the focus classifies the earthquake as a shallow, intermediate or deep earthquake, and is directly related to the area affected by the ground motion as well as the intensity of the felt earth tremor. An overview of the correlation between plate boundary motion, fault type, physical collision mechanism, and depth and magnitude of the earthquake is listed in Table 2.1.

The energy released at the focus depends on the source characteristics, and the energy that reaches a structure located a certain epicentral distance away from the focus depends on the source-to-site effects. *Source effects* relate to the geometry (shape, size, depth, orientation) and dynamics of faulting (plate motion, faulting type, rise time, rupture velocity), and determine the initial amount of released energy. Wave propagation effects, – or *source-to-site effects* –, such as attenuation over epicentral distance, amplification over soft soil layers, and wave directivity, determine how much energy of the seismic wave still remains when the wave reaches the structure. Both effects determine the intensity of the perceived ground motion. However, quantifying these effects remains challenging, and as such it still proves hard to predict the earthquake magnitude from known faults. On top of that, each combination of factors leads to a completely new seismic record, causing a lot of variation in recorded ground motion by different accelerographs of the same earthquake incident.

Table 2.1: *Link between plate tectonics, plate movement, collision mechanism, earthquake depth & magnitude [68] [21].*

Plate boundary	Relative plate movement	Fault type	Collision mechanism	Depth Magnitude	Examples
Divergent	Separating	Normal or reverse dip-slip	Ridge	Shallow, small	Mid-Atlantic ridge
			Rift valley	Shallow, moderate	East-African rift
Convergent	Colliding	Normal or reverse dip-slip	Oceanic-continental plate	Shallow to deep[a], moderate	Peru-Chile trench
		Normal or reverse dip-slip	Oceanic-oceanic plate	Shallow to deep[a], moderate	Aleutian Island Chain
		Normal or reverse dip-slip	Continental-continental plate	Shallow to deep[a], large	Himalayan Mountains
Transform	Sliding	Strike-slip or transform	Transcurrent horizontal slip	Shallow, large	San Andreas fault

[a] The Wadati-Benioff zone marks the depth to which seismic energy release can occur along the subduction plate. The foci can be as deep as 700 km. Past this depth, the plate's properties change from solid to a highly viscous type fluid of molten rock and solid particles in the asthenosphere. The release of seismic energy is inhibited, as no further straining and fracturing of solid material can take place.

The vast amount of influential factors on the seismic wave cause a high variability in observed ground motions from the same fault, or even the same earthquake event. That is why dynamic analysis with only one ground motion does not capture all possible scenarios of earthquake exposure. In spectral analysis, design spectra are composed of multiple earthquake recordings, where all observed and estimated maximum events are included. For time-history analysis, it is recommended to use either multiple earthquake recordings or to scale available earthquake records to different magnitude, this to capture the variation is earthquake intensity. This latter approach, called *incremental dynamic analysis*, will be applied in this thesis project to analyze the capacity behaviour of the structure to increasing levels of strong ground motion. By including all possible events and events unlikely to be exceeded during the structure's lifetime, the design converges to an earthquake-resistant structure.

2.3. Incremental Dynamic Analysis

Incremental dynamic analysis (IDA), or dynamic pushover analysis, provides an estimate of the structural capacity under earthquake loads of varying intensity, and sheds light on the progress of elastic over yielding to collapse behaviour of a structure. It is the recommended method for time-history analysis that can capture the high variability in earthquake magnitude by artificially modifying the record's amplitude to levels that comply with probabilistic events such as the ELE and ALE, events of which no record exists.

For one ground motion record, multiple dynamic analyses are executed. In each dynamic analysis, the amplitude of the ground motion record is scaled to a certain intensity, for example:

$$\ddot{y}_{g,\text{scaled}} = \lambda \cdot \ddot{y}_{g,\text{original}} \tag{2.1}$$

where λ is the intensity measure or scale factor. For λ <1 the ground motion record is scaled down to a lower intensity, for λ >1 the intensity of the ground motion record is increased [93]. The intensity levels are selected such that they cover the range of elastic to collapse response of the structure, or such that they cover the minimum acceleration level up to the ALE acceleration level.

For each level of intensity λ, a dynamic response-history analysis is performed to observe the response behaviour of the system under earthquake loading of such intensity. The maximum response – in terms of top displacement, base shear or any other damage measure – is plotted versus the intensity level. The procedure is repeated for all levels of intensity of the same earthquake record to predict the response of the structure under earthquake loading of rare intensity. The resulting IDA curve provides a continuous picture of the capacity progress of a structure [93].

A single record IDA may not provide insight in all possible behaviours of the structure under random earthquake loading, as only the magnitude of the record is scaled and not the period or duration – ground motion characteristics which highly influence the nonlinear response of the system. Ideally, different records of the same earthquake event or records of different earthquake occurrences should be scaled to the same levels of intensity to analyze all possible dynamic capacity behaviour of the structure [93]. The result would be a family of IDA curves, as shown in Figure 2.4, where each IDA curve is record-specific. However, time series records of earthquakes are scarce, and it might not be possible to identify earthquake records of distinctly different frequency content and duration. Nevertheless, IDA of a record associated with the worst-ever-recorded ground motion can already provide valuable insight on how the structure would behave if it was to ever experience such an event during its lifetime.

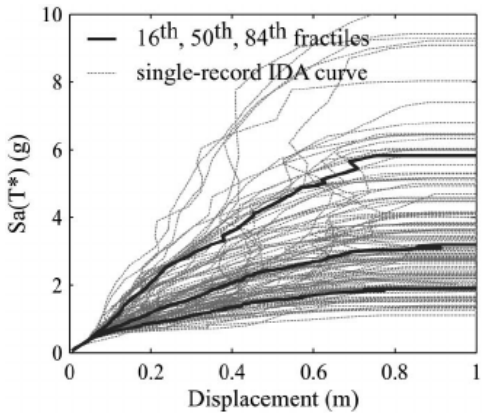

Figure 2.4: *Incremental dynamic analysis – Family of curves from different input motions, showing that the structural response is not only defined by the motion intensity but also the motion period and duration [6].*

The selection of the intensity levels and damage measure depends on the purpose of the analysis and the structural system under consideration [68]. When the purpose of the analysis is to identify the ultimate limit capacity (Chapter 2.4) of a wind turbine structure, it might be worthwhile to focus on the base shear stress as the damage measure of interest; in case of a ductile system, the intensity levels should cover the yield state of the system. For serviceability response analysis, a useful damage measure can be the top rotor displacement.

The IDA method is valuable in providing better understanding of the structural implications of rare ground motion levels [68]. Additionally, it provides insight into the changes in structural response with increasing intensity level when strength and stiffness degradation – of the structure or soil – occur. Lastly, IDA curves are a visualization of the dynamic stability of the structure, making it easy to identify structural collapse.

Considering the advantages of this method over other seismic dynamic analyses, incremental dynamic analysis will be applied to the design problem in this thesis work. For a comparison of all analysis methods, please see the literature study preceding this document [95].

2.4. Effects of Earthquakes on a Structure

Earthquakes can lead to different types of failure of a wind turbine structure. The three main categories are described below.

2.4.1. Ultimate Limit State

Earthquakes can induce violent shaking in a structure, which can lead to plastic deformation of the structural material known as an Ultimate Limit State (*ULS*) failure. Deformations of the material are no longer reversible, and the structure is left with permanent damage.

2.4.2. Serviceability Limit State

Earthquake vibrations can also cause a structure to tilt beyond its allowable or workable limits, thereby causing a serviceability failure. It does not necessarily mean that the structure has suffered a ULS failure. It might be that the soil beneath the structure gave way due to the intense vibrations, or it might be that the elastic response of the structure surpasses its workable limits.

2.4.3. Fatigue Limit State

Lastly, earthquake vibrations are cyclic, and can therefore introduce cyclic or fatigue damage. Even though fatigue damage in seismic design studies is most often neglected, *"several analytical studies have demonstrated that the duration of the ground motion and the corresponding number of cycles are of importance for the assessment of low-cycle fatigue damage"*[68]. It might be that a structure would not normally fail when exposed to only one occurrence of a certain peak ground acceleration, but might do so by repeated exposure; this failure is known as fatigue limit state failure.

The three structural failure modes might occur due to earthquake loading, but also due to forcing by the other environmental conditions such as wind, wave and current. The failure modes are shown in Figure 2.5.

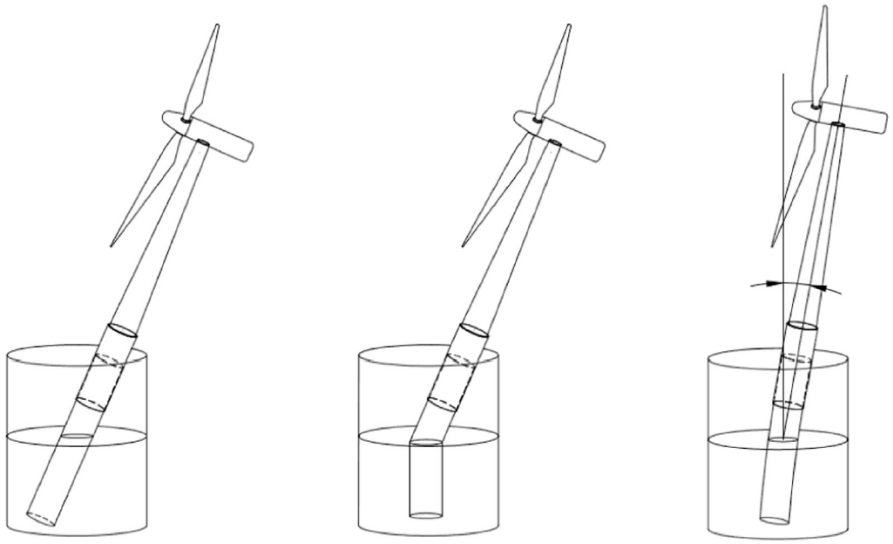

Figure 2.5: *Structural failure modes: serviceability limit state failure (SLS), ultimate limit state failure (ULS) and fatigue limit state failure (FLS) [56].*

In this thesis project, the focus lies on ULS and SLS failure behaviour of the structure. This because only one record is used in an incremental dynamic analysis set-up, where the focus lies on the capacity behaviour and not the damage behaviour from repeated loading.

2.5. Effects of Earthquakes on a Soil Profile

The earthquake will not only have an effect on the structure, but also on the soil encompassing the monopile foundation. The moderate to strong ground motion may cause the properties of the soil medium to change.

The influence between the earthquake and the soil is two-ways. The soil alters the seismic wave as it travels from source to site by attenuating its energy, as was explained in Paragraph 2.2. But the energy of the seismic wave will in turn alter the properties of the soil medium, and the ground motion will induce friction, loading and unloading of the soil. As a result, the soil may lose its strength, either by cyclic degradation, fracture or liquefaction.

Assuming elastic behaviour of a soil-structure system is therefore not consistent with physical observations during moderate to strong ground motion. Soft to medium soil samples are known to exhibit nonlinear behaviour that may induce an inelastic response of the foundation, such as yielding, fracturing, cyclic softening or liquefaction [31].

Consequently, it is key to incorporate as many nonlinear soil-structure interaction effects in a seismic computational model of the design, as they will govern the response of the system for ground motions of increasing intensity. Ignoring these effects may result in erroneous estimations of the structure's response. Assuming an elastic soil-structure interaction may not capture the likely behaviour of the system when it is subjected to earthquakes of high intensity.

As such, the analysis recommendations by design standards (Paragraph 2.1), where it is advised to use nonlinear elastic soil resistance behaviour[(2)] in combination with an elastic response assumption of the pile, should be compared to a model that incorporates nonlinear inelastic responses of the soil-structure system. This to verify if an elastic model is capable of capturing the response of a pile foundation to strong ground motion. The seismic soil-structure model used in this thesis project is introduced in the next paragraph, Chapter 2.6.

2.6. Seismic Soil-Structure Interaction Models

The interaction between a pile foundation and the surrounding soil is most simply and computational cost-efficiently modeled by a nonlinear Winkler spring foundation. The resistance of the soil to lateral pile motion is reflected in the stiffness of the soil springs that are distributed along the embedded pile length, as shown in Figure 2.6. The soil spring stiffness is computed with empirical expressions for different types of soil that have been derived in the past [2] [95]. These p-y curves are nonlinear elastic expressions of the soil loading and unloading (or *soil resistance*) to lateral pile displacement.

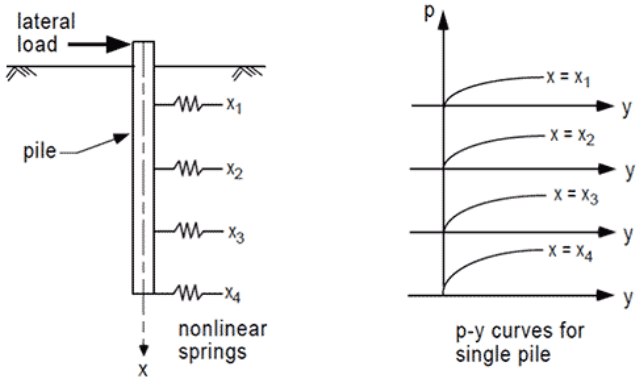

Figure 2.6: *Illustration of a nonlinear Winkler spring foundation for lateral pile motion analysis [25].*

Concerns exist regarding the validity of these p-y expressions for applications for which they were not experimentally derived, such as large diameter piles, but also regarding the limited amount of experimental results on which they are based. Additionally, the expressions were derived under static loading circumstances, and may not be reliable in modeling a highly dynamic environment such as a seismic soil-pile system.

The responses of pile foundations in soft soils subjected to strong ground motion can become rather large compared to the pile length, and consequently can no longer be approximated as linear elastic. For the linear elastic theory to be valid, the relative displacements between soil and structure should remain small, which is mostly the case in firm ground where the soil-structure body is subjected to low intensity earthquakes [89]. In loose or soft soils, under moderate to strong earthquake loads, the relative displacement can become large; soil nonlinearities become predominant, and will highly influence the dynamic response of the SSI system.

[(2)] The nonlinear elastic soil resistance behaviour with pile displacement refers to the recommended p-y curves, developed for different types of soil, as stated in the API design standard [2]. In these elastic p-y relations, the loading path of the soil is assumed identical to the unloading path, thus neglecting hysteretic damping by slack zone development, cyclic degradation, liquefaction or radiation damping. For an elaborate discussion on the p-y formulae, please see [95]

Nonlinear inelasticity can be caused by [89]:

- soil or structural yielding,
- gapping (clay) or cave-in (sand), also known as slack-zone development,
- cyclic softening or hardening (in general referred to as cyclic degradation),
- liquefaction,
- radiation damping.

A BNWF model used to analyze the soil-structure response under seismic action should include as much of these nonlinear inelastic effects as possible to arrive at a reasonable approximation of the true response [89]; Boulanger et al. [13] and El Naggar et al. [31] have proposed different formulations of an inelastic BNWF. Inelastic BNWF use adaptations of the static elastic p-y curves, also referred to as *dynamic* p-y curves.

Proof of nonlinear inelasticity in the soil-structure response can be found when [13]:

1. *"the fundamental period of the structure changes by permanent deformations of the soil or structure"*,
2. *"the calculated response is sensitive to the duration, frequency and level of shaking of the input motion"*.

These observations from experimental research necessitate the development of a BNWF model that can incorporate nonlinear inelastic effects, such as soil or structural nonlinear behaviour, discontinuity conditions at the soil-pile interface, and energy dissipation through soil radiation damping [31]. It also advocates the use of dynamic time-history analysis, as spectral analysis will not capture the sensitivity of the response to the characteristics of the input motion (*amplitude, frequency* and *duration*).

The choice of BNWF model and the definition of its parameters will influence the soil-structure response. Two seismic soil-structure interaction models are discussed and compared hereafter; the series hysteretic-viscous damping model developed by Boulanger et al. (Sub. 2.6.1) [13] and the semi-series hysteretic-viscous damping model by El Naggar et al. (Sub. 2.6.2) [31][1].

2.6.1. Series Hysteretic-Viscous Damping Model

Boulanger et al. [13] proposed a *series hysteretic-viscous damping* model, which incorporated soil-pile slack zone development by a parallel drag and closure spring. The nonlinear p-y element is shown in Figure 2.7. The pile is connected to the gapping element, in series with a plastic deformation spring and elastic spring with viscous (or radiation) damping. Hysteretic damping is caused by the gapping and plastic behaviour, thus arriving at the name *"series hysteretic-viscous damping"*. This seismic soil-structure interaction model is available in OpenSees, a software framework for simulating the seismic response of structural and geotechnical systems, developed at the University of California, Berkeley.

The lateral response of the element y is equal to the sum of responses of the elastic, plastic and gap springs, the total resistance force p is equal to the sum of the force exerted by the drag and closure spring. The backbone curves to the dynamic p-y curves are the ones recommended by the American Petroleum Institute API; the stiffness of the linear elastic spring in the element is retrieved from these standard nonlinear elastic p-y curves. The original equations describing the plastic, closure and drag spring can be consulted in Boulanger et al. [13], the simplified expressions are presented in Paragraph 3.1.3 of this report.

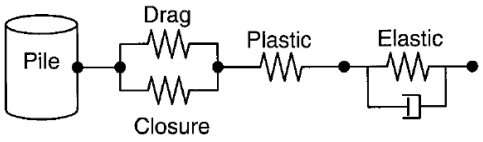

Figure 2.7: *The nonlinear elastoplastic p-y element of the series hysteretic-viscous damping model by Boulanger et al. [13].*

The input to the nonlinear elements, at the elastic outer node, is the ground motion derived from site response analysis (see Paragraph 4.5.2). In the research conducted by Boulanger et al. [13], the response of the soil-pile structure proved to be more sensitive to the SRA method than to variation in the p-y element characteristics; equivalent linear SRA introduced a high level of uncertainty in the model, and reduced the accuracy of seismic soil-structure analysis [13]. Even when applying nonlinear site response analysis, as strong ground motion is known to induce nonlinear inelasticity in the soil, the sensitivity of the response to the SRA results remained. The use of borehole data significantly improved the accuracy of the computation, however, this type of data is not widely available.

Even though some approximations and assumptions were made, such as [13]:

- the use of equivalent linear site response analysis for the input strong motion (thereby ignoring nonlinearities in the soil),
- the uncoupling of the site response and soil-structure response (reflected in the use of different soil resistance models, respectively Kelvin-Voigt (see 4.5.2) and series hysteretic-viscous elements),
- the implementation of independent p-y springs (thus neglecting interaction between soil layers, radial and three-dimensional effects),
- the uncertainties in the definition of the soil properties and p-y characteristics,
- the uncertainties in the site response analysis that produce the input motion,

the analysis method still held reasonable results when compared to experimental tests.

2.6.2. Semi-Series Hysteretic-Viscous Damping Model

The simplified model proposed by El Naggar et al. [31] of the Boulanger model — which was further developed into a generalized dynamic Winkler model for nonlinear soil–structure interaction analysis by Allotey and El Naggar [1], and implemented in the commercial software SeismoStruct — is denoted a *semi-series hysteretic-viscous damping model*, where no drag term is considered at the gapping element and the elastic and plastic spring are merged into one (see Figure 2.8). The elastic p-y curves from the API standard are again used as the backbone curve for the dynamic p-y curves, just as in the method proposed by Boulanger [13]; the initial stiffness of the dynamic p-y curves is equal to the soil-structure stiffness of the static elastic curves.

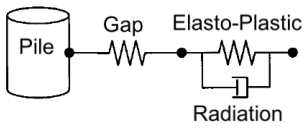

Figure 2.8: *The dynamic p-y element of the semi-series hysteretic-viscous damping model by El Naggar et al. [31] [1].*

The results in the study by El Naggar et al. [31] showed a slightly poorer correlation with experimental values compared to the series hysteretic-viscous damping model by Boulanger et al. [13], which could be attributed to either neglecting the drag term in the soil-structure surface discontinuity or to the radiation damper being in parallel rather than in series with the plastic spring (which may cause excessive dashpot forces).

The accuracy of the analysis, just as for the series hysteretic-viscous damping model, is affected by [31]:

1. the input motions from one-dimensional wave propagation site response analysis (linear or nonlinear),
2. the uncoupling of the site response analysis and the soil-structure interaction response analysis,
3. uncertainties in the soil properties and elastoplastic dynamic p-y curves,

but specifically by [31]:

4. the omission of drag resistance and soil degradation effects in the soil hysteric behaviour.

It is this last point that causes the inelastic BNWF model by El Naggar et al. [31] to show slightly poorer correlation with experimental data than the Boulanger model [13].

2.6.3. Selection of the Seismic Soil-Structure Interaction Model for this Project

Seismic SSI systems can be cost-efficiently approximated by a beam on a nonlinear Winkler spring foundation. Although this type of model ignores three-dimensional effects and assumes no interaction between the soil layers, it provides insightful estimates of the real-life structural responses in an early design stage. *Inelastic BNWF* can incorporate nonlinear inelastic behaviour of the soil and structure. The nonlinear dynamic p-y curves in the BNWF model as formulated by Boulanger et al. [13] show results that agree well with the true response of the pile under seismic action.

It should be noted that series damping models are preferred over parallel damping models, as the latter risk excessive dashpot forces that might unrealistically dominate the p-y behaviour [13]. Therefore, the series hysteretic-viscous damping model by Boulanger et al. [13] is preferred over the semi-series hysteretic-viscous damping model by El Naggar et al. [31].

However, careful use and interpretation of the backbone p-y curves is warranted; they were derived for slender flexible piles, where cyclic degradation and liquefaction is neglected, from limited experimental tests performed under different circumstances. On one hand the option is raised to adjust the elastic backbone curves for liquefaction conditions; possible ways to adjust the p-y curves recommended by API have been proposed by Lombardi et al. [61] and Dobry et al. [29], but with limited increased accuracy in analyses. Additionally, small diameter flexible piles were exposed to low cyclic loading unlike seismic loading [61], and the results were extrapolated to arbitrary pile dimensions and soil conditions by theoretical analysis in 2D [50]. Attempts to formulate analytical expressions to account for pile dimension effects, three dimensional interaction and soil effects have reached no consensus yet. Therefore it is still recommended to use the p-y curves as recommended by API while keeping in mind their limitations in structural design analysis.

Lastly, this model can be valuable to compute the seismic soil-structure response with reasonable accuracy, given that the designer remains aware of the sensitivity of the model to the results of the site response analysis. If possible, borehole data should be used as input to the nonlinear series-hysteretic viscous damping model, as this would eliminate the uncertainties introduced by the SRA. However, this data is not readily available for all locations in the world. In Taiwan, no borehole data exists prior to 2007[(3)], and for the area of interest in this study no records of strong ground motion exist after deployment of the borehole nationwide network. Only free-field motions can be used, making SRA necessary prior to SSI analysis. More on the site response analysis of the earthquake time-series record used in this study, is presented in Chapter 4.5.2.

[(3)] The Taiwanese borehole seismic network construction commenced in 2007, and is still expanding. On authority of Mr. Hsin-Chih Hsu of the Central Weather Bureau, the organization operating the seismic networks in Taiwan, it was learned that there exists no borehole data yet of a significant earthquake near the location of the monopile foundation. Only free-field records of strong ground motion exist. [Information as received on 16th of May, 2018].

3

Seismic Soil-Structure Interaction Modeling

For any piled foundation, the embedded structure and the surrounding soil will interact and influence each other. The structure will experience resistance from the soil to any lateral or vertical motion, while the soil will be loaded by the pile motion and hence may experience changes in its overall behaviour. Modeling the interaction between the soil and the piled foundation is of paramount importance when analyzing a monopile design and predicting its short- and long-term response behaviour.

Seismic action poses an additional challenge in accurately describing and predicting soil-structure responses. Earthquakes are of a highly variable nature, and may propagate as small to large amplitude waves in the same area due to the same fault. The energy contained in the seismic wave will mobilize a response in the soil medium and the structure, and will be altered in return following the soil-structure response. But also the structure and especially the soil properties may change due to the energy wave, – resulting in structural or soil yielding, and cyclic degradation, liquefaction, or radiation damping of the soil –, the extent of which is defined by the amount of energy the seismic wave carries.

In this research study, the lateral seismic soil-structure interactive response behaviour is under investigation. It is questioned whether a classical beam on a nonlinear Winkler spring foundation model is accurate enough to capture all or most nonlinear inelastic action in the soil or structure that is associated with earthquakes. As such, two seismic soil-structure interaction models will be introduced in this chapter. One structural model is presented in Chapter 3.2, that will be coupled to either one of two soil interaction models introduced in Chapter 3.1.

3.1. The Soil

The soil profile presented herein is a simplification of the actual soil conditions at the site, a non-disclosed location off the coast of Taiwan.

The interaction between this soil medium and the monopile foundation will largely determine the overall behaviour of the entire structure. In addition, – as could be taken away from the discussion on earthquakes in the preceding Chapter 2 and from the literature review project [95] –, the properties of the soil will determine how the seismic wave propagates from source-to-site and how much energy this wave still has left when it excites the foundation. Vice versa, the seismic wave will potentially influence the soil properties and may consequently force the foundation responses in a more indirect manner.

Defining the soil properties as accurately as possible, and constructing a seismic soil interaction model that approximates real behaviour as closely as possible, is key to achieving a computational model that can predict the response of the offshore wind support structure to reasonable accuracy.

3.1.1. Properties of the Soil Profile

The soil profile at the location of the monopile foundation consists of five distinct layers, shown in Figure 3.1 and Figure 3.22, with parameters as presented in Table 3.1. This soil profile and these characteristics will be used throughout this study.

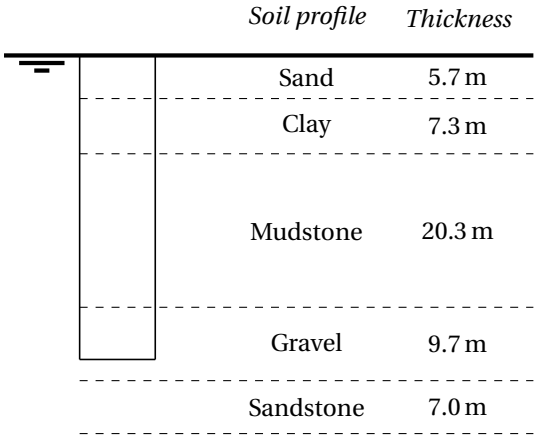

Figure 3.1: *Soil profile used in this thesis study.*

It is important to use a soil profile that reflects the true conditions at the site as closely as possible, as the interaction of the foundation with the soil will largely determine the response behaviour of the entire structure. In addition, the foundation design under analysis was specifically designed for the soil profile in Figure 3.1 with soil conditions presented in Table 3.1, and may prove inadequate for other locations with dissimilar properties.

Table 3.1: *Reference soil profile at the non-disclosed monopile location.*

	Sand	**Clay**	**Mudstone**	**Gravel**	**Sandstone**	Units
Effective density ρ'	897	958	1009	1019	1009	kg/m^3
Friction angle ϕ	25	-	-	32	-	°
Undrained shear strength σ_u	-	55	150	-	265	kPa
Strain factor 50 % ϵ_{50}	-	1.000	0.018	-	0.018	%
Shear wave velocity V_s	200	290	540	375	700	m/s

It is assumed that the soil layers described in Table 3.1 are perfectly horizontal and extend to infinity. In addition, it is assumed that these parameters remain constant in those soil layers. Lastly, the soil is assumed to be saturated with water as the soil profile is located at a subaqueous site.

3.1.2. The Nonlinear Elastic Model

The first soil model presented hereafter is based on the recommended practice by the American Petroleum Institute (API, [2]), and is referred to by other design standards such as IEC, ISO and DNV-GL.

The Beam on a Nonlinear Winkler Spring Foundation

The lateral interaction of the soil layers with the foundation can be modeled in different ways, listed hereafter in order of descending complexity [38]:

1. *"numerical methods such as finite element and boundary element that treat the soil as a continuous medium discretized into elements",*

2. *"the continuum approach, with closed form solutions by considering the soil as a semi-infinite space",*

3. *"the beam on a nonlinear Winkler foundation, which treats the soil as a series of disconnected springs".*

The continuum approach, or the finite element discretized numerical methods of this approach, provide a high level of detail and accuracy in predicting the soil resistant force in response to pile displacement, but those numerical methods come at a high computational cost.

The BNWF method uses uncoupled springs to simulate the soil resistance, and is most popular due to its simplicity as compared to the (numerical) continuum approach. The BNWF method approximates the soil behaviour by distributed springs along the pile's embedded length, where the stiffness of those springs represents the resistance of the soil against pile displacement. It is the preferred method in engineering practice, and is recommended by design standards for general offshore structures – see the standard by the American Petroleum Institute [2] – although validation of this method by means of numerical FE analysis is recommended for piled structures with diameters surpassing 1 m [28]. On top of that, it can account for soil nonlinearities with limited computational effort [38]. It is a simple and computationally inexpensive approach, that can approximate the soil behaviour adequately. Considering these two major benefits of the BNWF method, this method is applied to the thesis problem. An illustration of the beam on a nonlinear Winkler spring foundation was presented in Figure 2.6 of Chapter 2.6.

However, the BNWF method has some limitations::

1. the three-dimensional problem is simplified to a one-dimensional, in-plane pile contact, thereby neglecting radial and 3D interaction effects [31],

2. the springs in each soil layer are uncoupled, thereby arriving at independent calculations that ignore response interaction between soil layers [31],

3. the empirical backbone nonlinear p-y curves to this method may have been derived under different conditions, and may not be representative of the actual soil-structure loading conditions.

Zooming in on the last point, the stiffness of the springs in the nonlinear Winkler foundation model is derived from empirical p-y curves in this study, where p denotes the lateral soil resistance per unit length and y the pile displacement in lateral direction. These standardized expressions for the soil resistance to lateral pile movement were estimated from slender pile experiments in homogeneous soils of distinct properties.

But, offshore wind support structures are rarely considered slender (with diameters exceeding 8 m on occasion), nor is the soil homogeneous (mostly layered profiles), or can it be classified as one type (mixed soils, e.g. silty-clay, are common). In addition, these curves do not account for cyclic effects accurately or may not account for them at all. The concern regarding the application of the p-y method is expressed in the DNV-GL standard [27] as a guidance note, stating:
«"Caution must be exercised when the recommended nonlinear p-y curves are used in other contexts than for evaluation of lateral pile capacity in the ULS. Such contexts include, but are not limited to, SLS analysis of the pile, fatigue analysis of the pile, determination of equivalent spring stiffnesses to represent the stiffness of the pile-soil system as boundary condition in analyses of the structure that the pile-soil system supports, and in general all cases where the initial slope of the p-y curves may have an impact." »[27]

This concern is reflected in the uncertainty on how to simulate the changing soil under the influence of dynamic loading. ULS analysis is most often a *static* analysis, where the properties of the soil are not expected to change. However, in dynamic analysis, the soil will suffer from cyclic degradation due to the cyclic nature of the environmental forces. Additionally, strong ground motion associated with earthquakes can lead to liquefaction in saturated sand soils.

Numerous adaptations of the existing p-y curves have been proposed to account for large diameter effects [101], three-dimensional effects [83], liquefaction [61] [24] [20], cyclic degradation/hardening [89] [13], and gapping between the pile and the soil leading to inelastic hysteretic response of the soil-structure [31] [89] [13], – all effects which the p-y curves recommended by API [2] were not validated for. For simplicity reasons, it was decided to work with the standard p-y expressions in the nonlinear elastic soil-structure interaction model. The only correction made is for the soil layering effect according to the method described by Georgiadis [34], presented hereafter.

The Static P-y Curves

The reaction force of the soil against lateral pile movement can easily be modeled by simplifying the soil to a continuous system of springs, distributed over the leading edge of the embedded monopile. The soil resistance force per unit length, p, is a nonlinear function of the pile displacement y. The soil spring stiffness, k, is the gradient of the nonlinear elastic p-y curve or the *tangent* stiffness, as illustrated in Figure 3.2.

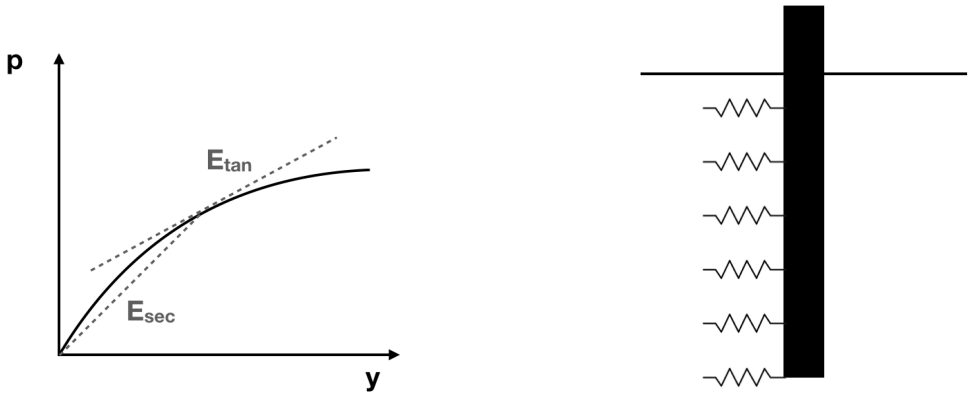

Figure 3.2: *Illustration of a beam on a nonlinear Winkler spring foundation approach, using p-y curves to express the soil resistance per unit length with pile deflection.*

A nonlinear p-y curve generally consists of an initial perfectly elastic zone, where small pile displacements do not cause permanent deformations of the soil. Only where the p-y relation is linear elastic, is the tangent stiffness equal to the secant stiffness. Following the elastic zone, is a region of mixed elastic and plastic behaviour until the soil starts yielding; during this phase, some deformations are becoming permanent, which decreases the soil stiffness. After yielding, the soil behaves elastoplastic up to when it reaches its ultimate capacity, after which it responds fully plastic. Beyond the ultimate soil resistance limit, the soil fails, and its stiffness is reduced to zero.

The nonlinear p-y curves will be referred to as *nonlinear elastic* in this study since the soil loading path is assumed identical to the unloading path. There is no inelastic cyclic degradation, hysteretic or radiation damping, or gap formation incorporated in the nonlinear elastic soil-structure interaction model that may cause the loading path to differ from the unloading path.

It should be highlighted that the nonlinear p-y curves will not be the same across the entire embedded pile length. The resistance of the soil with pile displacement is influenced by:

1. the soil type,
2. the depth below mudline,
3. the water table,
4. the loading type (static, dynamic, cyclic),
5. the diameter of the pile cross-section,
6. the shape of the pile cross-section,
7. the flexural stiffness of the pile,
8. the friction coefficient between foundation and soil,
9. the installation conditions of the pile.

The API recommended standardized curves account for some of these influential factors – such as soil type, depth, water table, diameter, friction angle –, but even then the influential factors are idealized by assuming:

- one distinct type of soil in a layer (no mixes, such as silty-clay, sandy-clay,...),
- perfectly horizontal layers with no interaction at their boundaries,

or the p-y curves are used outside their experimentally validated range, leading to:

- the equation derived for a slender pile being applied to a large diameter monopile,
- the use of static p-y curves in dynamic/cyclic analysis problems such as seismic design.

As highlighted before, attempts to formulate analytical expressions to account for large pile diameter effects, three dimensional interaction, highly dynamic environments and soil cyclic degradation/liquefaction effects have led to results of varying quality. For simplicity reasons, the API recommended p-y expressions, that account for points 1 - 5[4], will be used. The shortcomings and pitfalls of these expressions as aforementioned should be kept in mind.

The Sand and Gravel Layer The top layer of the soil profile consists mostly of sand particles, and the fourth layer of gravel particles (see Table 3.1). Both layers are assumed to behave according to the empirical p-y relation for submerged sand. O'Neill and Murchison [72] developed a hyperbolic equation that expresses the soil resistance per unit length with pile displacement. This equation depends on the depth below the surface and was derived for static and cyclic loading conditions of sand soil below the water table.

The ultimate soil resistance can be computed as [72]:

$$p_{\text{ult}} = \min \begin{cases} (C_1 \cdot d + C_2 \cdot D) \cdot \gamma' \cdot d \\ C_3 \cdot D \cdot \gamma' \cdot d \end{cases} \tag{3.1}$$

where the ultimate soil resistance p_{ult} is the minimum of the ultimate soil resistance to either shallow surface (wedge) failure or deep (flow) failure in sand, as illustrated in Figure 3.3. The coefficients C_1, C_2 and C_3 depend on the internal friction angle ϕ, and can be derived from Figure 3.4 [98] [2]. The depth d in this equation is the absolute value of depth, D is the diameter of the pile, and γ' is the effective unit weight of the soil. Values for d, γ' and ϕ are listed in Table 3.1. The effective unit weight is related to the effective density as $\gamma' = \rho' \cdot g$, where g is the gravitational acceleration constant.

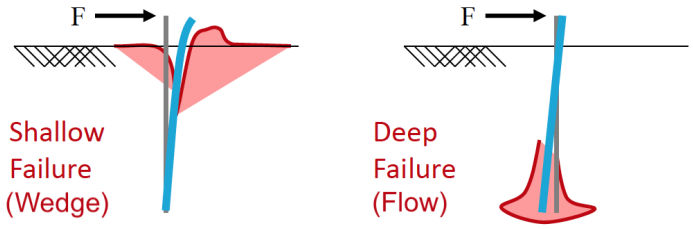

Figure 3.3: *Shallow failure versus deep failure in sand [43].*

According to the hyperbolic equation derived by O'Neill and Murchison [72], the variation of soil resistance per unit length p with pile deflection y can be computed as:

$$p = A \cdot p_{\text{ult}} \cdot \tanh\left(\frac{E_s \cdot d \cdot y}{A \cdot p_{\text{ult}}}\right) \tag{3.2}$$

where the constant A depends on the type of loading:

$$A = \begin{cases} 0.9 & \text{for cyclic loading} \\ 3.0 - 0.8 \cdot \frac{d}{D} \geq 0.9 & \text{for static loading} \end{cases} \tag{3.3}$$

[4] Points 4 and 5 are accounted for in the sense that (4) the parameters can be selected for a dynamic environment, although the empirical p-y curves were derived for low cycle loading (5) the diameter of the pile is included in the empirical equations, but these equations were only validated for piles up to 1.2 m.

and E_s is the initial modulus of subgrade reaction depending on the internal friction angle ϕ, which can be derived from Figure 3.5[(5)] for sand below the water table (conform the assumptions made in Section 3.1.1). Considering the nature of earthquake loading, which is highly dynamic and cyclic, it is assumed that the constant A is equal to 0.9 in this analysis.

The p-y curve for sand and gravel at some depth below the mudline, for the soil parameters as defined in Table 3.1, can be found in Figure 3.10 and 3.13.

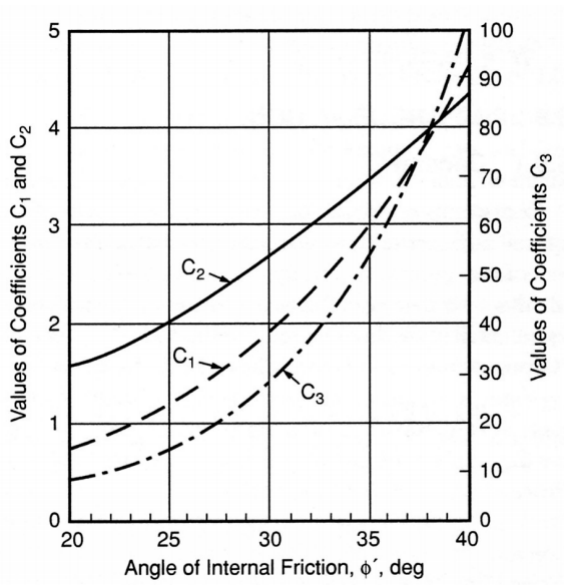

Figure 3.4: *Determination of the coefficients C_1, C_2 and C_3 for the computation of the ultimate soil resistance of sand below the water table [98].*

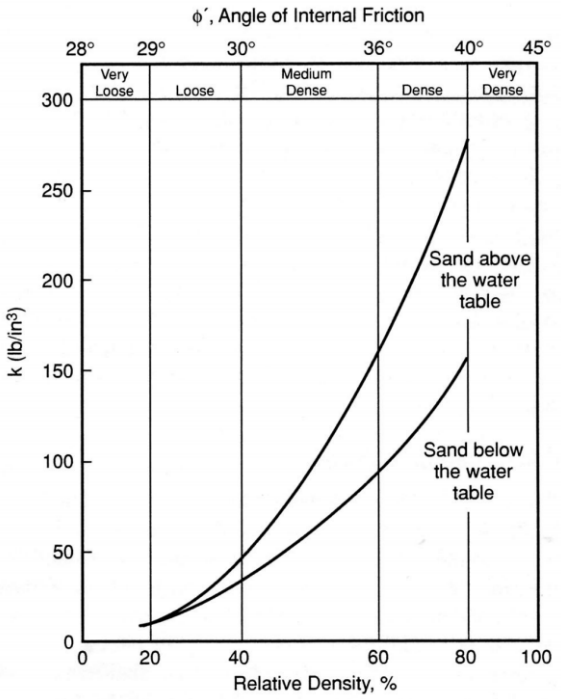

Figure 3.5: *Initial modulus of subgrade reaction k, dependent on the internal angle of friction, for sand above and below the water table [98].*

The Clay Layer The clay layer from Table 3.1.1 would be classified as *medium* to *stiff* according to Terzaghi et al. [87] in Table 3.2. According to another definition, for an undrained shear strength below 75 kPa clay is generally assumed to be soft [54]; the soil layer in this study has an undrained shear strength of 55 kPa, which would thereby classify as soft. Therefore, the clay soil layer in Table 3.1 will be treated as medium soft, meaning the soft clay equations by Matlock [65] will be applied with its parameters tuned to account for the rather stiff nature, as shown hereafter.

Table 3.2: *Consistency of clay in terms of unconfined compressive strength, copied from [87].*

Consistency	**Undrained shear strength[(6)] [kPa]**
Very soft	≤ 12.5
Soft	12.5 - 25
Medium	25 - 50
Stiff	50 - 100
Very stiff	100 - 200
Hard	≥ 200

[(5)] The initial modulus of subgrade reaction E_s can be found from the figure, – where the initial modulus of subgrade reaction is denoted as k –, provided that lb/in^3 is properly converted to N/m^3, i.e. times 271,447.14. For friction angles as low as 25° initial stiffness values are not shown in Figure 3.5, but it was assumed that the curve progresses at zero tangent below 29°.

API recommends the use of the Matlock equations [65] to compute the soil resistance in a soft submerged clay layer. The shape of the p-y curve depends on the loading type, as shown in Figures 3.6a and 3.6b for a monotonic and cyclic loading condition respectively. Considering the nature of earthquake loading, the cyclic equations are implemented in the nonlinear elastic seismic soil-structure interaction model.

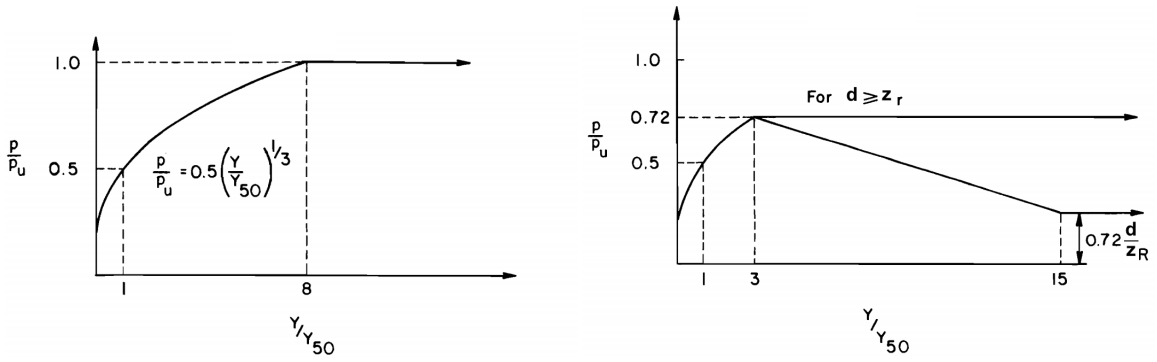

(a) *Monotonic soft clay p-y curve.* ***(b)*** *Cyclic soft clay p-y curve.*

Figure 3.6: *P-y curves as formulated by Matlock for soft submerged clay [65]. Image copied from [67].*

The equation to compute the ultimate soil resistance of a soft submerged clay layer is [65]:

$$p_{\text{ult}} = \min \begin{cases} 3 \cdot \sigma_u \cdot D + \gamma' \cdot d \cdot D + J \cdot d \cdot \sigma_u \\ 9 \cdot \sigma_u \cdot D \end{cases} \tag{3.4}$$

where – just as for the sand and gravel layer – the minimum value of the ultimate soil resistance is sought for, complying with the soil suffering from a surface wedge or deep flow failure when the ultimate resistance of the soil is reached. The constant J in this equation indicates whether the clay is in fact soft or rather medium soft. In this case, the latter condition holds, meaning J can be assumed equal to 0.25 [79].

The soil resistance p can be found according to the procedure explained in the book by Reese & Impe [79]. First, the y_{50} value and transition depth z_r need to be computed:

$$y_{50} = 2.5 \cdot \epsilon_{50} \cdot D \tag{3.5}$$

$$z_r = \frac{6 \cdot \sigma_u \cdot D}{\gamma' \cdot D + J \cdot \sigma_u} \tag{3.6}$$

where y_{50} signifies the pile displacement for which the soil resistance reaches 50 % of the ultimate soil resistance, and is hence a measure of the ductility of the clay. The transition depth identifies the boundary layer below which the clay starts behaving elastic-perfectly plastic (see Figure 3.6b for $d \geq z_r$) under cyclic loading conditions.

If the depth d is larger or equal to z_r, then:

$$p = \begin{cases} \frac{1}{2} \cdot p_{\text{ult}} \cdot \left(\frac{y}{y_{50}}\right)^{(1/3)} & \text{for } y \leq 3 \cdot y_{50} \\ \frac{1}{2} \cdot p_{\text{ult}} \cdot 3^{(1/3)} & \text{for } y > 3 \cdot y_{50} \end{cases} \tag{3.7}$$

If the depth d is smaller than the transition depth z_r, then according to Figure 3.6b:

$$p = \begin{cases} \frac{1}{2} \cdot p_{\text{ult}} \cdot \left(\frac{y}{y_{50}}\right)^{1/3} & \text{for } y \leq 3 \cdot y_{50} \\ 3^{1/3} \cdot \left[\left(\frac{d}{z_r} - p_{\text{ult}}\right) \cdot \frac{y}{24 \cdot y_{50}} + \frac{5}{8} \cdot p_{\text{ult}} - \frac{1}{8} \cdot \frac{d}{z_r}\right] & \text{for } 3 \cdot y_{50} < y \leq 15 \cdot y_{50} \\ \frac{1}{2} \cdot \frac{d}{z_r} \cdot 3^{1/3} & \text{for } y > 15 \cdot y_{50} \end{cases} \tag{3.8}$$

(6) In Terzaghi et al. [87], the classification is based on the unconfined compressive strength q_u, which relates to the undrained shear strength as $q_u = 2 \cdot \sigma_u$.

However, these cubic expressions in Equation 3.7 and 3.8 predict infinite initial stiffness (see Figures 3.6a and 3.6b), which is not physical. Therefore, according to the DNV-GL standard comment F2.4.6 [28], the initial soil stiffness is relaxed according to the expression:

$$k = \frac{10 \cdot p_{\text{ult}}}{D \cdot (\epsilon_{50})^{0.25}} \tag{3.9}$$

Figure 3.11 shows the p-y curve for clay at a certain depth, for the soil parameters as defined in Table 3.1.

The Mudstone and Sandstone Layers The mudstone and sandstone layer both classify as (extremely) weak rock according to the undrained shear strength in Table 3.1; their respective shear strengths are 150 kPa and 265 kPa, which compares to a compressive strength of 300 kPa and 530 kPa[(6)]. Hoek [39] classified rock as extremely weak when the unconfined compressive strength is between 250 - 1,000 kPa.

Considering the strength of the rock layers, their resistance to lateral pile movement is best approximated by the weak rock equations of Reese [78]. The equations to compute the ultimate soil resistance are:

$$p_{\text{ult}} = \begin{cases} \alpha_r \cdot q_u \cdot D \cdot \left(1 + \frac{1.4 \cdot d}{D}\right) & \text{for } 0 \leq d \leq 3D \\ 5.2 \cdot \alpha_r \cdot q_u \cdot D & \text{for } d > 3D \end{cases} \tag{3.10}$$

where q_u is the unconfined compressive strength of the soil material[(6)], d is the depth and D is the pile diameter. The strength reduction factor α_r is computed as:

$$\alpha_r = 1 - \frac{2}{3}\frac{\text{RQD\%}}{100\%} \tag{3.11}$$

with RQD the rock quality designation as defined by Deere [26]:

$$\text{RQD} = \frac{\text{length core pieces} > 100\,\text{mm}}{\text{length total core run}} \tag{3.12}$$

The soil resistance p with pile deflection y can then be calculated by [70][78]:

$$p = \begin{cases} K_{ir} \cdot y & \text{for } y \leq y_A \\ \frac{p_{\text{ult}}}{2} \cdot \left(\frac{y}{y_{rm}}\right)^{0.25} \leq p_{\text{ult}} & \text{for } y > y_A \end{cases} \tag{3.13}$$

where K_{ir} is the initial elastic modulus:

$$K_{ir} = k_{ir} \cdot E_{ir} \tag{3.14}$$

with E_{ir} the intact or initial modulus of rock and k_{ir} a dimensionless constant depending on the depth of the soil layer and the diameter of the pile. E_{ir} can be estimated from the unconfined compressive strength by an empirical relation proposed by Hoek & Diederichs [40]:

$$E_{ir} = \text{MR} \cdot q_u \tag{3.15}$$

where MR is the modulus ratio, which is assumed equal to 300 for mudstone and 350 for sandstone according to Hoek [39]. The dimensionless coefficient k_{ir} can be calculated as:

$$k_{ir} = \begin{cases} 100 + \frac{400 \cdot d}{3 \cdot D} & \text{for } 0 \leq d \leq 3D \\ 500 & \text{for } d > 3D \end{cases} \tag{3.16}$$

The variable y_{rm} in Equation 3.13 can be found by:

$$y_{rm} = k_{rm} \cdot D \tag{3.17}$$

The constant k_{rm} determines the overall stiffness of the p-y curve. The smaller the value, the smaller the elastic zone of the curve, the more stiff the initial elastic curve is and the sooner the curve becomes perfectly plastic. Considering the extremely weak and therefore expected soft/ductile behaviour of the rock layers, a high k_{rm} value is selected. It is assumed constant over depth and equal to 0.007 for both mud- and sandstone.

Just as with the clay layer, the p-y expression for weak rock predicts an infinite initial stiffness. As the DNV-GL standard [28] makes no recommendations towards the correction of the weak rock equations' initial stiffness, this stiffness is relaxed according to the expression for clay albeit with a different factor:

$$k = \frac{40 \cdot p_{\text{ult}}}{D \cdot (\epsilon_{50})^{0.25}} \tag{3.18}$$

This factor was determined based on the requirement of having a zone of at least 0.02 m elasticity, see Figures 3.12 and 3.14.

The Soil Layering Effect - The Georgiadis Correction Method

It is important to realize that the p-y curves by O'Neill & Murchison [72], Matlock [65] and Reese [78] were empirically derived for homogeneous soil specimens. Design standards such as DNV-GL [28], ISO [48] and API [2] warn for the use of these p-y curves in applications for which they were not validated, of which soil layering is an example. In this case study, the soil is horizontally layered. The overburden pressure of the overlying soil layers will influence the resistance of the lower layers. The standard p-y curves need to be adapted for this soil layering effect, as otherwise the soil resistance may be underestimated (in case of a more dense layer overlying a lighter one) or overestimated (in case of a less dense layer overlying a heavier one).

Basu & Salgado [9] and Suzuki et al.[85] amongst others have highlighted that "*soil layering is an important factor that affects laterally loaded pile response*" [10]. In reality, discrete soil layers will often be present, but rather limited analyses considering discrete soil layer effects in the p-y approach exist [10]. The method developed by Georgiadis [34] is one of the few, and is recommended by the API recommended practice 2GEO for geotechnical and foundation design considerations [3]. But, as the method is not explained step-by-step in this standard, it is not often applied in practice. The method is however easy to implement in a BNWF model, and as such it was decided by this author to follow the method as developed by Georgiadis [34] and described in the textbook by Reese & Van Impe [79].

Georgiadis [34] proposed a corrective method where the *equivalent depth* of the layers below the upper layer is determined. This equivalent depth signifies the depth at which the underlying layer would have virtually started if the overlying layer would have been of the same material. This depth is found by equating the sum of ultimate resistances of the top layer to the underlying layer, and identifying the depth boundary where the two equations become equal.

For the first soil layer (in this case, sand) the ultimate resistance p_{ult} is calculated with the standard equation (Eq. 3.1), from mudline (d = 0 m) to the end of the sand layer (d =-5.7 m). The ultimate resistance force over this depth is:

$$F_1 = \int_0^{\text{d, sand}} p_{\text{ult,sand}}\, dx \tag{3.19}$$

The underlying layer is a soft clay layer. Simply applying the standard empirical soil resistance formula for soft clay would lead to a result that corresponds to a homogeneous soil profile, i.e. where the overlying layer also consists of clay particles. This is not the case, and these results would overestimate the soil resistance in the clay layer: the overlying sand is less dense than the clay, and will lead to a lower overburden pressure than clay would have. Consequently, due to less dense sand overlying the clay, the soil resistance in the clay will be lower than would be estimated by the standard formula for homogeneous soils.

With the method proposed by Georgiadis [34], one tries to identify the depth for which the ultimate resistance force of a supposedly homogeneous clay soil would be equal to the force F_1 of the overlying sand soil [79]:

$$F_1 = \int_0^{\text{d, sand end}} p_{\text{ult,sand}}\, dx = \int_0^{d_{\text{eqv}}, \text{ clay}} p_{\text{ult,clay}}\, dx \tag{3.20}$$

where $p_{\text{ult,clay}}$ is calculated with Eq. 3.4. The equivalent depth d_{eqv} is the unknown variable, which can be found by solving the equating formula.

Once found, d_{eqv} signifies the depth where the clay layer would *equivalently* start, that is, from where the computed soil resistance for an assumed homogeneous clay soil would compare correctly to the layered sand plus clay soil. A visualization of this explanation is shown in Figure 3.7 and 3.8. The length of the soil layer does not change, it is merely the start- and endpoint that are shifted, such that the clay layer starts at the equivalent depth and ends at the equivalent depth plus the thickness of the layer.

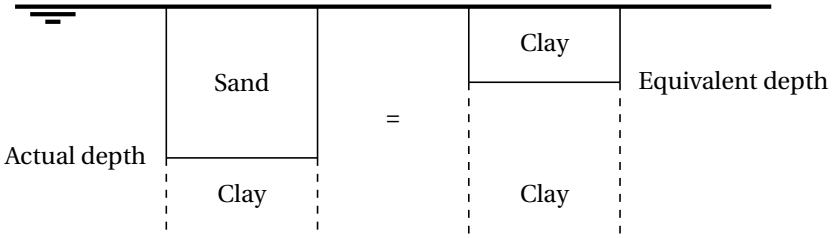

Figure 3.7: *Visualization of the Georgiadis method.*

For all subsequent layers, the procedure is the same. The equivalent depth of the mudstone layer underlying the clay layer is found by finding the equilibrium between:

$$F_2 = \int_0^{d_{eqv},\text{ clay end}} p_{ult,clay}\,dx = \int_0^{d_{eqv},\text{ mudstone}} p_{ult,mudstone}\,dx \tag{3.21}$$

The resulting equivalent depths for all soil layers are visualized in Figure 3.8. From the figure it can be clearly observed that when less dense soil layers overly heavier layers, the equivalent depth of the underlying layer is less deep than the physical depth. This is because the lighter overlying layers have created less overburden pressure than when the overlying layers would have been of equal density material as the underlying layer.

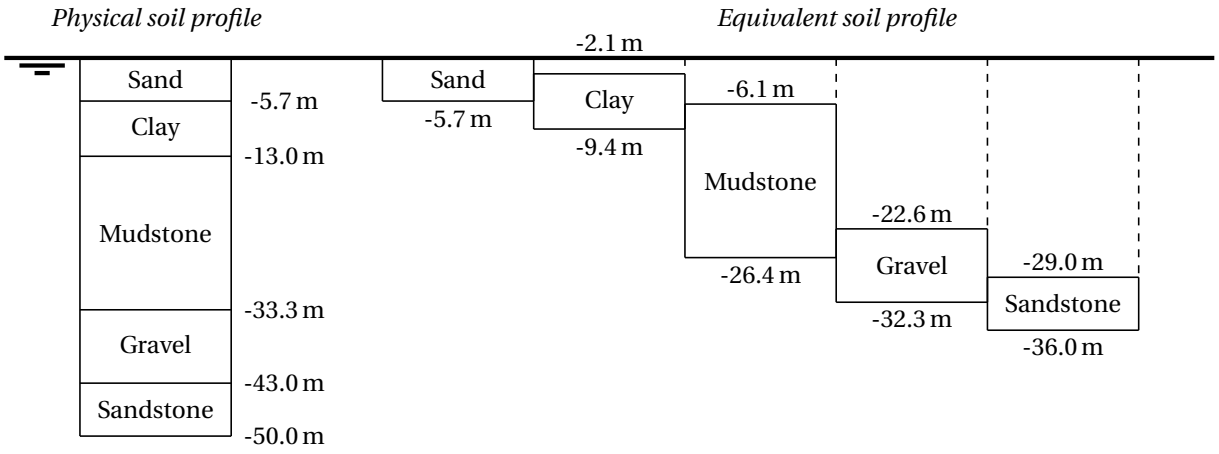

Figure 3.8: *Equivalent depths as calculated for all soil layers, and compared to the physical soil profile.*

The Resulting Layered Static P-y Curves

With these equivalent depths now determined, the ultimate soil resistances and p-y curve values for all underlying layers should be recalculated with the physical start- and endpoints of each layer replaced by the equivalent ones. This way, the computed values better approximate a layered soil profile. The ultimate soil resistance per unit length and soil resistance per unit length are visualized in Figures 3.9 to 3.14. It should be noted that the soil resistance at the mudline, which corresponds to zero depth, is assumed to be equal to zero (or of negligible magnitude).

The results presented hereafter are for a beam on a nonlinear Winkler spring foundation, with structural properties of the monopile foundation as presented in Chapter 3.2.1. The p-y curves presented are the empirical p-y curves as recommended by API [2], including the correction by Georgiadis [34] for the soil layering effect. Some observations can be made regarding the p-y behaviour of the soil layers.

First of all, as no gapping, hysteretic damping or any other inelastic effect is included in the p-y behaviour of the soil springs, the loading path is equal to the unloading path.

Secondly, it may be seen from the graphs that the sand and gravel layer reach their ultimate resistance quicker with increasing pile displacement than the more ductile clay and weak rock layers do. The tangent stiffness of the former layers will reduce to zero at smaller pile displacements, and consequently these layers will hold no stiffness against the motion of the foundation for displacement levels where the clay, mud- and sandstone layer still will; the soil spring stiffness is reduced to zero.

Lastly, for the sandstone the ultimate resistance is equal over the entire layer thickness. Consequently, the p-y behaviour is equal over the total depth of the layer; that is why the two displayed p-y curves in Figure 3.14 coincide. For the other layers, where the ultimate soil resistance increases gradually with increasing depth, the soil resistance increases with depth; the p-y behaviour at two different nodes in the same layer are distinct, see Figures 3.10 to 3.13.

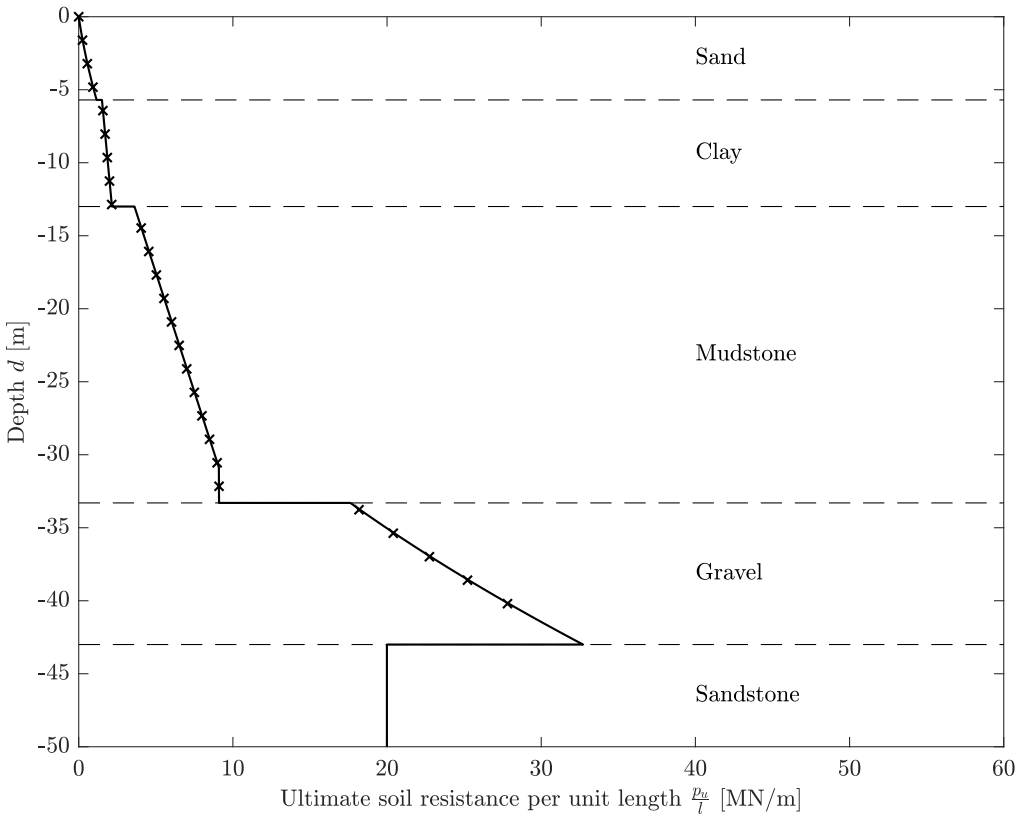

Figure 3.9: *Ultimate soil resistance per unit length for each soil type layer along the depth of the inhomogeneous soil profile. The crosses indicate the location of the soil spring at each node in the finite element model.*

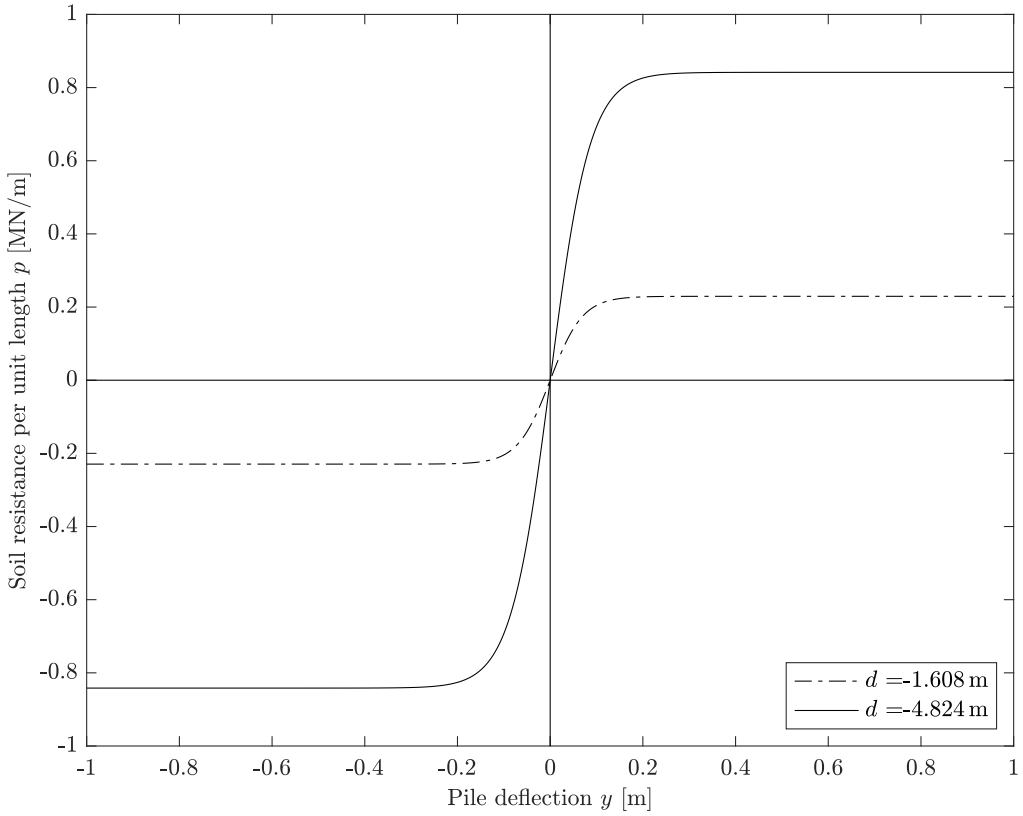

Figure 3.10: *P-y behaviour in the top sand layer, for the first node below mudline and at the end of the layer.*

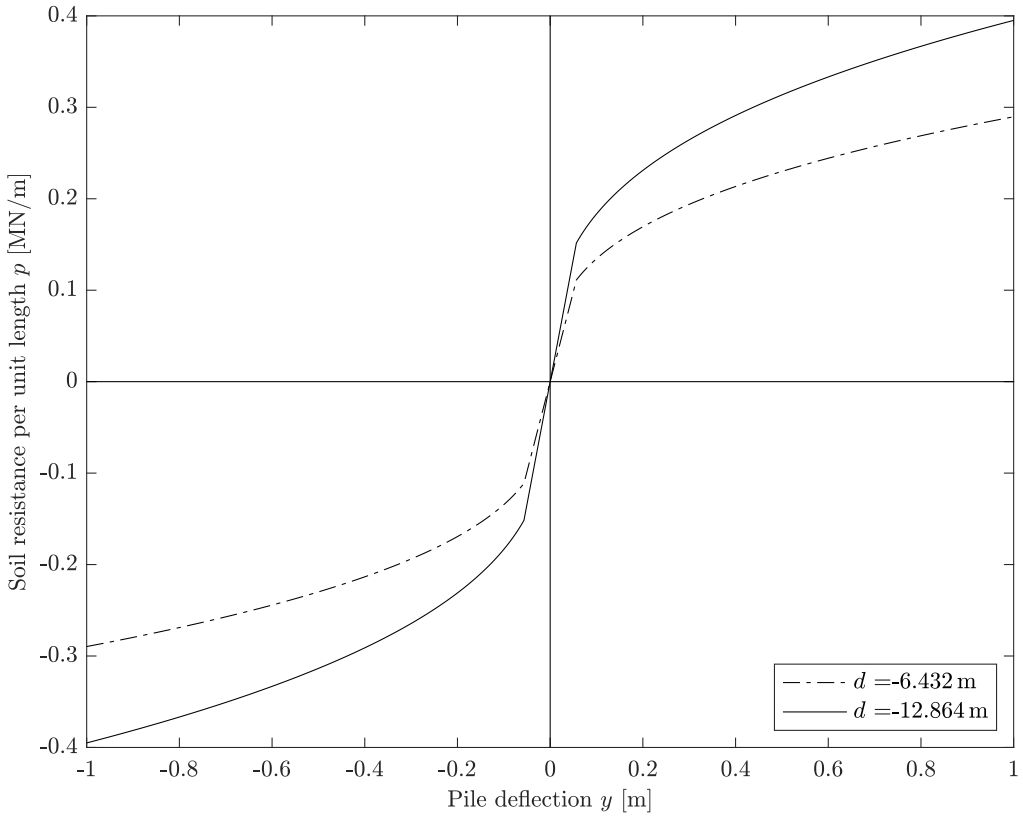

Figure 3.11: *P-y behaviour in the clay layer, at the start and at the end of the layer.*

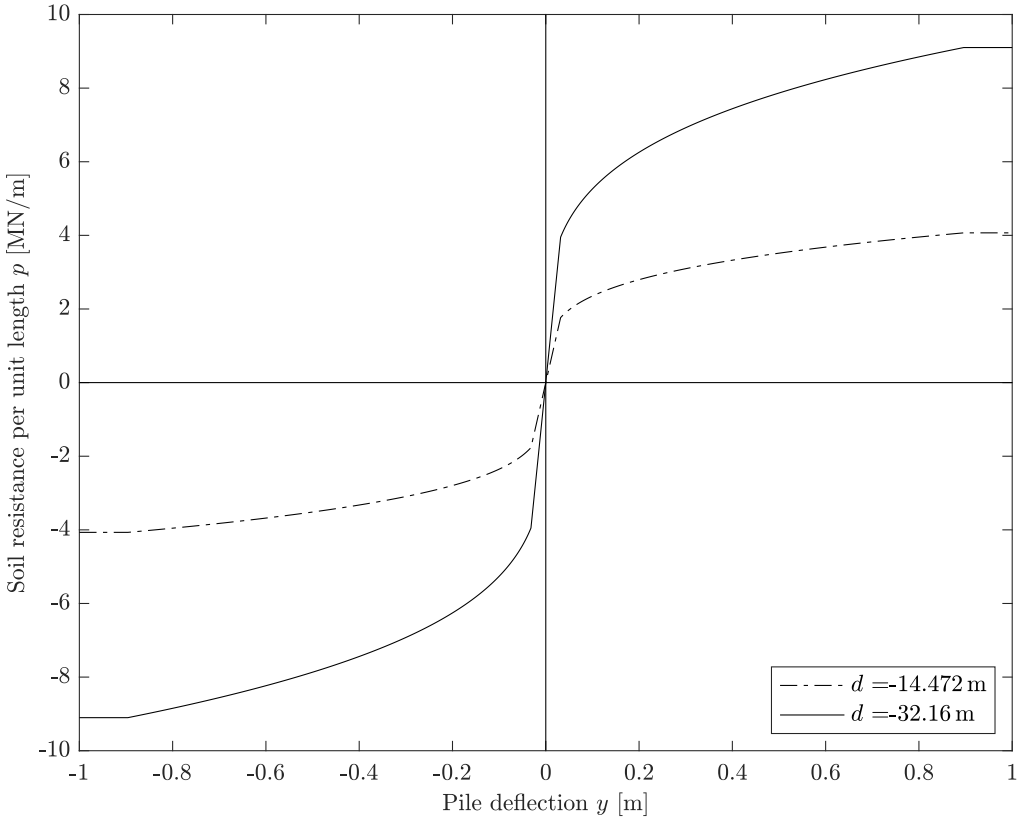

Figure 3.12: *P-y behaviour in the mudstone layer, at the start and at the end of the layer.*

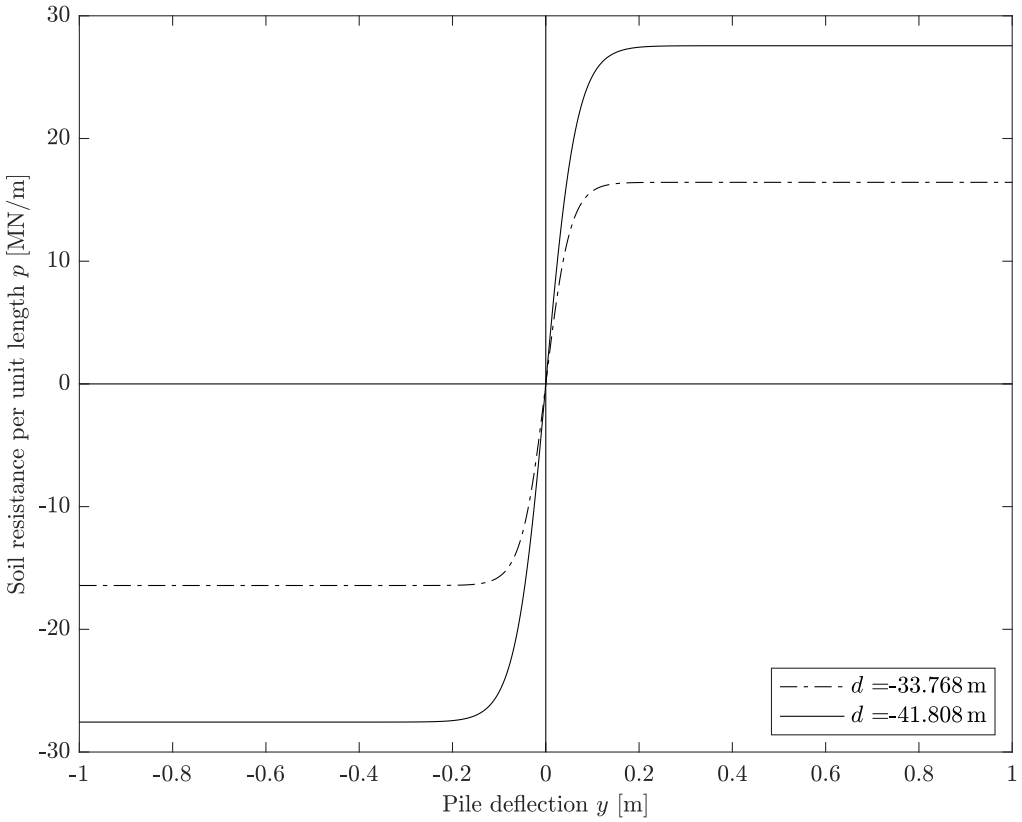

Figure 3.13: *P-y behaviour in the gravel layer, at the start and at the end of the layer.*

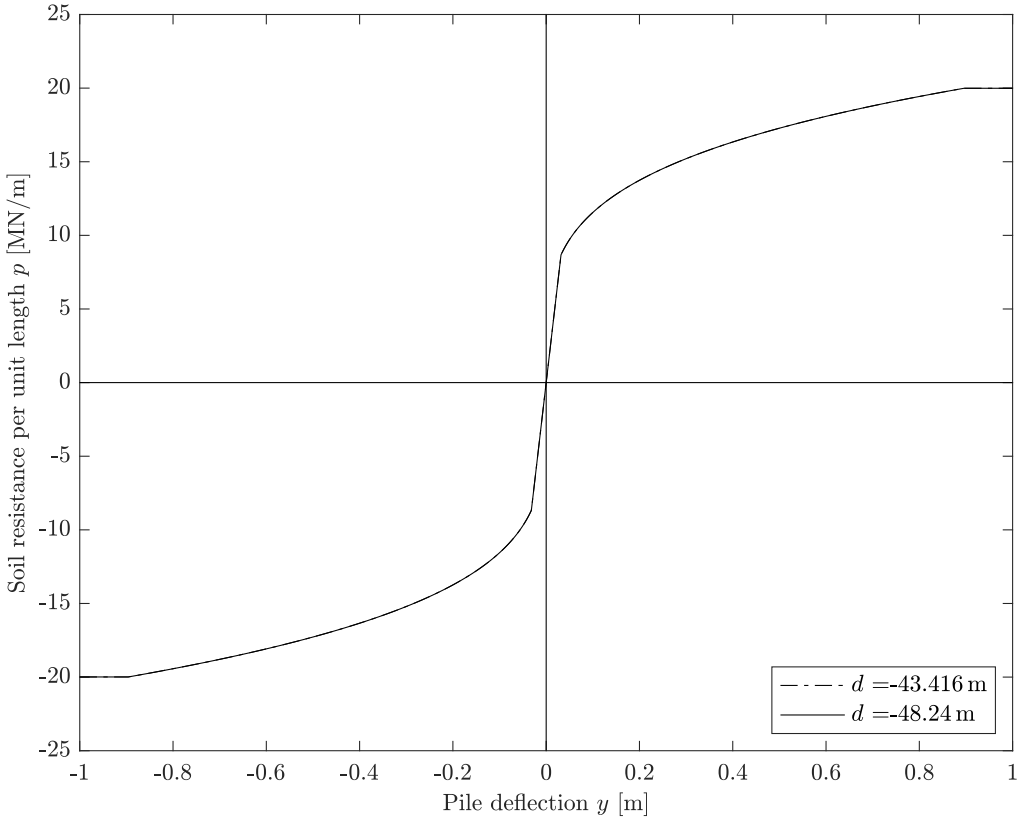

Figure 3.14: *P-y behaviour in the sandstone layer, at the start and at the end of the layer.*

3.1.3. The Nonlinear Series Hysteretic-Viscous Damping Model

The standard BNWF p-y curve approach fails to capture most nonlinear inelastic effects associated with strong ground motion, which cause the loading path to differ from the unloading path of the soil. The soil modeling technique proposed by Boulanger et al. [13] – which is still based on the BNWF approach using p-y curves – manages to show better agreement between actual and computed structural responses of piled structures under seismic conditions; it captures more of the inelastic effects, such as gapping, soil weakening due to pore pressure built-up, hysteretic and radiation damping. Still, the three limitations to the static p-y BNWF approach (1D approximation of a 3D problem, uncoupled soil springs, empirical curves; see Chapter 3.1.2) also apply to the method proposed by Boulanger et al. [13].

The Dynamic P-y Curves

The classic static p-y curve approach as described in Chapter 3.1.2, – using empirical nonlinear elastic expressions to compute the soil resistance with pile deflection –, has a limited applicability in highly dynamic analyses, such as for earthquake analysis of structures. The development and use of dynamic p-y curves in earthquake structural analysis, that incorporate many of the nonlinear inelastic behaviours of soil and structure alike under earthquake motion, becomes necessary. This section explains the advantages of an inelastic BNWF in seismic structural analysis, and how a series hysteretic-viscous damping model is applied in this thesis study. This soil model is referred to as the *nonlinear inelastic* seismic soil-structure interaction model in this report.

Soil Response Under Strong Ground Motion The soil is known to behave nonlinear inelastic when subjected to strong ground motions [38]. Proof for the nonlinear inelastic behaviour of soft soils is found in all strong ground motion studies; they show nonlinear site amplification at soft soil sites when subjected to large amplitude motions [41]:

1. In time domain solutions, this is observed in a reduction of the amplitude of the waveform over time. In frequency domain solutions, a shift in predominant frequency and peak reduction can be found. Both are due to the changes in elastic properties of the soil.

2. The velocity of the S-wave before and after the main shock is different, indicating that the soil properties have changed.

3. The spectra of observed data between surface and bedrock during strong and weak ground motions are fundamentally different, indicating that weak ground motions are governed by a linear elastic response while strong ground motions cause permanent deformation (leading to a nonlinear inelastic response).

4. The comparison of recorded and linearly computed site responses shown a pertinent difference. This difference can be attributed to nonlinearity effects, next to uncertainties in the soil properties.

The responses of pile foundations in soft soils subjected to strong ground motion can become rather large compared to the pile length, and consequently can no longer be approximated as linear elastic. For the linear elastic theory to be valid, the relative displacements between soil and structure should remain small, which is mostly the case in firm ground where the soil-structure body is subjected to low intensity earthquakes [89]. In loose or soft soils, under moderate to strong earthquake loads, the relative displacement can become significant; soil nonlinearities become predominant, and will highly influence the dynamic response of the seismic SSI system. As mentioned in Chapter 2.6, nonlinear inelasticity can be caused by [89]:

- soil or structural yielding,
- gapping (clay) or cave-in (sand), also known as slack-zone development,
- cyclic softening or hardening (in general referred to as cyclic degradation),
- liquefaction,
- radiation damping.

A BNWF model used to analyze the soil-structure response under seismic action should include as much of these nonlinear inelastic effects as possible to arrive at a reasonable approximation of the true response [89]. Inelastic BNWF use adaptations of the nonlinear elastic p-y curves, which were presented in Chapter 3.1.2.

Proof of nonlinear inelasticity in the soil-structure response can be found when [13]:

1. *“the amplification ratios of peak structural response to peak base motion decrease with increasing peak base acceleration"*,

2. *"the fundamental period of the structural model changes, caused by permanent deformations of the soil or structure"*,

3. *“the calculated response is sensitive to the duration, frequency and level of shaking of the input motion”*.

The choice of BNWF model and the definition of its dynamic parameters will influence the accuracy of the soil-structure response under strong ground motion. A seismic soil-pile-structure interaction model that showed reasonable agreement with test results is the dynamic BNWF model developed by Boulanger et al. [13], the *series hysteretic-viscous damping model*.

The Series Hysteretic-Viscous Damping Model Boulanger et al. [13] proposed a *series hysteretic-viscous damping* model, which incorporates a series connection of:

- a gap element, consistent of a parallel drag and closure spring to represent hysteretic damping,
- a plastic element,
- an elastic element with a parallel viscous damper to represent radiation damping,

as shown in Figure 3.15. This formulation is consistent with the observation that radiation damping consists largely of elastic wave propagation in the far-field, whereas hysteretic damping dominates the near-field response [15]. The origin of the name lies in the configuration of the element: the near-field hysteretic damping by the gapping element (drag and closure) is positioned in series with the viscous (radiation) damping of the far-field. This element is distributed along the leading edge of the embedded pile.

The response of the element y is equal to the sum of responses of the elastic (y_e), plastic (y_p) and gap springs (y_g), the resistance load p is equal to the sum of the load exerted by the drag and closure spring ($p_d + p_c$).

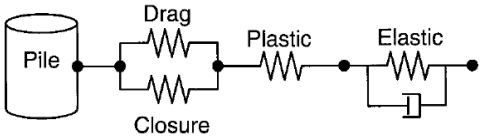

Figure 3.15: *The nonlinear dynamic p-y element of the series hysteretic-viscous damping model by Boulanger et al. [13].*

Even though some approximations and assumptions were made, such as [13]:

- the uncoupling of the site response and soil-structure response (reflected in the use of different soil resistance models, respectively Kelvin-Voigt (Chapter 4.5.2) and series hysteretic-viscous damping),
- the implementation of independent p-y springs (thus neglecting interaction between soil layers, radial and three-dimensional effects),
- the uncertainties in the definition of the soil properties and p-y characteristics,

the analysis method still held reasonable results when compared to experimental tests in the study conducted by Boulanger et al. [13].

It should be noted that series damping models are preferred over parallel damping models (such as the generalized dynamic Winkler model for nonlinear soil–structure interaction analysis by Allotey and El Naggar [1], see Chapter 2.6.2), as the latter risk excessive dashpot forces that might unrealistically dominate the p-y behaviour. Additionally, careful use and interpretation of the backbone static p-y curves is warranted; the same approximations and limitations hold as for the static p-y approach, as the backbone empirical curves were derived for slender flexible piles, where liquefaction is neglected (see Chapter 3.1.2).

The Spring and Dashpot Equations The method to compute dynamic p-y curves from the series hysteretic-viscous damping model first appeared in Boulanger et al. [13]. It was later described in more detail in Boulanger et al. [14] and Wallace et al. [97], both researches conducted for the Californian Department of Transportation regarding the design of piled foundations in highly cyclic environments. The hysteretic-viscous element was implemented in the open-source software OpenSees as "PySimple1 Material" [66] [12], and has been used in other seismic soil-structure interaction studies for piled foundations in its original [5] [77] or simplified form [31] [94] [60]. The equations presented hereafter and used in this project are the original equations as presented by Boulanger et al. [13].

The *elastic spring* behaves linear elastic until it reaches its full capacity. The range over which the elastic spring is active, $p_e \leq \left|C_r \cdot p_{\text{ult}}\right|$, is derived from the static p-y backbone curves (see Chapter 3.1.2). The constant C_r is defined as the ratio between the soil resistance at first onset of yielding and the ultimate resistance:

$$C_r = \frac{p_{\text{yield}}}{p_{\text{ult}}} \tag{3.22}$$

$$p_e = \frac{C_r \cdot p_{\text{ult}}}{y_{\text{yield}}} \cdot y \tag{3.23}$$

where p_{yield} and y_{yield} are the soil resistance and pile displacement at first yield of the soil. The ultimate soil resistance for each layer is calculated with the same empirical expressions as for the static p-y curves (Chapter 3.1.2). Table 3.3 summarizes the approximate elastic results for all soil layers.

Table 3.3: *Elastic spring constants and parameter values in the dynamic p-y model.*

	Sand	**Clay**	**Mudstone**	**Gravel**	**Sandstone**	Units
p_{ult}	0 - 1.560	1.507 - 2.156	3.616 - 9.102	1.762 - 3.271	1.999	[MN/m]
C_r	0.09	0.07	0.43	0.09	0.43	[-]
y_{yield}	0.008	0.057	0.032	0.006	0.032	[m]

After the first onset of yield, the elastic spring has reached its full capacity and the *plastic spring* becomes active [97]. This plastic spring is called rigid, as it only becomes active after the onset of yield, shown in Figure 3.16. The plastic p-y behaviour is described by:

$$p_p = p_{\text{ult}} - (p_{\text{ult}} - p_0) \cdot \left[\frac{c \cdot y_{50}}{c \cdot y_{50} + [y - y_0]} \right]^n \tag{3.24}$$

where p_0 is the last soil resistance value of the elastic spring, and y_0 is the equivalent last pile displacement of the elastic excursion during virgin loading. In subsequent loading cycles, where the elastic spring may no longer be active, the values of p_0 and y_0 are simply the values of the last plastic cycle. Except for the clay layer,– where the y_{50} value is known from the relation with the 50 % strain factor ϵ_{50} (Eq. 3.5) –, the y_{50} value is determined as the pile displacement for which the soil resistance reaches 50 % of the ultimate soil resistance.

The constants c and n, respectively the constant to control the tangent modulus and the sharpness of the curve, are derived from finding the minimum of squared sum errors (SSE) between the plastic expression in Equation 3.24 and the plastic range of the static p-y curves. The result of that curve fitting is shown in Figures 3.17 to 3.21. It can be observed that a reasonable fit was achieved, although the sand and gravel resistance is slightly underestimated at yielding, and overestimated in its elastic region and when nearing the ultimate resistance. For the clay and weak rock layers the fit is nearly perfect. The approximate values for the constants c, n and y_{50} are summarized in Table 3.4.

Table 3.4: *Plastic spring constants and parameter values in the dynamic p-y model.*

	Sand	**Clay**	**Mudstone**	**Gravel**	**Sandstone**	Units
c	0.45	0.01	20	0.33	20	[-]
n	0.73	0.075	4.43	0.62	4.43	[-]
y_{50}	0.05	20	0.056	0.035	0.056	[m]

The *closure spring* is part of the gapping element. It models the closing of the gap, when the shaft regains contact with the soil [97], and works in parallel with the drag spring. This element acts as a switch, which is on when the gap is open and off as soon as the gap is closed and the shaft has regained contact with the soil [97]. It represents the contact or loss of contact between the pile and the soil, and is described by [13]:

$$p_c = C_c \cdot p_{\text{ult}} \cdot \left[\frac{y_{50}}{y_{50} + 50 \cdot (y_0^+ - y_g)} - \frac{y_{50}}{y_{50} - 50 \cdot (y_0^- - y_g)} \right] \tag{3.25}$$

where p_c is the closure resistance, C_c is a constant depending on the soil properties which should be determined iteratively, y_0^+ is the memory term for the positive gap developed and y_0^- is the term for the negative gap developed, and y_g is the deflection of the pile through the gap. The initial values of the memory terms are $y_{50}/100$ and $-y_{50}/100$ for y_0^+ and y_0^- respectively [97].

A gap is created when unloading occurs. The gap on the positive side, y_0^+, grows when plastic deformation occurs on the negative loading side. Therefore, the y_0^+ variable is updated after each loading cycle to the opposite value of the largest past negative value of the plastic displacement, plus some rebounding of the gap (assumed equal to $1.5 y_{50}$). The enlargement of the gap on the negative side y_0^- follows the same logic:

$$y_0^+ = -\max\left(-y_p - y_g + 1.5 \cdot y_{50}\right) \tag{3.26}$$

$$y_0^- = -\max\left(+y_p + y_g - 1.5 \cdot y_{50}\right) \tag{3.27}$$

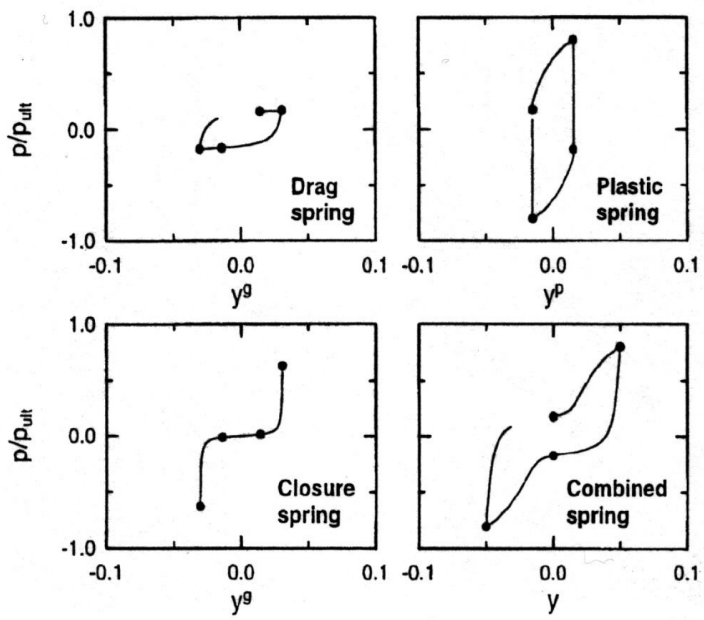

Figure 3.16: *P-y behaviour of the plastic, closure, drag and combined nonlinear spring element [13].*

The factor C_c needs tuning such that p_c reaches p_{ult} during virgin loading. When y_g reaches y_0^+ on the virgin loading path, the equation should be equal to p_{ult} and reduces to:

$$p_c = p_{\text{ult}} = C_c \cdot p_{\text{ult}} \cdot \left[1 - \frac{y_{50}}{y_{50} - 50 \cdot \left(\frac{-y_{50}}{100} - y_0^+ \right)} \right] \tag{3.28}$$

from where C_c can be determined, given that y_0^+ is known. As y_0^+ and y_0^- are updated following enlargement of the gap, this C_c factor should be iteratively re-evaluated after each loading-unloading cycle. Besides ensuring that p_c reaches p_{ult} during virgin loading, C_c also ensures continuity between the plastic and drag-closure load-displacement curve. As such, the closure spring allows for a smooth transition between gapping and elastoplastic loading as the gap opens or closes [12].

The tangent modulus of the closure p-y curve is infinite as long as the gap is closed. It is nonzero when the gap is opening or closing, and becomes zero when the pile loses contact with the soil. When the pile loses contact, the shaft moves through the gap; here, only drag friction governs the element response.

As the gap opens, closes or is open, the *drag spring* is active in parallel with the closure spring. The drag element represents the friction force developed along the sides of the pile as it moves through the gap, and is expressed as:

$$p_d = C_d \cdot p_{\text{ult}} - (C_d \cdot p_{\text{ult}} - p_0) \cdot \left[\frac{y_{50}}{y_{50} + 2 \cdot |y_g - y_0|} \right] \tag{3.29}$$

where p_d is the drag friction, C_d is the drag constant equal to the ratio between the maximum drag force expected to develop and the ultimate soil resistance, p_0 is the soil resistance at the start of the current unloading cycle and y_0 is the associated pile displacement.

Values for C_d depend on the soil type and its characteristics. The higher the value of C_d, the higher the expected drag participation in the load-displacement behaviour and thus the more stiff the soil-structure interaction response will be. Based on Assareh & Asgarian [5], the value of C_d for sand is assumed 0.1 and for clay 0.3. For the weak rock layers, a value of 0.5 is assumed as more drag participation is expected than in the clay layer. For the gravel layer, which is approximated by undrained sand behaviour in this study, a value of 0.15 is assumed. Table 3.5 summarizes the drag equation parameters.

Table 3.5: *Drag spring constants and parameter values in the dynamic p-y model.*

	Sand	**Clay**	**Mudstone**	**Gravel**	**Sandstone**	Units
C_d	0.1	0.3	0.5	0.15	0.5	-

The *viscous damper* is active at all times during earthquake-induced pile motion. In dynamic analysis, it is important to include radiation damping for a soil-pile interaction case under high frequency earthquake loading; the energy loss due to radiation may be significant for the higher order vibration modes for the structure. The amount of viscous or radiation damping of the soil, c_v, depends on the soil properties and on the energy of the seismic wave travelling through the soil layers.

The hysteretic-viscous damping model assumes that the radiation damper works in series with the hysteretic damping elements and is in parallel with the elastic spring only. From Wang et al. [99], it was concluded that these type of seismic soil-structure interaction models show the best agreement with test results. In case the damper is placed in parallel with the gap and plastic elements, excessive dashpot forces are developed which exceed the ultimate capacity of the p-y springs [31] [97]. Also, it does not correctly model the shift in natural frequency of the pile. Series damping models avoid these shortcomings, as their *"damping is dependant on the stiffness and strength of the p-y curves, which seems realistic and avoids the excessive damping forces that is developed with a parallel model"* [97].

The expression used to compute the damping value of c_v in Boulanger et al. [13] is the equation developed by Wang et al. [99] for undrained soils:

$$c_v = 4 \cdot D \cdot \rho_{soil} \cdot V_s \tag{3.30}$$

where c_v is the radiation damping per unit length in the far field, D is the pile diameter, ρ_{soil} is the bulk density of the soil, and V_s is the shear wave velocity. Based on Lee et al. [57], Lee & Tsai [58], Martin & Diehl [64] and Holzer [88], the shear wave velocities in each soil layer are assumed to be piece-wise constant over depth and equal to the values in Table 3.6.

Wallace et al. [97] offer the alternative dashpot equation by Gazetas & Dobry [33]:

$$c_v = 2 \cdot D \cdot \rho_{soil} \cdot (V_p + V_s) \tag{3.31}$$

But since in undrained analyses the soil is nearly incompressible, the P-wave[7] velocity V_p can become large, causing the damping to be overestimated. More possible expressions to compute the soil radiation damping are offered in Tabesh & Poulos [86], but the definition by Wang et al. [99] is deemed most appropriate for the undrained seismic analyses in this study, thereby following the approach by Boulanger et al. [13].

Table 3.6: *Assumed shear wave velocities in each soil layer [57], [58], [64] and [88].*

	Sand	**Clay**	**Mudstone**	**Gravel**	**Sandstone**	Units
Classification	Soft (E)	Medium soft (D1)	Weak rock (C2)	Medium soft (D2)	Soft rock (C3)	-
Shear wave velocity V_s	200	290	540	375	700	m/s

It is important to emphasize that the radiation damping value c_v is the damping per unit length. In any force-displacement computation this value should first be multiplied by the height of the discretized soil layer, before multiplying it with the velocity of horizontal displacement to arrive at the force (see the equations of motion in Chapter 4.6). This height compares to the difference in height between the mudline and the *equivalent* soil layer depth (as previously determined in Chapter 3.1.2).

[7] P-waves and S-waves are two types of body waves that travel through the interior layers of the Earth. P-waves are normal stress waves, alternating between tension and compression, and are the first to arrive at an observation point, therefore denoted as *Primary* waves. They exhibit a small amplitude and short period and have little damage potential [21] [68]. S-waves are shear waves, where the rock mass moves side-to-side in horizontal and vertical direction. Their propagating speed is lower than that of the P-waves, causing them to arrive second to the P-waves at the observatory; that is why they are also referred to as *Secondary* waves. Having a large amplitude and long period, they have a significant damage potential. More on body and surface waves in [95].

A final note to the dynamic inelastic p-y curve approach developed by Boulanger et al. [13], is that:

- the backbone p-y curves (based on the API recommended load-displacement curves),
- the empirical parameters, such as initial gap size (y_0^+ / y_0^-), closure coefficient (C_c), drag coefficient (C_d), and radiation viscous damper (c_v),
- the iteration methods for the parameters that can be determined by curve matching with the p-y backbone curves (C_r, y_{yield}, c and n),

were all estimated or determined for slender, flexible piles. Validation of the parameters used here is recommended for large diameter, rigid monopiles by finite-element numerical approaches.

Dynamic Load-Displacement Behaviour During unloading, when the gap opens or closes, the drag and closure element govern the spring behaviour. The tangent modulus of the closure spring is no longer infinite. When the shaft moves away from the edge, inside the gap, only drag friction governs the load-displacement response. Once the gap is closed, the elastic and plastic element dictate the spring behaviour.

So in the load-displacement curve, the soil resistance when the shaft is in contact with the soil during loading is due to the elastic and plastic element, and when the gap opens during unloading the soil resistance is equal to the drag and closure load. Just before regaining contact with the soil again in the opposite loading direction, the soil resistance increases from the load at drag to the ultimate soil resistance for the previous maximum gap displacement, marking the transition zone between gapping (unloading) and elastoplastic (loading) behaviour. A short overview of the elements' consecutive behaviour is presented here [97]:

a) When the gap is closed, only the elastic and plastic spring are activated.

$$\begin{aligned} p &= p_e && \text{for } p < p_{\text{yield}} \\ p &= C_r \cdot p_{\text{ult}} + p_p && \text{for } p \geq p_{\text{yield}} \\ p_d &= p_c = 0 \end{aligned}$$

b) When the gap is open, only the drag and closure spring are activated.

$$\begin{aligned} p &= p_d + p_c \\ p_e &= p_p = 0 \end{aligned}$$

c) When the gap is opening or closing, the behaviour of the element switches from gapping to elastic.

$$\begin{aligned} p &= \min\left(p_d + p_c; C_r \cdot p_{\text{ult}}\right) \\ p_p &= 0 \end{aligned}$$

Simplification of the Nonlinear Series Hysteretic-Viscous Damping Model The influence of the gap element will be ignored in this study, leaving only the influence of the viscous radiation damper as a source of inelasticity in the model. This decision was made given that in the top sand layer the creation of a gap would be followed almost immediately by cave-in of the soil surrounding the gap, thereby closing the gap instantaneously.

Second to that, it is doubted that drag friction is relevant for the current case, where a large diameter monopile moves in soft soil and hence no gap development is expected.

Lastly, contrary to the study by Boulanger et al. [13], the soil profile is subaqueous. It is expected, for underwater conditions, that the in- and outflow of water in any formed gap would dominate over drag friction. Concluding from these three points, it was decided to remove the gap element from the model, thereby reducing the series hysteretic-viscous damping element to an parallel viscous-elastoplastic element. However, the mathematics to implement the full series hysteretic-viscous damping element in a beam on a Winkler spring foundation FEM is still detailed in Chapter 4.6.

Results of the Curve-matching Between the Static and Dynamic P-y Curves The dynamic p-y curves for this study during virgin loading are presented hereafter, excluding the influence of the radiation damper. The elastic and plastic soil resistance load during virgin loading is shown in Figures 3.17 to 3.21, and is compared with the API recommended p-y curves. It can be observed that a reasonable fit was achieved between the elastoplastic expression proposed by Boulanger et al. [13] and the API recommended p-y expressions [2]. The sand and gravel resistance is slightly underestimated at yielding, and overestimated in its elastic region and when nearing the ultimate resistance. For the clay and weak rock layers the fit is nearly perfect, except for a small underestimate of the soil resistance near its ultimate resistance.

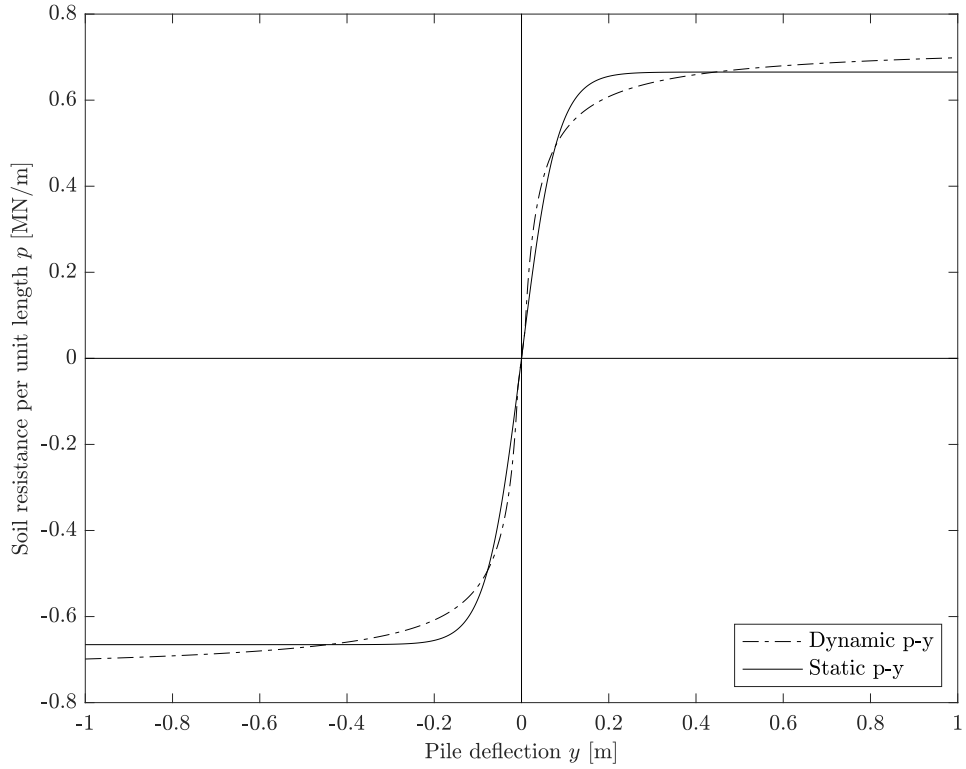

Figure 3.17: *Match between the empirical static p-y curve for sand and the dynamic expression for the nonlinear elasto-plastic soil behaviour by Boulanger et al. [13], at a depth of 4 m.*

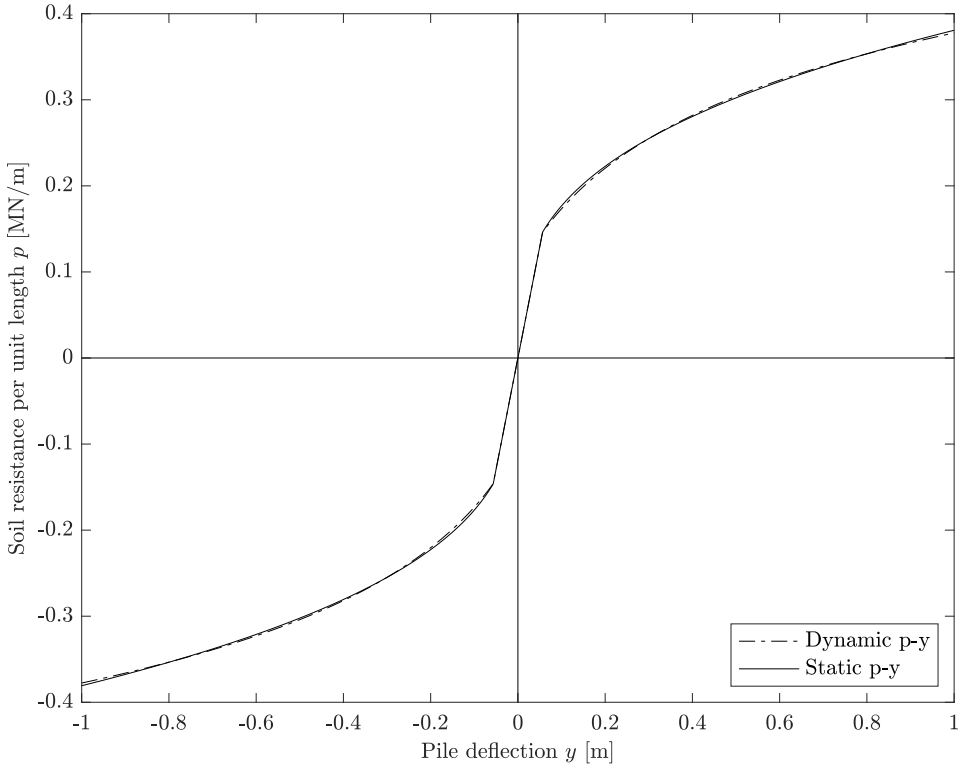

Figure 3.18: *Match between the empirical static p-y curve for clay and the dynamic expression for the nonlinear elastoplastic soil behaviour by Boulanger et al. [13], at a depth of 12 m.*

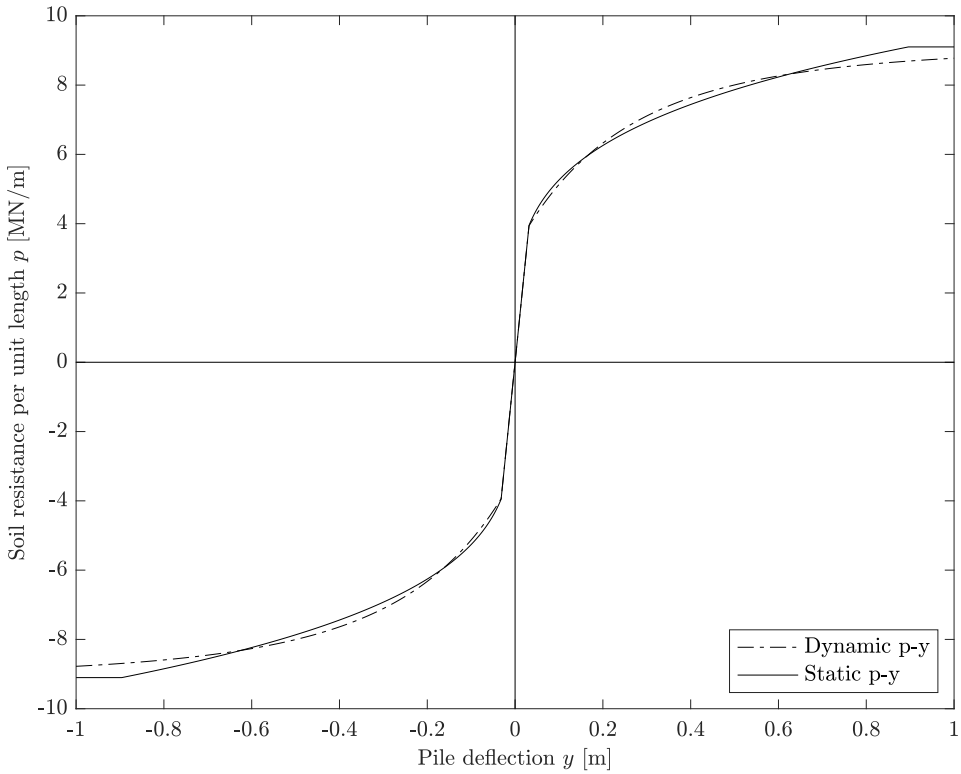

Figure 3.19: *Match between the empirical static p-y curve for mudstone and the dynamic expression for the nonlinear elastoplastic soil behaviour by Boulanger et al. [13], at a depth of 32 m.*

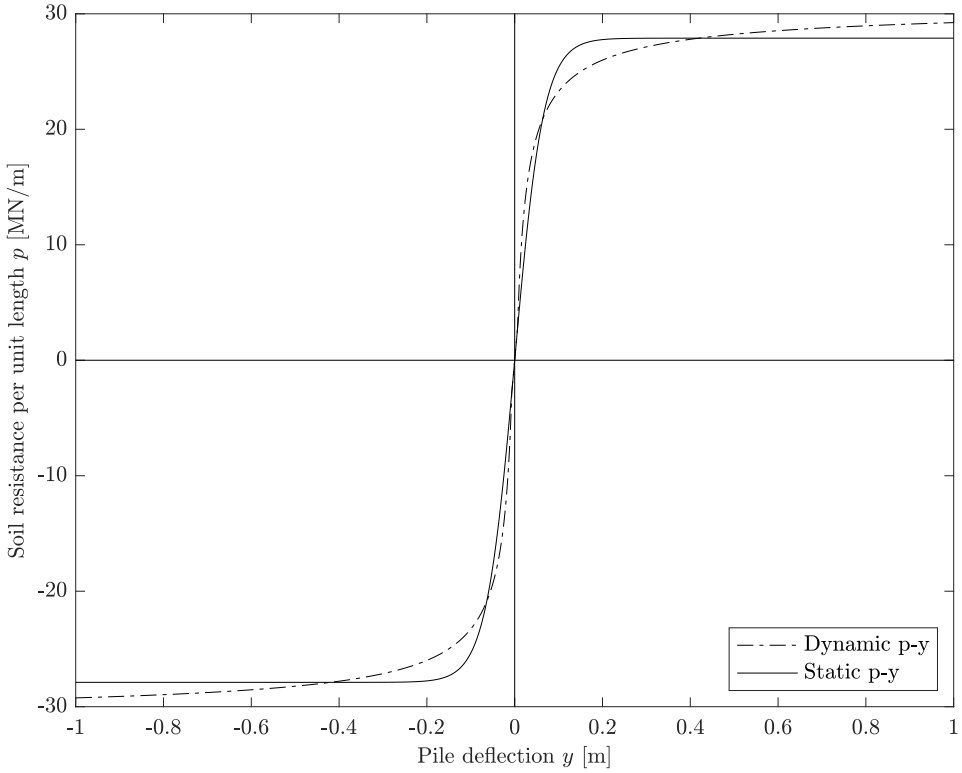

Figure 3.20: *Match between the empirical static p-y curve for gravel and the dynamic expression for the nonlinear elasto-plastic soil behaviour by Boulanger et al. [13], at a depth of 42 m.*

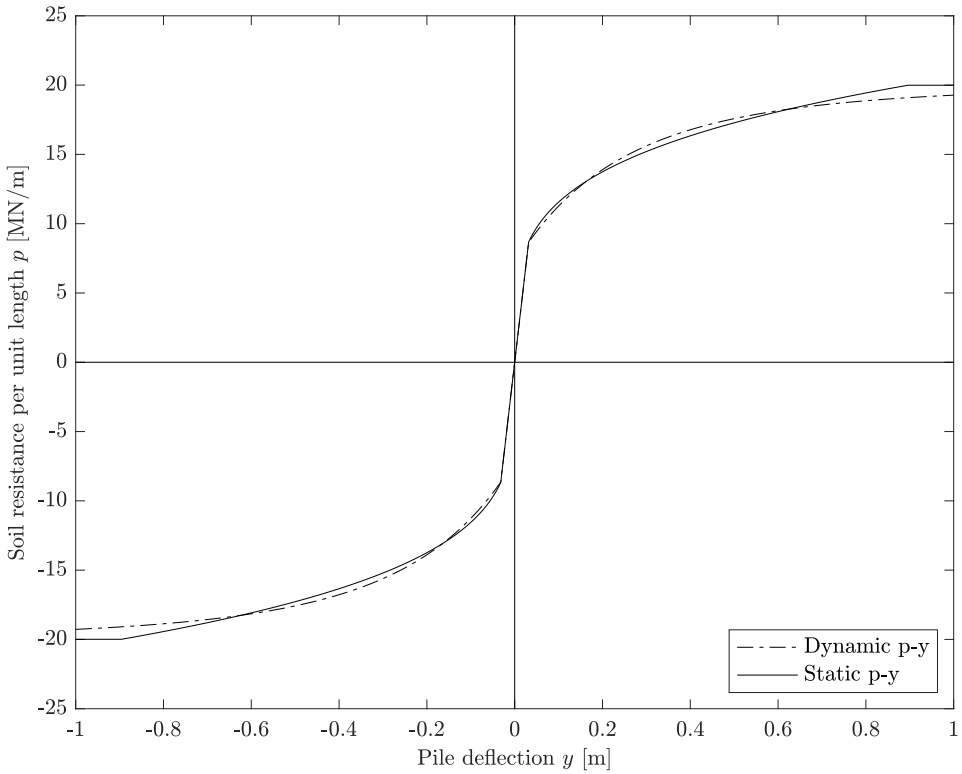

Figure 3.21: *Match between the empirical static p-y curve for sandstone and the dynamic expression for the nonlinear elastoplastic soil behaviour by Boulanger et al. [13], at a depth of 48 m.*

3.2. The Structure

The monopile foundation that is investigated in this case study was specifically designed for the soil conditions at the non-disclosed location. The foundation is supporting a transition piece, a tower and an NREL 5 MW reference turbine [51]. The dimensions and general properties of the structure are listed in Chapter 3.2.1. The finite-element model description is presented in Chapter 3.2.2.

3.2.1. Properties of the Structural Design

The monopile, transition piece and tower are modeled as a simplified uninterrupted cylinder of variable diameter with no surface discontinuities (such as holes or protrusions). The total length of the structure in the model is 155.2 m, of which 40.2 m of the monopile is embedded in the ground (see Figure 3.22). Secondary steel structures,– such as ladders, boatlandings, railings and concrete working platforms –, and internal structures,– such as cabling –, are not included in the model as separate features but are accounted for in the increased mass density of the transition piece and the tower (respectively 9,000 and 8,500 kg/m^3 instead of 7,850 kg/m^3 for steel).

The monopile and transition piece are connected by grout in the gap where they overlap. However, this grouted connection is not modeled. Instead, the gap is ignored and the TP and MP are assumed to slide perfectly over one another. Consequently, the thickness t of the section where TP and MP overlap is locally increased, hence also the local cross-sectional area A, inertia I and section modulus W. The mass density ρ, elastic modulus E, shear modulus G and shear strength σ_y of the material are assumed to be weighted averages of the TP and MP, based on their respective thicknesses.

The axial thrust force and aerodynamic damping of the operational rotor are included in the response analysis, but the structure itself is modeled as a simple point mass at hub height. No other operational influences of the rotor are included except for the aforementioned force and damping, which are consequently implemented as point forces acting at hub height.

The gross properties of the turbine, monopile, transition piece and the tower as used in the computational model are listed in Tables 3.7 to 3.8. The structural dimensions are visualized in Figure 3.22 with respect to the water level and soil layers. More detailed turbine properties, structural and aerodynamic, can be consulted in Appendix B and in the technical report by Jonkman et al. [51] of the National Renewable Energy Laboratory. The blade aerodynamic properties listed in the Appendix are used in the blade element momentum theory MATLAB code to compute the rotor aerodynamic force and damping, see Chapter 4.2.

Table 3.7: *Gross structural and aerodynamic properties of the NREL 5 MW reference turbine, adapted from [51].*

Structural properties	
Rated power	5 MW
Configuration	Upwind, 3-bladed
Control	Variable speed, collective pitch
Diameter rotor and hub	126 m, 3 m
Mass RNA	350,000 kg
Hub height	115 m
Center of mass	0 m*
Aerodynamic properties	
Rated, cut-in and cut-out wind speed	11.4 m/s, 3 m/s, 25 m/s
Minimum and maximum rotor speed	6.9 rpm, 12.1 rpm

* The center of mass of the RNA is assumed to coincide with the centerline of the structure, thereby inducing no moment about the longitudinal dimension of the structure.

Table 3.8: *Gross structural properties of the monopile, transition piece and tower design.*

	Tower	**Transition piece**	**Monopile**	Units
Length	68.6	28.6	69.5	m
Diameter, top and bottom	3.87 - 5.73	5.73 - 7.09	5.7 - 8	m
Thickness	50	80	74	mm
Elastic modulus	210	210	210	GPa
Shear modulus	80	80	80	GPa
Density	8500	9000	7850	kg/m^3
Yield strength	355	355	355	MPa

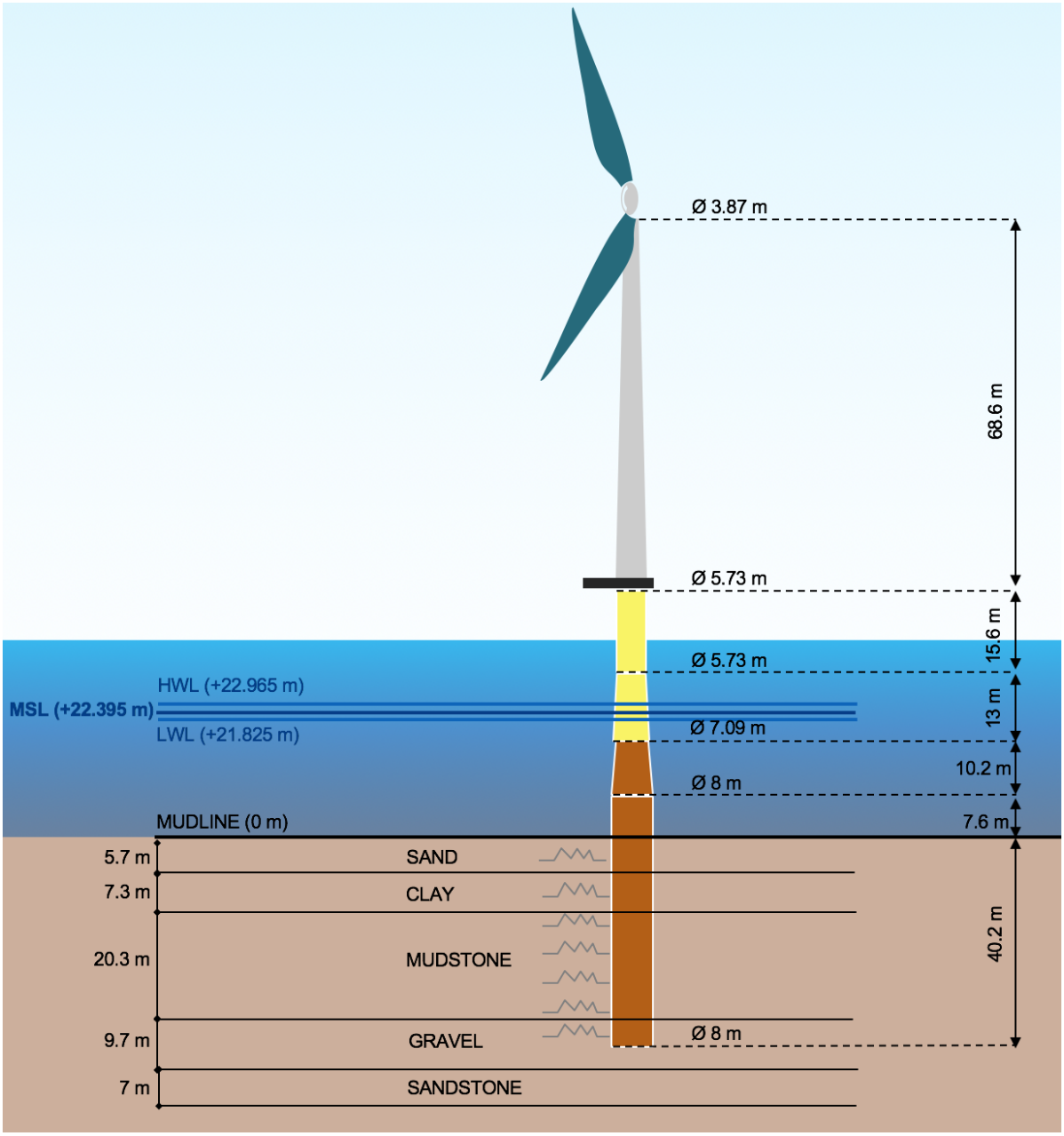

Figure 3.22: *Visualization of the structure, the soil profile and water depth.*

3.2.2. Elastic Timoshenko Beam Finite-Element Modeling

The offshore wind support structure is modeled as a beam on a nonlinear elastic foundation under axial load due to its self-weight. The Timoshenko beam formulation is used rather than the Euler-Bernoulli beam approach, as the foundation is categorized as a thick beam ($L/D = 40.2^{(8)}\,\text{m}/8\,\text{m} = 5 \leq 10$) [74]. In thick beams, the effect of transverse shear deformation and of rotational inertia on the solution may not be neglected. As opposed to slender Euler-Bernoulli beams, thicker beams are not rigid in shear and will exhibit shear deformation under bending loads. Therefore, the Timoshenko beam description is deemed a better approximation of the response behaviour of the offshore wind foundation.

It is assumed that the column is perfectly straight before the loads are applied. The material of the beam is isotropic and homogeneous, such that the beam axis coincides with the neutral axis. The Timoshenko beam hypotheses are [74]:

1. the lateral deflections of the beam are small and equal to the deflection of the beam axis,
2. no out-of-plane displacement takes place,
3. cross-sections normal to the beam axis before deformation remain plane but not necessarily orthogonal to the beam axis after deformation.

This latter hypothesis allows for the effect of transverse shear deformation, and differs from the orthonormal assumption in classic Euler-Bernoulli beam theory. It is equivalent to assuming average rotation of the plane but deformed cross-sections with respect to the neutral axis (see Figure 3.23):

$$\theta = \frac{dy}{dz} + \phi \tag{3.32}$$

where θ is the cross-sectional rotation, ϕ is the additional rotation due to distortion of the cross-section, and $\frac{dy}{dz}$ is the beam deflection. The normal and shear stress is therefore, in a linear elastic formulation:

$$\sigma_z = E \cdot \epsilon_z = -y \cdot E \cdot \frac{d\theta}{dz} \tag{3.33}$$

$$\tau_{zy} = G \cdot k \cdot \gamma_{zy} = G \cdot k \cdot \phi = G \cdot k \cdot \left(\frac{dy}{dz} - \theta \right) \tag{3.34}$$

where k is the shear correction parameter ($0 < k \leq 1$) which takes into account the distortion of the cross-section when the beam suffers shear deformation. The in-plane shear strain γ_{zy} is equal to the shear rotation.

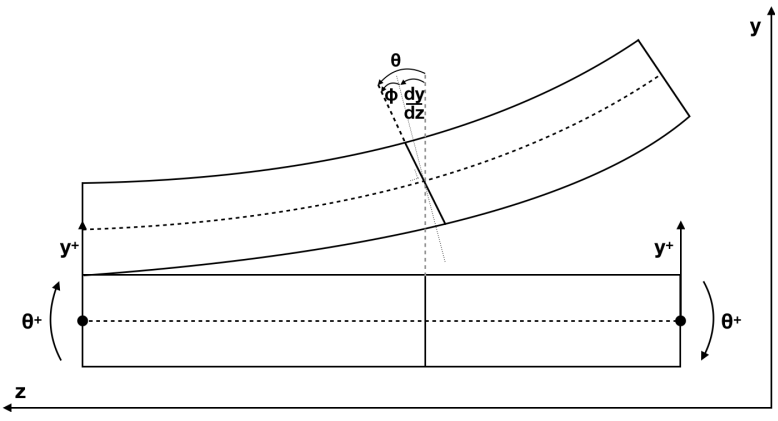

Figure 3.23: *Two-node Timoshenko beam element: definition of cross-sectional rotation, shear angle and deflection, and sign convention for the lateral displacement and beam rotation.*

(8) This is the embedded length of the monopile.

The shear force and bending moment are thus [74]:

$$Q = G \cdot \phi \cdot k \cdot A \tag{3.35}$$

$$M = E \cdot I \cdot \frac{d\theta}{dz} \tag{3.36}$$

where $k \cdot A$ is the reduced cross-sectional area of the beam after deformation.

The shear correction parameter k depends on the cross-sectional shape of the beam. For a hollow cylindrical beam, such as the monopile foundation model, the shear coefficient according to Hutchinson [44] is:

$$k = \frac{6 \cdot \left(R_i^2 + R_o^2\right)^2 \cdot (1+\nu)^2}{7 \cdot R_i^4 + 34 \cdot R_i^2 \cdot R_o^2 + 7 \cdot R_o^4 + \nu \cdot \left(12 \cdot R_i^4 + 48 \cdot R_i^2 \cdot R_o^2 + 12 \cdot R_o^4\right) + \nu^2 \cdot \left(4 \cdot R_i^4 + 16 \cdot R_i^2 \cdot R_o^2 + 4 \cdot R_o^4\right)} \tag{3.37}$$

with R_o the outer and R_i the inner radius of the hollow cross-section, and ν the Poisson ratio of the steel.

The monopile, transition piece and tower are divided into a finite number of elements, where each element is modeled as a two-node Timoshenko beam and each node has one lateral displacement degree of freedom (y) and one rotational degree of freedom (θ), see Figure 3.23. The support structure is resting on an elastic foundation and is subjected to axial load due to the RNA and its own self-weight. A cubic displacement distribution for y is assumed over the element in the derivation of the element matrices, see Appendix C and the reference work by Yokoyama [102] [103] for more details. The explicit expressions for the element matrices can be found in Appendix C.

The bending resistance and shear resistance of the material of the structure will deliver stiffness of the structure to lateral displacement or rotation. The soil, modelled as an elastic or inelastic spring foundation depending on the SSI model used (see Chapter 3.1.2 and 3.1.3), will add stiffness to the soil-structure system by the resistance of the soil springs to lateral motion. The compressive load by the gravitational pull on the RNA and the material of the cylindrical structure will decrease the stiffness; this effect is included in the geometric stiffness matrix. Summarized, the overall stiffness matrix $\underline{\underline{\mathbf{K}}}$ of the system becomes:

$$\underline{\underline{\mathbf{K}}} = \underline{\underline{\mathbf{K}}}_b + \underline{\underline{\mathbf{K}}}_s + \underline{\underline{\mathbf{K}}}_f - \underline{\underline{\mathbf{K}}}_{g,0} - \underline{\underline{\mathbf{K}}}_g \tag{3.38}$$

where $\underline{\underline{\mathbf{K}}}_b$ is the global bending, $\underline{\underline{\mathbf{K}}}_s$ the global shear, $\underline{\underline{\mathbf{K}}}_f$ the global foundation, and $\underline{\underline{\mathbf{K}}}_g$ and $\underline{\underline{\mathbf{K}}}_{g,0}$ the geometric stiffness matrices by the weight of the element itself and by the top weight on the element respectively.

The structure will have translational and rotational inertia. The overall mass matrix $\underline{\underline{\mathbf{M}}}$ becomes:

$$\underline{\underline{\mathbf{M}}} = \underline{\underline{\mathbf{M}}}_t + \underline{\underline{\mathbf{M}}}_r \tag{3.39}$$

with $\underline{\underline{\mathbf{M}}}_t$ the global translational mass matric, and $\underline{\underline{\mathbf{M}}}_r$ the global rotational mass matrix .

The governing equation of the system, neglecting damping and external forcing for the moment, becomes:

$$\underline{\underline{\mathbf{M}}} \cdot \underline{\ddot{q}} + \underline{\underline{\mathbf{K}}} \cdot \underline{q} = 0 \tag{3.40}$$

where $\underline{q}$ is the vector containing the lateral displacement y_i and rotation θ_i for each node $i = 1$ to N:

$$\underline{q} = \begin{bmatrix} y_1 & \theta_1 & y_2 & \theta_2 & \dots & y_N & \theta_N \end{bmatrix}^T \tag{3.41}$$

From the governing equation of motion, the eigenvalue problem can defined:

$$\det\left|\underline{\underline{\mathbf{K}}} - \lambda \underline{\underline{\mathbf{M}}}\right| = 0 \tag{3.42}$$

Solving the latter equation delivers the eigenvalues λ_i of the system, for $i = 1$ to $2N$ (i.e. the number of eigenvalues is equal to the degrees of freedom of the system $2N$, as each node has a translational and rotational degree of freedom).

The natural frequencies of the system are found by the relationship:

$$f_i = \frac{\sqrt{\lambda_i}}{2\pi} \tag{3.43}$$

The first natural frequency prior to loading is shown in Figure 5.1 of Chapter 5.1. The derivation of the element matrices and governing equation of motion can be consulted in Appendix C and the reference work by Yokoyama [102][103].

4

Preamble of the Simulations

In this chapter, the load cases examined in this research are introduced in Chapter 4.1. For the external environmental loads, – more specifically the aerodynamic (Chapter 4.2), hydrodynamic (Chapter 4.3), soil resistance (Chapter 4.4) and earthquake induced loads (Chapter 4.5), – the input parameters are defined as well as the computational method. The earthquake input motion and induced load is analyzed in more detail, scrutinizing the selection procedure of the earthquake accelerogram, the site response analysis of the free-field record through the soil profile, the incremental dynamic analysis scaling of the record, and finally the influence of the earthquake ground motion on the relative soil stiffness. To summarize this chapter, the full equations of motion for both seismic soil-structure interaction models are listed in Chapter 4.6.

4.1. The Simulated Load Cases

Based on the recommendations made by design standards (see Chapter 2.1), the response behaviour of the structure will be examined under both operational and shutdown conditions. Under operational conditions, the rotor is assumed to be working, thereby producing thrust force and aerodynamic damping. Under shutdown conditions, the blades of the turbine are feathered: the blades are parallel to the wind flow, thereby producing no lift or drag, and consequently no thrust force or aerodynamic damping is assumed to exist.

To analyze the influence of an earthquake on the wind turbine foundation, first the dynamic time-history response behaviour is analyzed under wind and wave loads only. This load case, where the structure is exposed to normal sea state conditions, will serve as the comparative basis in this study.

Following this analysis, the structure will be exposed to a normal sea state added with the selected as-recorded earthquake, to observe the change in response in case the structure would have been exposed to the locally recorded ground motion in addition to the other environmental factors. The combination of NSS and an earthquake is considered the most likely case in the structure's lifetime.

As highlighted in Chapter 2.2, the large pool of influential factors on an earthquake signal may cause two earthquake records, originating from the same fault and recorded at the same station, to be different in amplitude, frequency and duration. The possible variability in frequency and duration is not further investigated in this study, as the limited amount of earthquake records could not provide further insight on this matter. However, the amplitude of the largest recorded earthquake ground motion could be scaled to probabilistic levels based on hindcast data, thereby identifying the ELE and ALE peak ground acceleration levels of the non-disclosed location. This IDA method allows to investigate the progression in capacity behaviour of the structure with limited earthquake records. Here, only one record will be scaled to different amplitudes. However, it is recommendable in more detailed studies to analyze multiple records from the same area, as they may differ in duration and frequency and therefore lead to different load-response behaviour.

The load cases are summarized in Table 4.1. The resulting structural responses are presented in Chapter 5.

Table 4.1: *Summary of the load cases, detailing the operational, wind, wave and earthquake conditions.*

Load Case	Operation	Wind	Wave	Earthquake
1-N	Normal	NSS	NSS	-
1-S	Shutdown	NSS	NSS	-
2-N	Normal	NSS	NSS	As-recorded
2-S	Shutdown	NSS	NSS	As-recorded
3-N	Normal	NSS	NSS	ELE
3-S	Shutdown	NSS	NSS	ELE
4-N	Normal	NSS	NSS	ALE
4-S	Shutdown	NSS	NSS	ALE
Total simulations	$8 \cdot 2^{*} = 16$			

* The load cases are imposed on two different seismic soil-structure interaction models.

4.2. The Aerodynamic Load

The rotor, tower and above-sealevel transition piece are exposed to a steady incoming wind. The wind speed corresponds to normal sea state conditions, where the wind speed is the expected wind speed based on hindcast data. After processing the metocean data of the non-disclosed location, gathered over a period from 1992 to 2017 by BMT Argoss [11], the expected wind speed at reference height[(11)] is 8.32 m/s.

As a direct result of the wind flowing past the structure, the steady wind will cause aerodynamic loading over the support structure, or *tower loading*. Indirectly, the rotor which is caused to rotate by the incoming wind flow, will induce a thrust force and moment at hub height, referred to as *rotor loading*. Methods to compute both types of aerodynamic loading are introduced hereafter.

4.2.1. Rotor Loading and Damping

This steady wind, above cut-in and below cut-out wind speed of the NREL 5 MW turbine, will cause the rotor to produce thrust. It is this thrust force that induces a lateral acting load at hub height. In the current computational model, the steady thrust force (following a steady wind flow assumption) is considered to act as a point force at hub height. As a consequence, the thrust force introduces shear and moment loads in the support structure below the turbine.

The thrust force is computed with *Blade Element Momentum* (BEM) theory. It is an extension to 1D momentum theory, where in the BEM theory the influence of the number of blades, twist and chord distribution, and airfoil shape is no longer neglected. For steady flows, it is possible to calculate the thrust and power for different settings of wind speed, rotational speed and pitch angle [36]. The streamtube is discretized in a number of annular element of width δR, with R the radius of the rotor. The theory assumes [36]:

1. a steady, non-turbulent flow,
2. no radial dependency between annular rings,
3. the force of the blades on the incoming flow is constant in each annular element, corresponding to an infinite number of blades and assuming no tip losses,
4. no flow exists across the elements, as the lateral boundary are streamlines,

To correct for a finite number of blades and consequential tip losses, the Prandtl tip loss correction was introduced in the MATLAB code. Additionally, to correct for a turbulent wake of the rotor causing a large thrust on the disc, – much larger than that predicted by the momentum theory –, the Glauert correction was introduced [16]. More on the BEM theory, equations and corrections can be consulted in Hansen [36] and Burton et al. [16]. The equations were implemented in a MATLAB script, including the blade and rotor geometry of the NREL 5 MW turbine as listed in Appendix B. For a wind speed at hub height of 10.03 m/s (using Equation 4.4), the turbine settings and power/thrust production are as listed in Table 4.2.

Table 4.2: *Blade element momentum theory results for NSS steady wind at hub height of 10.03 m/s.*

Wind speed	Local angle of attack	Pitch angle	RPM	Power	Thrust	Aerodynamic damping
10.03[9] m/s	0.078°- 1.015°	0°	11.30	3.856 MW	601,7 kN	63.2[10] kNs/m

An operating rotor will produce not only power and thrust, but will also deliver aerodynamic damping to the responses of the system. The amount of aerodynamic damping in fore-aft direction for a steady flow on a rotating turbine, was approximated by the equations proposed by Valamanesh et al. [92], which use the output of the BEM theory and could therefore be easily implemented in the MATLAB BEM code:

$$\begin{aligned} C_{AD} = B \cdot \Bigg(& \rho \int_0^R V_0 (1-a) c(r) \left[c_l \cos\phi + c_d \sin\phi \right] dr \\ & + \frac{1}{2} \rho \int_0^R \Omega r (1+a') c(r) \left[\left(\frac{\delta c_l}{\delta \alpha} + c_d \right) \cos\phi + \left(\frac{\delta c_d}{\delta \alpha} - c_l \right) \sin\phi \right] dr \Bigg) \end{aligned} \tag{4.1}$$

where C_{AD} is the aerodynamic damping of the rotor, B is the number of blades, ρ is the air density, R is the rotor radius, V_0 is the incoming steady wind speed at hub height, a is the axial induction factor and a' the tangential induction factor, $c(r)$ is the chord length at distance r along the radius R, c_l and c_d are the lift and drag coefficient per unit length respectively, Ω is the rotational speed of the rotor, and ϕ is the flow angle equal to:

$$\phi = \alpha + \theta_p + \theta_t \tag{4.2}$$

with α the angle of attack of the blade with respect to the wind, θ_p the pitch angle and θ_t the twist angle. The induction factors, direction of lift and drag, incoming wind and flow angles can be seen in the velocity triangle in Figure 4.1 [19]. The aerodynamic damping of an NREL 5 MW for an incoming wind speed of 10.03 m/s is about 63.2 kNs/m[10], as listed in Table 4.2.

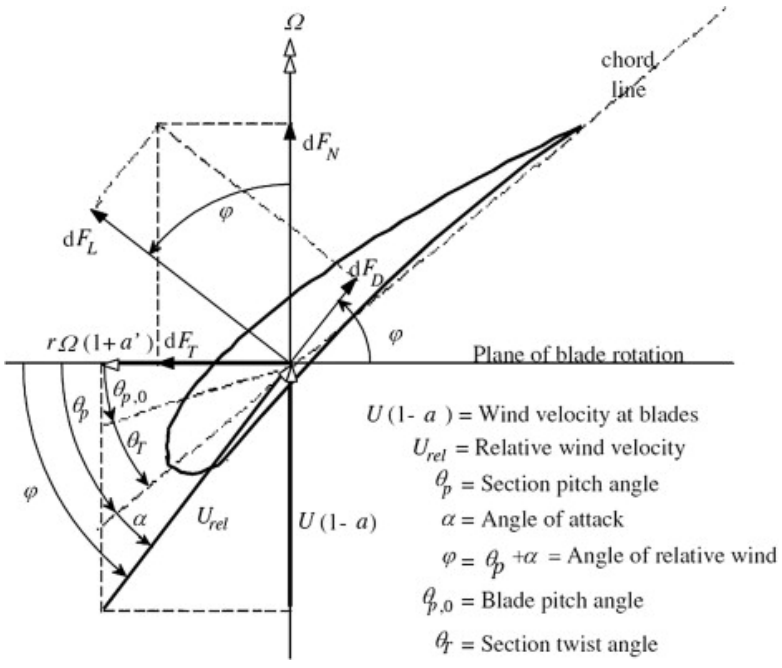

Figure 4.1: *Velocity triangle of wind speed, flow angles, and lift and drag direction across an airfoil [19].*

[10] This damping value corresponds to a damping ratio of about 3.5 %, which is within expectations of 1 % to 5 % rotor aerodynamic damping [96].

4.2.2. Tower Loading

As the wind flows across the cylindrical cross-section of the support structure, the surface roughness of the structure will cause drag friction forces acting in-line with the wind direction. Small deflections of the tower are assumed, where the flow of the wind remains perpendicular to the structure.

The aerodynamic load on a portion of the cylindrical structure can be computed by:

$$f_{\text{aero}}(z,t) = \frac{1}{2}\rho_{\text{air}} C_d \left(v(z) - \dot{y}(z,t)\right)\left|v(z) - \dot{y}(z,t)\right| D(z) \tag{4.3}$$

where f_{aero} is the aerodynamic tower load per unit length, C_d is the drag coefficient of the cylinder, $v(z)$ is the wind speed perpendicular to the cylinder section, and $\dot{y}$ is the velocity of displacement of the structure. This load should be integrated over the structural elements to arrive at the shear force in each element, and the moment. The drag coefficient is related to the Reynolds number according to Figure 4.2 – where $Re = \frac{v(z)\cdot D(z)}{\nu}$ with ν the kinematic viscosity constant ($1.460 \cdot 10^{-5}$ m^2/s for the atmosphere at sea level) – and to the surface roughness of the cylindrical structure k_s/D. In this study, a constant C_d value of 0.6 is assumed for the smooth tower structure, although this coefficient normally varies both over the length of the structure (depending on the local diameter/surface roughness) and in time (depending on the turbulence of the flow expressed by the Reynolds number).

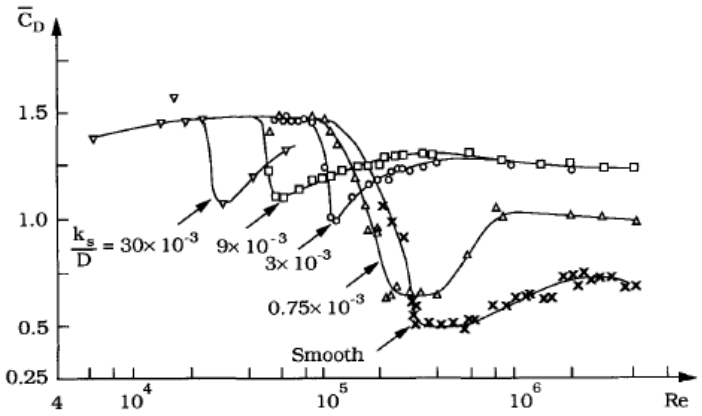

Figure 4.2: *Relation between aerodynamic drag coefficient of a cylinder, surface roughness and Reynolds number [84]*

.

It should be noted that the wind speed across the height of the tower is not constant. In the surface layer of the atmospheric boundary, the wind speed reduces towards the surface. The rate at which the wind speed decreases in the wind shear profile, depends on the surface roughness of the surface boundary. Onshore, the surface roughness is much higher than offshore, where only waves disturb the surface as opposed to buildings and geological relief. Multiple wind shear profile models exist, here a logarithmic wind distribution is used:

$$v(z) = V_0 \cdot \frac{\log\left(\frac{z}{z_0}\right)}{\log\left(\frac{h_{\text{ref}}}{z_0}\right)} \tag{4.4}$$

where V_0 is the steady wind speed at reference height[(11)], z is the actual tower section height with respect to MSL, h_{ref} is the reference height (10 m above MSL), and z_0 is the surface roughness constant. Offshore, it is recommended to assume z_0 equal to 0.0002.

For TP and tower sections above mean water level, the aerodynamic tower loads range from 132.3 N/m near the water surface, to 145.3 N/m at hub height (see Table 4.3). Over this length, the aerodynamic load becomes maximal at the start of the tower structure (height of +56.7 with respect to the mudline), with a load of 174.8 N/m. These numbers are for a structure which is not moving in the wind (thus $\dot{y} = 0$), which has the dimensions as specified in Chapter 3.2.1, and is exposed to a steady wind of 10.03 m/s at hub height according to Equation 4.4.

[(11)] The reference height is at 10 m above MSL following the guidelines from the metocean data provided by BMT Argoss [11].

Table 4.3: *Summary of the tower loading input conditions and resulting loads from hub to free water surface, at t=0 s.*

Wind speed hub	Wind shear profile	Surface roughness	Air density	Drag coefficient	Diameter	Loading range
10.03 m/s	10.03 - 7.54 m/s	0.0002	1.244 kg/m^3	0.65	3.87 - 5.73 m (tower) 5.73 - 6.23 m (TP)	145.3 - 174.8 N/m 173.5 - 132.3 N/m

4.3. The Hydrodynamic Load

Besides wind, the waves in the offshore environment will force the support structure and foundation. It is assumed that a regular sinusoidal wave is exciting the structure. The hydrodynamic load on the submerged elements of the structure is approximated by the fully nonlinear Morison equation for a moving body:

$$\begin{aligned} f_{\text{hydro}}(z,t) = &\frac{\pi}{4}\cdot\rho_{\text{sea}}\cdot C_M\cdot D^2(z)\cdot\dot{u}(z,t) - \frac{\pi}{4}\cdot\rho_{\text{sea}}\cdot C_A\cdot D^2(z)\cdot\ddot{y} \\ &+\frac{1}{2}\cdot\rho_{\text{sea}}\cdot C_d\cdot D(z)\cdot\big(u(z,t)+u_c(z)-\dot{y}(z,t)\big)\big|u(z,t)+u_c(z)-\dot{y}(z,t)\big| \end{aligned} \tag{4.5}$$

which is the sum of inertia plus drag forces imposed by the flowing water on a cylinder.

The inertia force is equal to the sum of the added mass force or disturbance force ($\rho C_A\dot{u}D^2$) and the Froude-Krylov force ($\rho\dot{u}D^2$); this is the contribution to the inertia force by the waves [52]. A moving body in water only changes the added mass force ($\rho C_A\dot{u}D^2$) of the inertia term, and has no influence on the Froude-Krylov force. Therefore:

$$f_{\text{hydro,inertia}}(z,t) = \frac{\pi}{4}\cdot\rho_{\text{sea}}\cdot D^2(z)\cdot\dot{u}(z,t) + \frac{\pi}{4}\cdot\rho_{\text{sea}}\cdot C_A\cdot D^2(z)\cdot\dot{u}(z,t) - \frac{\pi}{4}\cdot\rho_{\text{sea}}\cdot C_A\cdot D^2(z)\cdot\ddot{y} \tag{4.6}$$

which, in the fully nonlinear Morison of Equation 4.5, reduces to:

$$f_{\text{hydro,inertia}}(z,t) = \frac{\pi}{4}\cdot\rho_{\text{sea}}\cdot C_M\cdot D^2(z)\cdot\dot{u}(z,t) - \frac{\pi}{4}\cdot\rho_{\text{sea}}\cdot C_A\cdot D^2(z)\cdot\ddot{y} \tag{4.7}$$

where C_M is the inertia coefficient, equal to $1+C_A$ with C_A is the added mass coefficient. $\dot{u}$ is the horizontal wave acceleration, and $\ddot{y}$ is the displacement acceleration of the structure.

Drag forces result from the flow disturbance and wake near the cylinder [52]. For a moving body in water, it is reasonable to state that the drag force depends on the relative velocity between water flow and pile motion. The drag load:

$$f_{\text{hydro,drag}}(z,t) = \frac{1}{2}\cdot\rho_{\text{sea}}\cdot C_d\cdot D(z)\cdot\big(u(z,t)+u_c(z)-\dot{y}(z,t)\big)\big|u(z,t)+u_c(z)-\dot{y}(z,t)\big| \tag{4.8}$$

includes the influence of a steady current u_c[12], of the horizontal wave velocity u, and of the pile motion velocity $\dot{y}$. The motion of the pile in the water body will create additional hydrodynamic damping, other than the drag damping created by the flow of waves and current over the cylindrical cross-section. Again, the drag coefficient is derived from the surface smoothness-slenderness-Reynolds relation as depicted in Figure 4.2.

It should be noted that the expression in Equation 4.5 was derived based on the slender pile assumption, where the ratio of the diameter divided by the wave length is less than 0.2. Below this ratio, the structural member does not influence the wave field. For slender structures, an inertia coefficient of $C_M = 2$ may be assumed. However, larger diameter structures do influence the wave field as diffraction around the structure occurs. For the large diameter monopile foundation structure in this study, diffraction will occur and will reduce the inertia forces acting on the structure. MacCamy-Fuchs [63] proposed a correction to the inertia force that makes the inertia force decrease for an increasing structural diameter, which reflects the drag force becoming more dominant when wave diffraction occurs. For a large diameter structure, the inertia coefficient C_M reduces with increasing diameter as depicted in Figure 4.3.

[12] The current is assumed steady and constant over depth, with a value equal to 0.20 m/s retrieved on the design basis for the non-disclosed location.

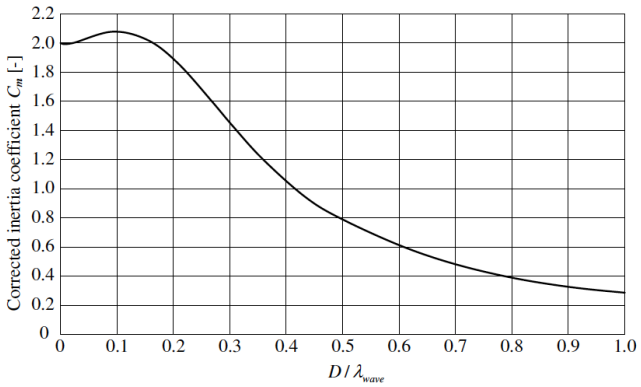

Figure 4.3: *The MacCamy-Fuchs correction to the inertia coefficient C_M in the Morison equation, dependent on the ratio between structure diameter and wavelength [96].*

However, in the present case, the inertia force is dominant according to the Keulegan-Carpenter number in Eq. 4.15, which is confirmed by the MacCamy-Fuchs inertia coefficient. According to Figure 4.3, for the structure in Chapter 3.2.1, a constant inertia coefficient C_M of 2.045 is assumed, together with a constant drag coefficient of 0.65. The wave velocity and acceleration are calculated from linear airy wave theory, which is explained hereafter.

Linear Airy Wave Theory

The velocity of wind-generated waves is most commonly computed by application of the linear wave theory. This theory – a simplified mathematical description of the progressive water wave – assumes that [91]:

1. the flow is homogeneous and incompressible (ρ is constant),
2. the surface tension can be neglected,
3. the Coriolis effect due to the Earth's rotation can be ignored,
4. the pressure at the free surface is uniformand constant,
5. the fluid is an ideal inviscid medium,
6. the flow is irrotational,
7. the bottom boundary (mudline) is fixed, horizontal and impermeable, meaning the vertical flow velocity at the mudline is zero,
8. the wave amplitude is small, and the waveformis invariant in time,
9. the waves are plane or long-crested (two-dimensional).

The progressive wave is assumed to have a sinusoidal waveform. Mathematically, the linear airy wave theory describes the wave elevation η, potential ϕ, horizontal velocity u and vertical velocity w as:

$$\eta(t) = \frac{H_s}{2}\cos(\omega t - kx) \tag{4.9}$$

$$\phi(z,t) = -\frac{\omega H_s}{2k}\frac{\cosh(k(z+d))}{\sinh(kd)}\sin(\omega t - kx) \tag{4.10}$$

$$u(z,t) = \frac{\omega H_s}{2}\frac{\cosh(k(z+d))}{\sinh(kd)}\cos(\omega t - kx) \tag{4.11}$$

$$w(z,t) = -\frac{\omega H_s}{2}\frac{\sinh(k(z+d))}{\sinh(kd)}\sin(\omega t - kx) \tag{4.12}$$

where d is the absolute water depth (positive value), z is the variable water depth ranging from zero at SWL to minus the water depth at mudline (negative value), and ω is the wave frequency:

$$\omega = \frac{2\pi}{T} \tag{4.13}$$

The wave frequency ω and wave number k are related according to the wave dispersion relation:

$$\omega^2 = g k \tanh(kd) \tag{4.14}$$

The wave period T used in this study is the expected peak period T_p associated with a normal sea state. It was estimated from the hindcast data by BMT Argoss [11] to be equal to 5.69 s. The expected significant wave height for a normal sea state was derived to be 1.14 m.

It should be noted that the linear airy wave theory is valid up to SWL. Above SWL, the velocity of the wave particles grows exponentially, which is nonphysical. Given that the amplitude of the waves is assumed to be small in linear wave theory, the wave elevation should remain small as well. Wheeler stretching corrects the velocity profile of the wave, such that the velocities from sea bed to SWL are stretched from seabed to the free surface elevation η.

The wave elevation η, horizontal velocity u and acceleration $\dot{u}$ at some depth beneath SWL are depicted in Figures E.1 to E.3 of Appendix E. These graphs are the result for a regular, sinusoidal wave for a normal sea state with peak period 5.69 s and significant wave height of 1.14 m. The hydrodynamic load at highest water level,– computed from Equation 4.5 to 4.14 with the input as listed in Table 4.4 and 4.5 –, ranges from 48.055 kN/m at the free surface to 9.284 kN/m at the mudline.

From Table 4.5 it can be deduced that the wave loads are inertia dominated. The Keulegan-Carpenter number is a measure of drag versus inertia dominance in the Morison equation:

$$KC = \pi \cdot \frac{2 \cdot u_a}{D} \tag{4.15}$$

where u_a is the wave velocity amplitude. According to Table 4.5, the maximum wave velocity amplitude (near free water surface) is 0.681 m. The diameter of the monopile is 8 m from highest water level to mudline, and thus is KC =0.535 maximum (since the wave velocity amplitude decreases towards the mudline). For KC values below 15, the inertia force is dominant. For values below 3, as is the case, the drag force could have actually been neglected [52]. Lastly, from Figure 12.3 and 12.4 of Journée and Massie [52], the range in which the KC value lays in this study additionally justifies the selected values for C_M and C_D of Table 4.4. For KC values below 10, the C_M value reaches it theoretical value of 2; the selected value of 2.045, with the MacCamy-Fuchs diffraction correction for large diameter piles, is close. Also for $KC < 3$, the drag coefficient C_D has a minimal value of 0.6 for a smooth cylinder and remains rather constant until reaching $KC = 10$.

Lastly, Table 4.5 illustrates that the wave velocity u is in phase with the wave elevation η; both reach their absolute maximum at the same time instance $t = 0 + l \cdot \frac{T_p}{2}$ (l = 0,1,2,...,L), with negative maxima at $t = 0 + l \cdot \frac{T_p}{2}$ (l = 1,3,5,...,L). The wave acceleration is 90° out of phase with η and u, and reaches its absolute maximum at $t = 0 + l \cdot \frac{T_p}{4}$ (l = 1,3,5,...,L), with negative maxima at $t = 0 + l \cdot \frac{T_p}{4}$ (l = 1,5,7,...,L).

Table 4.4: *Summary of the hydrodynamic loading input conditions and resulting loads from free water surface to mudline, at t=0 s.*

MSL	Water density	H_s	T_p	C_M	C_d	Diameter	Loading range
22.395 m	1025 kg/m^3	1.14 m	5.69 s	2.045	0.65	6.55 - 7.03 m (TP) 7.11 - 8.00 m (MP)	48.055 - 34.934 kN/m 30.036 - 9.284 kN/m

Table 4.5: *Summary of the regular waves' elevation, velocity and acceleration, and the current velocity.*

Time	η	u	$\dot{u}$	u_c
t = 0 s	0.57 m	0.681 - 0.077 m/s	0 m/s^2	0.20$^{(12)}$ m/s
t = $\frac{3 \cdot T_p}{4}$	0 m	0 m/s	0.752 - 0.085 m/s^2	0.20$^{(12)}$ m/s

4.4. The Soil Resistance Load

The static and dynamic load-displacement relations introduced in Chapter 3.1.2 and 3.1.3 describe the progression of soil resistance load with pile displacement. In a finite element formulation, the stiffness of the soil springs is implemented rather than the soil resistance load, see Chapter 3.2.2 and 4.6. The stiffness of the soil depends on the soil characteristics, pile dimensions, relative pile displacement, and on the soil modeling method, that is nonlinear elastic versus nonlinear series hysteretic-viscous damping.

4.4.1. The Static Nonlinear Elastic P-y Curves

For a beam on a nonlinear elastic Winkler spring foundation, the stiffness of the soil springs is equal to the *secant* modulus as long as the response is elastic. In the elastic region of the p-y curve, the secant stiffness is equal to the *tangent* stiffness of the curve. From the moment the p-y curve becomes nonlinear elastoplastic, the stiffness of the spring is described by the *tangent* stiffness, as shown in Figure 4.4. The soil stiffness behaviour in the finite-element model is described by the tangent stiffness as:

$$k_{py} = \frac{\delta p}{\delta y} \tag{4.16}$$

where δ represents the gradient of the loading curve at a specific displacement point. The value of k_{py} is implemented as the soil stiffness k_f in the element soil stiffness matrix of Equation C.29.

For the static nonlinear elastic p-y curves, the loading path is identical to the unloading path; no inelastic effects are implemented that may cause the paths to differ. Consequently, the soil spring stiffness during loading will be the same as during unloading, as the slope of the curve remains identical.

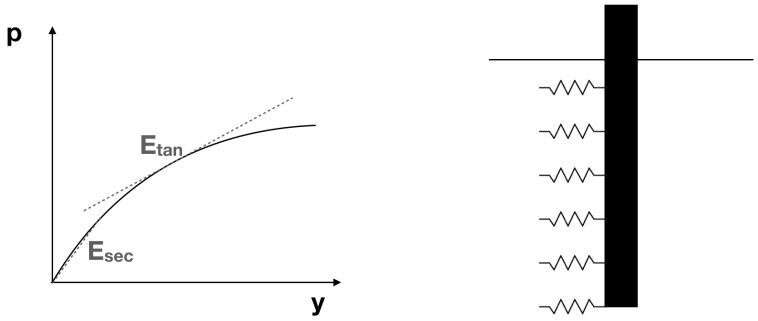

Figure 4.4: *Difference between the secant and tangent modulus of the p-y curve.*

4.4.2. The Dynamic Nonlinear Inelastic P-y Curves

For the dynamic nonlinear elastic p-y curves, the process of determining the value of k_f in the element soil stiffness matrix of Equation C.29 is slightly more complex. As explained in Chapter 3.1.3, the series hysteretic-viscous soil element consists of four springs – elastic, plastic, drag and closure – of which the elastic spring is in parallel with a viscous damper, and the drag and closure spring are in a parallel configuration forming the gap element. As such, considering the series and parallel configuration of the springs, an equivalent soil stiffness system can be formulated.

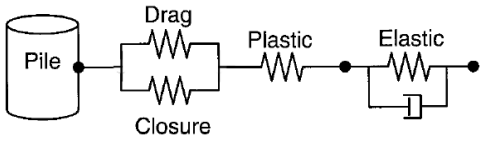

Figure 4.5: *The series hysteretic-viscous damping element with point masses at soil-gap, plastic-elastic and elastic-soil interfaces, to arrive at an equivalent soil element: step 1 [13].*

Consider a point mass at the pile-gap interface, plastic-elastic interface and elastic-soil interface as shown in Figure 4.5. The stiffness of each soil spring is defined by the tangent stiffness of their p-y curve, as:

$$k_d = \frac{\delta p_d}{y_g} \tag{4.17}$$

$$k_c = \frac{\delta p_c}{y_g} \tag{4.18}$$

$$k_p = \frac{\delta p_p}{y_p} \tag{4.19}$$

$$k_e = \frac{\delta p_e}{y_e} \tag{4.20}$$

The stiffness of the drag and closure spring can be combined in an equivalent gap spring stiffness as:

$$k_{\text{eqv,g}} = k_d + k_c \tag{4.21}$$

as shown in Figure 4.6.

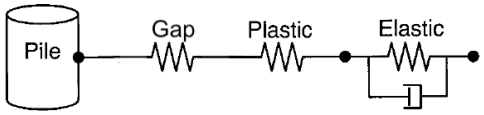

Figure 4.6: *The series hysteretic-viscous damping element with point masses at soil-gap, plastic-elastic and elastic-soil interfaces, to arrive at an equivalent soil element: step 2.*

The gap and plastic spring, positioned in series, can be combined into an equivalent gap-plastic spring as:

$$\frac{1}{k_{\text{eqv,gp}}} = \frac{1}{k_{\text{eqv,g}}} + \frac{1}{k_p} = \frac{k_p + k_{\text{eqv,g}}}{k_{\text{eqv,g}} \cdot k_p}$$

$$k_{\text{eqv,gp}} = \frac{(k_d + k_c) \cdot k_p}{k_p + k_d + k_c} \tag{4.22}$$

The series hysteretic-viscous damping element is reduced to an element with two springs and one damper. To be able to implement the equivalent element in the finite element formulation, a dummy mass is implemented on the interface between the equivalent spring and elastic spring plus damper. This dummy point mass has no physical mass, but holds one translational degree of freedom y_d. The properties at the pile-equivalent spring interface are those of the structure. At the outermost point, at the elastic-soil boundary, the earthquake ground motion is assumed to act. Figure 4.7 summarizes the reduction of the series hysteretic-viscous damping element, the (dummy) degrees of freedom and the action of the ground motion.

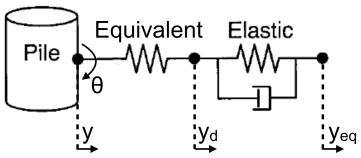

Figure 4.7: *The series hysteretic-viscous damping element with point masses at soil-gap, plastic-elastic and elastic-soil interfaces, to arrive at an equivalent soil element: step 3 (final).*

The exact implementation of the soil resistance elements into the Timoshenko element matrix formulation, both for the static and dynamic descriptions, is shown in detail in Chapter 4.6. First, the earthquake input motion is analyzed in more detail in Chapter 4.5.

4.5. The Earthquake Load

In most seismic analyses of structures, a spectral approach is employed to investigate the response and capacity behaviour, where the input ground motion is derived from design spectra. These design spectra summarize the peak acceleration, velocity or displacement expected for a certain natural frequency of the structure, and are a collection of all peaks in recorded accelerograms and/or historical events in a certain region [95]. The use of spectral analysis is justified when an elastic response of the soil-structure system may be assumed.

However, for systems where nonlinear inelastic behaviour may occur, it is advisable to perform time-history analysis. For inelastic behaviour, the response and capacity of the structure does not only depend on the maximum amplitude of the motion, but also on the frequency and duration. Time series input is needed, which can either be re-derived from the design spectra, or can directly be implemented from accelerographic recordings.

The quality of time series record through random noise generation from design spectra is often deemed low, and preference is given to actual time recordings [95]. Most countries located around the Pacific Ring of Fire have invested in accelerographic networks (see Figure 4.8), such as Kyoshin Net (K-NET) in Japan and the Taiwanese TSMIP network. Illustrations of the nations' strong-motion accelerograph arrays are shown in Fig. 4.9. By the year 2000, Taiwan had 640 free-field accelerographs deployed, while Japan operates 1000 stations. From the recordings of these stations, engineers can obtain the time series records of ground accelerations at an observatory; they provide insight on the amplitude, frequency and duration of an earth tremor, all important measures in defining the inelastic response of a structure. The Pacific Earthquake Engineering Research Center (PEER) has compiled a database on most strong ground motion recordings in the Pacific.

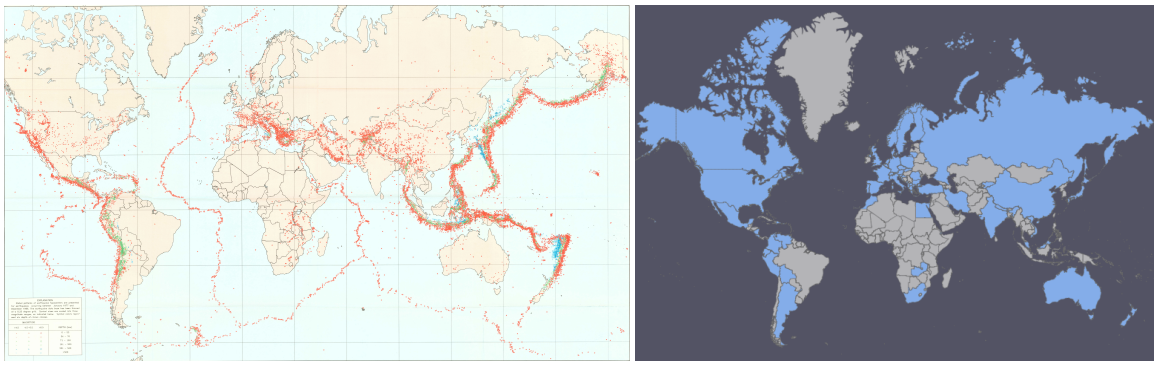

(a) *World seismic map [35].* ***(b)*** *Strong motion instrumentation programs (blue).*

Figure 4.8: *Correlation between seismic activity and development of strong ground motion networks in the world.*

But, as already highlighted in the introductory chapter in earthquakes in Ch. 2.2, not one earthquake accelerogram is the same, not even when they originate from the same fault and are recorded at the same observatory. It poses a challenge on selecting the most appropriate record for the time-history analysis, see Chapter 4.5.1. *Incremental Dynamic Analysis* (IDA), briefly introduced in Chapter 2.2 and implemented in the analysis in Chapter 4.5.3, is a method that works around the shortcoming of limited time series records by artificially scaling the amplitude of one or multiple recordings, this to account for the variability in the recordings' characteristics.

Besides that, the soil body is known to not only influence the ground motion over distance, but also over depth [95]. The ground acceleration at bedrock will not be the same as the recording at the soft surface sediment layer. The first step in any seismic soil-structure analysis is therefore to perform *Site Response Analysis* (SRA) of the seismic shear wave from bedrock through the soft sediment soil. Methods and programs to compute the acceleration history in each soil layer are detailed in Chapter 4.5.2.

4.5.1. The Input Earthquake Record

Taiwan is located on the fault zone between the Eurasian and Philippine Sea plate [82]. *"In northeastern Taiwan, the Philippine Sea plate subducts beneath the Eurasian plate. Conversely, the Eurasian plate subducts beneath the Philippine Sea plate in southern Taiwan"* [82]. Physical prove of the collision between the continental and oceanic plate is found in the mountain chain running north to south across the island, a result from the upward thrusting of the continental plate [95].

The collision of the two plates results in frequent seismic energy release across the nation, translated in earthquakes from small ($M_L = 2$) to large magnitude ($M_L = 7.3$[13]). The high seismic activity in the area pushed the modern seismological program that was initiated in the early 1970's, with strong motion instrumentation as an integral component [90].

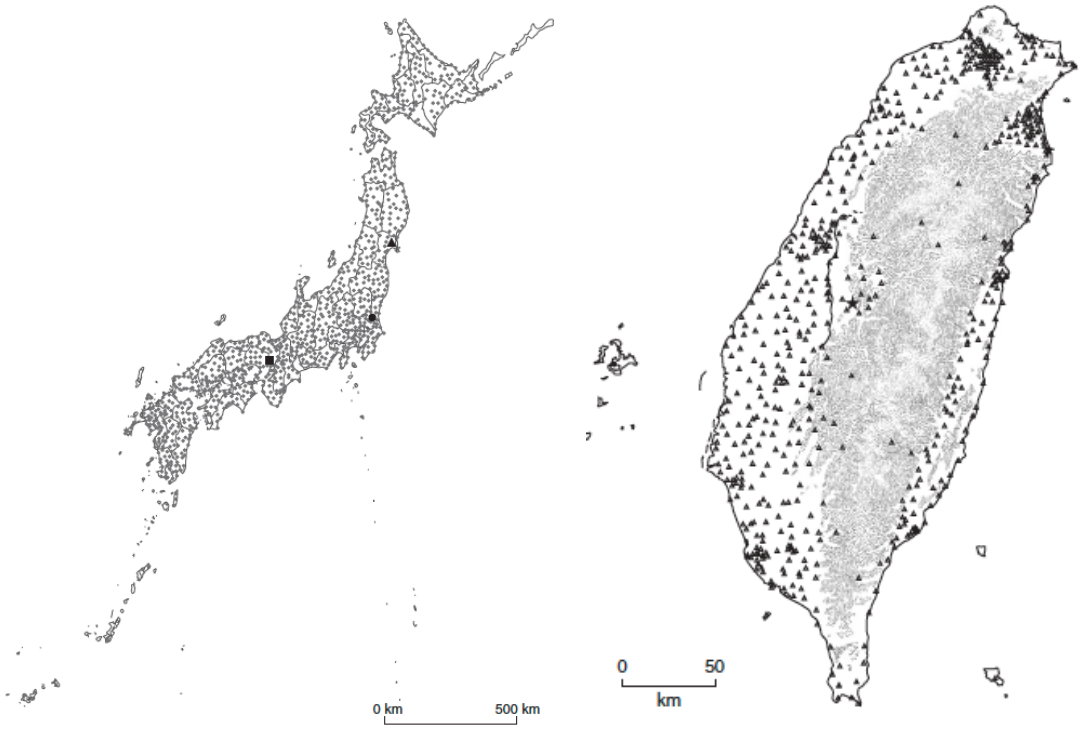

(a) *K-NET Japan [59].* ***(b)*** *TSMIP Taiwan [59].*

Figure 4.9: *The Japan and Taiwan strong motion instrumentation programs' nationwide cover.*

Two institutes invested in the deployment of seismometers. The Institute of Earth Sciences (IES), Academia Sinica, first started operating accelerographic arrays of which the early generation arrays are now closed down [47][81][90]. Still operating today are the SMART2, Taiwan Mountain Seismic Network (MTN), Strong Motion Downhole Accelerometer Arrays in the Taipei Basin (DART, and the Broadband Seismic Array in the Taipei area [47] [81].

The second institute is the Seismology Center of the Central Weather Bureau (CWB). The Taiwanese Strong Motion Instrumentation Program (TSMIP) by the CWB operates nearly 1000 stations [82], of which 640 free-field strong motion stations [81], 56 structural arrays [81], a broadband and short-period seismic system, a GPS to detect crustal deformation, and groundwater observation stations. The TSMIP consequently provides various types of geophysical data, which is managed in and can be accessed through the Geophysical Database Management System (GDMS) [17], an online portal operated by the CWB. Normally, this paid database is only accessible for Taiwanese researchers, but for this thesis research the CWB distributed all available recordings of stations nearby the non-disclosed location. Only free-field data of the free-field strong motion stations could be used.

[13] The Chi-Chi earthquake main shock on the 21st of September 1999 in Nantou County [18].

From all records, the record from a station closest to the wind structure's location was selected, this to minimize the attenuation effect over distance between the station and the structure for which the record will not be corrected[14]. From the remaining pool of earthquake time series, the record that showed the largest peak ground acceleration and longest duration was selected, this because it is expected that this recorded earthquake strong ground motion held the largest damage potential in the past.

The free-field station name is not disclosed here, but the record originates from the Chi-Chi earthquake and is shown in Figure 4.10 as it was recorded by the station. The record corresponds to one of the horizontal recording directions, H2[15]. The peak ground acceleration (PGA) is about 0.253 g and occurs at time 45.9 s of the 90 s record. The free-field accelerographs of the TSMIP have a recording frequency of 200 Hz, registering the earthquake acceleration every 0.005 s.

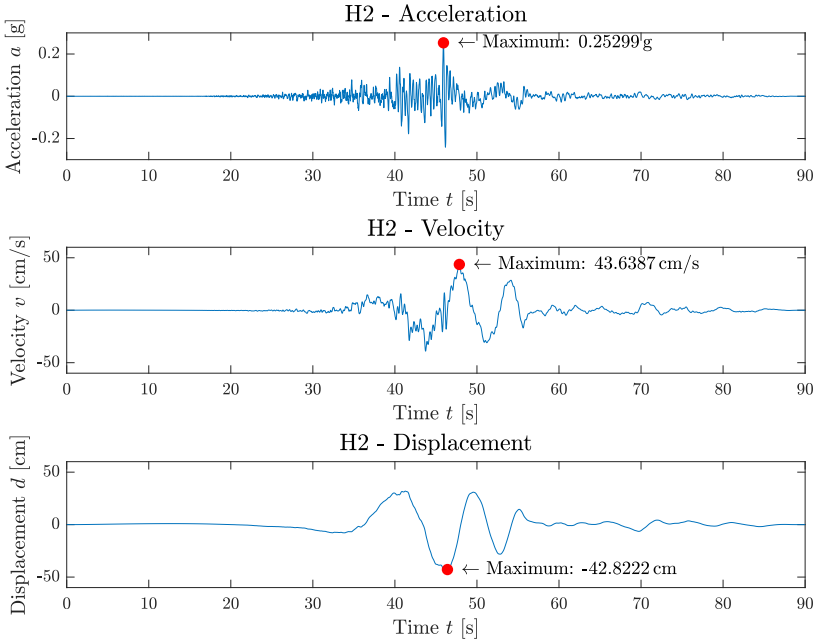

Figure 4.10: *Ground acceleration, velocity and displacement recorded by the TSMIP free-field station near site [18].*

The earthquake strong motion record as presented in Figure 4.10 is the motion at the free surface. Site response analysis should be performed prior to seismic soil-structure interaction evaluation to arrive at the earthquake acceleration, velocity and displacement at every soil layer as these will be dissimilar due to the dissimilar soil properties of each layer. More specifically, for a seismic soil-structure interaction problem, the acceleration, velocity and displacement history at each element node will have to be defined; this is achieved by discretizing the soil layers in strata that correspond to the nodal heights of the pile elements below mudline as described hereafter in Chapter 4.5.2.

4.5.2. Site Response Analysis

Soft soil deposits are known to amplify earthquake ground motions very locally. High-frequency seismic waves coming from a rock-type soil and arriving at a soft soil basin can only be conveyed at lower frequencies, and to convey the same amount of energy the amplitude of the wave increases [95]. Seismic site effects are a major issue in earthquake engineering projects due to the large local amplification of ground motion [41], leading to a very localized increase in seismic demand of a structure.

[14] Normally, earthquake spectra and records are corrected for source-to-site distance effects by ground motion prediction models that account for variability in the geology between site and source. However, as could be taken away from the discussion in [95], these equations depend on a high number of factors that are to date not well understood nor quantified. Therefore, it was decided not to introduce the uncertainty relating to ground motion prediction equations into this seismic soil-structure interaction investigation. Instead, a record of a ground station located <10 km from the offshore location was used.

[15] In this research, only in-plane lateral motion of the structure is investigated. No combination of horizontal records is applied here, nor is the vertical acceleration response investigated, which would require the H1 and V record next to the H2 record to provide the full three-dimensional picture.

Whenever the seismic wave reaches a new (softer) soil layer, the amplitude of the wave will change. This effect is highly pronounced over the range of just a few dozen meters, as shown in Figure 4.11. Consequently, piled structures such as monopile foundation of wind turbines will experience very localized effects along their embedments, apart from the local site effects from structure to structure.

The input to any SRA is the computed or recorded acceleration time history at rock outcrop or bedrock, and a complete description of the dynamic properties of the soil layers. The output is the response of the soil columns to the earthquake shear waves, and derived from that response the amplitude amplification of the earthquake acceleration signal due to the soil sediments. It is important to understand the seismic response of the soil in order to arrive at a reliable SSI model [4]. The acceleration signals at discretized depths will be the input to the nodes of the soil-structure interaction model, hence an accurate description of the amplitude amplification of the earthquake motion by soft sediments is important for the reliability of the SSI model.

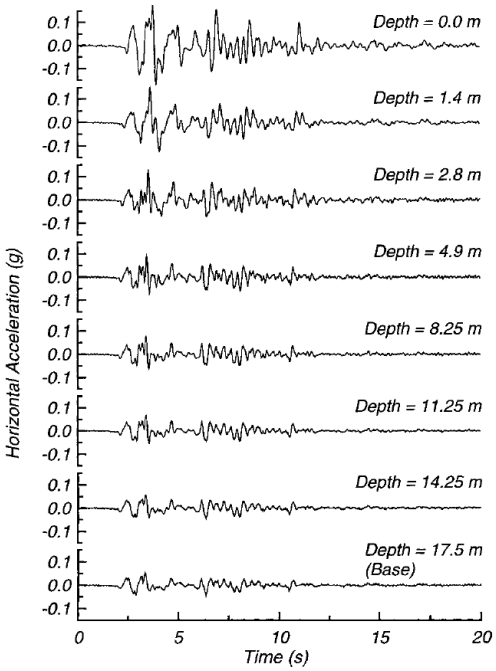

Figure 4.11: *The amplitude of the seismic wave increases towards the soft-sediment surface [13].*

Site response analysis provides methods that can approximate the amplification of a seismic shear wave as it travels through the soil column. The most common approach is to assume one-dimensional wave propagation. The site response can be computed by assuming either a *linear* or *nonlinear* response of the soil column. Both response methods were tried in this study.

Linear Equivalent Site Response Analysis

Linear response analysis relies on the principle of superposition; it is assumed that each earthquake input motion is the summation of a set of harmonic sine waves of different amplitude, frequency and phase angle [4]. The sum of responses of the soil layer to each individual sine waves is equal to the overall soil response. The soil properties are assumed to remain constant over time; the result is a linear elastic set of equations that can be solved individually in the frequency domain and can be superimposed to obtain the total response [41]. It makes linear SRA a computationally convenient analysis method, which holds reasonable results [4].

The site parameters known to influence the soil response are [4];

- the shear modulus G,
- the damping ratio ξ,
- the type of soil (clay, sand, silt,...),
- the location of the water table,
- and the depth of bedrock.

In linear analysis, the soil properties are assumed to remain constant over time, with a constant shear modulus G and damping ratio ξ.

Equivalent linear site response analysis is the most widely used approach to approximate the soil column response [4]. The soil response is approximated by a piecewise-linear solution, where the soil properties are adjusted iteratively to be consistent with an effective level of shear strain [4]; the dynamic properties are approximated by an equivalent shear modulus and equivalent damping ratio compatible with the effective level of shear strain. The equivalent system is most commonly modeled by an equivalent linear Kelvin-Voigt soil model (Figure 4.12) [41][7].

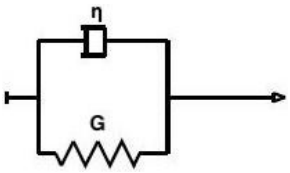

Figure 4.12: *Equivalent linear Kelvin-Voigt soil spring-damper model.*

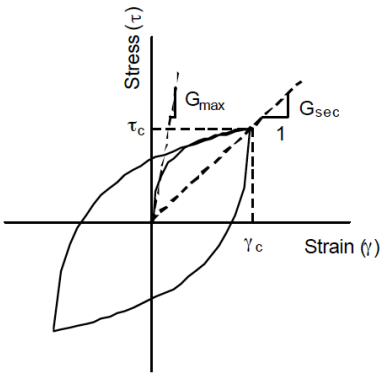

Figure 4.13: *Equivalent shear modulus or secant shear modulus G_S.*

The assumptions made in the linear approximation have inherently introduced some error in the results and set limitations to the application of the analysis method, especially with regard to strong ground motion. The **assumptions** made in equivalent linear response analysis are:

1. The soil layers are horizontal and extend to infinity [4].
2. The incident earthquake waves are pure shear waves (S-wave) [4]. They are spatially uniform, horizontally polarized and propagate vertically [41].
3. The ground surface is level [41].
4. Each soil layer is completely defined by the equivalent shear modulus G and damping ratio ξ as a function of effective shear strain γ, layer thickness and unit weight [41].
5. The nonlinear cyclic behaviour is represented by the linear viscoelastic Kelvin-Voigt model [41].
6. No interaction takes place at the interfaces between layers [30].

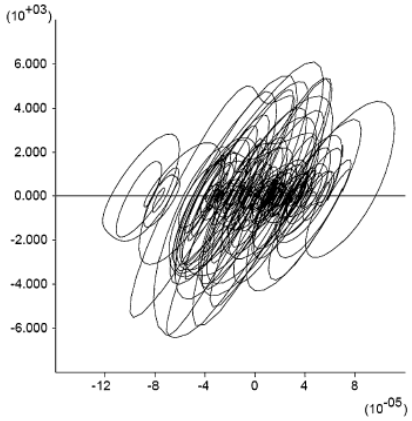

(a) *Nonlinear stress-strain curve.*

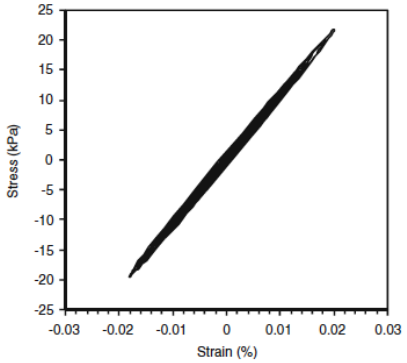

(b) *Linear stress-strain curve.*

Figure 4.14: *Difference between a nonlinear stress-strain curve and linear stress-strain curve from equivalent linear SRA; no permanent strain is built up in equivalent linear analysis [41].*

Consequently, the method has some **limitations** and inherent errors in the response calculation [4]:

1. The strain-compatible shear modulus G and damping ratio ξ remain constant over the duration of the earthquake motion, even though strong ground motion induces nonlinear inelastic stress-strain behaviour in the soil, with G and ξ changing with load intensity.
2. Consequently, no permanent strains can be computed as the response of the soil is assumed to be linear elastic (see Figure 4.14).
3. Pore pressures cannot be computed, therefore liquefaction hazards cannot be modeled.
4. The method cannot represent true changes in soil stiffness under cyclic loading, and hence cannot determine the true fundamental frequency of the site [41].
5. The method does not allow for nonlinear stress-strain behaviour as the input is represented as a Fourier series of harmonic waves, with its response found by transfer functions in the frequency domain; it is a method that relies on the principle of superposition, which is only valid for linear systems.
6. The method is applied to one-dimensional problems. Multiple dimension problems are limited to exemplary case studies [41].

As a consequence of the assumptions and limitations in equivalent linear site response analysis, the computed response will be an underestimate of the true response for moderate to strong ground motion [13]. This is because the strain-compatible shear modulus G remains constant over time – leading to an overestimated soil shear strength – when in fact the soil might suffer from strength degradation over time due to the inelastic behaviour of the soil under strong ground motion [4]. Plastic deformations would cause the value of G to diminish, leading to lower shear strength of the soil and consequently larger responses. Equivalent linear SRA is unable to pick up these nonlinear effects. As such, the method cannot correctly account for resonant frequencies and the true hysteretic soil behaviour [41].

More information on the equivalent site response analysis can be found in [7], and the calculation procedure can be consulted in Appendix D. Commercialized codes that implemented the mathematics described in Appendix D are EERA, SHAKE91, DEEPSOIL, Strata, and ShakeVT2 [55]. As SHAKE91 and ShakeVT2 are known to suffer from bugs and lack of precision, and Strata is still under development [55], EERA and DEEPSOIL were tried. The results of the SRA analyses are discussed later in this Chapter 4.5.2.

Nonlinear Equivalent Site Response Analysis

In linear analysis, it is assumed that the soil properties remain constant over time, with a constant shear modulus G and damping ratio ξ. However, geological materials are known to behave nonlinearly under moderate to strong earthquake loading [4]; all strong ground motion studies have shown presence of nonlinear site amplification at soft soil sites when subjected to large amplitude motions [41]. This means that the shear modulus G is constantly changing in the loading history, indicating a nonlinear stress-strain relation. Energy is dissipated from the system, causing the loading path to be different from the unloading path, resulting in a hysteretic stress-strain curve.

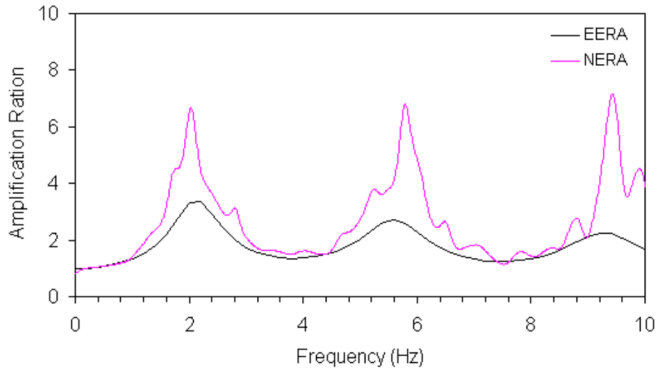

Figure 4.15: *Difference in predicted soil response amplification by nonlinear site response analysis (NERA) and equivalent linear site response analysis (EERA), as documented in the NERA manual [8].*

Linear SRA is known to underestimate the magnitude and duration of the soil column response to strong earthquake motion [62] (Fig. 4.15) as a result of keeping the linear soil properties constant and thus overestimating the soil resistance [4]. This might potentially be very dangerous in the design of an earthquake-retaining structure, leading to unforeseen structural response behaviour surpassing the design limits. Fully *nonlinear site response analysis* might be the better option in strong motion site response analysis, as soil is known to behave nonlinear inelastic under strong ground motion, and potential changes in soil stiffness may highly influence the soil-structure response.

Proof for the nonlinear inelastic behaviour of soil is found in all strong ground motion studies; they show nonlinear site amplification at soft soil sites when subjected to large amplitude motions [41]:

1. In time domain solutions, this is observed in a reduction of the amplitude of the waveform over time. In frequency domain solutions, a shift in predominant frequency and peak reduction can be found. Both are due to the changes in elastic properties of the soil.
2. The velocity of the S-wave before and after the main shock is different, indicating that the soil properties have changed.
3. The spectra of observed data between surface and bedrock during strong and weak ground motions are fundamentally different, indicating that weak ground motions are governed by a linear elastic response while strong ground motions cause permanent deformation (leading to a nonlinear inelastic response).
4. Proof of differences in amplification between weak and strong ground motion is also found in recordings from vertical arrays of seismometers.
5. The comparison of recorded and linearly computed site responses shown a pertinent difference. This difference can be attributed to nonlinearity effects, next to uncertainties in the soil properties.

In nonlinear analysis the dependence of the shear modulus G and damping ratio ξ is directly modeled by an elastoplastic Mohr-Coulomb model, also referred to as the Iwan-Mroz model (Fig. 4.16a), which is a nonlinear hysteretic model represented by a series of linear Kelvin-Voigt elements [30]. The nonlinear G is constantly changing after onset of yield, most often decreasing due to strength degradation of the soil by cyclic loading [41]. The inelastic soil unloads along a different path than the loading path in the hysteretic curve, thereby dissipating energy in the process (Fig. 4.16b). The changing values of G and ξ is the major difference with equivalent linear SRA, where the strain-dependence of G and ξ is approximated by equivalent G and ξ – which are dependent on an effective level of strain to mimic the change in soil properties under strong ground motion, but which are in fact kept constant.

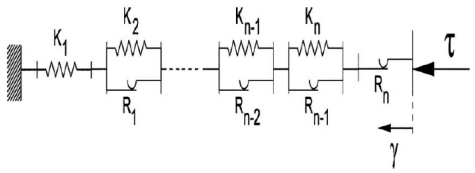

(a) *Iwan-Mroz hysteretic elastoplastic model [31].*

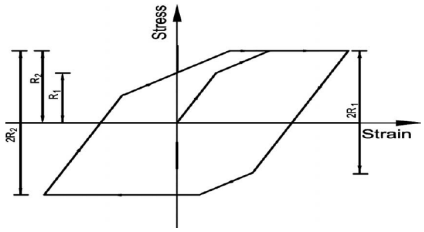

(b) *Hysteretic stress-strain curve Iwan-Mroz model [31].*

Figure 4.16: *Nonlinear soil stress-strain Iwan-Mroz model used in NERA nonlinear site response analysis.*

The algorithm used to compute the stress due to a certain strain increment, and the finite difference formulation to compute the soil response, can be consulted in the NERA manual [8]. NERA is a commercial software tool that can be used to perform fully nonlinear site response analysis. Also DEEPSOIL enables nonlinear earthquake site response analysis. Both programs are used and compared hereafter.

Comparison of the Results of Both Approaches

The previously selected free-field record, shown in Figure 4.10, is applied to the soil column, with properties as described in Table 3.1. The soil profile was discretized into its five main layers, and then subdiscretized into layers consistent with the finite element discretization. This way, the nodes of the finite element model

below mudline correspond to the top surface of each SRA soil sublayer. As such, following the SRA of the free-field acceleration signal, the acceleration time history – and derived velocity and displacement history – of the soil at every element node of the structure can be implemented directly on the outer node of the spring element at each node, see Chapter 4.6.

Three different programs were used to compute the response of each soil layer to the input acceleration time series record. EERA and DEEPSOIL were used to compute the soil column response under linear conditions. NERA and DEEPSOIL in nonlinear settings were used on the other hand to compute the assumed nonlinear soil column response to the input motion. The similarities and differences between the input data and computation scheme from all four SRA simulations is shown in Table 4.6.

The results from the equivalent linear analysis in EERA and DEEPSOIL compared well, as can be seen in Figures 4.18 and 4.17. Only slight differences exist due to the definition of the damping and strain relations in DEEPSOIL versus EERA, where DEEPSOIL allows for a wider selection of conditions than EERA does and therefore allows for more detail in the strain-damping curves. Both software packages produce results consistent with expectations, where the peak acceleration at the free surface is equal to the free-field recording; 2.48 m/s^2 from the SRA anal. This isboth EERA and DEEPSOIL, with respect to 2.481 m/s^2 in the earthquake recording of Figure 4.10 to be expected, as the sysis for oft sediment conditions at the recording station and the wind foundation location are roughly comparable. As the soil grows more stiff with increasing depth, the shear wave can propagate at increasing frequency. Consequently, the amplitude of the acceleration is expected to decrease with increasing depth, as previously explained in the first paragraph of Chapter 4.5.2.

The results from the nonlinear analyses executed in NERA and DEEPSOIL were less accurate. Both showed the sensitivity of the computational algorithm to numerical errors when discretizing the main soil layers. At the transition from one sublayer to the other, both programs predict peak ground acceleration which are nonphysical. For DEEPSOIL (Figure 4.19), this behaviour was previously noticed in the work by Lasley et al. [55]. The results from *NERA* did not comply at all with expectations (Figure 4.20) where the peak ground acceleration is supposedly picking up again in the gravel layer to levels comparable to the sand layer, even though the gravel layer is much more stiff. Besides that, the peak acceleration at the free surface is overestimated with respect to the actual record. With *DEEPSOIL*, besides the numerical sensitivity of the algorithm to discretization of the soil layers, it was noticed that the program seems to have unit errors in the integration of the acceleration output to velocity and displacement time series.

Conclusion on Site Response Analyses Methods and Results

Although nonlinear site response analysis should provide a better fit with the recorded earthquake data, a strong ground motion record, it was seen in the analyses that EERA and DEEPSOIL in equivalent linear setting provided a smoother acceleration profile over depth. NERA and DEEPSOIL in nonlinear analysis setting introduced numerical peaks in the PGA over depth profile at soil discretization boundaries. These peaks are nonphysical and would introduce a too high demand on the structural section. As such, the results of the DEEPSOIL linear site response analysis will be used even though the response of the soil column may be underestimated. DEEPSOIL is preferred over EERA as it has a feature that allows for IDA scaling in the analyses. The amplitude levels selected for the incremental dynamic analyses in this study are detailed in Chapter 4.5.3.

An important consideration when applying site response analysis in a seismic soil-structure interaction problem is the sensitivity of the SSI response to the SRA parameters. In Boulanger et al. [13], it was experimentally proven that the parameters used in the site response analysis will severely influence the calculated response in a soil-structure interaction model, more than the parameters of the SSI model itself would. The study showed that the agreement between the recorded response of a structure and the computed response improved when the site response analysis input to the SSI model was replaced by recorded borehole soil responses; the structural response was no longer underestimated. This indicates that the use of a linear equivalent or nonlinear site response analysis will introduce an error due to linearization, oversimplification or uncertainties regarding the soil properties. Caution should be exercised when defining the site response parameters, and careful interpretation of the structural response of the SSI model is warranted if the input accelerations to that model are retrieved from site response analysis. Preference is given to borehole time series records across the depth of the structure's location, but by lack of such data for this research free-field SRA results are used.

Table 4.6: *Input and analysis method comparison between DEEPSOIL Nonlinear, Equivalent Linear, NERA and EERA, based on application in this study. More on SRA software comparison studies in [55] [42] and [4]. More on the software programs in their respective manuals [37], [8] and [7].*

	Earthquake Motion	**Analysis Method**	**Units**	**Soil Profile**	**Shear Modulus and Damping Curves**	**Bedrock**	**Integration Scheme**
DEEPSOIL - Nonlinear	• Free-field • Within (inside) at surface • Deconvolution	• Nonlinear • Time domain • No pore pressure generation • General Quadratic-Hyperbolic Model • Non-Masing Re-/Unloading Hysteretic Model	Metric	• Layered profile: Tab. 3.1 • $\Delta d = 1.608$ m • Unit weight: Tab. 3.1 • Shear wave V_s: Tab. 3.1	• Sand: Seed & Idriss (mean) • Clay: Vucetic & Dobry • Mudstone: Vucetic & Dobry • Gravel: Seed & Idriss (mean) • Sandstone: Vucetic & Dobry • Frequency-independent: $G^* = G \cdot (1 + 2i\xi)$ • No damping matrix update	• Rigid halfspace	• Newmark-Beta: unconditionally stable • Flexible time step
DEEPSOIL - Linear	• Free-field • Within (inside) at surface • Deconvolution	• Equivalent Linear • Frequency domain • *No info pore pressure* • General Quadratic-Hyperbolic Model • Non-Masing Re-/Unloading Hysteretic Model	Metric	• Layered profile: Tab. 3.1 • $\Delta d = 1.608$ m • Unit weight: Tab. 3.1 • Shear wave V_s: Tab. 3.1	• Sand: Seed & Idriss (mean) • Clay: Vucetic & Dobry • Mudstone: Vucetic & Dobry • Gravel: Seed & Idriss (mean) • Sandstone: Vucetic & Dobry • Frequency-independent: $G^* = G \cdot (1 + 2i\xi)$ • *No info damping matrix*	• Rigid halfspace	• Newmark-Beta: unconditionally stable • Flexible time step
NERA	• Free-field • Inside	• Nonlinear • Time domain • *No info pore pressure* • Iwan-Mroz Model	Metric	• Layered profile: Tab. 3.1 • $\Delta d = 1.608$ m • Unit weight: Tab. 3.1 • Shear wave V_s: Tab. 3.1	• Sand: Seed & Idriss (mean) • Clay: Vucetic & Dobry • Mudstone: Vucetic & Dobry • Gravel: Seed & Idriss (mean) • Sandstone: Vucetic & Dobry • Frequency-independent: $G^* = G \cdot (1 + 2i\xi)$ • *No info damping matrix*	• Elastic halfspace	• *No info integration* • *No info time-stepping*
EERA	• Free-field • Inside at surface	• Equivalent Linear • Frequency domain • *No info pore pressure*	Metric	• Layered profile: Tab. 3.1 • $\Delta d = 1.608$ m • Unit weight: Tab. 3.1 • Shear wave V_s: Tab. 3.1	• Sand: Seed & Idriss (mean) • Clay: Vucetic & Dobry • Mudstone: Vucetic & Dobry • Gravel: Seed & Idriss (mean) • Sandstone: Vucetic & Dobry • Frequency-independent: $G^* = G \cdot (1 + 2i\xi)$ • *No info damping matrix*	• Elastic halfspace	• *No info integration* • *No info time-stepping*

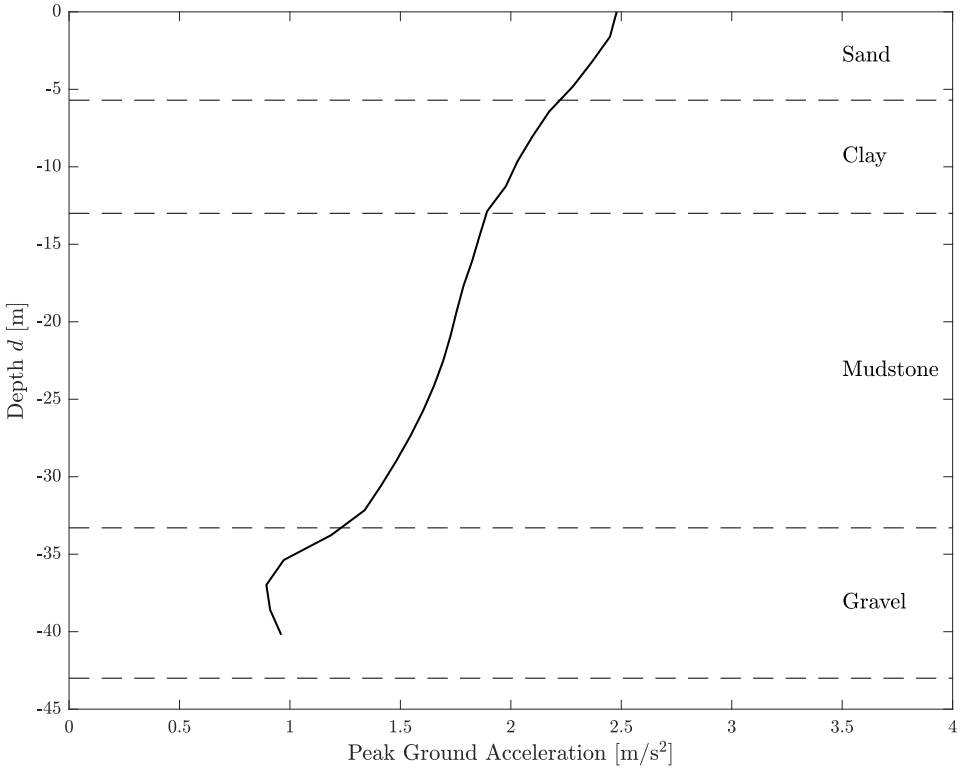

Figure 4.17: *Peak ground acceleration at the top of each discretized soil layer. Results as computed by DEEPSOIL, assuming linear equivalent site response.*

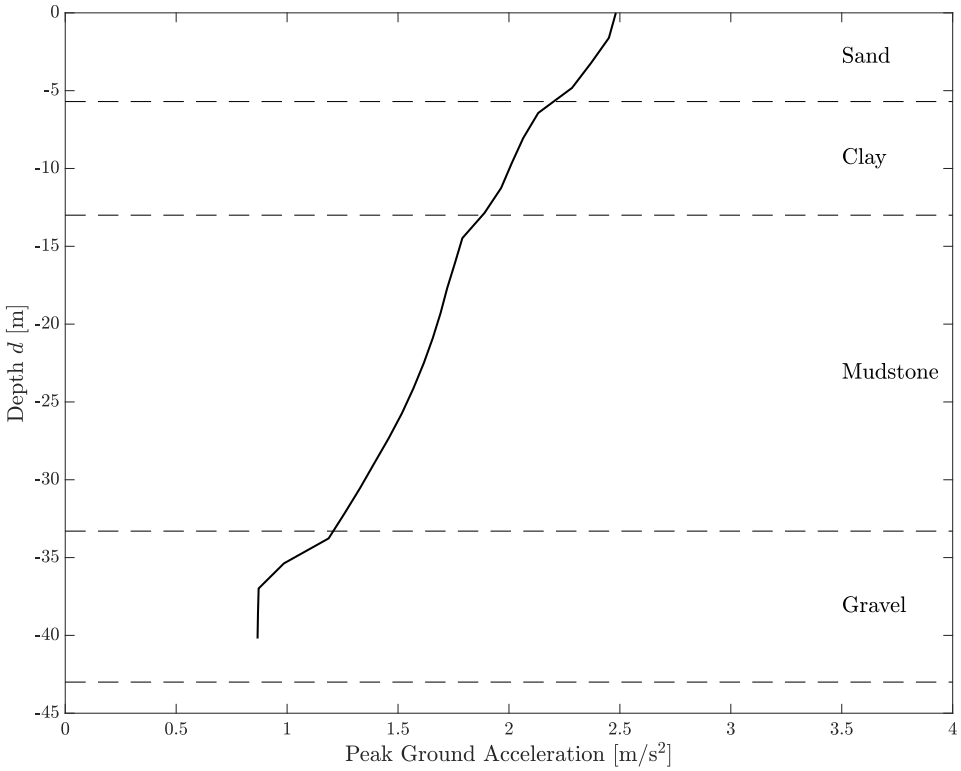

Figure 4.18: *Peak ground acceleration at the top of each discretized soil layer. Results as computed by EERA, assuming linear equivalent site response.*

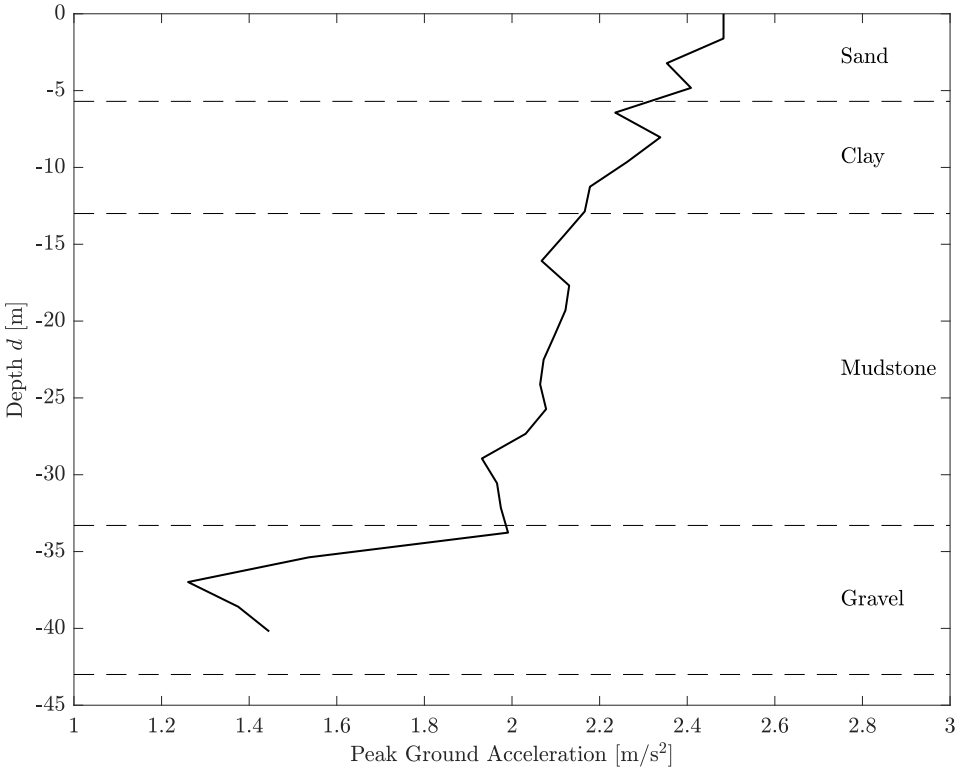

Figure 4.19: *Peak ground acceleration at the top of each discretized soil layer. Results as computed by DEEPSOIL, assuming nonlinear site response.*

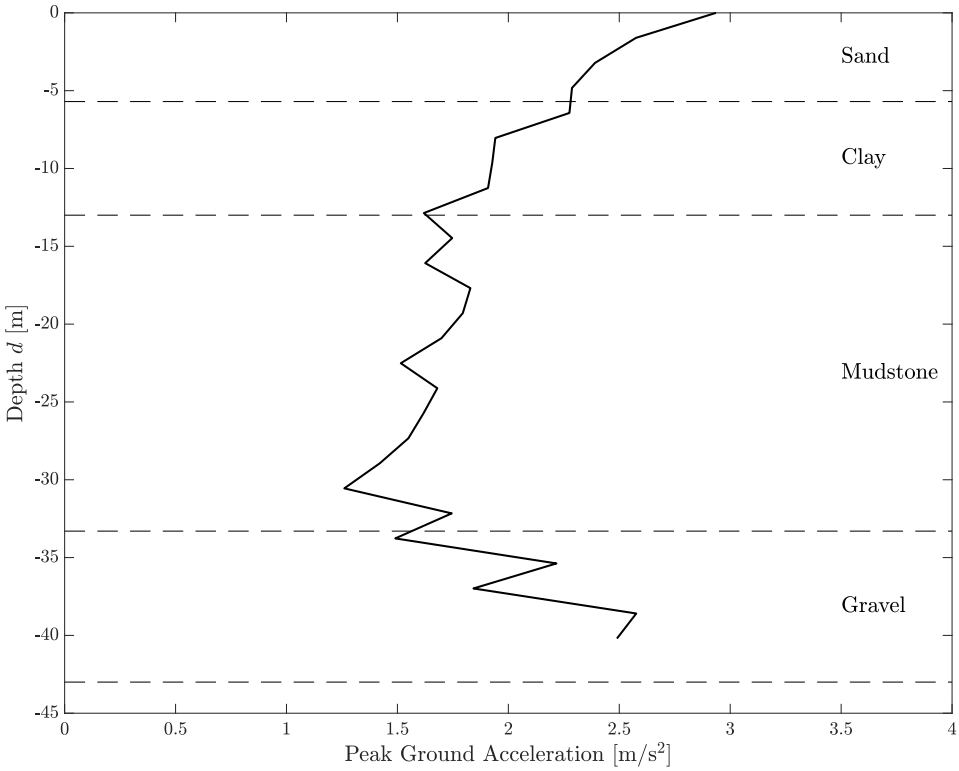

Figure 4.20: *Peak ground acceleration at the top of each discretized soil layer. Results as computed by NERA, assuming nonlinear site response.*

4.5.3. Incremental Dynamic Analysis

The free-field earthquake record will be scaled to acceleration levels compliant with the *Extreme Level Earthquake* and *Abnormal Level Earthquake* as previously specified in the performance requirements for the structure in Chapter 2.1.7. These probabilistic events, which identify the earthquakes the structure is unlikely to experience but should survive, are based on historical and recorded data of past earthquake occasions. All recorded earthquakes in Taiwan can be consulted in the GDMS database by the CWB [17][18].

The *Extreme Level Earthquake* (ELE) holds reasonable likelihood of not being exceeded during the structure's life, comparing to a 475 year return period event [28][32][2]. No structural damage should exist after this return period event, and the structural response should remain elastic. No structural yielding is allowed (ULS requirement), nor should there be an accumulation of permanent tilt of the structure (SLS requirement). For the wind foundation location, the peak acceleration is 0.7534 g for the ELE event, which is about trice the amount of g's the earthquake free-field record poses (0.253 g).

The *Abnormal Level Earthquake* (ALE) should be a rare, intense earthquake, with a return period of 2475 years. Irreparable damage may exist but the structure should hold enough reserve capacity to prevent a collapse. Structural stresses should not exceed the ultimate structural strength (ULS requirement), and the permanent tilt of the structure should not exceed 0.5° (SLS requirement). For the wind foundation location, the peak acceleration is 1.1669 g for the ALE event.

The return periods for the ELE and ALE event are based on the assumption that the structure is at L-1 exposure risk, a combination of life-safety category S-3 (unmanned) and consequence level C-1 (high financial consequence). The ELE event is defined as a 10/50 event [32], the corresponding return period is 475 years (or 50 years divided by 10.5 %). The ALE event corresponds to a 2/50 event, which in turn reflects a 2475 return period event (calculated as 50 years divided by 2.02 %).

Although the ELE and ALE are unlikely to occur during the structure's lifetime, the structure should still prove to perform adequately under the sustained loads. IDA can provide valuable insight in the expected versus computed capacity behaviour of the structure under strong ground motion of increasing intensity. The IDA peak ground acceleration levels are summarized in Table 4.7.

Table 4.7: *Incremental dynamic analyses peak ground acceleration levels for capacity analysis.*

IDA Level	**Recorded**	**ELE**	**ALE**	Units
PGA	0.2530	0.7534	1.1669	g

The full time-history of the earthquake record is scaled by a constant factor such that the peak amplitude reaches the desired level. The damage variables used to assess the progression of the structural capacity with increasing ground motion intensity are:

1. the structural yield stress,
2. the structural permanent tilt angle,
3. the structural buckling.

Besides that, the soil resistance capacity will be tracked to detect soil failure in case the ultimate soil resistance is reached. Past this point, the soil holds no more stiffness against lateral motion.

The IDA scaling levels identified in Table 4.7 are used to scale the free-field input acceleration signal, after which the scaled signal is processed in the SRA by DEEPSOIL prior to implementation in the SSI model. The resulting PGA, PGV and PGD behaviour over depth for all scaling levels is shown in Figures 4.21a to 4.23c; each discrete point in these plots corresponds to the nodal height of a beam element below mudline. The time history of each of the three earthquake acceleration signals over depth is shown in Figures 4.24 to 4.26, the velocity time history in Figures 4.27 to 4.29, and the displacement time history in Figures 4.30 to 4.32; one time history corresponds to the motion experienced by one node of the structure below mudline.

The general trend in the SRA results, for all IDA levels, is that the PGA, PGV and PGD decrease with increasing depth; as the soil continues to grow more stiff with depth, the shear wave can propagate at increasing frequency, thereby decreasing the amplitude of the signal.

It is straightforward that a higher-amplitude input motion will lead to higher amplitude SRA responses over depth, as can be observed between the PGA plot of the recorded motion and the ALE motion in Figures 4.21a and 4.21c respectively. However, one cannot directly scale the SRA result by the same factor used to scale the recorded motion to the IDA level motion. The recorded acceleration signal is scaled by a factor of 4.6 approximately to the ALE level (from 0.253 g to 1.1669 g according to Table 4.7). Scaling the PGA profile of the recorded motion as in Figure 4.21a by that same factor would not lead to an ALE PGA profile identical to the one in Figure 4.21c. The discrepancy is expected to be even more pronounced in nonlinear site response analyses, when the extent of nonlinear soil effects on the site response will be governed by the magnitude of the input motion. Hence, IDA scaling is recommended to be done prior to site response analysis, which in turn should be conducted prior to implementation of the earthquake motion signal at each node of the soil-structure model.

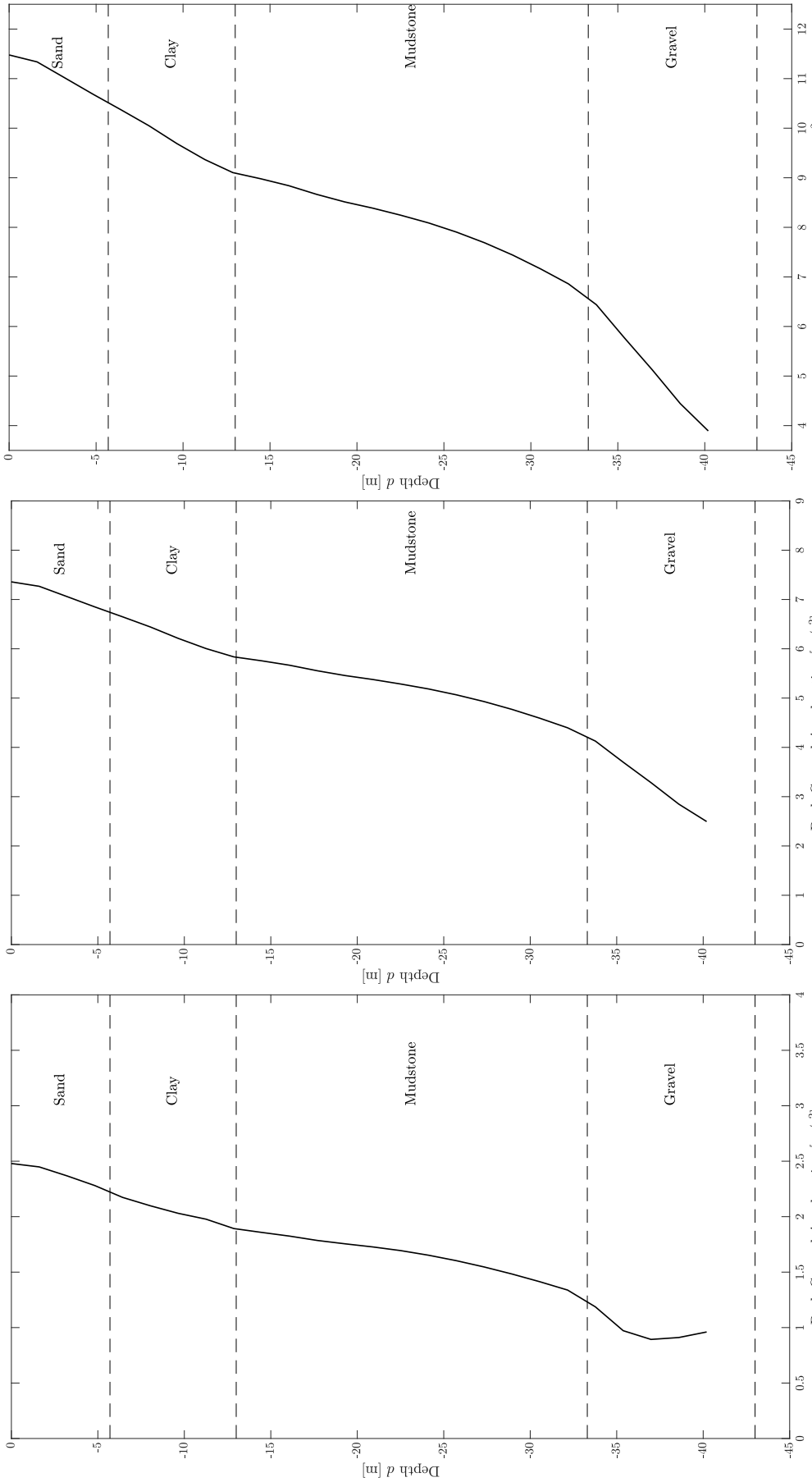

***(a)** Free-field ground motion record.*

***(b)** Extreme Level Earthquake.*

***(c)** Abnormal Level Earthquake.*

***Figure 4.21:** Peak ground acceleration (PGA) profile from DEEPSOIL linear site response analysis for all IDA levels.*

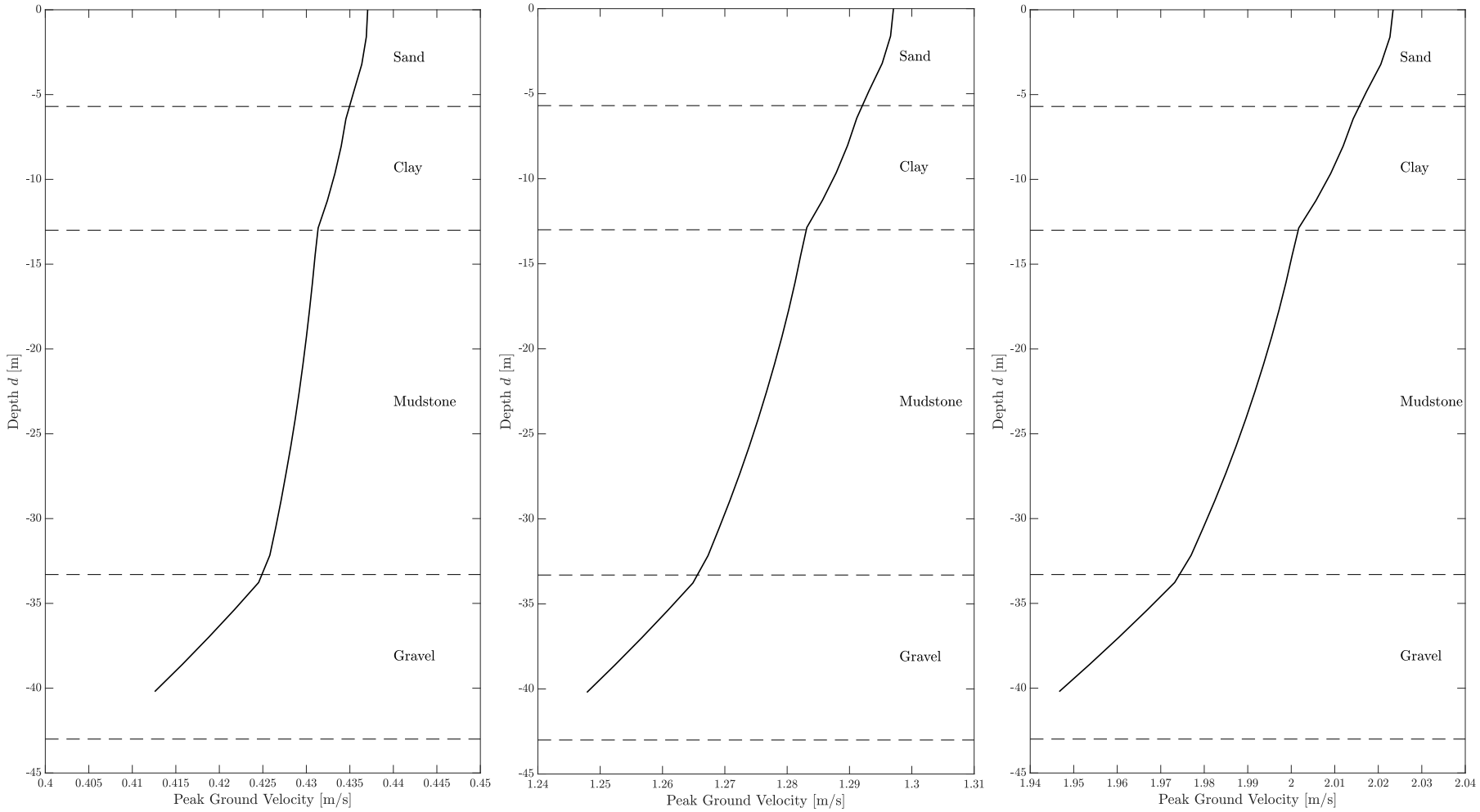

(a) *Free-field ground motion record.*

(b) *Extreme Level Earthquake.*

(c) *Abnormal Level Earthquake.*

Figure 4.22: *Peak ground velocity (PGV) profile from DEEPSOIL linear site response analysis for all IDA levels.*

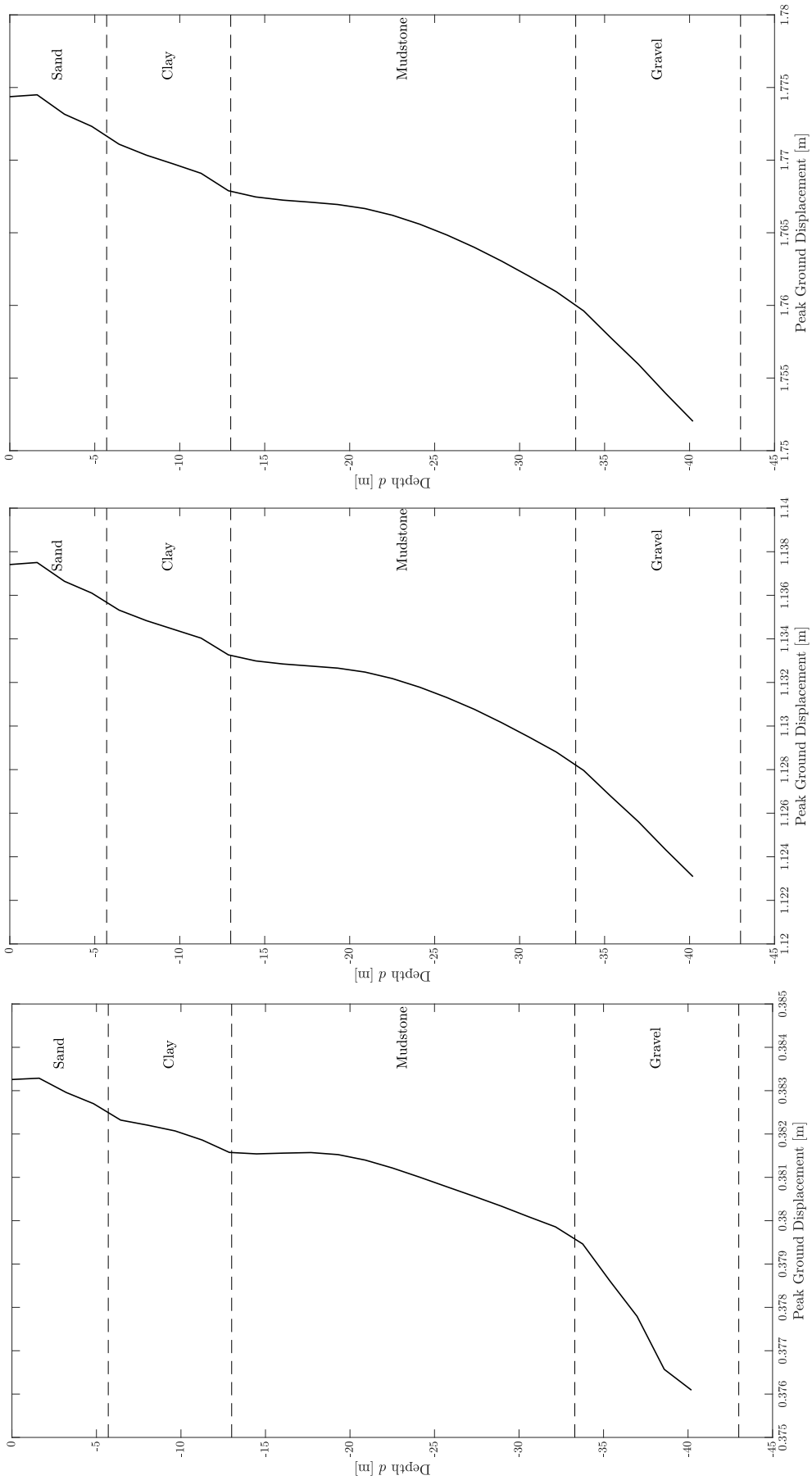

***(a)** Free-field ground motion record.*

***(b)** Extreme Level Earthquake.*

***(c)** Abnormal Level Earthquake.*

***Figure 4.23:** Peak ground displacement (PGD) profile from DEEPSOIL linear site response analysis for all IDA levels.*

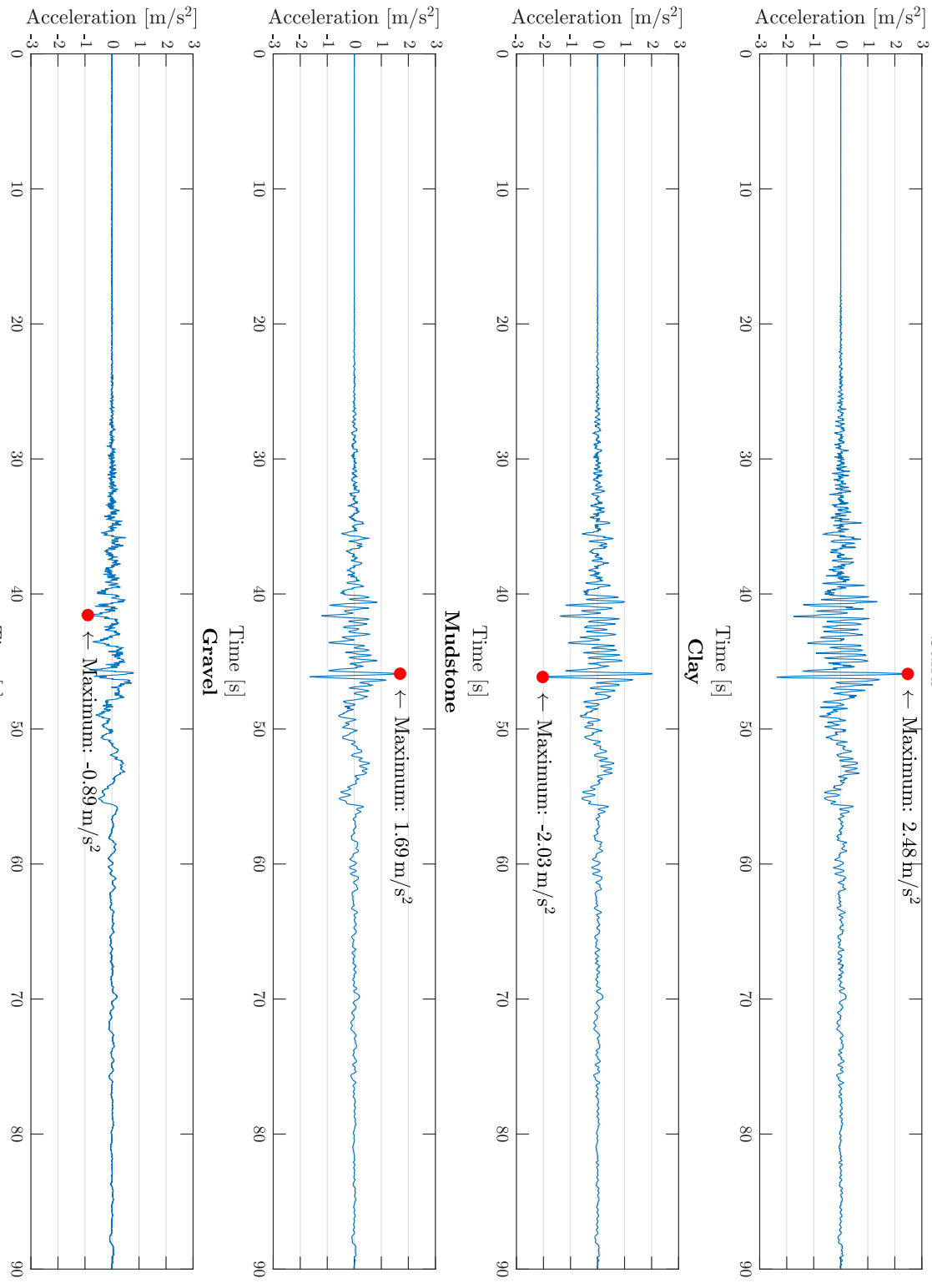

Figure 4.24: *Acceleration time history profile for the as-recorded free-field acceleration signal, for one selected depth in each soil layer: 0 m (sand), -9.65 m (clay), -22.51 m (mudstone) and -36.98 m (gravel).*

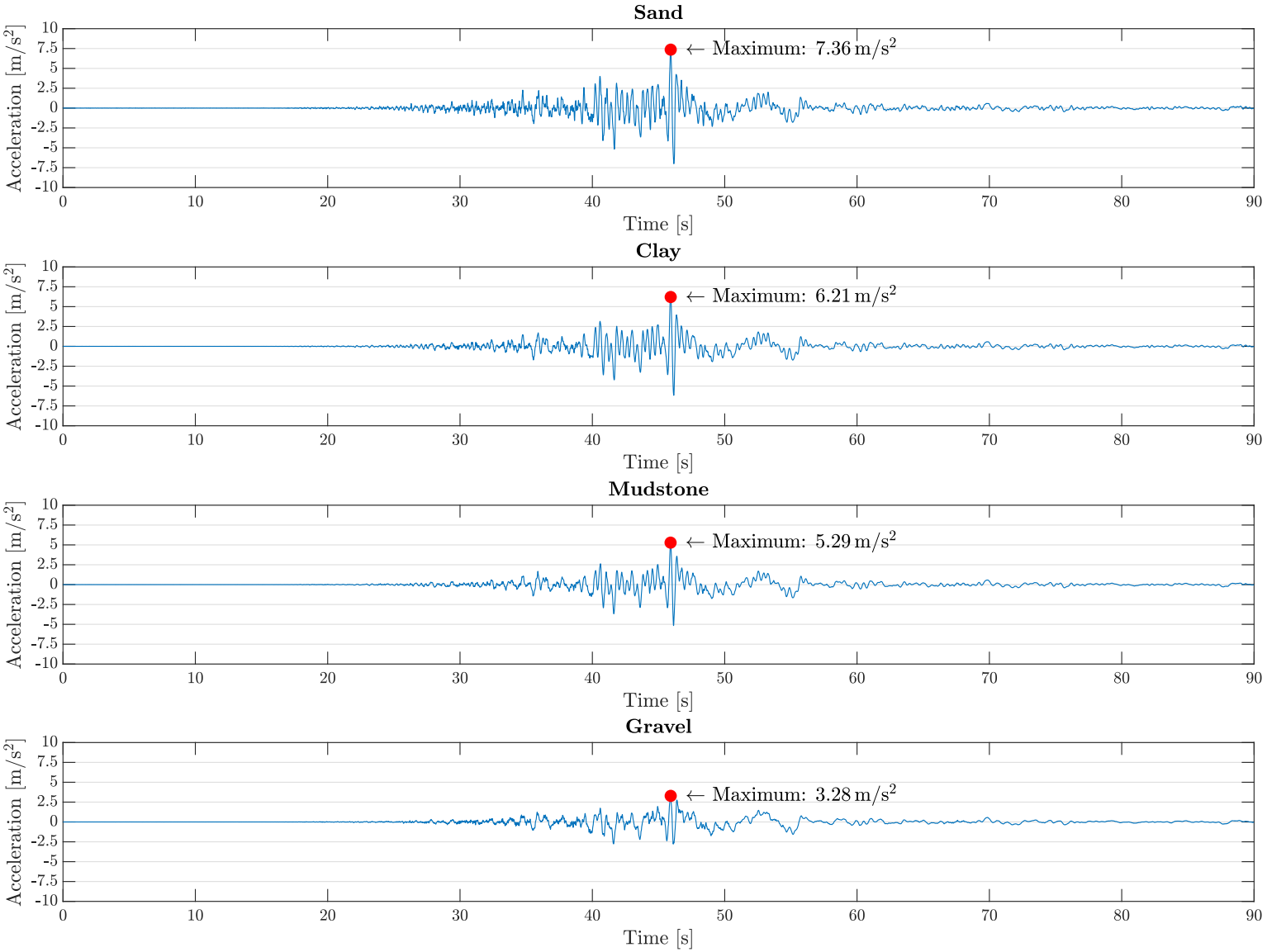

Figure 4.25: *Acceleration time history profile for the Extreme Level Earthquake acceleration signal, for one selected depth in each soil layer: 0 m (sand), -9.65 m (clay), -22.51 m (mudstone) and -36.98 m (gravel).*

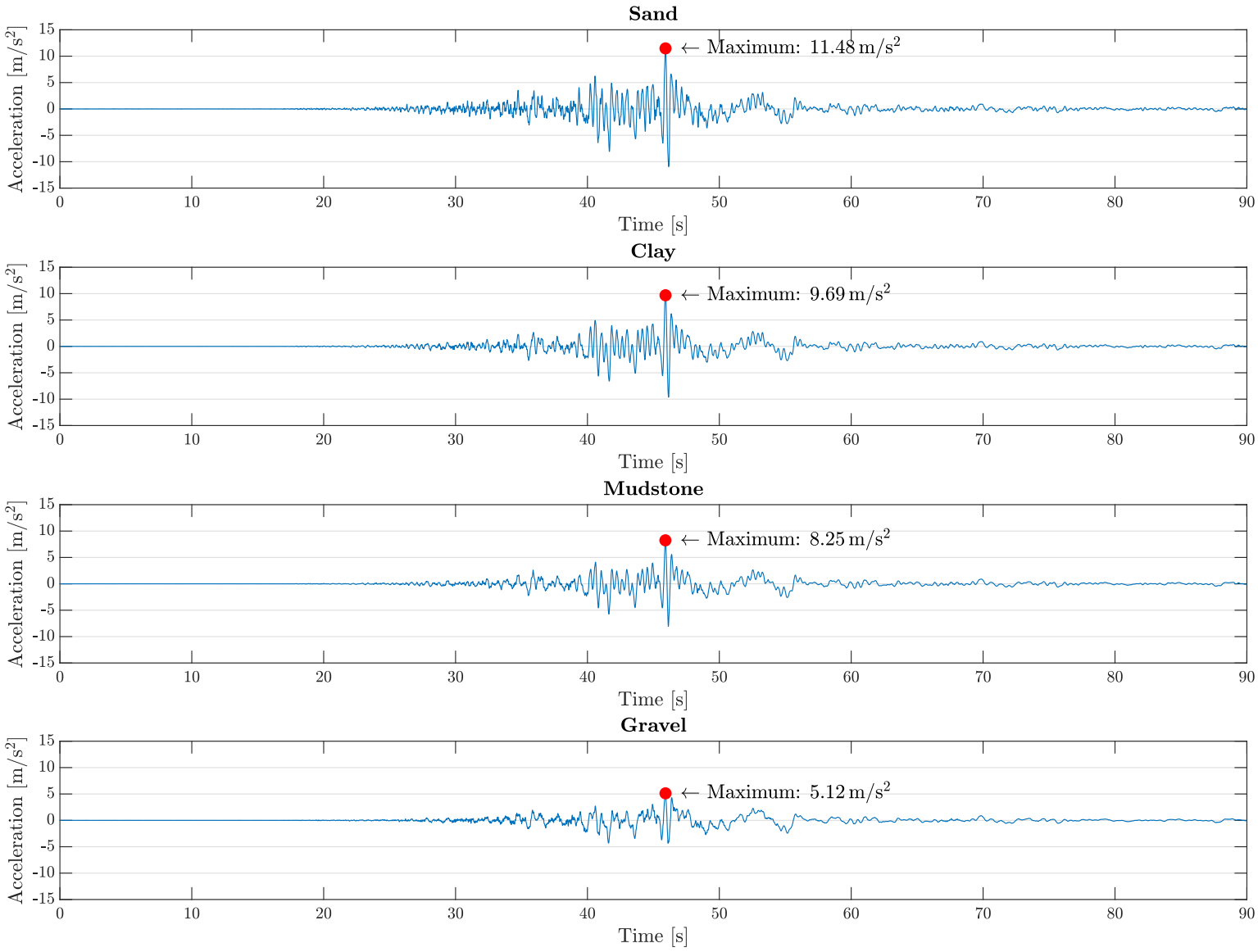

Figure 4.26: *Acceleration time history profile for the Abnormal Level Earthquake acceleration signal, for one selected depth in each soil layer: 0 m (sand), -9.65 m (clay), -22.51 m (mudstone) and -36.98 m (gravel).*

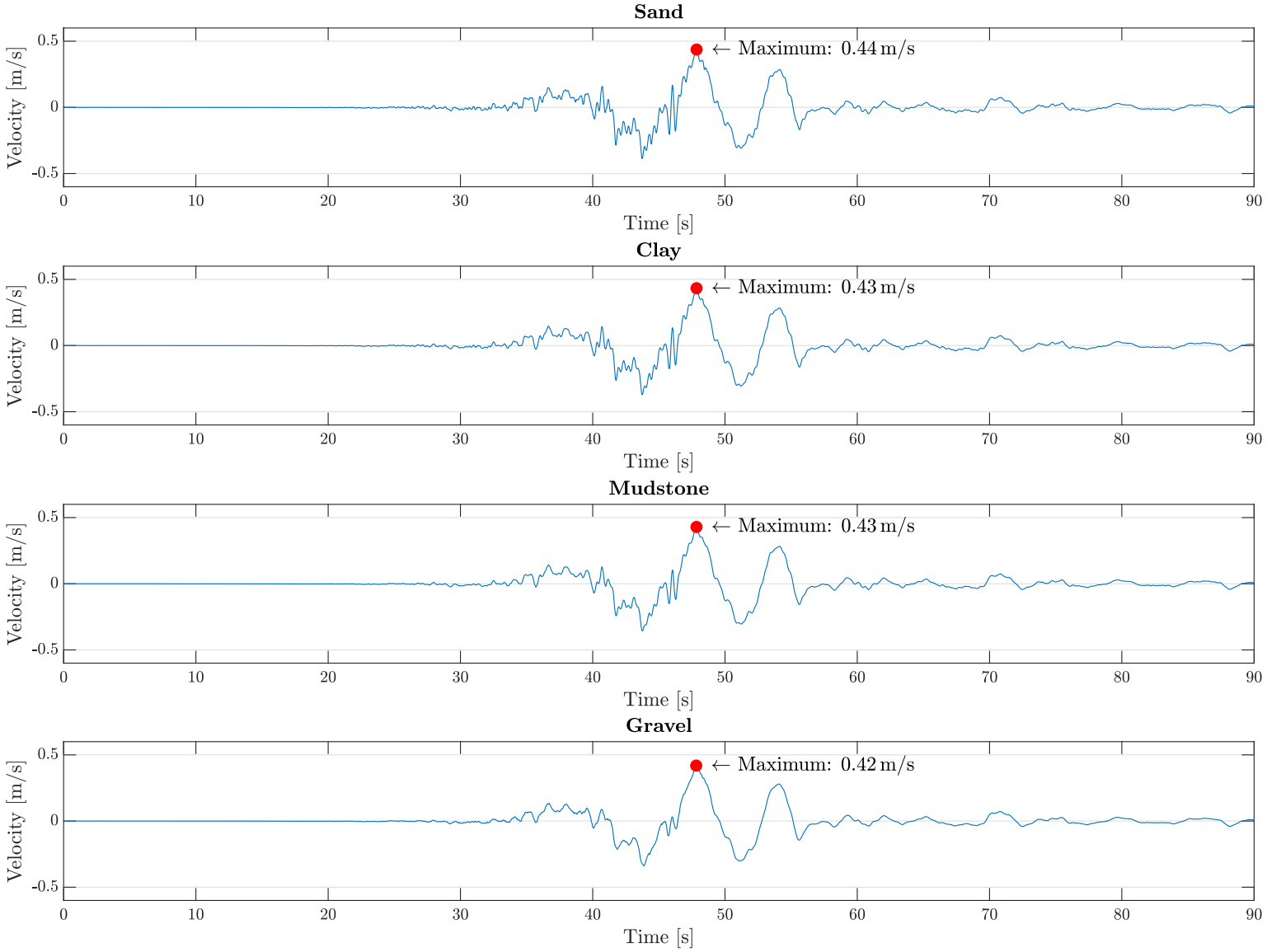

Figure 4.27: *Velocity time history profile for the as-recorded free-field acceleration signal, for one selected depth in each soil layer: 0 m (sand), -9.65 m (clay), -22.51 m (mudstone) and -36.98 m (gravel).*

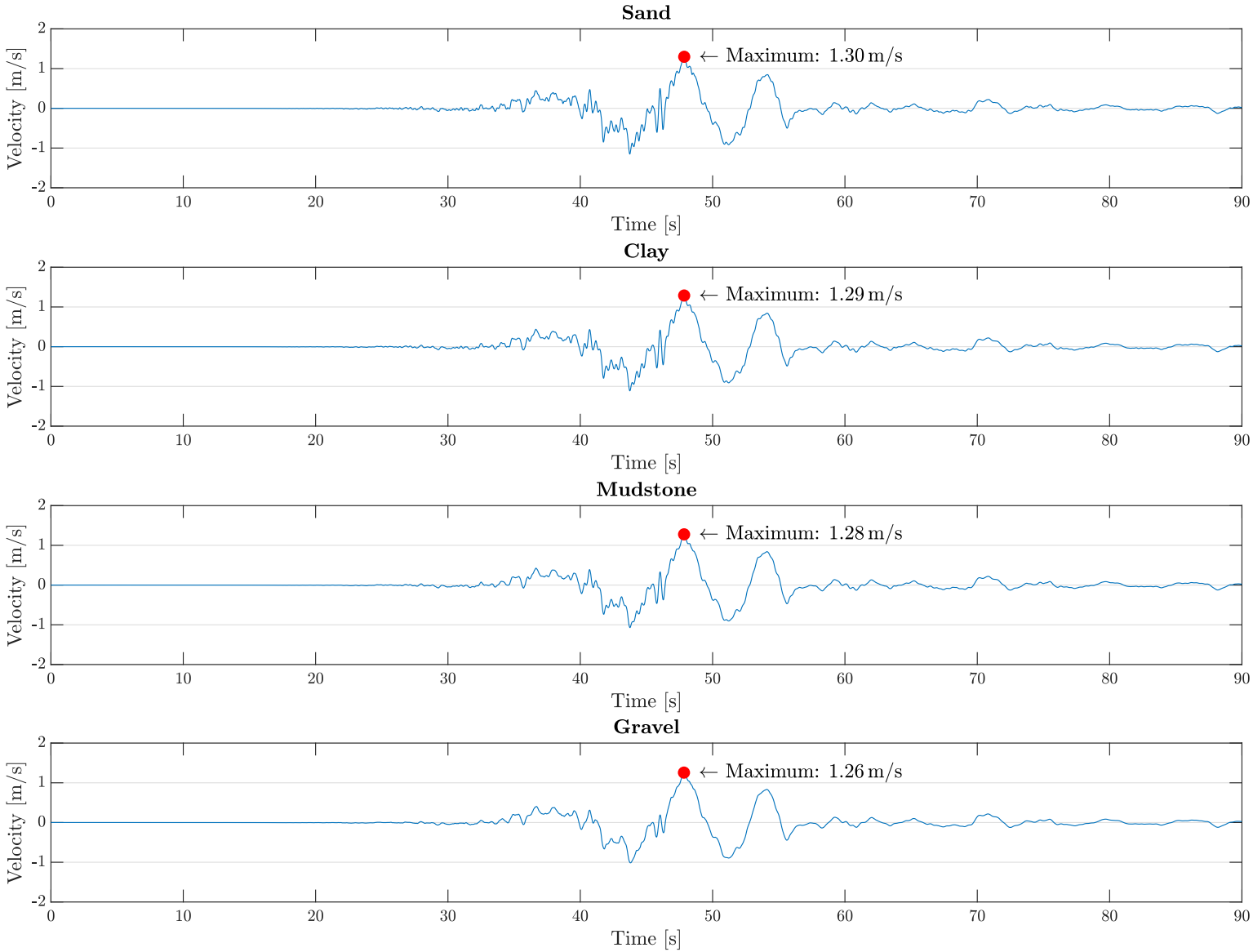

Figure 4.28: *Velocity time history profile for the Extreme Level Earthquake acceleration signal, for one selected depth in each soil layer: 0 m (sand), -9.65 m (clay), -22.51 m (mudstone) and -36.98 m (gravel).*

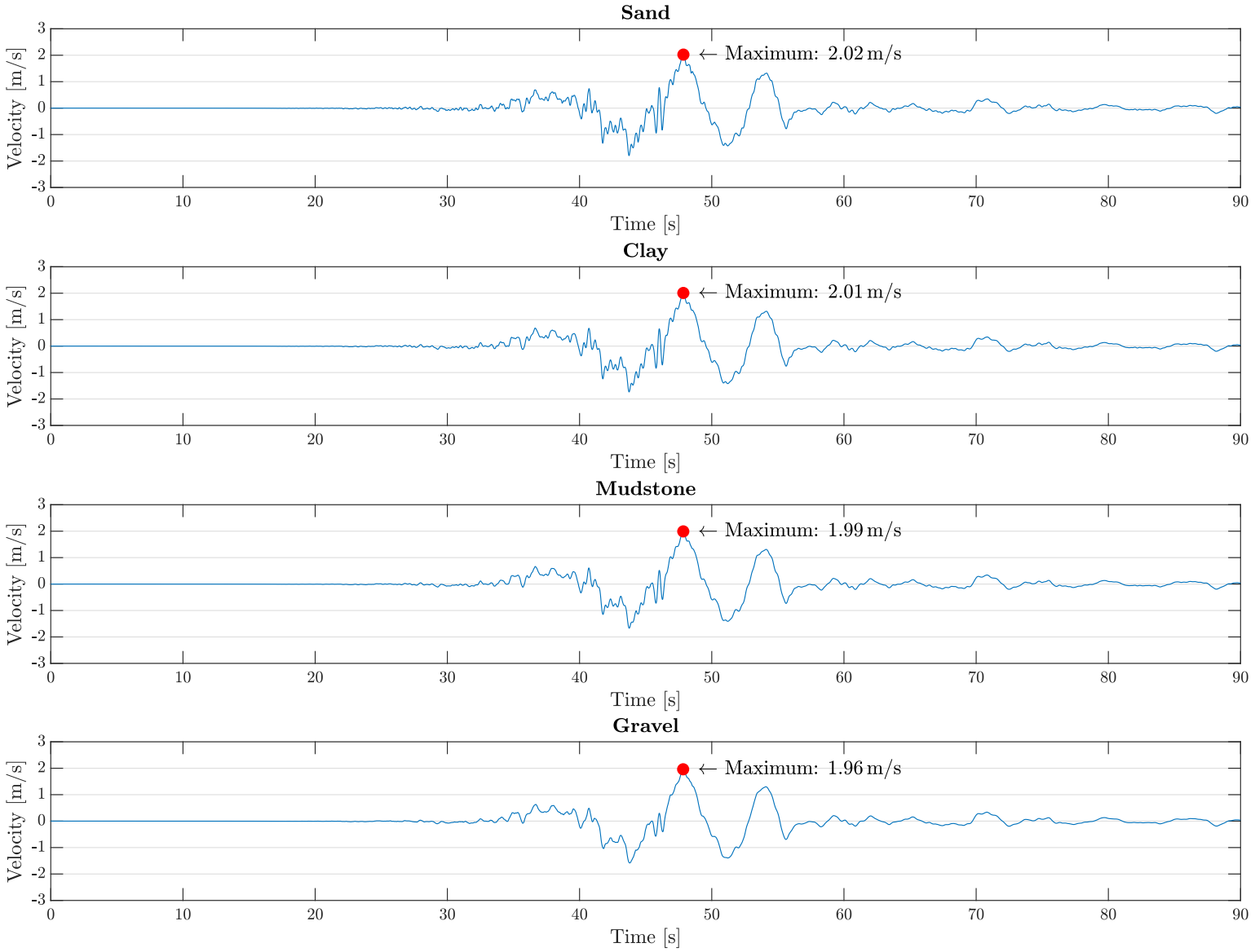

Figure 4.29: *Velocity time history profile for the Abnormal Level Earthquake acceleration signal, for one selected depth in each soil layer: 0 m (sand), -9.65 m (clay), -22.51 m (mudstone) and -36.98 m (gravel).*

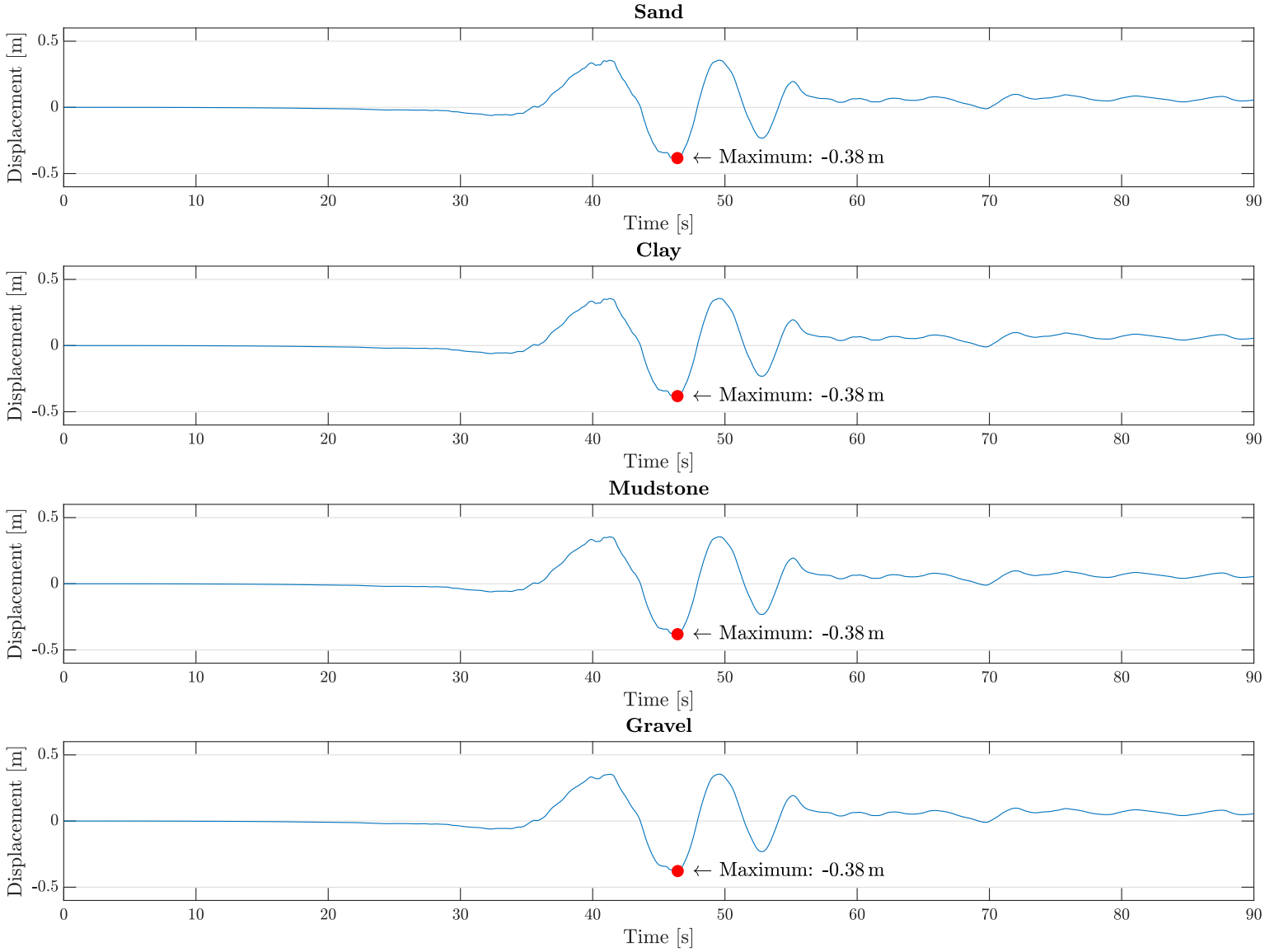

Figure 4.30: *Displacement time history profile for the as-recorded free-field acceleration signal, for one selected depth in each soil layer: 0 m (sand), -9.65 m (clay), -22.51 m (mudstone) and -36.98 m (gravel).*

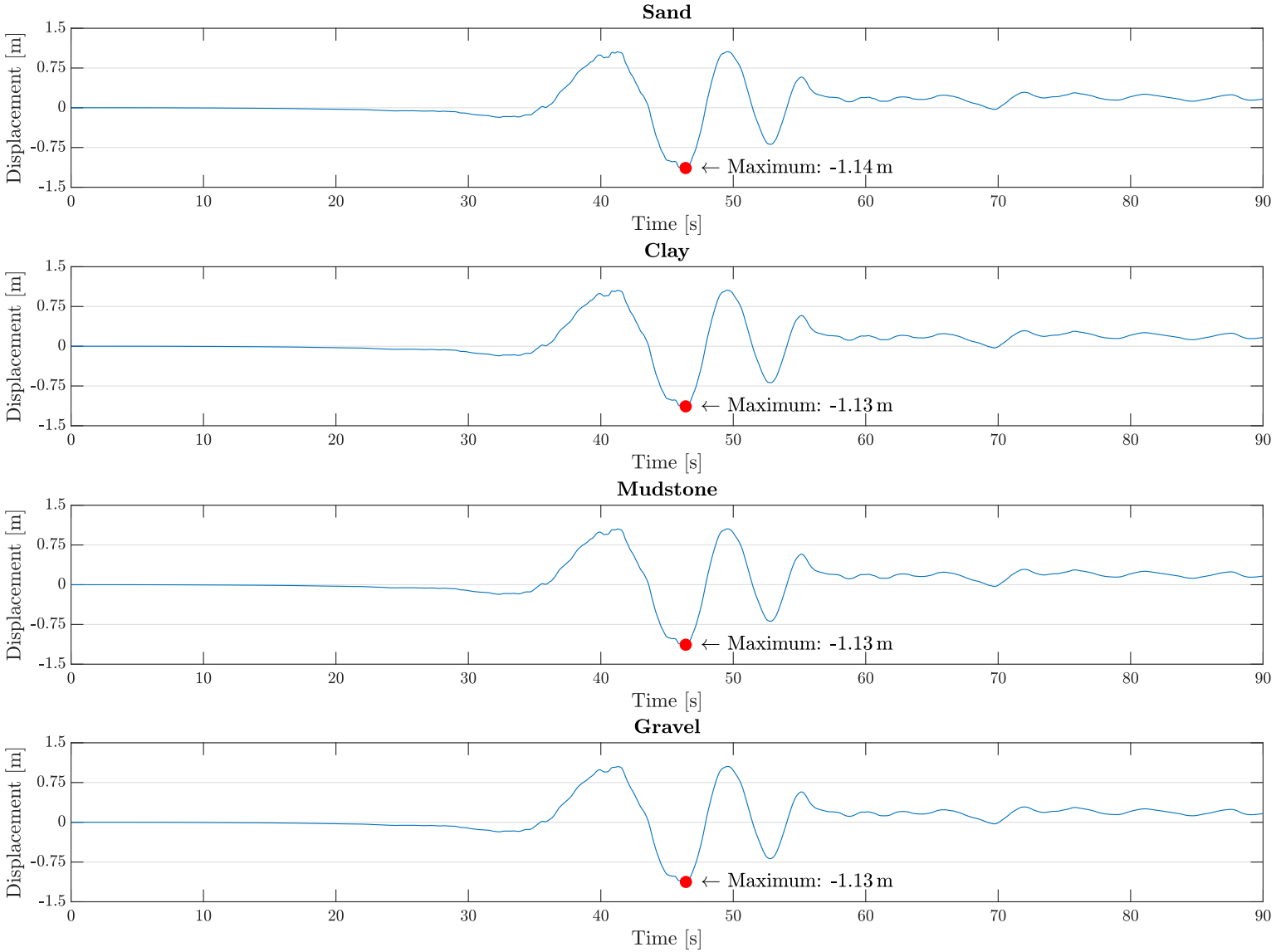

Figure 4.31: *Displacement time history profile for the Extreme Level Earthquake acceleration signal, for one selected depth in each soil layer: 0 m (sand), -9.65 m (clay), -22.51 m (mudstone) and -36.98 m (gravel).*

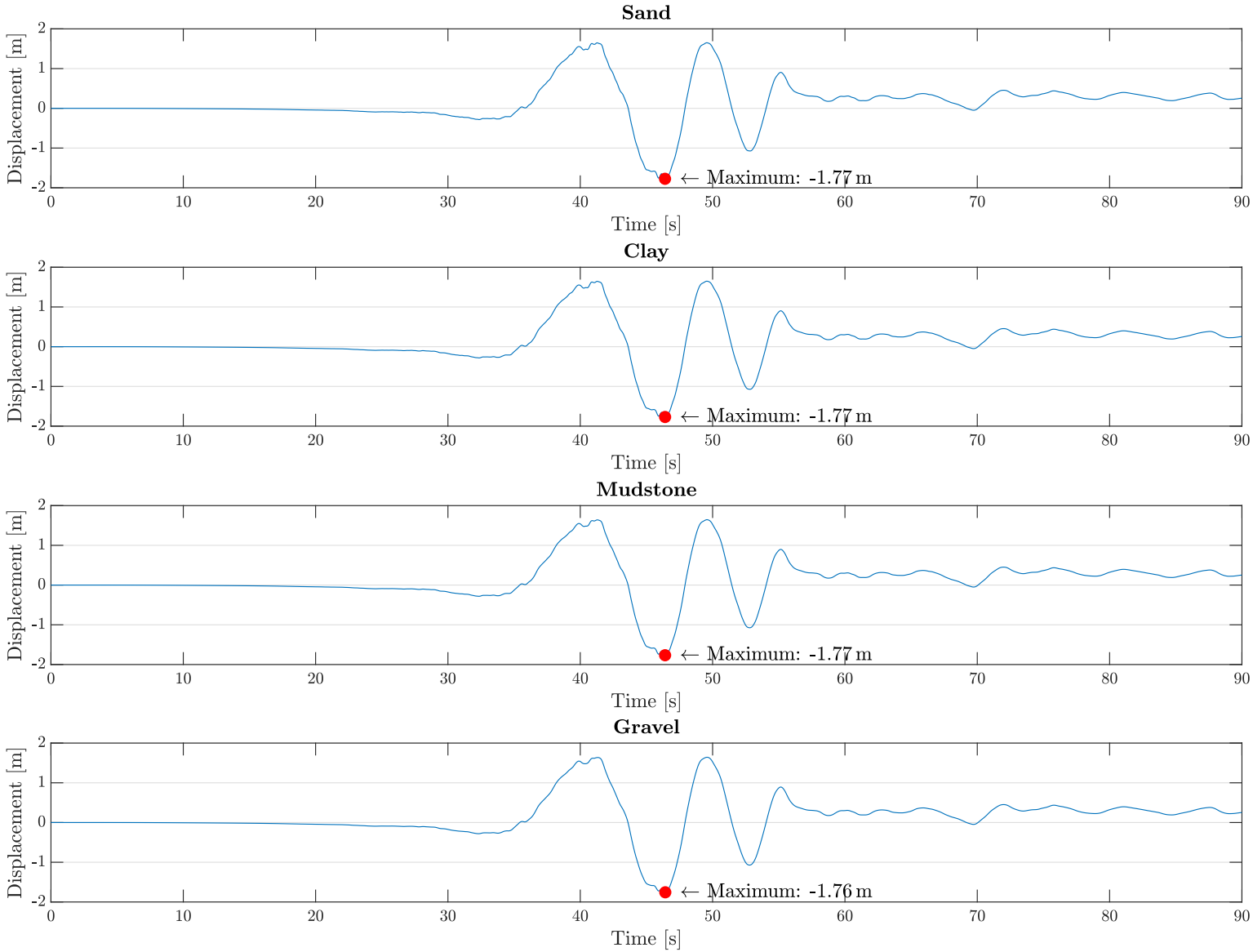

Figure 4.32: *Displacement time history profile for the Abnormal Level Earthquake acceleration signal, for one selected depth in each soil layer: 0 m (sand), -9.65 m (clay), -22.51 m (mudstone) and -36.98 m (gravel).*

4.5.4. Influence of Earthquake Ground Motion on the Soil Resistance Load

It is important to note that the soil spring stiffness k_{py} – the gradient or tangent stiffness of the p-y curve, see Chapter 4.4 – is the stiffness relating to the *relative* displacement between the pile and soil body. The relative motion between the pile and soil will cause the nonlinear soil spring or series hysteretic-viscous damping element to contract or stretch, depending on the nonlinear elastic or nonlinear inelastic soil formulation used respectively. As the relation between the pile displacement and soil resistance load is nonlinear for both soil-structure interaction models, one cannot use linear superposition of the loads associated with pile displacement and soil displacement separately.

The soil stiffness for the nonlinear elastic SSI model is hence calculated as:

$$k_{py} = \frac{\delta p}{\delta \left(y - y_{\mathrm{EQ}} \right)} \tag{4.23}$$

where y is the pile displacement and y_{EQ} is the ground displacement of the soil layer, computed through integration from the SRA acceleration results. Graphs of the time history of the displacement at different nodes are shown in Figures 4.30 to 4.32.

For the nonlinear inelastic SSI model, where series hysteretic-viscous damping elements are employed, the process is slightly more complicated. In this model the total displacement across the element y, equal to the pile displacement, is the sum of the elastic y_e, plastic y_p and gap element y_g displacement. The relative displacement is:

$$y_{\mathrm{rel}} = y - y_{\mathrm{EQ}} \tag{4.24}$$

The iterative p-y calculator in the MATLAB code searches for a balance in the spring at every displacement increment between the elastic, plastic and gap element by considering the displacement equilibrium $y = y_e + y_p + y_g$ and the load equilibrium $p = p_e = p_p = p_d + p_c$. As such, the easiest approach to define the stiffness of each element under *relative* motion is to implement the *relative* total displacement y_{rel} in the p-y calculator. The target displacement balance becomes $y_{\mathrm{rel}} = y_e + y_p + y_g$, – with y_{rel} defined as in Equation 4.24 –, from where the *relative* elastic, plastic and gap participation can be determined. The resulting relative loads and displacements are used to calculate the soil stiffness:

$$k_{\mathrm{d,rel}} = \frac{\delta p_{\mathrm{d,rel}}}{y_{\mathrm{g,rel}}} \tag{4.25}$$

$$k_{\mathrm{c,rel}} = \frac{\delta p_{\mathrm{c,rel}}}{y_{\mathrm{g,rel}}} \tag{4.26}$$

$$k_{\mathrm{p,rel}} = \frac{\delta p_{\mathrm{p,rel}}}{y_{\mathrm{p,rel}}} \tag{4.27}$$

$$k_{\mathrm{e,rel}} = \frac{\delta p_{\mathrm{e,rel}}}{y_{\mathrm{e,rel}}} \tag{4.28}$$

4.6. Equations of Motion

As previously shown in Chapter 3.2.2, the equation describing the motion of a dynamic system relates the inertia, damping, stiffness and external forces of the system:

$$\underline{\underline{\mathbf{M}}} \cdot \ddot{\vec{q}} + \underline{\underline{\mathbf{C}}} \cdot \dot{\vec{q}} + \underline{\underline{\mathbf{K}}} \cdot \vec{q} = \underline{\mathbf{F}} \tag{4.29}$$

The global matrices $\underline{\underline{\mathbf{M}}}$, $\underline{\underline{\mathbf{C}}}$ and $\underline{\underline{\mathbf{K}}}$ describing the mass, damping and stiffness of the soil-structure system were previously explained in Chapter 3.2.2 and Appendix C.

Structural damping is ignored in this study, only aerodynamic damping and soil viscous damping are included in the damping $\underline{\underline{\mathbf{C}}}$ (if applicable in the simulation case). The external forcing matrix $\underline{\mathbf{F}}$ discussed hereafter, includes the external excitation of the system by wind, wave, soil and earthquake loads as introduced in Chapters 4.2 to 4.5. Lastly, this section focuses on the differences between the damping and soil stiffness matrix of the nonlinear elastic soil-structure interaction model (SSI1) versus the nonlinear inelastic series hysteretic-viscous damping soil-structure interaction model (SSI2).

4.6.1. The Nonlinear Elastic Seismic SSI Model

In this first soil-structure interaction model, displacement vector $\vec{q}$ is formatted as:

$$\vec{q} = \begin{bmatrix} y_1 & \theta_1 & y_2 & \theta_2 & \dots & y_N & \theta_N \end{bmatrix}^T \tag{4.30}$$

with y_n the translation at each node (positive right), and θ_n the rotation at each node (positive clockwise). Node 1 corresponds to hub height, node N is located at the pile toe.

In the nonlinear elastic seismic soil-structure interaction model, where static p-y curves simulate the soil resistance with pile response, the global damping matrix $\underline{\underline{\mathbf{C}}}^g$ is only nonzero on the diagonal term corresponding to hub height:

$$\underline{\underline{\mathbf{C}}}^e = \begin{bmatrix} C_{AD} & 0 & \dots & 0 \\ 0 & 0 & \dots & 0 \\ \vdots & \vdots & \ddots & 0 \\ 0 & 0 & \dots & 0 \end{bmatrix} \tag{4.31}$$

Structural damping is ignored in this study, and the nonlinear springs used in the foundation model deliver no soil damping to the system. At hub height, the aerodynamic damping is known to be active as long as the rotor is operational. From the moment the turbine function is stopped, the damping matrix is assumed to be void.

The global stiffness matrix $\underline{\underline{\mathbf{K}}}^g$ is the sum of the global bending, shear, geometric and foundation stiffness matrices as described in Chapter 3.2.2. It should be noted that the foundation stiffness matrix depends on the relative displacement between pile and soil, since the foundation spring stiffness term k_f in the element matrix formulation is defined by Equation 4.23:

$$k_f = k_{\text{py,rel}} = \frac{\delta p}{\delta \left(y - y_{\text{EQ}} \right)} \tag{4.32}$$

Because of the different formulation of the p-y curves for SSI1 in comparison to SSI2, these values for k_f will be specific for the nonlinear elastic model. As such, the soil stiffness matrix $\underline{\underline{\mathbf{K_f}}}$ cannot be assumed equal for both soil-structure interaction models.

Because of the nonlinear nature of the p-y curves in SSI1, the soil stiffness should be determined as the gradient to the *relative* displacement between ground motion and pile displacement (Chapter 2.5). Finding a solution to the dynamic equation of motion Eq. 4.29 hence becomes an iterative process where k_f needs to be updated for every node depending on the computed pile displacement y in the displacement vector $\vec{q}$. In each time step of the MATLAB script, iteration of the dynamic equilibrium is requested.

The same iterative procedure is required for the force and moment computation at each node, as the wind and wave force both depend on pile lateral velocity and acceleration (see Equations 4.3 and 4.5). The forcing matrix $\underline{\underline{\mathbf{F}}}$ is formatted as:

$$\underline{\underline{\mathbf{F}}} = \begin{bmatrix} F_1 & M_1 & F_2 & M_2 & \dots & F_N & M_N \end{bmatrix}^T \tag{4.33}$$

with F_n the shear force at each node and M_n the moment at each node.

4.6.2. The Nonlinear Series Hysteretic-Viscous Damping Seismic SSI Model

To be able to implement the nonlinear series hysteretic-viscous damping element behaviour is the Timoshenko finite element formulation, the degrees of freedom $\vec{q}$ needs to be expanded with a dummy variable at the node between the equivalent plastic-gap element and the elastic spring element as shown in Figure 4.33:

$$\vec{q} = \begin{bmatrix} y_1 & \theta_1 & y_1^d & y_2 & \theta_2 & y_2^d & \dots & y_N & \theta_N & y_N^d \end{bmatrix}^T \tag{4.34}$$

This dummy variable represents the lateral displacement at the massless point between the equivalent gap-plastic spring and elastic spring, of which the spring stiffness derivation was detailed in Chapter 4.4.2 and 2.5.

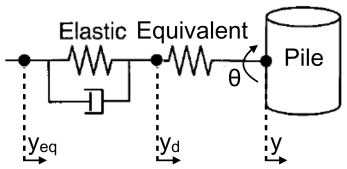

Figure 4.33: *The series hysteretic-viscous damping element with point masses at soil-gap, plastic-elastic and elastic-soil interfaces, to arrive at an equivalent soil element: step 3 (final).*

The global mass matrix remains equal to the mass matrix for the nonlinear elastic SSI model, except for the zero terms on the indices relating to the dummy displacement y^d. The translational element mass matrix becomes:

$$\underline{\underline{\mathbf{M}}}^e_t = \frac{\rho A l}{(1+\Phi)^2}\begin{bmatrix} \frac{13}{35}+\frac{7\Phi}{10}+\frac{\Phi^2}{3} & \left(\frac{11}{210}+\frac{11\Phi}{120}+\frac{\Phi^2}{24}\right)l & 0 & \frac{9}{70}+\frac{3\Phi}{10}+\frac{\Phi^2}{6} & -\left(\frac{13}{420}+\frac{3\Phi}{40}+\frac{\Phi^2}{24}\right)l & 0 \\ \left(\frac{11}{210}+\frac{11\Phi}{120}+\frac{\Phi^2}{24}\right)l & \left(\frac{1}{105}+\frac{\Phi}{60}+\frac{\Phi^2}{120}\right)l^2 & 0 & \left(\frac{13}{420}+\frac{3\Phi}{40}+\frac{\Phi^2}{24}\right)l & -\left(\frac{1}{140}+\frac{\Phi}{60}+\frac{\Phi^2}{120}\right)l^2 & 0 \\ 0 & 0 & 0 & 0 & 0 & 0 \\ \frac{9}{70}+\frac{3\Phi}{10}+\frac{\Phi^2}{6} & \left(\frac{13}{420}+\frac{3\Phi}{40}+\frac{\Phi^2}{24}\right)l & 0 & \frac{13}{35}+\frac{7\Phi}{10}+\frac{\Phi^2}{3} & -\left(\frac{11}{210}+\frac{11\Phi}{120}+\frac{\Phi^2}{24}\right)l & 0 \\ -\left(\frac{13}{420}+\frac{3\Phi}{40}+\frac{\Phi^2}{24}\right)l & -\left(\frac{1}{140}+\frac{\Phi}{60}+\frac{\Phi^2}{120}\right)l^2 & 0 & -\left(\frac{11}{210}+\frac{11\Phi}{120}+\frac{\Phi^2}{24}\right)l & \left(\frac{1}{105}+\frac{\Phi}{60}+\frac{\Phi^2}{120}\right)l^2 & 0 \\ 0 & 0 & 0 & 0 & 0 & 0 \end{bmatrix} \tag{4.35}$$

The same transformation is applied to the rotational element mass matrix, the bending and shear element stiffness matrix, and the geometric element stiffness matrix of Appendix C.

The element foundation stiffness matrix needs some more elaborate tuning. Consider the pile element in Figure 4.33. The equilibrium of forces is:

$$m\cdot\ddot{y} + k_{\text{eqv}}\cdot\left(y - y^d\right) = 0 \tag{4.36}$$

$$0\cdot\ddot{y} + k_{\text{eqv}}\cdot\left(y^d - y\right) + k_e\cdot\left(y^d - y_{eq}\right) + c_v\cdot\left(\dot{y}^d - \dot{y}_{eq}\right) = 0 \tag{4.37}$$

Due to the nonlinear nature of the equivalent spring, the stiffness should relate to the *relative* displacement between pile and dummy mass as explained in Chapter 2.5. Considering the dynamic equilibrium in the above equations, the foundation element stiffness matrix is split in two matrices where the first matrix is an expansion of the Timoshenko foundation stiffness, and the second matrix only includes the influence of the dummy displacement:

$$\underline{\underline{\mathbf{K}}}^e_{f,1} = \frac{k_{\text{eqv}} l}{(1+\Phi)^2}\begin{bmatrix} \frac{13}{35}+\frac{7\Phi}{10}+\frac{\Phi^2}{3} & \left(\frac{11}{210}+\frac{11\Phi}{120}+\frac{\Phi^2}{24}\right)l & 0 & \frac{9}{70}+\frac{3\Phi}{10}+\frac{\Phi^2}{6} & -\left(\frac{13}{420}+\frac{3\Phi}{40}+\frac{\Phi^2}{24}\right)l & 0 \\ \left(\frac{11}{210}+\frac{11\Phi}{120}+\frac{\Phi^2}{24}\right)l & \left(\frac{1}{105}+\frac{\Phi}{60}+\frac{\Phi^2}{120}\right)l^2 & 0 & \left(\frac{13}{420}+\frac{3\Phi}{40}+\frac{\Phi^2}{24}\right)l & -\left(\frac{1}{140}+\frac{\Phi}{60}+\frac{\Phi^2}{120}\right)l^2 & 0 \\ 0 & 0 & 0 & 0 & 0 & 0 \\ \frac{9}{70}+\frac{3\Phi}{10}+\frac{\Phi^2}{6} & \left(\frac{13}{420}+\frac{3\Phi}{40}+\frac{\Phi^2}{24}\right)l & 0 & \frac{13}{35}+\frac{7\Phi}{10}+\frac{\Phi^2}{3} & -\left(\frac{11}{210}+\frac{11\Phi}{120}+\frac{\Phi^2}{24}\right)l & 0 \\ -\left(\frac{13}{420}+\frac{3\Phi}{40}+\frac{\Phi^2}{24}\right)l & -\left(\frac{1}{140}+\frac{\Phi}{60}+\frac{\Phi^2}{120}\right)l^2 & 0 & -\left(\frac{11}{210}+\frac{11\Phi}{120}+\frac{\Phi^2}{24}\right)l & \left(\frac{1}{105}+\frac{\Phi}{60}+\frac{\Phi^2}{120}\right)l^2 & 0 \\ 0 & 0 & 0 & 0 & 0 & 0 \end{bmatrix} \tag{4.38}$$

$$\underline{\underline{\mathbf{K}}}^e_{f,2} = \begin{bmatrix} 0 & 0 & -k_{\text{eqv}}\cdot l & 0 & 0 & 0 \\ 0 & 0 & 0 & 0 & 0 & 0 \\ -k_{\text{eqv}}\cdot l & 0 & (k_{\text{eqv}}+k_e)\cdot l & 0 & 0 & 0 \\ 0 & 0 & 0 & 0 & 0 & -k_{\text{eqv}}\cdot l \\ 0 & 0 & 0 & 0 & 0 & 0 \\ 0 & 0 & 0 & -k_{\text{eqv}}\cdot l & 0 & (k_{\text{eqv}}+k_e)\cdot l \end{bmatrix} \tag{4.39}$$

The forcing matrix $\underline{\mathbf{F}}$ for nodes $i = 1$ to N hence becomes:

$$\underline{\mathbf{F}} = \begin{bmatrix} F_1 & M_1 & 0 & F_2 & M_2 & 0 & \dots & F_N & M_N & k_{e,N}\cdot l_N\cdot y_{eq,N} + c_{v,N}\cdot l_N\cdot\dot{y}_{eq,N} \end{bmatrix}^T \tag{4.40}$$

thereby treating the induced soil stiffness and soil damping by the earthquake ground motion from Equation 4.37 as an external force. Again, this earthquake induced load is only present below mudline.

Lastly, the global damping matrix is now not only nonzero on the first diagonal term, but is nonzero below mudline for all diagonal terms relating to the dummy displacement y^d when earthquake ground motion exists:

$$\underline{\underline{\mathbf{C}}}^e = \begin{bmatrix} C_{AD} & 0 & 0 & \dots & 0 & 0 & 0 & 0 & 0 & 0 \\ 0 & 0 & 0 & \dots & 0 & 0 & 0 & 0 & 0 & 0 \\ \vdots & \vdots & \vdots & \ddots & \vdots & \vdots & \vdots & \vdots & \vdots & \vdots \\ 0 & 0 & 0 & \dots & 0 & 0 & 0 & 0 & 0 & 0 \\ 0 & 0 & 0 & \dots & 0 & 0 & 0 & 0 & 0 & 0 \\ 0 & 0 & 0 & \dots & 0 & 0 & c_v & 0 & 0 & 0 \\ 0 & 0 & 0 & \dots & 0 & 0 & 0 & 0 & 0 & 0 \\ 0 & 0 & 0 & \dots & 0 & 0 & 0 & 0 & 0 & 0 \\ 0 & 0 & 0 & \dots & 0 & 0 & 0 & 0 & 0 & c_v \end{bmatrix} \tag{4.41}$$

In case the gap element – containing the drag and closure spring – can be ignored, the equations of motion can be simplified. When considering only one elastoplastic spring – just as for the SSI model based on the API recommended p-y curves (Chapter 3.1.2 and 4.4) –, and the viscous damper in parallel to this elastoplastic element, then the dummy variable y_d becomes obsolete, see Figure 4.34. The expressions for the element mass matrix and foundation stiffness matrix reduce to the expressions in Equation C.33 and Equation C.29 of Appendix C. The damping matrix is similar to Equation 4.41, with the difference that rows and columns corresponding to the dummy displacement are removed. Hence, the damping matrix now has the same size as the damping matrix in the nonlinear elastic SSI model in Equation 4.31 of Chapter 4.6.1, but the diagonal terms corresponding to the pile displacement degree of freedom y have a nonzero damping value c_v below mudline when earthquake ground motion exists[16].

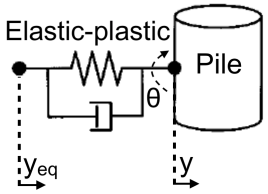

Figure 4.34: *The reduced series hysteretic-viscous damping soil-structure interaction element as used in this study, with the viscous dashpot in parallel with the spring representing elastic and plastic soil response.*

[16] When no ground motion exists due to shear wave propagation by the seismic waves, then the shear wave velocity is zero. Consequently, the viscous damper is zero according to Equation 3.30.

5

Simulations, Results and Discussion

In this chapter, the results of the different load cases in Table 4.1 from both soil-structure interaction models are shown and discussed. For convenience, the load cases are repeated here in Table 5.1.

Table 5.1: *Summary of the load cases, detailing the operational, wind, wave and earthquake conditions.*

Load Case	Operation	Wind	Wave	Earthquake
1-N	Normal	NSS	NSS	-
1-S	Shutdown	NSS	NSS	-
2-N	Normal	NSS	NSS	As-recorded
2-S	Shutdown	NSS	NSS	As-recorded
3-N	Normal	NSS	NSS	ELE
3-S	Shutdown	NSS	NSS	ELE
4-N	Normal	NSS	NSS	ALE
4-S	Shutdown	NSS	NSS	ALE
Total simulations	8·2 = 16			

Chapter 5.1 details the state of the soil-structure system prior to any loading by rotor operation, wind, waves or earthquake ground motion; i.e., the system at rest. Chapter 5.3 shows the dynamic response behaviour of both seismic soil-structure interaction models to wind and wave loading only. Chapter 5.4 follows by illustrating the influence of the recorded free-field ground motion on the dynamic response of both models. Lastly, Chapter 5.5 and 5.6 summarize the results from the incremental dynamic analysis, where the dynamic response results for the recorded, Extreme Level Earthquake and Abnormal Level Earthquake are compared.

All simulations are conducted for both the nonlinear elastic soil-structure interaction model (explained in Chapter 4.6.1) and the simplified nonlinear series hysteretic-viscous damping soil-structure interaction model (explained in Chapter 4.6.2), such that their response can be compared to evaluate the influence of radiation damping by the seismic shear wave in the soil body. Besides that, the simulations are executed under operational and shutdown conditions of the rotor, this to come to an early assessment of the usefulness of a shutdown-strategy in case of an earthquake event.

For the reader's convenience, an overview of the results from Chapter 5.3 to 5.6 is given in Table 5.4 of Chapter 5.2.

5.1. Response Behaviour Prior to Loading

Before exposing both seismic soil-structure interaction models to a combination of operational, wind, wave and earthquake-induced loads, the soil-structure body at rest is examined. The structure was discretized into beam elements in the finite-element Timoshenko formulation. Table 5.2 gives a summary of the number of elements, degrees of freedom and general structural properties.

Table 5.2: *Finite element discretization summary of the structure.*

Section	Aerial	Submerged	Embedded	
Number of elements, E	30	20	25	-
Number of nodes, N	31*	21**	26***	-
Element length, l	3.066	1.148	1.608	m
Diameter range, D	3.87 - 6.55	6.55 - 8	8	m
Thickness range, t	0.05 - 0.08	0.08 - 0.074	0.074	m
Density range, ρ	8,500 - 9,000	9,000 - 7850	7850	kg/m^3
Modulus of elasticity, E	210	210	210	GPa
Modulus of shear, G	80	80	80	GPa
Yield strength, σ	355	355	355	MPa

* Of which one node is shared with the adjacent submerged elements.
** Of which two nodes are shared with the adjacent aerial and embedded elements.
*** Of which one node is shared with the adjacent submerged elements.

The number of nodes in Table 5.2 were selected based on eigenvalue-convergence. Considering one lateral translation degree of freedom y and one rotation degree of freedom θ at each node, this means that for a 75 element finite-element model the total number of degrees of freedom is 152.

Prior to any loading and motion of the pile, the soil stiffness matrix of the system is governed by the initial stiffness of the soil layers. Consequently to there being no pile motion yet, there is no aerodynamic and hydrodynamic damping; these terms depend on the pile displacement velocity, as could be derived from Equations 4.3 and 4.5. Additionally, there exists no added hydrodynamic mass by the acceleration of the pile, see Equation 4.5. With the external loads ignored to assess the system at rest, the equations of motion:

$$\underline{\underline{\mathbf{M}}} \cdot \ddot{\vec{q}} + \underline{\underline{\mathbf{C}}} \cdot \dot{\vec{q}} + \underline{\underline{\mathbf{K}}}(y,t) \cdot \vec{q} = \underline{\mathbf{F}}(\dot{y},t) \tag{5.1}$$

reduce to:

$$\underline{\underline{\mathbf{M}}} \cdot \ddot{\vec{q}} + \underline{\underline{\mathbf{K}}} \cdot \vec{q} = \underline{\mathbf{0}} \tag{5.2}$$

From this initial state, the eigenfrequencies of the soil-structure system can be determined from the general eigenvalue problem with Equations 3.42 and 3.43.

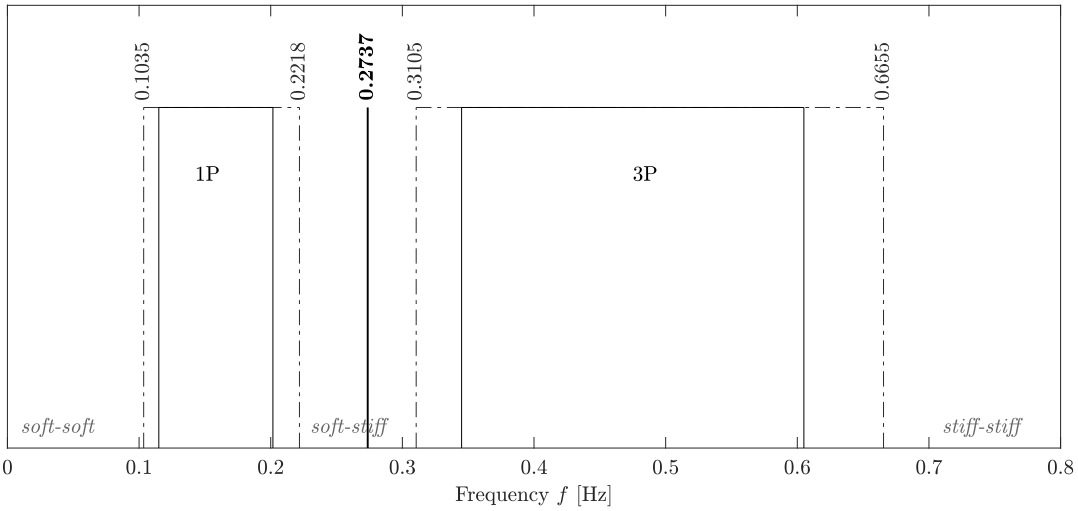

Figure 5.1: *The first natural frequency of the soil-structure system prior to ground motion, bounded by the 1P and 3P rotor frequency of the NREL 5 MW reference turbine [51].*

The first eigenfrequency of the system, and its location to the 1P and 3P rotor frequency, is shown in the frequency plot of Figure 5.1. With a first natural frequency of 0.2737 Hz, the dynamic properties of the nonlinear elastic seismic soil-structure model lay in the soft-stiff response region as aimed for in design. The natural

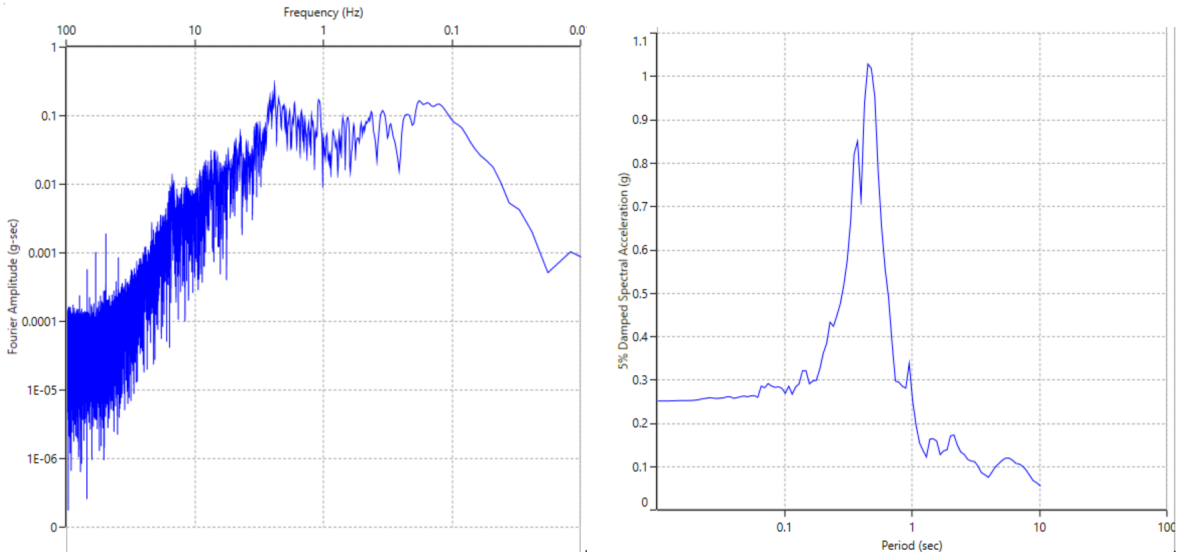

(a) *Fourier amplitude.* ***(b)*** *Damped spectral acceleration.*

Figure 5.2: *Spectral plots of the as-recorded free-field earthquake ground motion, retrieved from DEEPSOIL.*

frequency of the nonlinear simplified series hysteretic-viscous damping model, which uses another definition for the elastoplastic soil springs, barely differs with 0.2736 Hz. As such, only the dynamic rest state of the first nonlinear elastic seismic soil-structure model is detailed in this section.

The number of natural frequencies and mode shapes is equal to the total number of degrees of freedom, in this case 152. Performing full nonlinear time analysis on a system with 152 coupled equations of motion, over an earthquake signal of 90-150 s with time steps of 0.005 s (or 18,000-30,000 time steps, see Figure 4.10), would take a vast amount of computational time (>12h). To reduce this computation time, modal reduction of the equations of motion is performed.

Considering the nature of the studied earthquake acceleration signal, it is expected that strong ground motion will invoke a response in the higher modes. This may also be derived from the spectral acceleration plot of the recorded ground motion in Figure 5.2, where the largest accelerations are experienced in the range 100 to 1 Hz. As such, only using the first three modes as often applied – with natural frequencies between 0.2737 to 2.7795 Hz – would ignore the high energy participation of the higher modes on the structural response.

As such, it was determined that the full time history and modal reduction history compare best when using 18 modes or more. Figure 5.3 shows the differences in RNA displacement between both approaches when using the 20 first modes. The corresponding natural frequencies of these higher modes are listed in Table 5.3.

Table 5.3: *Natural frequencies of the soil-structure model for the first 20 modes.*

Natural frequency	$\mathbf{f_{n,1}}$	$\mathbf{f_{n,2}}$	$\mathbf{f_{n,3}}$	$\mathbf{f_{n,4}}$	$\mathbf{f_{n,5}}$	$\mathbf{f_{n,6}}$	$\mathbf{f_{n,7}}$	$\mathbf{f_{n,8}}$	$\mathbf{f_{n,9}}$	$\mathbf{f_{n,10}}$	**Units**
Value	0.2737	0.9641	2.7795	5.8902	9.8417	14.629	18.223	22.510	26.116	31.256	Hz
Natural frequency	$\mathbf{f_{n,11}}$	$\mathbf{f_{n,12}}$	$\mathbf{f_{n,13}}$	$\mathbf{f_{n,14}}$	$\mathbf{f_{n,15}}$	$\mathbf{f_{n,16}}$	$\mathbf{f_{n,17}}$	$\mathbf{f_{n,18}}$	$\mathbf{f_{n,19}}$	$\mathbf{f_{n,20}}$	**Units**
Value	36.790	43.987	49.646	55.007	61.671	68.558	76.253	81.545	87.522	94.255	Hz

It is important to note that the mode shapes used in the modal analysis of the full coupled nonlinear equations of motion, are the mode shapes for the initial state of the system. This means that the mode shapes have been derived for the initial soil spring stiffness matrix, although this matrix is known to change with pile displacement, as the gradient of the nonlinear p-y curves k_f (see Figures 3.17 to 3.21) decreases with increasing pile displacement. Changes in the soil spring stiffness k_f will change the natural frequencies and mode shapes of the system. Hence, using a constant modal matrix over time is a simplification of the true state. The solution from modal analysis will be different from the one by the full coupled nonlinear EOM, but it has not

been assessed to what level (although Figure 5.3 gives an indication of the influence of the constant instead of variable soil state on the modal versus complete analysis). Considering the time consuming computation of the full system and of updating the modal matrix to the current soil state, this simplification had to be implemented.

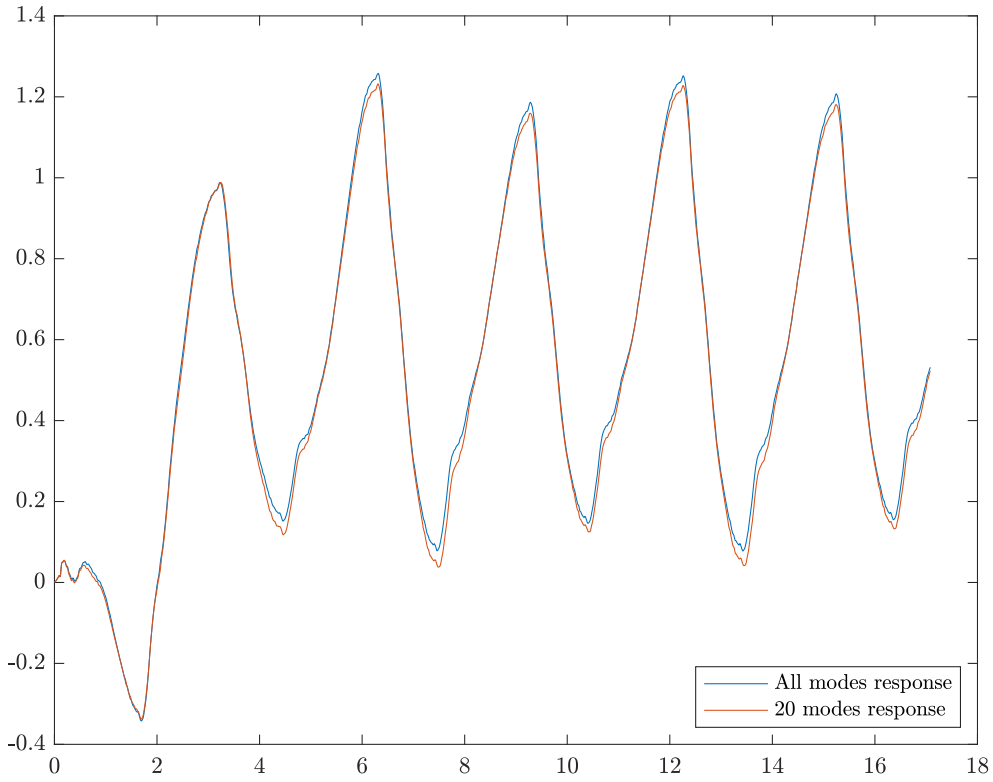

Figure 5.3: *Comparison between the RNA lateral displacement response of the structure exposed to all external forces, for all modes and for 20 modes.*

5.2. Overview of the Simulated Load Cases Results

In order to provide a clear overview of the numerous results in Chapter 5.3 to 5.6, Table 5.4 was created. This table provides a summary of the response behaviour, capacity demand and the failure mode of the structure (if applicable). For every load case of Table 5.1, it is detailed whether:

- the simulation was conducted for (increasing) earthquake ground motion,
- the turbine was in operation or shut down,
- the soil was assumed to behave elastic[17] or inelastic[18],
- the system remained dynamically stable or not,
- the structure met the serviceability limit criterion of a maximum 0.5° tilt at the RNA,
- the structural demand remained below the ultimate limit state criterion regarding yield,
- the structural demand remained below the ultimate limit state criterion regarding buckling.

[17] By elastic the nonlinear elastic soil-structure interaction model without hysteresis or radiation damping is meant.

[18] By inelastic the simplified nonlinear inelastic series viscous damping soil-structure interaction model without hysteresis but with radiation damping is meant.

Table 5.4: *Overview of the results from the simulated load cases in Table 5.1, detailed in Chapter 5.3 to 5.6.*

			DYNAMICS			SLS			ULS							
			Stability			Tilt			Yield			Buckling				
Simulation	**Operation**	**SSI**	Y/N*	f_n**	t	Y/N	θ	t	Y/N	UR	t	Y/N	BR	t	**Remarks**	**Chapter**
DLC-1	Operational	Elastic	Y	0.2682 Hz	5.69 s	Y	0.2692°	5.48 s	Y	0.1415	6.31 s	Y	0.3059	2.64 s	No hysteresis/radiation damping	5.3
(NSS)		Inelastic	Y	0.2412 Hz	0 s	Y	0.2668°	5.48 s	Y	0.1415	2.78 s	Y	0.3059	6.38 s	No hysteresis/radiation damping	
	Shutdown	Elastic	Y	0.2682 Hz	5.69 s	Y	0.2692°	5.48 s	Y	0.2066	80.64 s	Y	0.3059	79.60 s	No hysteresis/radiation damping	
		Inelastic	Y	0.2412 Hz	0 s	Y	0.2668°	5.48 s	Y	0.2115	87.65 s	Y	0.3059	79.44 s	No hysteresis/radiation damping	
DLC-2	Operational	Elastic	N	0.0359 Hz	108.94 s	N	0.9977°	109.47 s	N	2.8488	127.54 s	N	1.4475	129.54 s	No hysteresis/radiation damping	5.4
(Recorded earthquake)		Inelastic	Y	0.0780 Hz	106.41 s	Y	0.2669°	5.48 s	Y	0.9186	89.22 s	Y	0.5382	89.22 s	Radiation damping	
	Shutdown	Elastic	N	0.0345 Hz	114.95 s	N	-1.3462°	118.38 s	N	3.4911	127.46 s	N	1.4918	129.46 s	No hysteresis/radiation damping	
		Inelastic	Y	0.0759 Hz	106.42 s	Y	0.2669°	5.48 s	Y	1.0414	89.26 s	Y	0.5990	89.26 s	Radiation damping	
DLC-3	Operational	Elastic	N	0 Hz	118.08 s	N	2.3266°	115.98 s	N	5.9264	139.96 s	N	2.8919	145.03 s	No hysteresis/radiation damping	
(ELE)		Inelastic	N	0 Hz	109.87 s	N	0.6424°	106.41 s	Y	0.8695	80.34 s	Y	0.5139	80.34 s	Radiation damping	5.5
	Shutdown	Elastic	N	$\mathbb{I}$***	115.06 s	N	-3.4517°	122.59 s	N	5.7068	124.99 s	N	2.7319	124.39 s	No hysteresis/radiation damping	
		Inelastic	N	0 Hz	101.24 s	Y	0.3832°	106.41 s	Y	0.9660	114.03 s	Y	0.5617	114.03 s	Radiation damping	
DLC-4	Operational	Elastic	N	0 Hz	142.11 s	N	3.8768°	120.32 s	N	9.1048	125.12 s	N	4.4562	123.53 s	No hysteresis/radiation damping	5.6
(ALE)		Inelastic	N	0 Hz	112.52 Hz	N	0.8680°	106.41 s	Y	0.9212	77.54 s	Y	0.5395	77.54 s	Radiation damping	
	Shutdown	Elastic	N	0 Hz	120.03 s	N	-5.3927°	112.89 s	N	9.0315	119.35 s	N	4.5558	119.35 s	No hysteresis/radiation damping	
		Inelastic	N	0 Hz	112.47 s	N	0.6445°	106.41 s	Y	0.9212	77.54 s	Y	0.5395	77.54 s	Radiation damping	

* "Y" means the criterion is met, "N" means the soil-structure model fails to meet the criterion.
** This is the smallest natural frequency reached in the time history.
** The natural frequency has become imaginary, indicating a negative first eigenvalue and consequently a dynamically unstable system.

5.3. Response Behaviour Prior to Seismic Loading

To evaluate the influence of earthquake ground motion on the response of an offshore monopile, first the situation where no earthquake ground motion is present was analyzed for both soil-structure interaction models. The structure is only exposed to the wind and wave loads, and the turbine is either in operational or shutdown mode. The results of the simulated load case presented hereafter correspond to Load Case 1-N and 1-S of Table 5.1.

Operational condition is defined as normal operation of the wind turbine, which produces power, a thrust force and rotor aerodynamic damping. *Shutdown condition* is defined as the emergency braking of the turbine due to accidental or abnormal loads. In this case study, the response behaviour of the structure is evaluated for when the turbine would perform an emergency break when perceiving the first ground motion tremors, indicating an imminent earthquake event. According to the recorded earthquake motion in Figure 4.10, P-wave tremors occur at about 15 s down the earthquake signal. Implementing a 5 second lag for the system to perceive the tremors and process the emergency brake command, the shutdown time is fixed at 20 s in the earthquake signal.

Even though no earthquake ground motion is present in the first simulated load case, the response of the system to an emergency shutdown is simulated immediately after the transient response died out. An emergency shutdown would not normally be executed when the structure is only exposed to normal sea state conditions, but it is simulated here for the sake of comparison between a non-seismic situation and when earthquake motion does exist (Chapter 5.4), for the case where the turbine operation would stop.

The influence of higher modes on the structural response is expected to be lower than when earthquake strong ground motion would exist. This is because the rotor, wind and wave loads are expected to excite the first few modes of the system. As such, 5 modes were used to compute the response behaviour.

As no earthquake ground motion is present in the current simulation, the viscous damper modeling far-field radiation damping by the shear waves is null (as the shear wave velocity is zero). Hence, the responses of the pile for both soil models is expected to be similar, except for small differences due to the dissimilar formulation of the nonlinear elastic soil springs in both models.

5.3.1. Pile Displacement Behaviour

Operational Mode

Under wind and wave loading only, the displacement of:

- the RNA point mass,
- the beam node below maximum water level,
- and the node at pile base below mudline,

behave as the time history in Figure 5.4 when the turbine is operational.

The first part of the signal, for all three nodes, is dominated by the transient response of the system to the rotor thrust, wind and wave forces suddenly driving the structure out of its equilibrium. The created motion is actively damped by the operating rotor (*rotor aerodynamic damping*), and passively by the flow of air and water around the moving pile (*aerodynamic* and *hydrodynamic* drag damping)[19]. Between 50 to 60 seconds, a new equilibrium is found by the structure at approximately:

- +0.38 m for the RNA,
- +0.045 m for the node directly below the water level,
- -0.003 m for the node at the pile base.

[19] No material damping by the structure was included in the finite-element model.

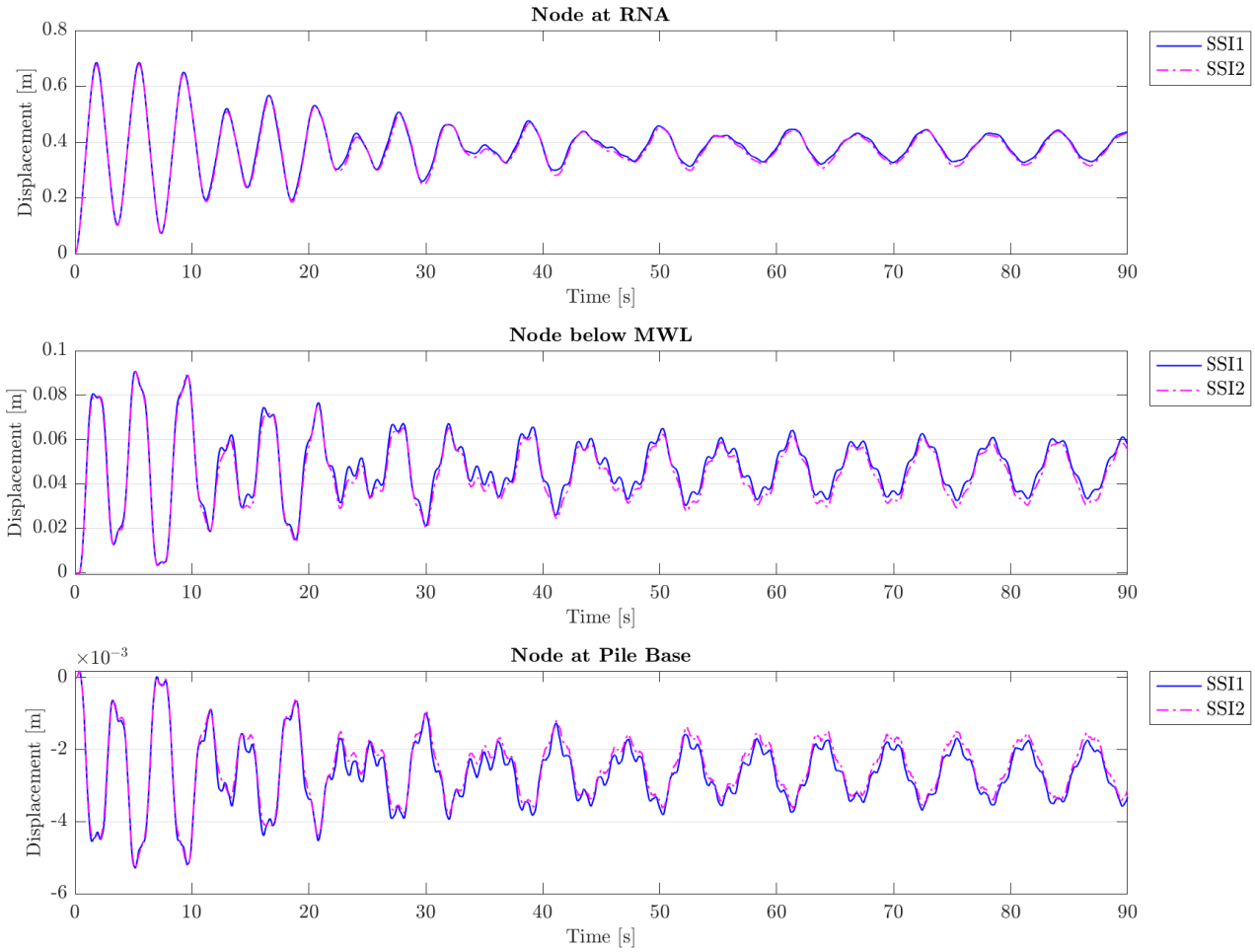

Figure 5.4: *Lateral pile displacement time history for SSI1 and the simplified SSI2 models, for wind and wave loads only (DLC 1-N), and under operational conditions. Time history depicted for the RNA node, the node directly below maximum water level, and the node at the pile base below mudline.*

about which the structure continues to oscillate at the frequency of the regular waves (period T_p = 5.69 s). The steady-state oscillation motion is thus governed by the wave loads. The transient state oscillation happens at first natural frequency of the soil-structure system, and is the decay response motion of the system to the sudden onset of external forces.

As no seismic shear waves are present in the current load case, and the viscous damper which models radiation damping in SSI2 is reduced to null, the responses of both soil-structure interaction models are very similar. The minor differences are due to the dissimilar equations used to describe the elastoplastic soil springs, resulting in slightly different soil gradients in the p-y curves (see Figures 3.17 to 3.21).

Focusing on the response behaviour of each of the three highlighted nodes individually, it is clear that the **RNA** reaches the largest deflection and largest deflected dynamic equilibrium state. Above sea level, the pile is free to move in the wind, as opposed to nodes below water level or mudline that experience much more resistance. Additionally, the RNA is a large mass on a long arm, creating a large moment about the mudline clamping point. The larger the thrust force, the longer the pile length above mudline, and the heavier the top mass, the more pronounced the RNA lateral deflection would be. The node achieves a dynamic equilibrium at +0.38 m in the steady state, caused by the constant positive thrust force and aerodynamic load. At 60 seconds down the time history, the steady state is achieved, and the motion is now dominated by the wave loads which oscillate at a period of 5.69 s.

Below maximum water level, the pile has a shorter arm to move about the pivot point below mudline and experiences more resistance by the water body because of its higher density. As such, the amplitude of the displacements is smaller although they follow the same general trend. The dynamic equilibrium is positive, at +0.045 m, as the thrust force creates the largest force and moment; each node above the pivot point in the soil is forced in positive lateral direction.

Apart from the smaller deflection amplitude, it can be seen that the response has many more peaks and troughs than the RNA response, although the dominant period in the steady state remains the wave period. The same can be seen in the response behaviour of the pile base node below mudline of Figure 5.4. This response behaviour is governed by the dependence of the soil stiffness on pile displacement and vice versa, as explained in more detail in Chapter 5.3.2.

Below mudline, at the pile base (or the bottom node of the FEM), the general behaviour of the pile displacement is similar to the displacement above mudline but in opposite sense. The bottom node of the pile is located below the pivot point in the soil, creating a negative deflected state for predominantly positive loads above this point because of the rigid[20] monopile behaviour. The displacements below mudline are very small (order of mm) because of the high resistance to lateral pile motion by the soil springs. Consequently, it is expected that the soil stiffnesses will barely change (as the pile movements lay in the elastic zone of the p-y curves), resulting in minimal changes in the natural frequency of the system in time. More on this in Chapter 5.3.2.

Emergency Shutdown Mode

If the turbine was to perform an emergency stop after the transient response had died out, then the lateral displacement response behaviour of the three elements looks like the time history in Figure 5.5.
Between 50-60 seconds in the time history the structural response reaches its steady-state, after which the turbine is instantly stopped at 60 s. This is not a realistic emergency shutdown situation, as normally the turbine would not perform this operation under normal sea state condition. However, it is interesting in this comparative study to know how the response of the system changes in case the turbine stops with respect to normal operating conditions.

For all three nodes highlighted here in Figure 5.5, the immediate nullification of the thrust force and rotor aerodynamic damping causes the structure to snap back to a zero deflected mean state. The pile oscillates significantly about this new mean state:

- for the RNA with an amplitude of 0.4 m about the baseline,
- for the node directly below MWL with an amplitude of 0.075 m,
- for the node at the pile base with an amplitude of 0.004 m

The amplitude of this oscillation after shutdown is barely damped, resulting in an almost constant amplitude progression. This is because the only sources of damping are now the passive aerodynamic and hydrodynamic drag damping by the pile motion, which are significantly smaller than the rotor aerodynamic damping. No material damping was implemented in the model that can alleviate the displacement amplitude.

After shutdown, the soil-structure response starts to oscillate at the first natural frequency of the system, and continues to do so as the decay motion is not damped. Just as for the transient response at the start of the simulated time, the sudden drop in the dominant thrust force causes the structure to vibrate at its natural frequency. As opposed to the operational mode, there is no more rotor damping active after shutdown to decay this new transient state. Because a steady-state is not reached, the motion after shutdown does not become in sync with the wave loads again. The motion instead continues at a period of about 3.6 s[21] (or 0.2737 Hz).

[20] A flexible pile would show no lateral pile motion at the shaft base. This supports the hypothesis to use Timoshenko beam theory to model the monopile, as it behaves as a rigid thick beam.

[21] Small changes to the first natural frequency of the soil-structure system occur due to changes in the soil spring stiffness by the pile displacement. A natural period of 3.6536 s is the average period over time of the soil-structure system.

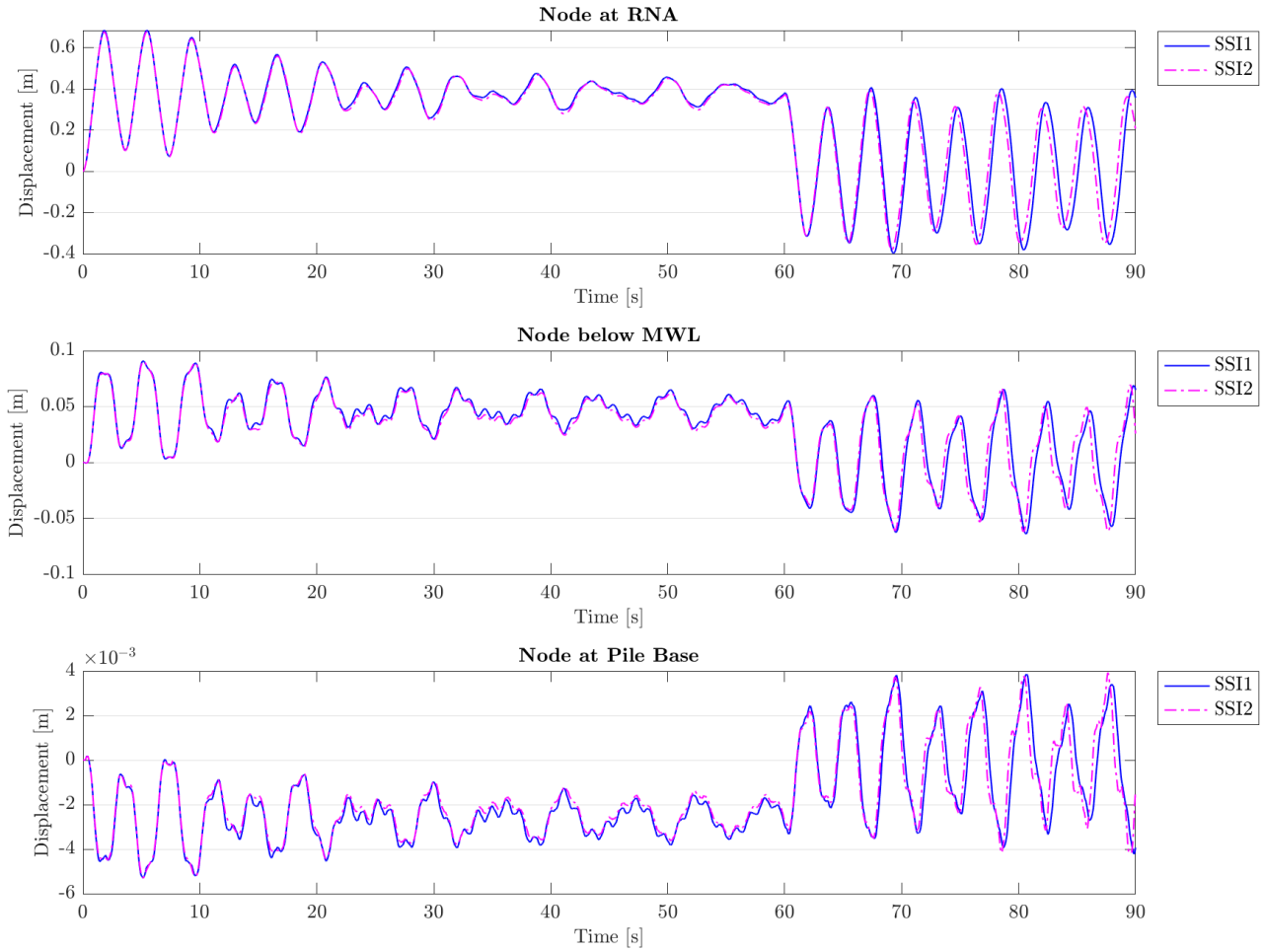

Figure 5.5: *Lateral pile displacement time history for SSI1 and the simplified SSI2 models, for wind and wave loads only (DLC 1-N), and under shutdown conditions. Time history depicted for the RNA node, the node directly below maximum water level, and the node at the pile base below mudline.*

5.3.2. Natural Frequency Progression

A change in natural frequency is directly related to a change in soil stiffness, and to a change in waterlevel. A change is soil stiffness follows a change in pile displacement, which in its turn is forced by external loads. Therefore, the correlation between change in natural frequency, soil stiffness, pile displacement and the external loads is discussed here. For the first load case, the external loads are only the rotor thrust force, tower aerodynamic load and wave hydrodynamic load.

Operational Mode

The Nonlinear Elastic Soil-Structure Interaction Model Figure 5.6 shows the upper and lower bounds of the first natural frequency of the soil-structure system during wind and wave loading, for the nonlinear elastic soil-structure interaction model that applies the API recommended p-y curves to express the soil stiffness (see Chapter 3.1.2).

From the figure it can be deduced that the soil springs are most stiff in the initial state of the system (prior to any shaft displacement). They lose stiffness for any small displacement, given that the natural frequency in Figure 5.6 never reaches the initial frequency again.

Figure 5.7 shows the change in the first natural frequency over time, and provides an overview of the correlation with soil stiffness, pile displacement and external loads. As the thrust force and tower aerodynamic load

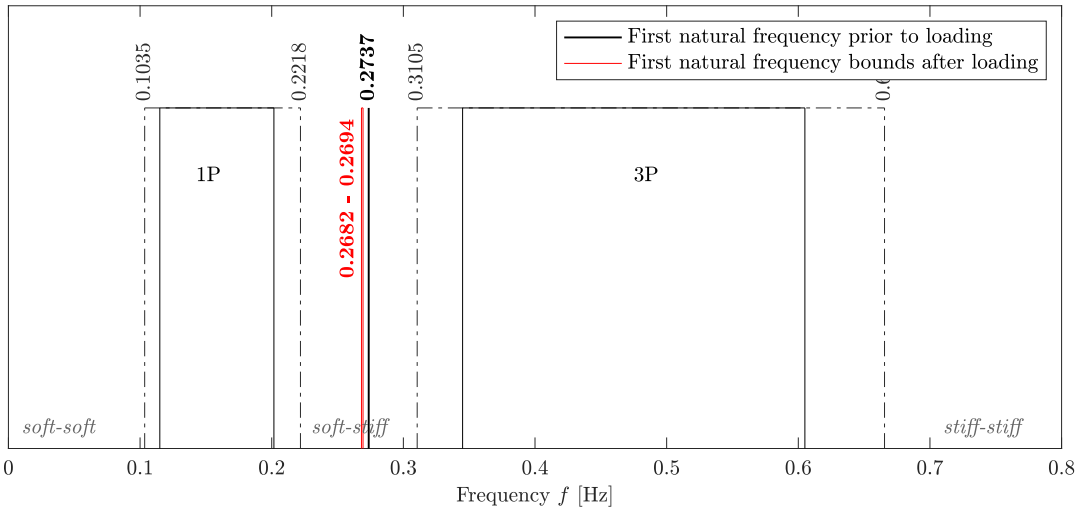

Figure 5.6: *The first natural frequency maximum-minimum range of the soil-structure system with wind and wave loading, for the nonlinear elastic soil-structure interaction model under operational conditions.*

are constant, only the wave loads' variation over time is shown. From this figure some observations could be made regarding the nonlinear elastic soil-structure interaction model's behaviour prior to exposure to earthquake ground motion, this with regard to the soil stiffness interaction and to the waterlevel.

First of all, as long as the shaft displacement remains virtually zero then the soil stiffness remains almost constant at maximum soil resistance (i.e., the gradient of the p-y curves used in this model is constant for small displacements <=1 mm). Regions of minimal pile displacement, constant soil stiffness and hence constant first natural frequency are present prior to 10 s down the time series. For any larger pile displacements, although they are still minimal (in the order of a few millimeters), the stiffness of the soil springs decreases because of the early onset of elastoplastic behaviour in the API recommended p-y curve expressions (see Figures 3.10 to 3.14). When the pile displacement grows beyond the elastic response of the soil springs, the soil stiffness to lateral motion decreases and hence the first natural frequency decreases accordingly. The change in natural frequency, although present, is however minimal (1.5 to 2 %).

Secondly, in the steady-state response, the frequency of the system appears to reach a minimum when the wave load is maximum in positive (right) direction. When the wave load is negative maximum (left loading direction), the frequency reaches a local maximum. This can be explained from the combination of loads, including thrust and wind loads which are assumed constant and act in positive (right loading) direction. Adding a co-directional positive wave load will create a larger force in the same direction as the thrust and wind, and will result in a larger pile deflection. This in turn leads to the smallest soil spring stiffness, and consequently the lowest natural frequency. If one adds a negative maximum wave load, acting in opposite direction to the thrust and wind load, the predominantly positive displacement will be reduced (given that the thrust force dominates the pile displacement and forces it to a positive equilibrium). The reduced positive displacement of the shaft creates an increase in soil spring stiffness, and leads to an increase in stiffness of the entire system such that the natural frequency picks up again. Maximum positive wave loads make the natural frequency drop, maximum negative wave loads make it restore.

Lastly, some spurious drops can be observed in the natural frequency behaviour that seem to have no correlation with the pile displacement and wave loading trend. These downward peaks coincide with the wave peak period (T_p = 5.69 s), when the wave load is almost zero. However it does correlate to the maximum water level of the regular waves. The drop in natural frequency signifies the occurrences in the time history where the interface node between the aerial and submerged elements becomes submerged. When this happens, the inertia of the system increases by the added hydrodynamic mass. This increase in the global mass matrix at time $t = N \cdot T_p$ reduces the natural frequency of the system at that same time instance, as added hydrodynamic mass will make the response of the system softer. This change in natural frequency is so pronounced because the change in added mass in larger than the change in soil spring stiffness in the time history response.

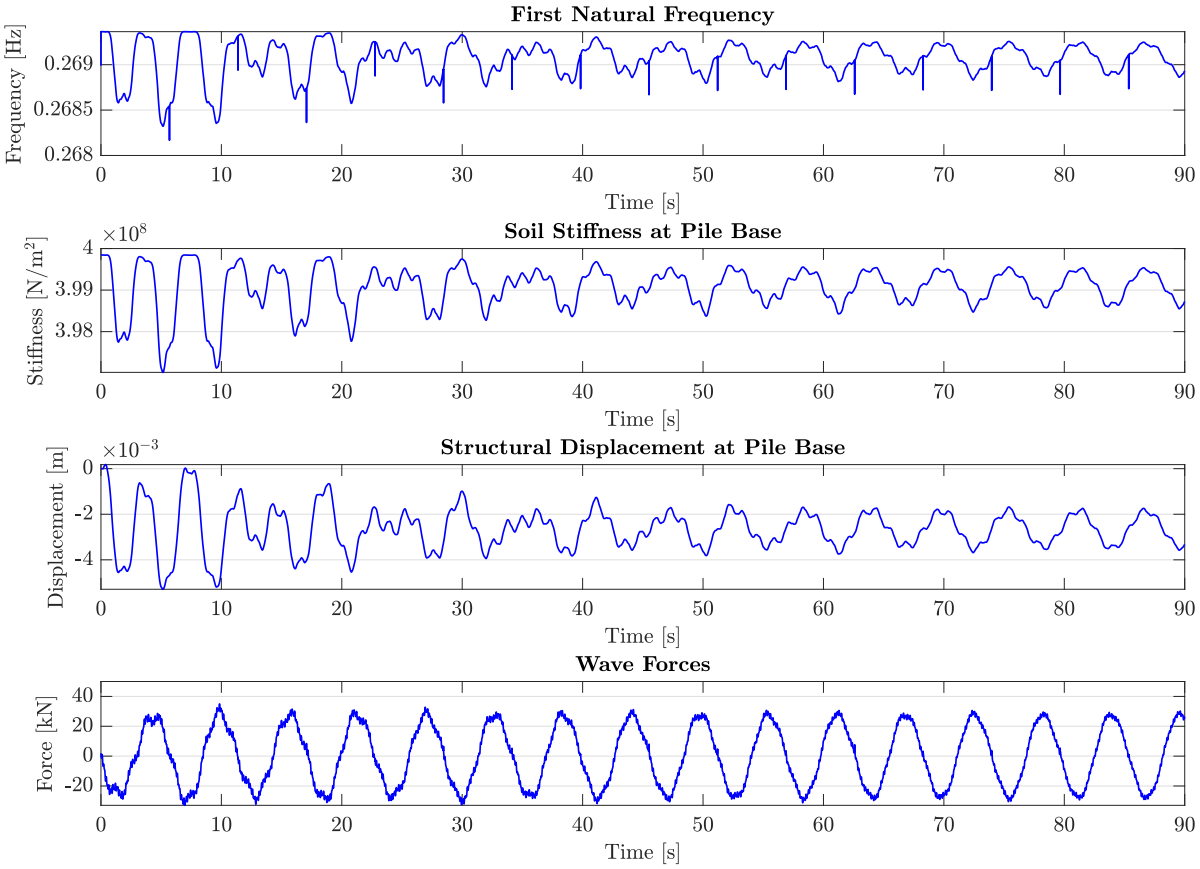

Figure 5.7: *Change in first natural frequency over time, compared to change in soil stiffness, change in pile base deflection and wave forcing, for the nonlinear elastic SSI model to wind and wave forcing only, while the turbine is operational.*

The Nonlinear Series Hysteretic-Viscous Damping Soil-Structure Interaction Model Figure 5.8 shows the upper and lower bounds of the first natural frequency of the second soil-structure system during wind and wave loading, i.e. for the nonlinear inelastic series hysteretic-viscous damping interaction model that applies the p-y curves as proposed by Boulanger et al. [13] to express the soil stiffness (see Chapter 3.1.3). The figure shows that the first natural frequency not only decreases over the loading history, but also increases to values above the initial state frequency. This indicates that the stiffness of the soil increases at certain pile displacements. Next to that, the range of first natural frequencies in the loading history is wider than for the nonlinear elastic SSI model, indicating that the small pile displacements of Figure 5.4 cause large differences in soil spring stiffness (i.e. there exist large gradient differences along the first section of the p-y curve).

The different soil stiffness behaviour of the nonlinear inelastic series hysteretic-viscous damping SSI model with respect to the nonlinear elastic SSI model also shows in Figure 5.9. Although the pile displacement behaviour is similar (see Figure 5.4), the frequency progression and soil stiffness progression over time are not. Overall, the stiffness of the soil springs is almost constant at 4x10^8 N/m^2 due to the minimal pile displacement under NSS conditions, which is comparable in magnitude to the soil spring stiffness in Figure 5.7. Hence the comparable pile displacement curves for both soil-structure interaction models.

There exist some drops in the soil stiffness, and with it in the natural frequency plot, that agree with pile displacements below 1 mm. By the definition of the sand and gravel layers in the work by Boulanger et al. [13], the initial k_f of these layers is actually lower than the tangent above 1 mm displacement in the p-y curves. Although not practically visible in Figure 3.17 and 3.20, one can still see that the p-y gradient increases before yielding with respect to the API recommended curves, and with respect to the initial state of the Boulanger [13] p-y curves. This lateral p-y behaviour is the reason why at virtually zero pile displacement the soil spring stiffness drops, and consequently the natural frequency of the system falls. And why for shaft displacements that are slightly larger than 1 mm k_f and f_n increase before starting to decrease towards yield.

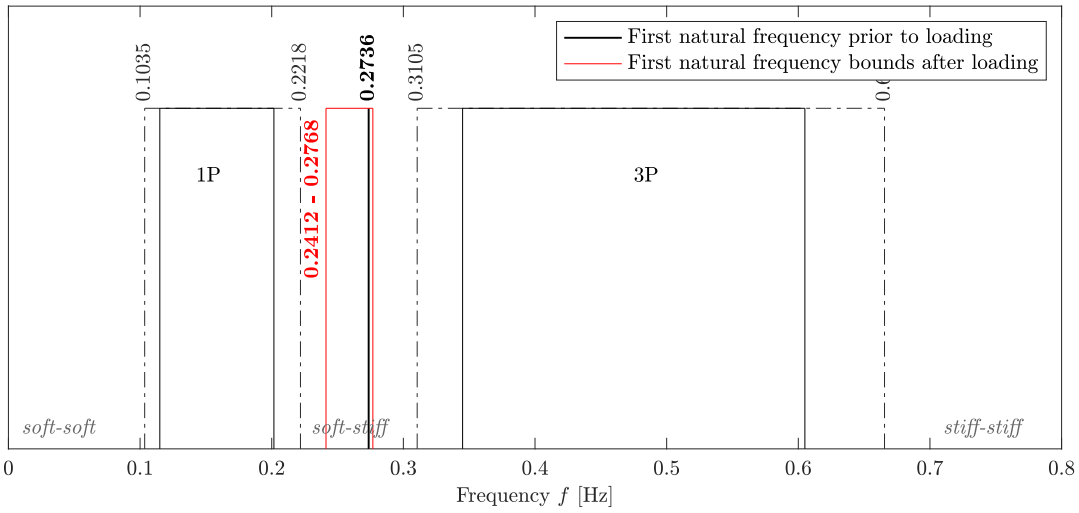

Figure 5.8: *The first natural frequency maximum-minimum range of the soil-structure system with wind and wave loading, for the nonlinear inelastic series hysteretic-viscous damping soil-structure interaction model under operational conditions.*

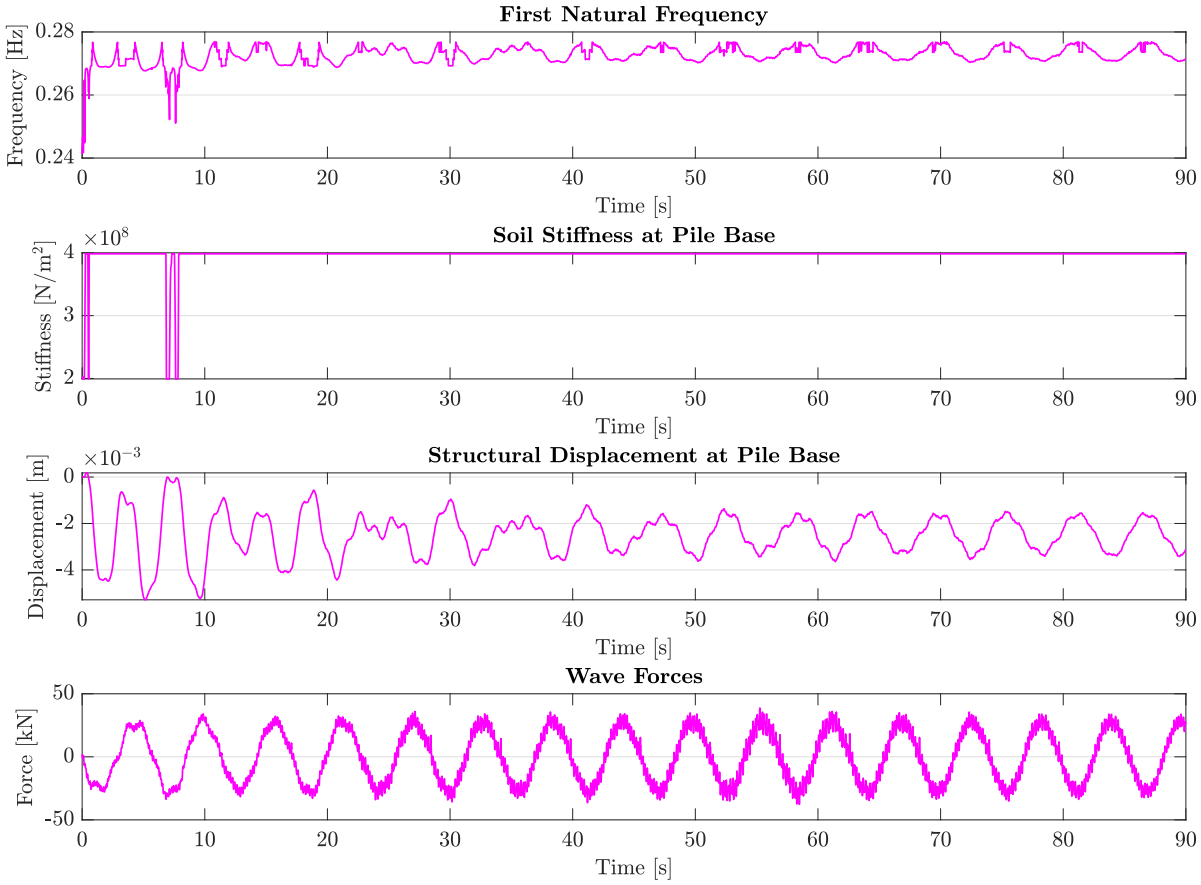

Figure 5.9: *Change in first natural frequency over time, in comparison to the change in soil stiffness, change in pile base deflection and wave forcing, for the nonlinear inelastic series hysteretic-viscous damping soil-structure interaction model to wind and wave forcing only, while the turbine is operational.*

The influence of the waterlevel on the natural frequency is less pronounced in Figure 5.9. In the range of pile displacements to NSS conditions, the influence of the softer initial state of the p-y curves of sand and gravel is of much greater influence than the added mass by the highest water level. To compare, the natural frequency oscillates between 0.2695 to 0.2680 Hz and the soil stiffness between $4x10^8$ N/m^2 to $3.97x10^8$ N/m^2 for SSI1. The range of soil stiffness for SSI2 is $4x10^8$ N/m^2 to $2x10^8$ N/m^2, consequently the change in soil stiffness will dominate over a change in added mass in the natural frequency.

Emergency Shutdown Mode

The Nonlinear Elastic Soil-Structure Interaction Model Figure 5.10 shows the range of first eigenfrequencies for the nonlinear elastic soil-structure interaction model in case the turbine would perform an emergency stop after the transient response of the system is damped. The frequency range is exactly the same as for operational conditions, see Figure 5.6. The figure hints that the pile displacement about zero deflection after emergency stop is not larger than the prior pile displacement, thus that the soil springs are not weakened more than in operational response mode. This is why the lowest natural frequency bound for shutdown conditions does not drop below the lowest natural frequency bound for operational conditions.

This is also confirmed in Figure 5.11, where it is shown that the maximum displacement with respect the zero deflected initial state does not exceed the -0.005 m displacement reached during the decay motion in the transient state. After shutdown, the displacement oscillates between -0.004 m and 0.004 m. The softest soil resistance response to lateral pile motion is thus reached in the transient response of the system, hence the lowest first natural frequencies is located in this part of the response.

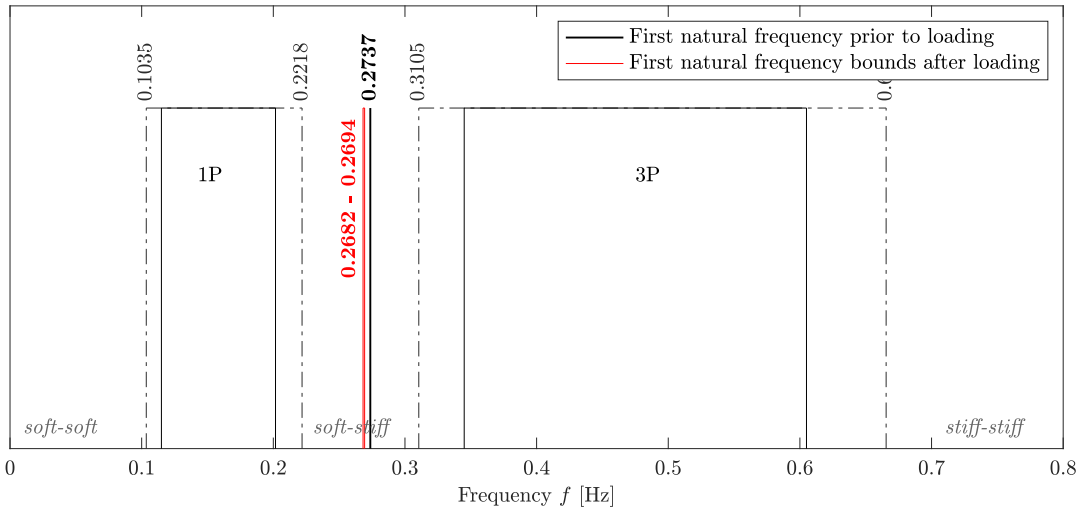

Figure 5.10: *The first natural frequency maximum-minimum range of the soil-structure system with wind and wave loading, for the nonlinear elastic soil-structure interaction model under shutdown conditions.*

It is however true that the sudden absence of rotor thrust force and aerodynamic damping leads to a new transient response of the system, that leads to displacements amplitudes far larger ($\frac{1}{2}$·0.008 m) than the displacement amplitude prior to shutdown in the steady-state response ($\frac{1}{2}$·0.005 m). Also, the structure oscillates at its first natural frequency again during the shutdown decay motion. As this motion is only damped by the passive aerodynamic and hydrodynamic drag damping by the pile motion, this decay motion continues far longer than the startup decay motion by the thrust. Consequently, after shutdown, the fluctuation in pile displacement, and consequently soil spring resistance and natural frequency, is not longer determined by the wave motion as during the steady-state but by the vibration of the structure itself.

When the decay motion coincides with the maximum wave load, it does amplify the decay motion (see t =70 s), and hence reduces the soil stiffness and natural frequency locally. But the wave loads are no longer the dominating influence after shutdown. The natural frequency progression over time is now dominated by the decay motion.

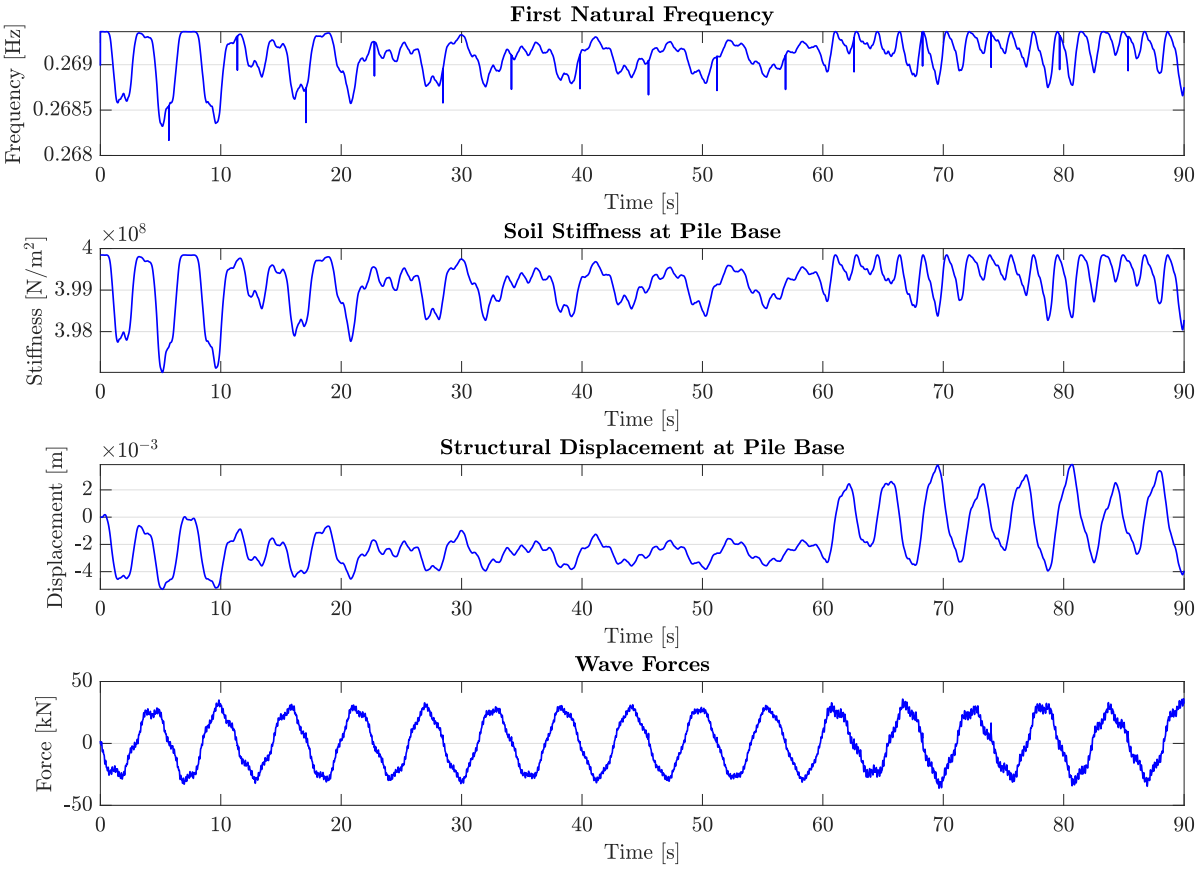

Figure 5.11: *Change in first natural frequency over time, in comparison to the change in soil stiffness, change in pile base deflection and wave forcing, for the nonlinear elastic soil-structure interaction model to wind and wave forcing only, after the turbine performed an emergency break.*

As the range of frequencies, – and thus the range of soil resistance to lateral pile motion –, is still the same as for the operational mode, the influence of the change in waterlevel is still pronounced in the frequency plot as it has a larger influence than the minor changes in soil stiffness on the frequency.

The Nonlinear Series Hysteretic-Viscous Damping Soil-Structure Interaction Model Figure 5.12 and Figure 5.13 for the nonlinear inelastic series hysteretic-viscous damping model hint at the same general behaviour in shutdown mode as for the nonlinear elastic soil-structure interaction model:

1. the absolute pile displacement during the barely damped decay motion following shutdown is not larger than the largest pile displacement during the decay motion following the turbine start-up. Hence the lower and upper frequency bounds are the same as for operational conditions,

2. the fluctuation in pile displacement, soil stiffness and consequently natural frequency after shutdown is no longer governed by the regular motion of the waves, but by the decay motion.

But again, just as for the operational mode, the difference in definition of the p-y curves in this second soil-structure interaction model lead to a different soil stiffness and frequency plot. Every time the pile displacement goes to zero (or the non-deflected state), the soil spring stiffness to lateral pile motion drops and so does the natural frequency. During the decay motion following shutdown, the pile displacement reaches zero far more times than during the steady-state response to the oscillating regular waves, hence the more frequent drops in k_f and f_n.

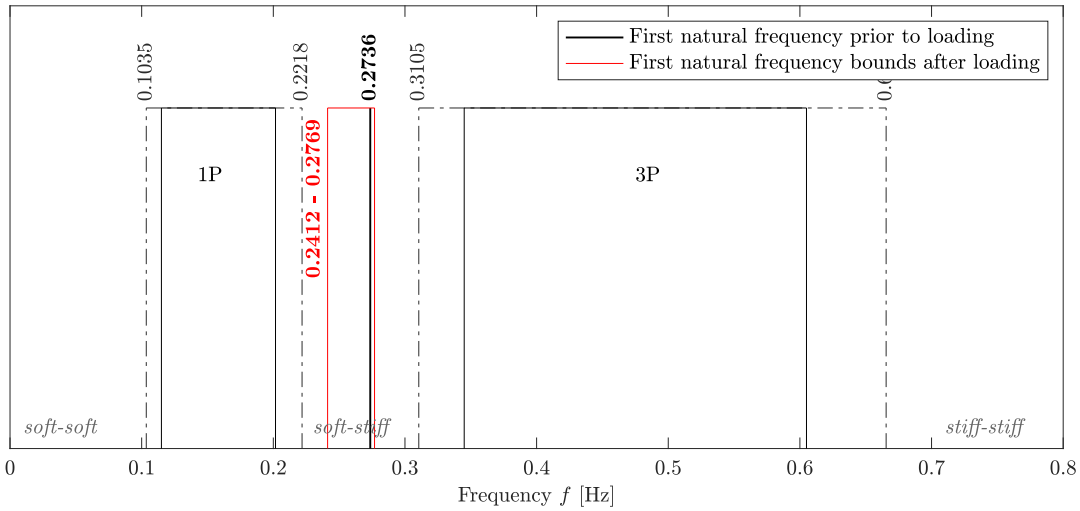

Figure 5.12: *The first natural frequency maximum-minimum range of the soil-structure system with wind and wave loading, for the nonlinear inelastic series hysteretic-viscous damping soil-structure interaction model under shutdown conditions.*

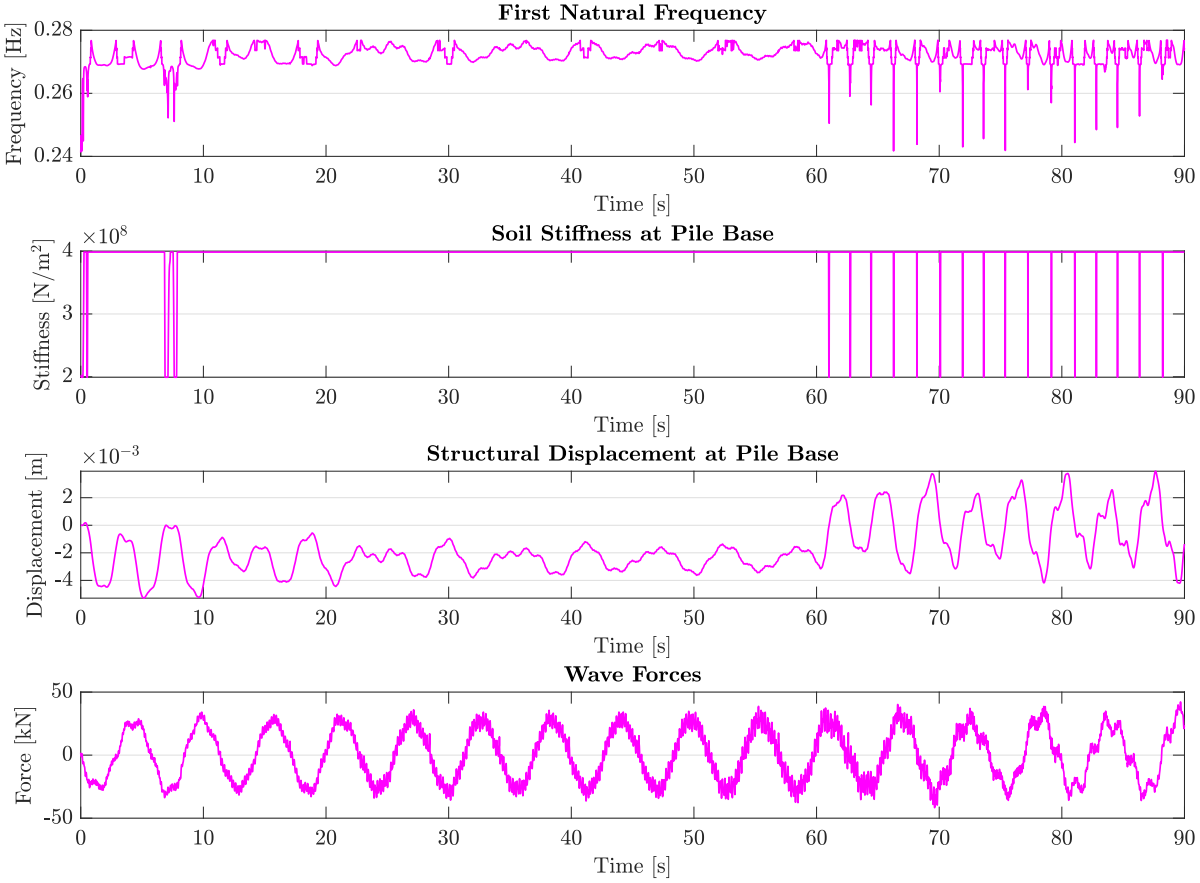

Figure 5.13: *Change in first natural frequency over time, in comparison to the change in soil stiffness, change in pile base deflection and wave forcing, for the nonlinear inelastic series hysteretic-viscous damping soil-structure interaction model to wind and wave forcing only, after the turbine performed an emergency break.*

5.3.3. Structural Tilt Behaviour

Gearbox turbine manufacturers often pose an out of vertical tolerance of 0.5° in total, i.e. the sum of installation and accumulated tilt, above the mudline. This is to guarantee optimal operation of the turbine. In this chapter it is verified whether the wind turbine structure selected for the seismic analyses that follow in Chapter 5.4 to 5.6 complies with the *serviceability limit state* (Figure 2.5) requirement of 0.5° maximum tilt for the pile above mudline.

Operational Mode

Figure 5.14 illustrates the maximum tilted displacement of the pile in time (Figures 5.14a and 5.14c), and the maximum tilt angle of that same displacement instance (Figures 5.14b and 5.14d) versus the serviceability limit indicated by the green shaded area in the plots. The figures clearly shows that when the pile is maximally deflected, at time $t = 5.48$ s in the decay motion, it is still within the serviceability limit tilt with a tilt angle of 0.269/0.267° at the RNA, which compares to a lateral deflection of 0.685/0.6792 m versus 1.27 m maximum for SSI1/SSI2 respectively.

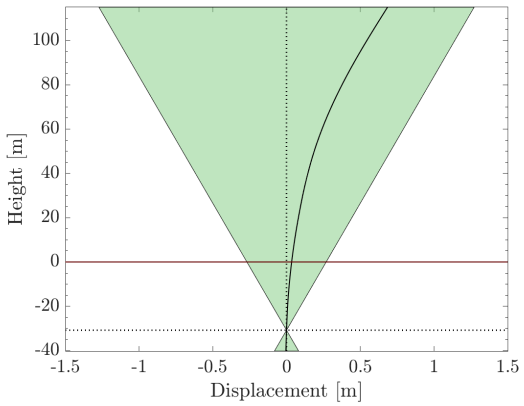

(a) *Ultimate tilt displacement versus limit - SSI1.*

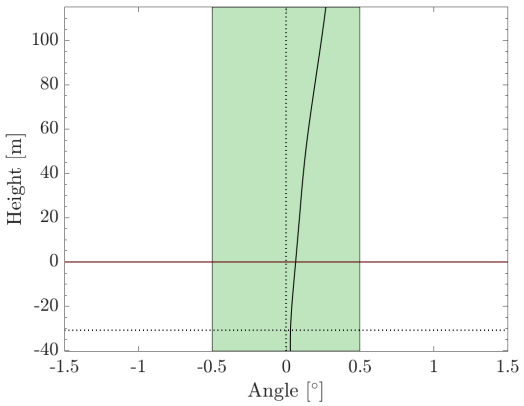

(b) *Ultimate tilt angle versus limit - SSI1.*

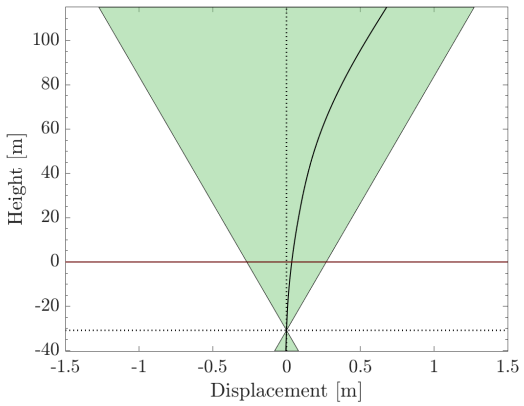

(c) *Ultimate tilt displacement versus limit - SSI2.*

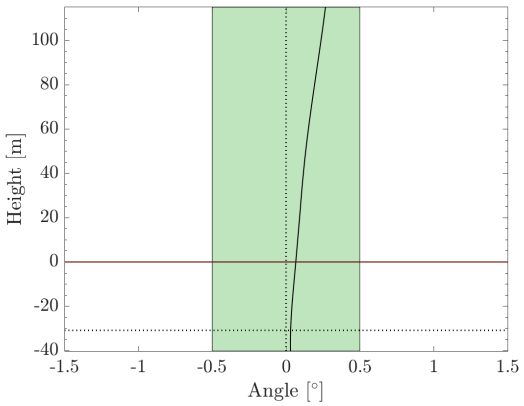

(d) *Ultimate tilt angle versus limit - SSI2.*

Figure 5.14: *Tilt limit check for the nonlinear elastic soil-structure interaction model (SSI1, 5.14a and 5.14b) and the nonlinear inelastic series hysteretic-viscous damping model (SSI2, 5.14c and 5.14d) under wind and wave loads only, when the turbine is in normal operation mode.*

For SSI1 (the elastic) and SSI2 (the inelastic) models, the ultimate deflected state is almost identical, as could also be seen in Figure 5.4 of the pile displacement versus time. The pivot point, or zero deflection point, below mudline is similar: -30.8051 m for SSI1 versus -30.8737 m for SSI2. The slightly higher pivot point and larger deflection of the pile for the elastic SSI1 model is due to the softer elastic response in the early loading stage of the soil springs as compared to the inelastic SSI2 model as previously discussed in Chapter 5.3.2.

Emergency Shutdown Mode

The pile's maximum deflected state is equal for the operational situation and the emergency shutdown mode when comparing Figures 5.14 and 5.15. As explained in Chapter 5.3.1 and 5.3.2, this is because the maximum deflection of the pile with respect to the zero deflected state occurs in the transient response of the system to the start-up of the turbine, not in the transient response following the turbine shutdown. That is why the maximum tilt and the pivot point below mudline are identical for the operational and shutdown state.

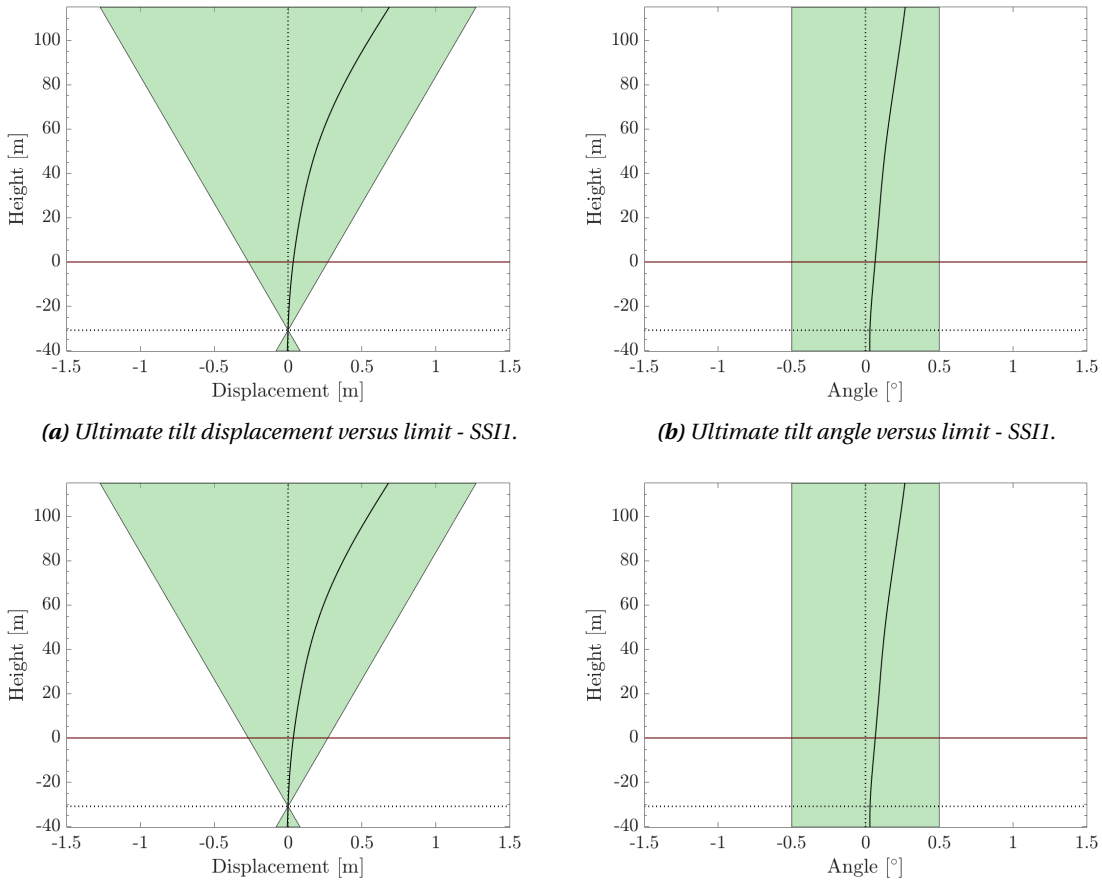

(a) *Ultimate tilt displacement versus limit - SSI1.*

(b) *Ultimate tilt angle versus limit - SSI1.*

(c) *Ultimate tilt displacement versus limit - SSI2.*

(d) *Ultimate tilt angle versus limit - SSI2.*

Figure 5.15: *Tilt limit check for the nonlinear elastic soil-structure interaction model (SSI1, 5.15a and 5.15b) and the nonlinear inelastic series hysteretic-viscous damping model (SSI2, 5.15c and 5.15d) under wind and wave loads only, after the turbine performed an emergency shutdown.*

5.3.4. Structural Capacity Behaviour

A global yield stress check and a global buckling check give an indication of the structural capacity used when the structure is subjected to a certain combination of environmental loads, here being a normal steady wind, regular waves sea state (NSS). Both indicate the level to which the structure is loaded in ultimate load cases, hence their use as indicators in *ultimate limit state* analysis (Figure 2.5).

Use has been made of safety factors in both the yield and the buckling check. For the yield stress developed in the structure, a material safety factor of 1.1 was multiplied with the developed yield stress. For the buckling check, a safety factor of 1.2 was applied to the buckling value [45]. No safety factors were applied to the loads.

If the utilization ratio of yield stress versus material strength or the buckling value exceeds one, the structure is considered to have failed in either yield or buckling. The mathematical expressions to compute the yield and buckling value are listed in Appendix F.

Operational Mode

Figure 5.16 shows the maximum yield stress in the structure for each node and at any given time. The green shaded area marks the zone in which the yield does not exceed the structural capacity, taking into account a material safety factor.

Three main conclusions can be drawn from the figure. First of all, the loads experienced by the structure under normal sea state conditions do not lead to structural failure in yield. For both soil-structure interaction models, the utilization factor is well below one. Secondly, the capacity behaviour of both models is very similar. With no earthquake active, both models predict approximately the same response behaviour (see Chapter 5.3.1), hence they also predict the same yield capacity progression in Figure 5.16. Lastly, the figure shows that with increasing normal force and moment towards the mudline, the yield stress in the structure grows too. However, in zones where the structure is locally thicker,– as for the transition from tower to transition piece (0.05 to 0.08 m) and from transition piece to the overlap between transition piece and monopile (0.08 to 0.154 m) –, the yield stress decreases as more structural area is available to redistribute the loads in.

Figure 5.17 shows the buckling behaviour of the structure under normal operating conditions of the rotor. It shows that the tower is more sensitive to buckling than the embedded monopile, which makes sense given that the surrounding soil body provides additional stiffness to the monopile. Just as with the yield stress, an increase in cross-sectional area will reduce the buckling factor (and hence the likelihood of experiencing buckling failure in that zone of the structure). This can be seen in the transition from tower to TP and TP+MP.

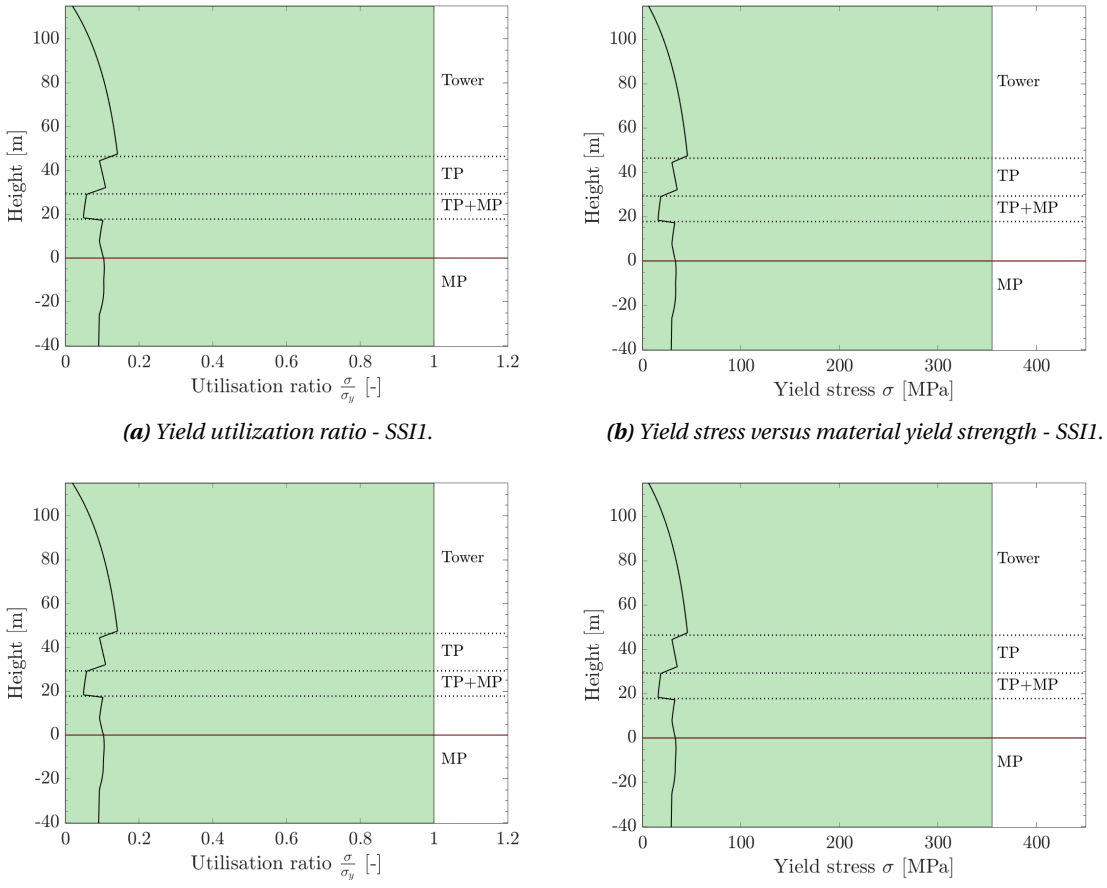

(a) *Yield utilization ratio - SSI1.*

(b) *Yield stress versus material yield strength - SSI1.*

(c) *Yield utilization ratio - SSI2.*

(d) *Yield stress versus material yield strength - SSI2.*

Figure 5.16: *Global yield limit check for the nonlinear elastic soil-structure interaction model (SSI1, 5.16a and 5.16b) and the nonlinear inelastic series hysteretic-viscous damping model (SSI2, 5.16c and 5.16d) under wind and wave loads only, when the turbine is in normal operation mode.*

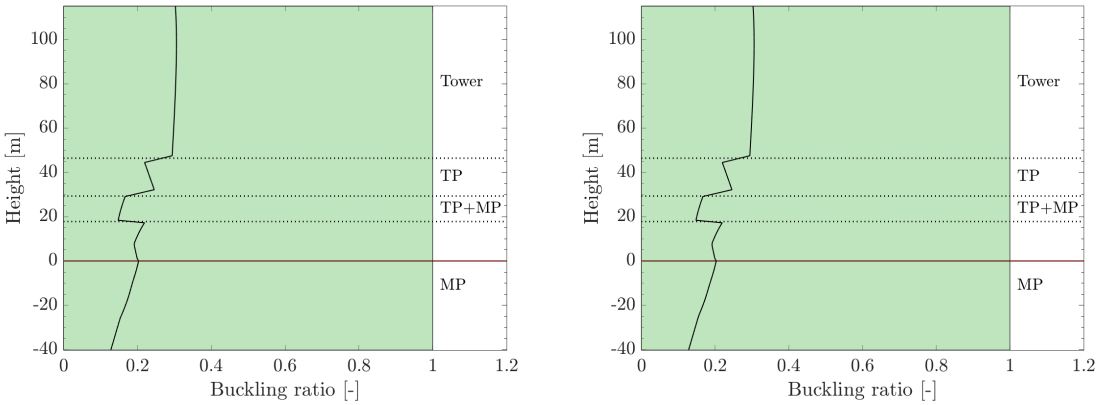

(a) *Buckling ratio versus limit - SSI1.*

(b) *Buckling ratio versus limit - SSI2.*

Figure 5.17: *Global buckling limit check for the nonlinear elastic soil-structure interaction model (SSI1, 5.17a) and the nonlinear inelastic series hysteretic-viscous damping model (SSI2, 5.17b) under wind and wave loads only, when the turbine is in normal operation mode.*

Emergency Shutdown Mode

Above mudline, Figure 5.18 shows similar yield stress development in the structure under shutdown conditions as under operational conditions for both models (Figure 5.16). This is because the maximum displacement above mudline is the highest in the decay motion following start-up of the rotor thrust force (>0.6 m), both for the operational and shutdown simulation. Following shutdown, the maximum deflection in any direction, positive or negative, is smaller than that (<0.4 m). As such, the largest moment experienced by the tower and TP is that by the decay motion to thrust initialization. Consequently, the maximum yield stress and buckling state experienced during operation is the same as when the rotor has stopped, but only for pile sections above the mudline.
Below mudline, the capacity behaviour of the monopile shows obvious differences with the capacity behaviour under operational conditions. Both soil-structure interaction models show an increasing yield capacity utilization below mudline (Figure 5.18a and 5.18c), as opposed to the fairly constant utilization ratio when the turbine is in operation (Figure 5.16a and 5.16c).

The soil resistance to lateral pile displacement is the load increasing the already positive moment by the positive thrust and wind load. Other than during operational mode of the turbine, the pile sections below mudline but above pivot point now reach negative displacement values instead of only fluctuating about a positive mean displacement. These negative pile displacements create a positive soil resistance load on the leading edge of the pile, where the soil springs resist the pile displacement by exerting a load in opposite sense. This positive soil resistance load in case of negative pile displacement – that previously to shutdown did not exist –, now creates an even larger positive moment, adding to the contribution of the thrust and wind in the same direction of motion. Previously, the mainly positive pile displacement below mudline and resulting negative soil resistance load decreased the large positive moment.

Consequently, due to the majority of negative pile displacements below mudline, the moment below mudline grows. As such, also the yield stress and buckling value increase for the shutdown response, as shown in Figures 5.18 and 5.19. Even thought the moment below mudline grows due to the shutdown operation, the structure is still within the ultimate limits of its capacity use.

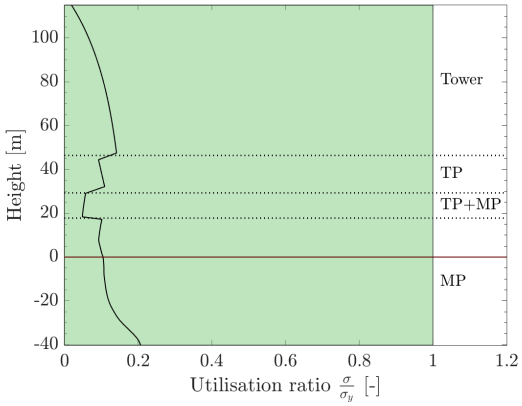

(a) *Yield utilization ratio - SSI1.*

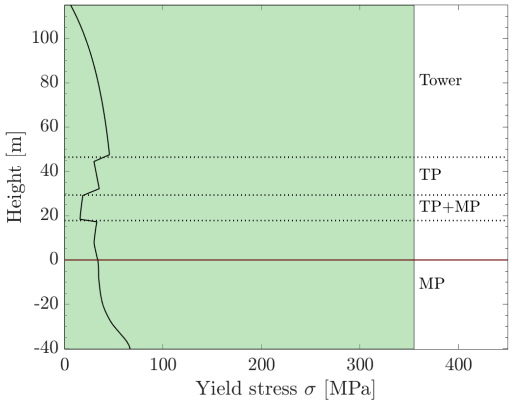

(b) *Yield stress versus material yield strength - SSI1.*

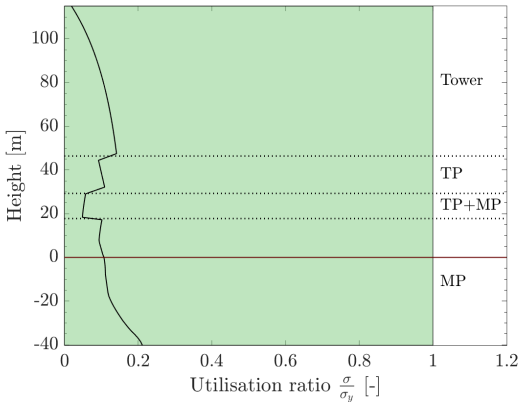

(c) *Yield utilization ratio - SSI2.*

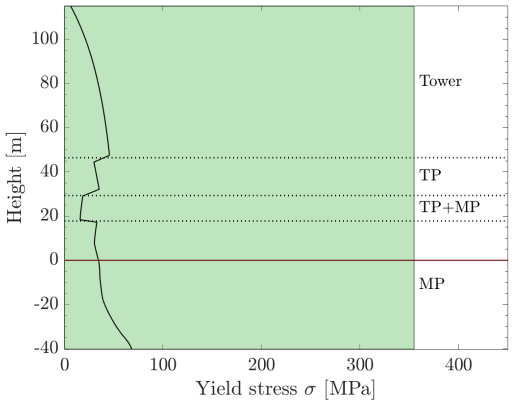

(d) *Yield stress versus material yield strength - SSI2.*

Figure 5.18: *Global yield limit check for the nonlinear elastic soil-structure interaction model (SSI1, 5.18a and 5.18b) and the nonlinear inelastic series hysteretic-viscous damping model (SSI2, 5.18c and 5.18d) under wind and wave loads only, when the turbine is in emergency shutdown mode.*

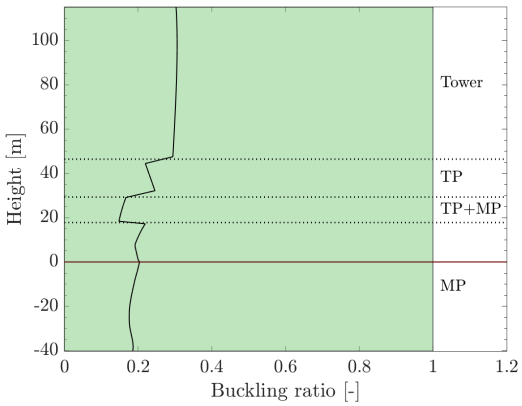

(a) *Buckling ratio versus limit - SSI1.*

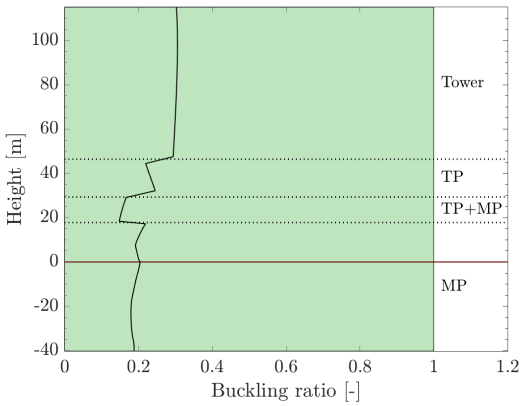

(b) *Buckling ratio versus limit - SSI2.*

Figure 5.19: *Global buckling limit check for the nonlinear elastic soil-structure interaction model (SSI1, 5.19a) and the nonlinear inelastic series hysteretic-viscous damping model (SSI2, 5.19b) under wind and wave loads only, when the turbine is in emergency shutdown mode.*

5.4. Response Behaviour During Seismic Loading - Recorded Earthquake

In addition to the steady wind and regular waves from the NSS analysis, a recorded earthquake ground motion near the wind foundation location is implemented as an external loading conditions. Wind, waves and the earthquake ground motion are assumed to act in the same plane and in the same direction.

5.4.1. Pile Displacement Behaviour

The lateral pile displacement behaviour is compared, between SSI1 and SSI2, and between operational and shutdown conditions of the turbine.

Operational Mode

Figure 5.20 clearly shows that from the moment earthquake-induced ground motion exists (t >60 s) the two soil-structure interaction models no longer predict the same structural response. SSI1 predicts a peak response at the RNA of almost four times the predicted peak response at RNA by SSI2; 2.7 m versus 0.6792 m respectively. SSI2 shows excellent agreement in trend with the ground motion below mudline, the elastic SSI1 structure response does not. The maximum deflection occurs during ground motion for SSI1 (t = 118 s), while for SSI2 it still occurs during rotor startup in the transient response of the system (t = 3.65 s).

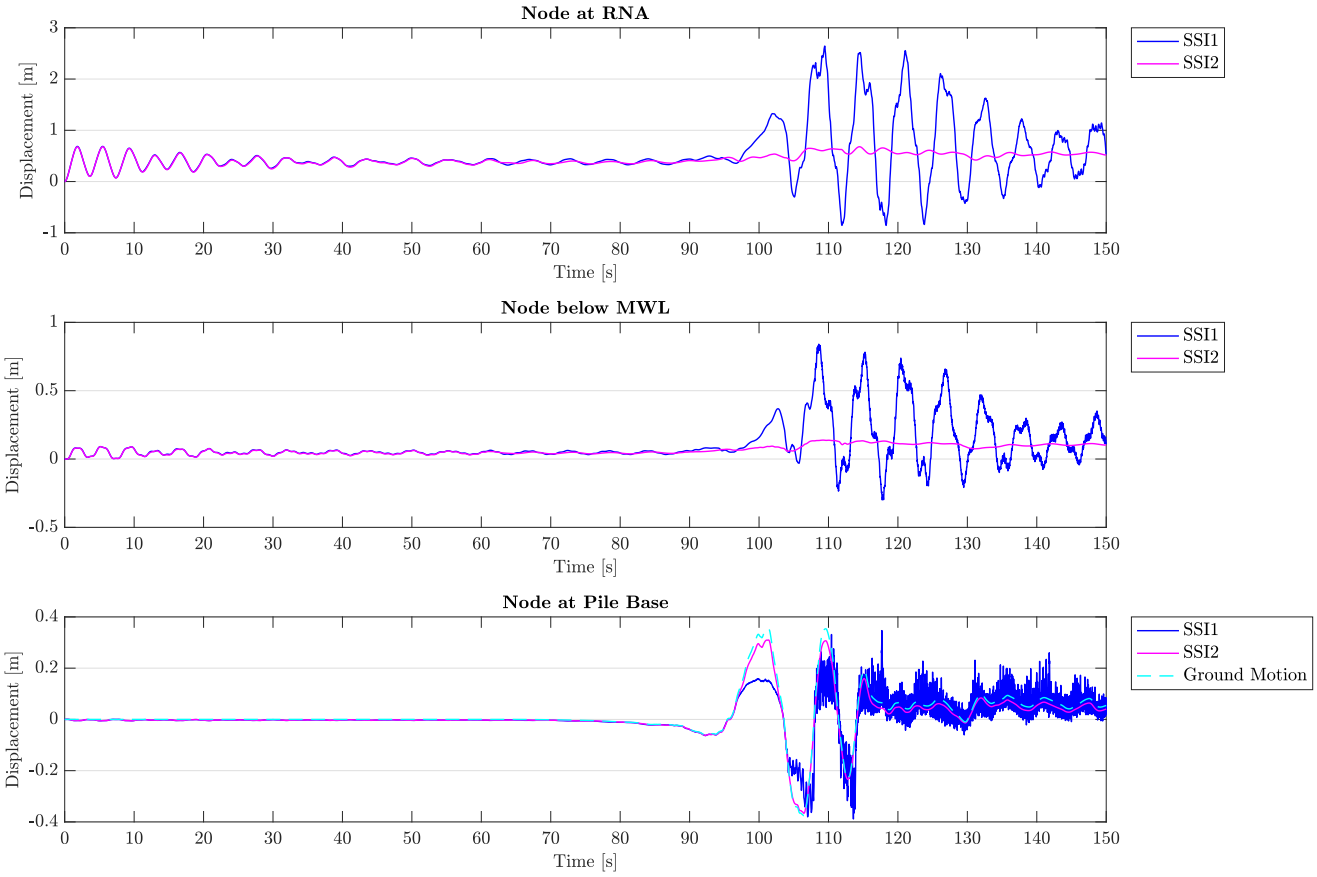

Figure 5.20: *Lateral pile displacement time history for SSI1 and the simplified SSI2 models, for co-directional loading by wind, waves and the recorded earthquake, under operational conditions (DLC 2-N). Time history depicted for the RNA node, the node directly below maximum water level, and the node at the pile base below mudline. As a reference, the ground motion is shown versus the pile displacement below mudline.*

The Nonlinear Elastic Soil-Structure Interaction Model For the nonlinear elastic soil-structure interaction model (SSI1), the correlation between the structural response and ground motion is less straightforward from Figure 5.21.

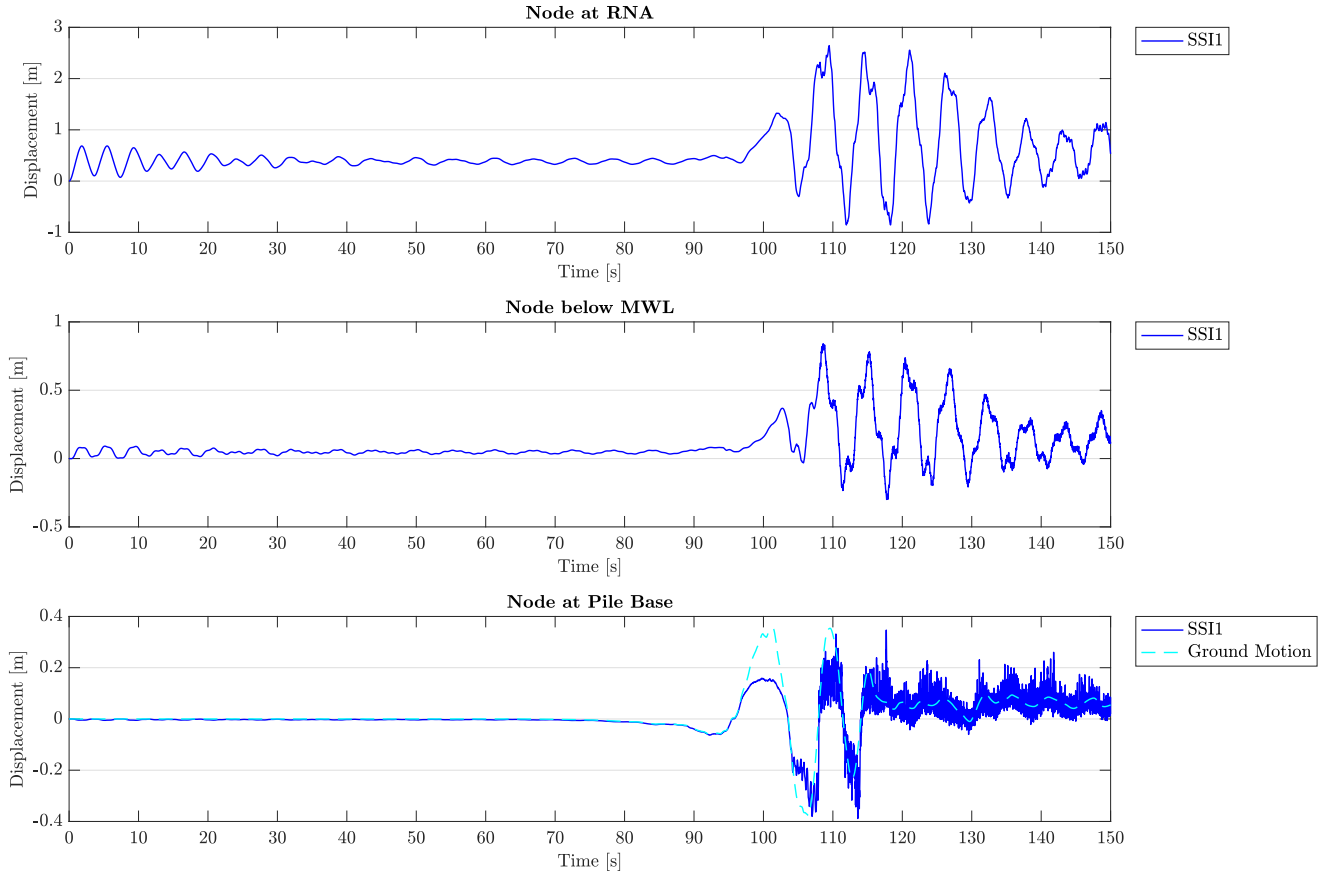

Figure 5.21: *Lateral pile displacement time history for the nonlinear elastic soil-structure interaction model (SSI1), for co-directional loading by wind, waves and the recorded earthquake, under operational conditions (DLC 2-N). Time history depicted for the RNA node, the node directly below maximum water level, and the node at the pile base below mudline. As a reference, the ground motion is shown versus the pile displacement below mudline.*

Below mudline, the pile first follows the ground motion displacement trend, but after the first ground motion peak (t =100 s) the displacement trend of the pile is much more erratic and is predicted to be larger than the ground motion. It was investigated that the pile's lateral acceleration increased up to an nonphysical 2,000 m/s^2 following large ground motion (>0.38 m).

Consequently, the inertia dominated wave loads computed by the Morison equation for a moving pile (Eq. 4.5) increased enormously, as shown in Figure 5.26; the added mass component by the pile motion grows excessively by the nonphysical acceleration response of the structure.

As a result, the response behaviour following the first large ground motion displacement is dominated by the wave loads, and hence follows the loading history of the wave loads. This can be clearly seen in Figure 5.21 for the nodes above the mudline, where the oscillation period following t = 115 s is approximately the wave period T_p = 5.69 s.

The Nonlinear Series Hysteretic-Viscous Damping Soil-Structure Interaction Model For the nonlinear inelastic series hysteretic-viscous damping model (SSI2), see Figure 5.22, the predicted pile response is much smaller.

Following ground motion, the pile below mudline follows the ground displacement almost perfectly, except for some small difference by the soil spring mobilization against lateral displacement on the monopile.

Above mudline, the ground motion 'displaces' the equilibrium about which the structure oscillated before due to the thrust, wind and waves; prior to ground motion, this lay at +0.38 m for the RNA (see Chapter 5.3),

now following ground motion starting at t =90 s this is displacement to +0.55 m. Although following the same trend in peaks and dips as the ground motion, the amplitude of the responses above mudline are smaller and seem damped by the other environmental conditions.

The responses below and above mudline follow the ground displacement, and not the wave load actions as in SSI1. This shows that the wave load action is not increased by a nonphysical growth in acceleration of the pile as in SSI1. The only difference between SSI1 and SSI2 is the activity of the viscous damper during ground motion, apart from some minor differences in soil resistance gradient (see Fig. 3.17 to 3.21). Hence it was identified that radiation damping has a significant impact on the pile response.

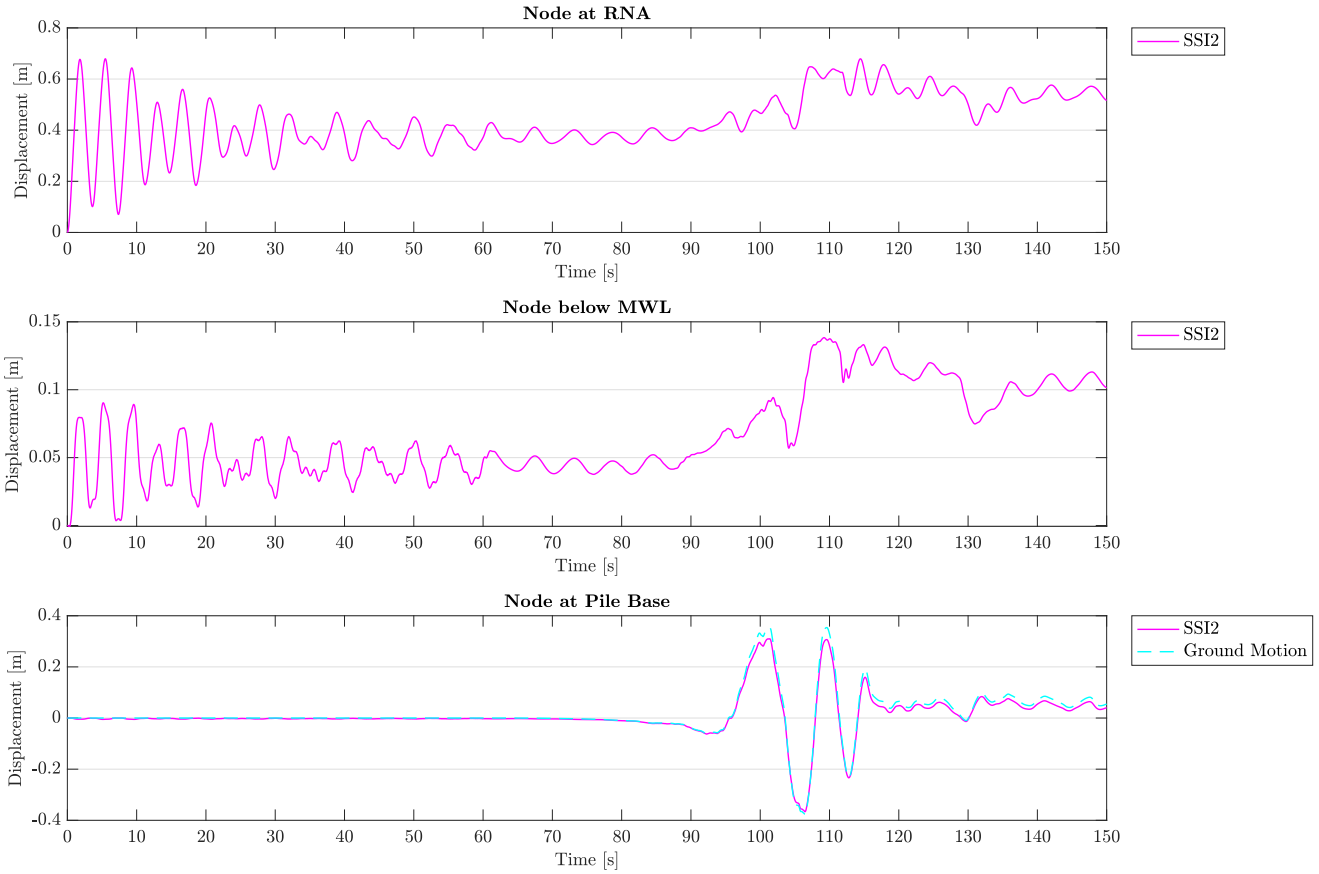

Figure 5.22: *Lateral pile displacement time history for the nonlinear inelastic series hysteretic-viscous damping soil-structure interaction model (SSI2), for co-directional loading by wind, waves and the recorded earthquake, under operational conditions (DLC 2-N). Time history depicted for the RNA node, the node directly below maximum water level, and the node at the pile base below mudline. As a reference, the ground motion is shown versus the pile displacement below mudline.*

Emergency Shutdown Mode

Figure 5.23 shows the responses of SSI1 and SSI2 with respect to each other for when the turbine would perform an emergency break following the registration of P-wave initial tremors at t =80 s. Just as for an operational turbine, SSI1 predicts a much larger amplitude response of the wind support structure; -3.5 m following shutdown for SSI1, compared to +0.68 m during rotor startup in the transient response of SSI2. Hence, an emergency stop of the rotor seems to have a detrimental effect on the response of the SSI1 response.

The Nonlinear Elastic Soil-Structure Interaction Model In Figure 5.24, the moment of shutdown can be identified by the return of the equilibrium position to zero at t = 80 s, as was also the case for the simulations without earthquake motion in Figure 5.5.

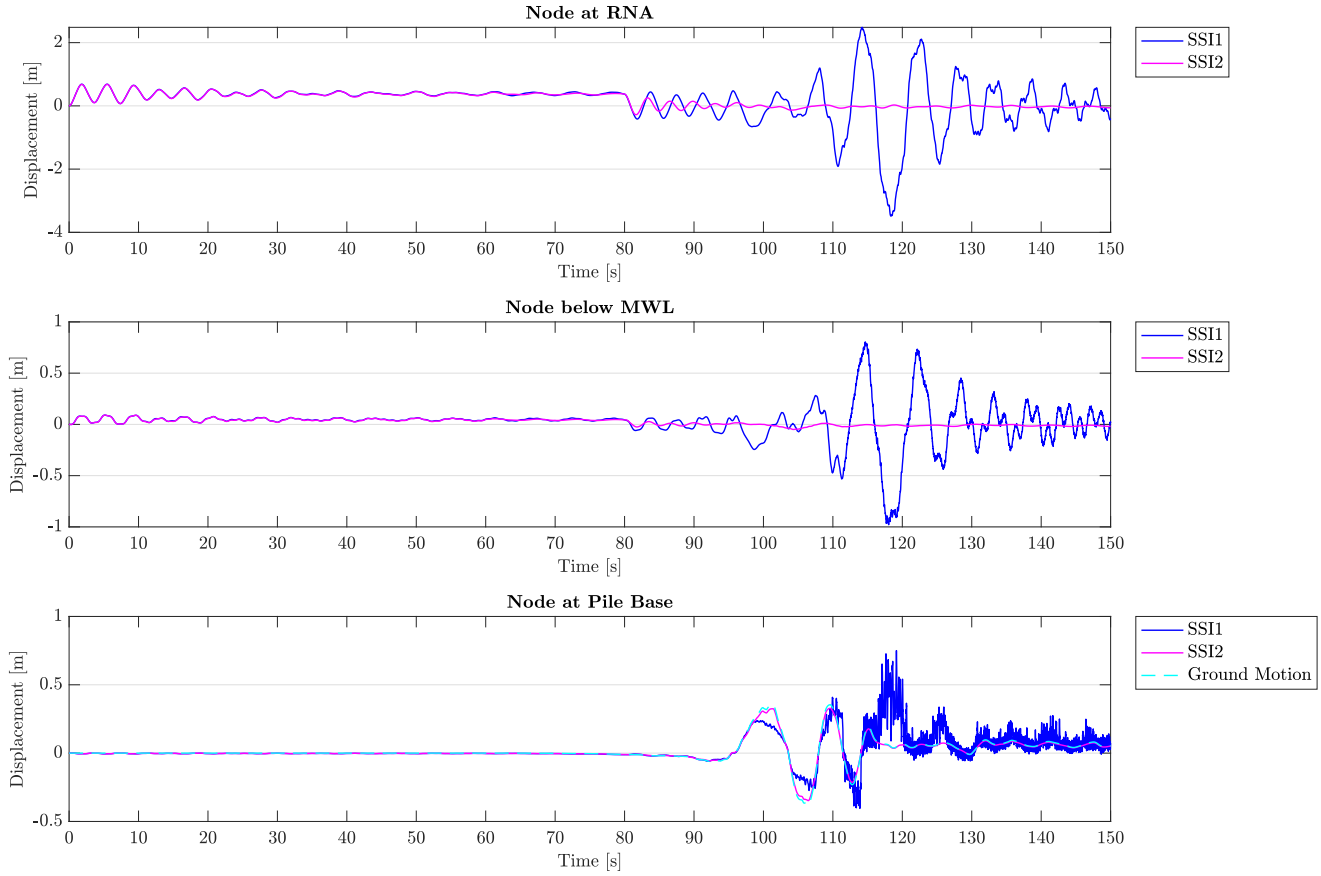

Figure 5.23: *Lateral pile displacement time history for SSI1 and the simplified SSI2 models, for co-directional loading by wind, waves and the recorded earthquake, under shutdown conditions (DLC 2-S). Time history depicted for the RNA node, the node directly below maximum water level, and the node at the pile base below mudline. As a reference, the ground motion is shown versus the pile displacement below mudline.*

From the moment earthquake ground motion exists, the amplitude of the response starts to pick up. Again, just as for the operational state of the rotor in Figure 5.21, the wave loads start to dominate the response as a result of large increments in inertia wave loads due to the immense acceleration of the structure. Hence, after the most significant ground motion has stopped at $t = 120$ s, the wave load action drives the response.

The effect of the stopped rotor is twofold. As the response of the structure is now no longer damped by the rotor operation, the amplitude of the responses are larger during ground motion than before. Rotor aerodynamic damping was the only form of damping in the soil-structure model, and its absence leads to larger amplitude motion. Secondly, the nullification of the thrust force makes that the structure no longer oscillates at a positively displaced offset, but is now returned to oscillate about a zero deflected state.

The Nonlinear Series Hysteretic-Viscous Damping Soil-Structure Interaction Model For SSI2, the equilibrium position in Figure 5.25 also returns to zero after shutdown at t =80 s. But opposite to SSI1, the nonlinear inelastic radiation damping model shows a decrease in pile amplitude deflection during ground motion following shutdown.

Two reasons for the reduced amplitude motion after shutdown could be identified. First of all, the viscous dashpot modeling radiation damping seems to reduce the transient response of the structure following the nullification of the thrust force; it is the only active source of damping still present in the model (apart from passive hydro- and aerodynamic drag damping), and is therefore identified as the main responsible for the decay in amplitude of the transient response starting from $t = 85$ s (when the ground motion increases). Secondly, the absence of an active thrust force makes the balance of the structure return to zero, about which it oscillates along with the ground motion up to the end of the simulated signal.

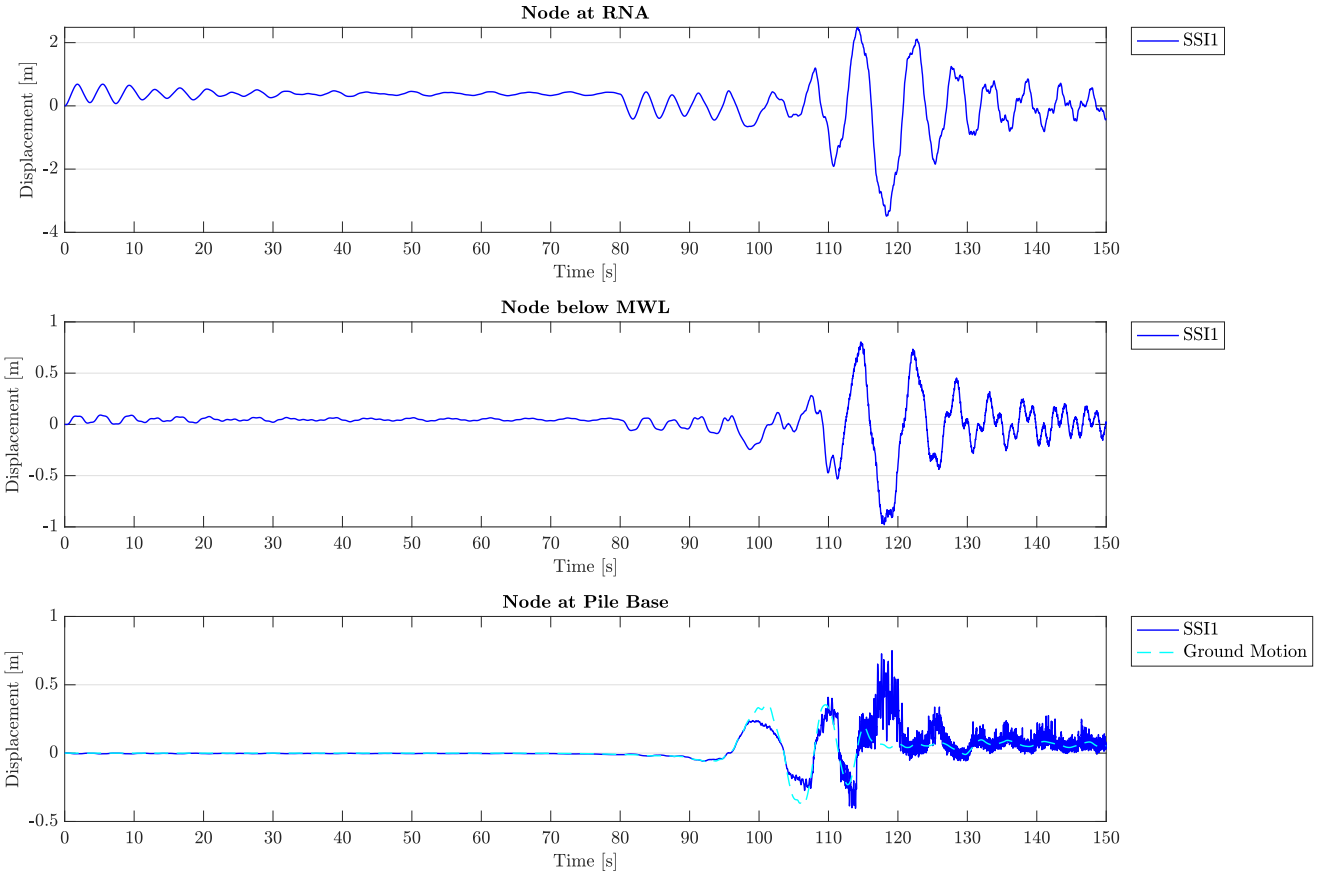

Figure 5.24: *Lateral pile displacement time history for the nonlinear elastic soil-structure interaction model (SSI1), for co-directional loading by wind, waves and the recorded earthquake, under shutdown conditions (DLC 2-S). Time history depicted for the RNA node, the node directly below maximum water level, and the node at the pile base below mudline. As a reference, the ground motion is shown versus the pile displacement below mudline.*

It is however remarkable that the displacement by the pile below mudline is that much larger than above mudline. This is counter-intuitive, as it would be expected that the ground shaking would induce larger deflections in the motion above mudline. Either the water body provides adequate damping of the motion, or the radiation damping may be exaggerated. The latter can be either by the definition and parameters used to define the radiation damping (see Chapter 3.1.3), or by the set-up of the soil spring element. In Wallace et al., it was already concluded that the parallel set-up of the radiation damper with the plastic soil spring may lead to excessive dashpot forces that overestimate the ultimate resistance response by the soil [97]; it may thus well be that it is the parallel configuration of the nonlinear elastoplastic spring with the viscous dashpot as in Figure 4.34 that leads to the overestimate of the radiation effect. This is food for sensitivity studies of soft soil-structure responses to the influence of the viscous dashpot parameters, see Chapter 7.

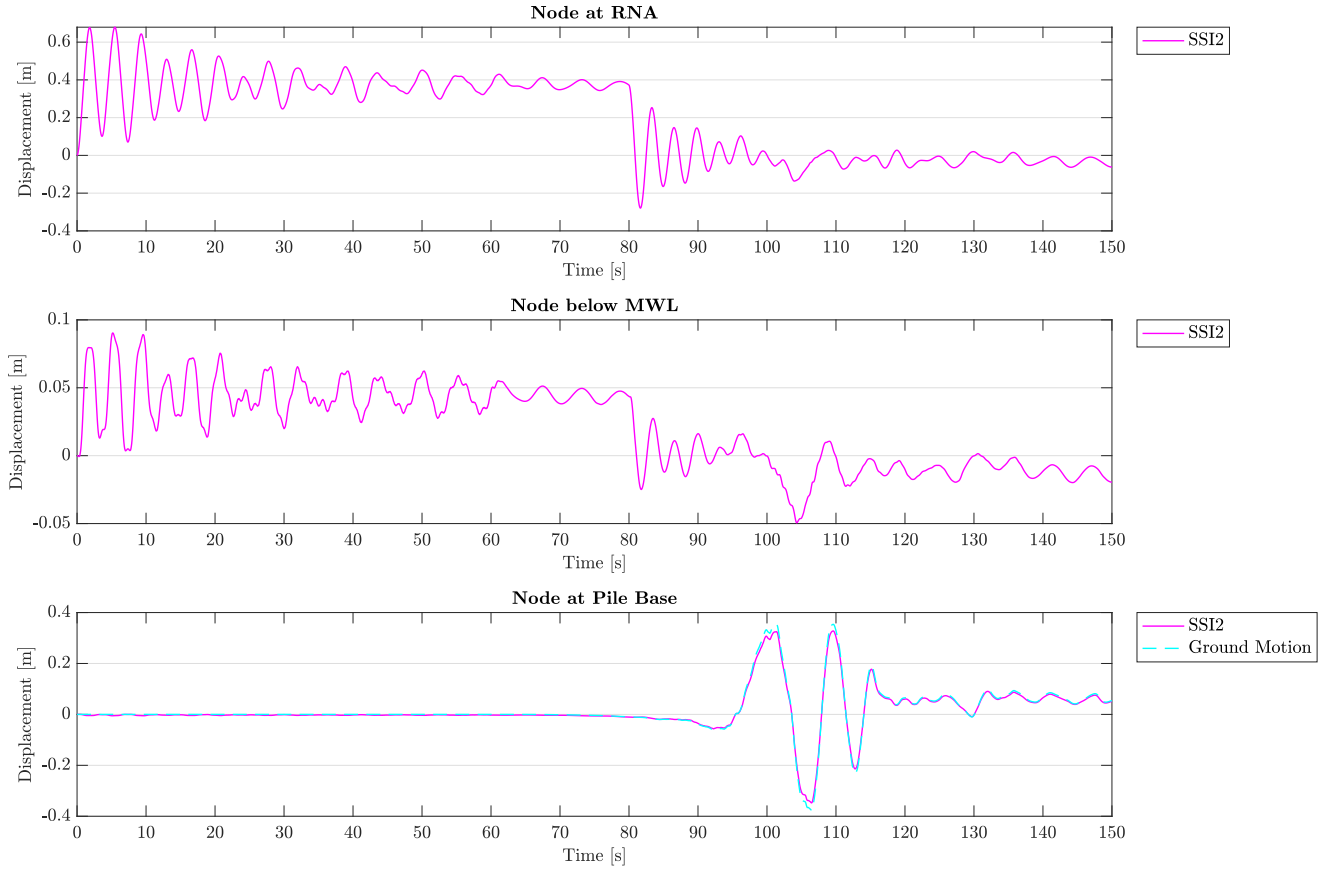

Figure 5.25: *Lateral pile displacement time history for the nonlinear inelastic series hysteretic-viscous damping soil-structure interaction model (SSI2), for co-directional loading by wind, waves and the recorded earthquake, under shutdown conditions (DLC 2-S). Time history depicted for the RNA node, the node directly below maximum water level, and the node at the pile base below mudline. As a reference, the ground motion is shown versus the pile displacement below mudline.*

5.4.2. Natural Frequency Progression

Operational Mode

The Nonlinear Elastic Soil-Structure Interaction Model Figure 5.26 shows that the decreasing soil stiffness due to the large ground motion by the earthquake, causes the first natural frequency of the system to reduce to almost zero for SSI1: the lower bound of the natural frequency becomes as low as 0.036 Hz. The system is growing more dynamically unstable by the seismic action.

In addition, some of the first natural frequencies over time of the system enter the 1P rotor frequency zone; the structure risks excessive cyclic damage when operating in this frequency range by resonance with the rotation of the rotor. The structure also risks resonance with the wave loads, when the natural frequency reduces to 0.176 Hz (or $1/T_p$).

Figure 5.28 shows the correlation between the natural frequency behaviour, soil spring stiffness, pile base displacement, wave loads and ground motion over time. It clearly shows that the first two dips in soil stiffness and consequently natural frequency are due to the ground motion (between $t = 85 - 105$ s). After that, the wave loads start to increase exponentially over a mere 0.005 s time step. As they grow from 50 kN under NSS conditions (see Fig. 5.7) to a staggering 10,000 kN, the pile motion becomes dominated by the wave forces. This can be seen in the pile displacement history from $t > 105$ s. By the sudden peaks and drops in displacement of the pile base, the soil stiffness and natural frequency follow a very erratic trend as well. Only when the pile displacement crosses zero displacement does the soil stiffness and natural frequency restore.

Figure 5.28 visualizes the influence of the wave loads, and their dominance in the structural response in Figure 5.21 following the earthquake ground motion ($t > 120$ s).

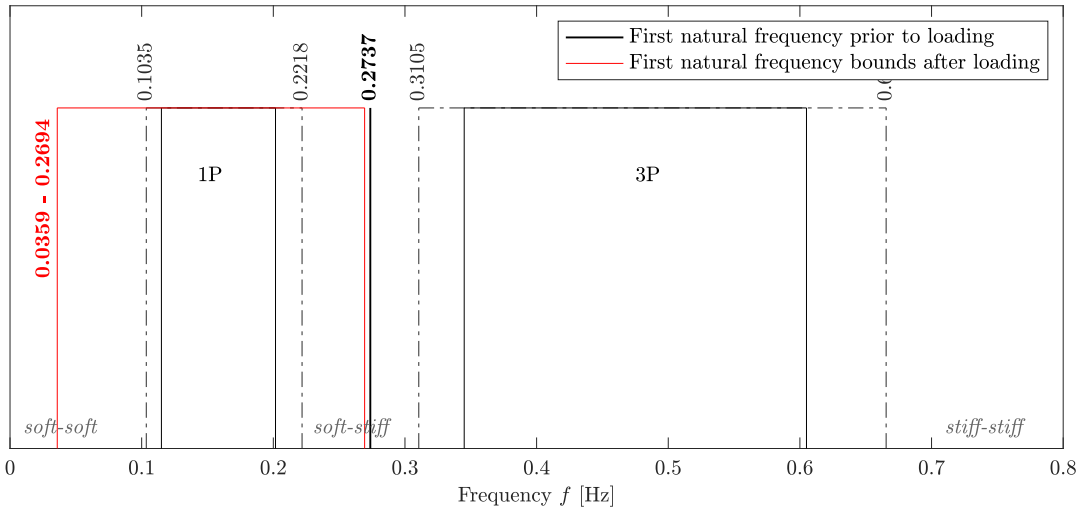

Figure 5.26: *The first natural frequency maximum-minimum range of the soil-structure system for the recorded earthquake, with the nonlinear elastic soil-structure interaction model under operational conditions.*

The Nonlinear Series Hysteretic-Viscous Damping Soil-Structure Interaction Model The predicted amplitude responses for the SSI2 model were lower than for SSI1 (Fig. 5.20). As a result, the soil springs are not forced to their ultimate capacity in almost all layers of the soil column as for SSI1, although the soil is severely weakened by the ground motion too. Consequently, the lowermost first natural frequency in the time history is higher than for SSI1, and is therefore more dynamically stable, albeit by a thread; the lowermost bound is 0.078 Hz.

Just as for SSI1, this wide range of frequency progression puts the structure at risk of suffering from substantial damage by resonance with the 1P rotor frequency and wave frequency.

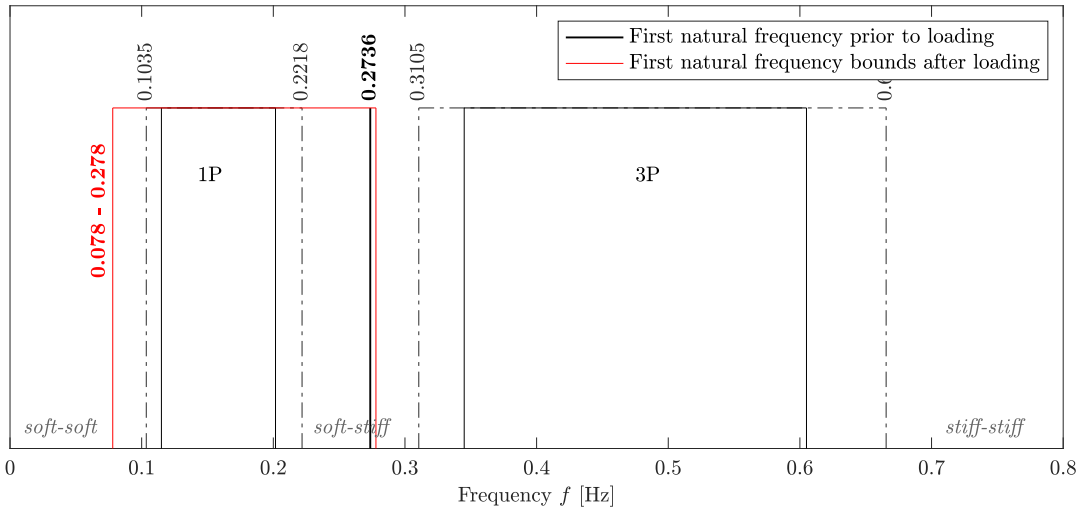

Figure 5.27: *The first natural frequency maximum-minimum range of the soil-structure system for the recorded earthquake, with the nonlinear inelastic series hysteretic-viscous damping soil-structure interaction model under operational conditions.*

Figure 5.28 shows the correlation between frequency, soil stiffness, displacement and load behaviour. From the wave action, it is clear that the viscous dashpot is highly active in two respects. First of all, prior to seismic wave action and hence activation of the radiation damper, the wave action is more erratic by the changes in pile acceleration in every time step (which lead to small differences in the wave inertia loads, as previously explained). Secondly, at $t = 60$ s, the first tremors of the earthquake occur (the P-wave ground motion reaches

the foundation). From this moment, radiation damping by the seismic wave action is active. It is followed immediately by a steady wave loading time history, as now the velocity and acceleration of the pile are highly damped; the added wave inertia loads by the pile motion are minimal.

The pile motion and ground motion follow the same displacement path, as previously explained in Chapter 5.4.1. Consequently, the variation in soil spring stiffness and natural frequency is indirectly caused by the ground motion (and not the wave loads as for SSI1). For the minimal P-wave tremor displacements at $t < 85$ s, the soil stiffness locally increases in the sand and gravel layers due to the definition of their p-y curves in SSI2 (see Fig. 3.17 to 3.21). The secondary S-waves, which cause the larger ground motion from $t > 90\,s$, force the soil springs to exert more resistance to the increasing relative motion of pile and soil, and causes them to reach their ultimate capacity (or zero stiffness) at time where the ground motion is maximal. This happens at times $t = 100$, $t = 105$ and $t = 110$. Only when the deflection crosses zero displacement do the soil springs restore themselves. For every drop in soil spring stiffness, their is an associated drop in natural frequency.

By the definition of the p-y curves of the soil springs, the soil layers still hold some minimal stiffness at large pile-ground displacement; the gradient in the hyperbolic expressions by Boulanger et al. [13] never truly becomes zero. This is in contrast to SSI1, where at large deflections the sand, mudstone and gravel layers' stiffness is zero (see Fig. 3.17, 3.19 and 3.20). This residual stiffness at ultimate loading, besides the smaller amplitude deflections caused by radiation damping, is the reason why the lowermost bound of the natural frequency progression is higher than for SSI1.

The permanent offset in ground level following the earthquake ground motion leaves the soil in a weakened state, as can be seen at the end of the time series for both SSI1 and SSI2 in Figures 5.28 and 5.27. The natural frequency of the system following ground motion is hence lower than it was prior to seismic loading, for both soil-structure models.

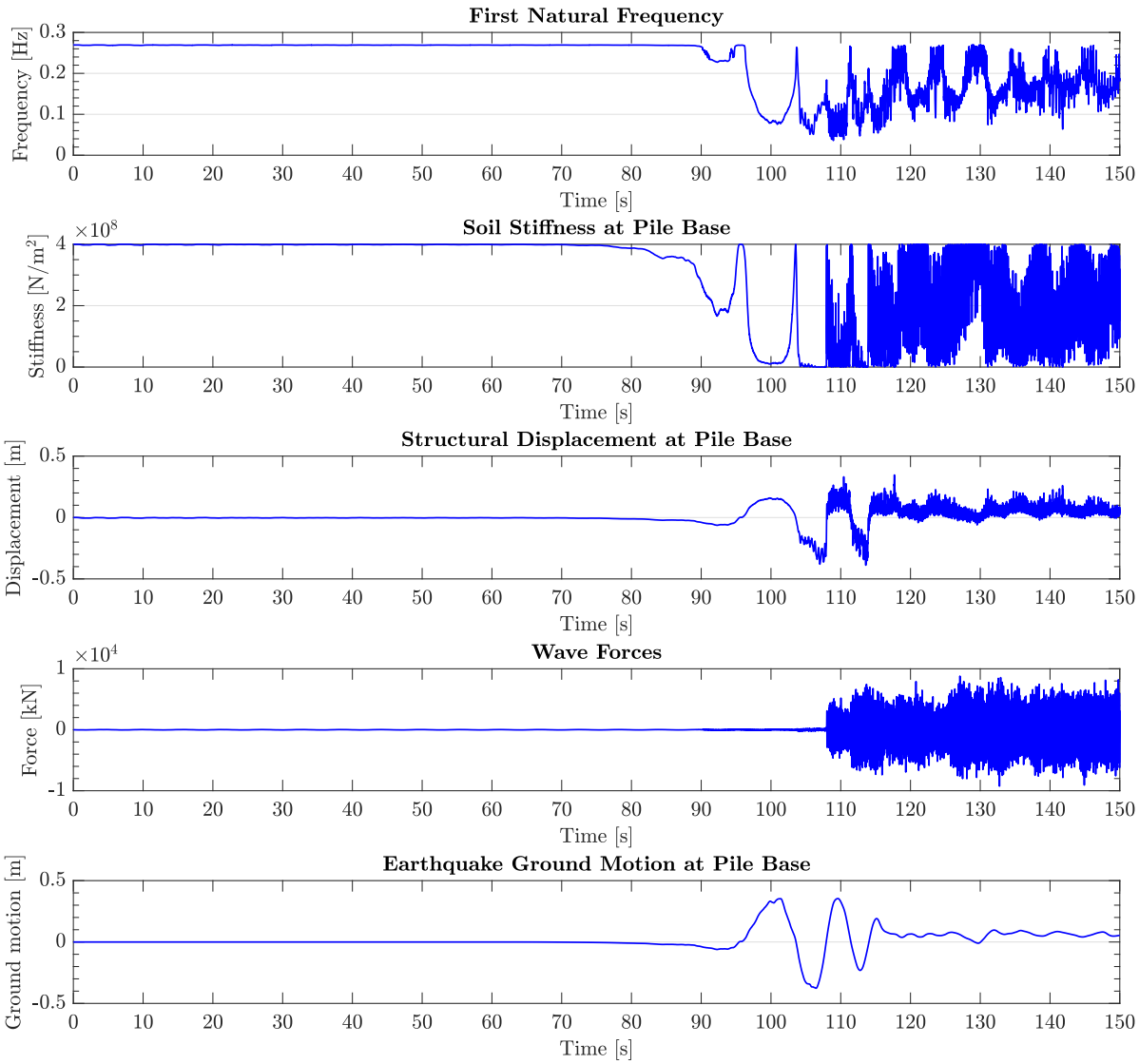

Figure 5.28: *Change in first natural frequency over time, in comparison to the change in soil stiffness, change in pile base deflection and wave forcing, for the nonlinear elastic soil-structure interaction model to wind, waves and the earthquake, while the turbine is operational.*

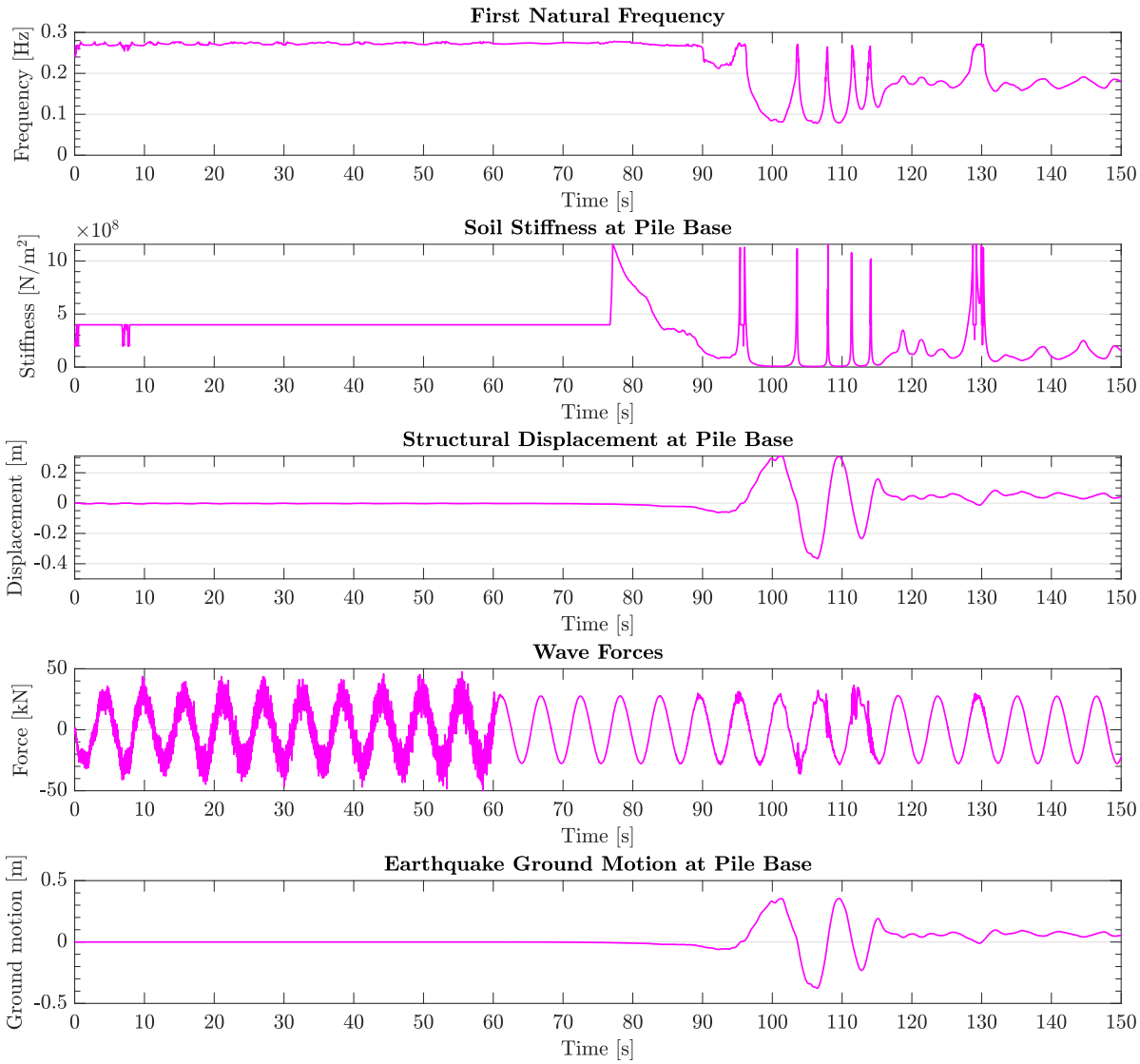

Figure 5.29: *Change in first natural frequency over time, in comparison to the change in soil stiffness, change in pile base deflection and wave forcing, for the nonlinear inelastic series hysteretic-viscous damping soil-structure interaction model to wind, waves and the earthquake, while the turbine is operational.*

Emergency Shutdown Mode

The Nonlinear Elastic Soil-Structure Interaction Model Comparing Figure 5.30 to Figure 5.26, it shows that the even larger pile response after shutdown (Fig. 5.24) leads to a further decrease in natural frequency.

Figure 5.32 shows generally the same correlation between ground motion, wave forces, pile displacement, soil stiffness and natural frequency as during operation of the rotor (Fig. 5.28). The observations regarding SSI1 response behaviour for operational or shutdown conditions are thus similar.

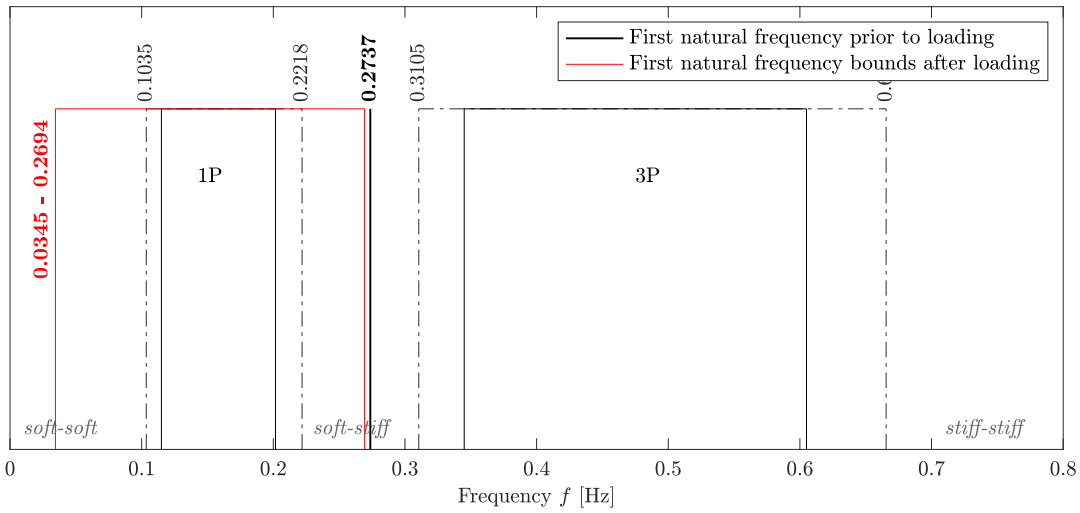

Figure 5.30: *The first natural frequency maximum-minimum range of the soil-structure system for the recorded earthquake, with the nonlinear elastic soil-structure interaction model under shutdown conditions.*

The Nonlinear Series Hysteretic-Viscous Damping Soil-Structure Interaction Model The lowermost bound of the natural frequency progression of the soil-structure system in Figure 5.31 indicates that the pile deflection below mudline is minimally larger following the emergency stop of the turbine. This is confirmed by the time history plots of the pile base motion; the pile base deflects to 0.241 m at maximum during operation (Fig. 5.29), and 0.245 m at maximum after shutdown (Fig. 5.33).

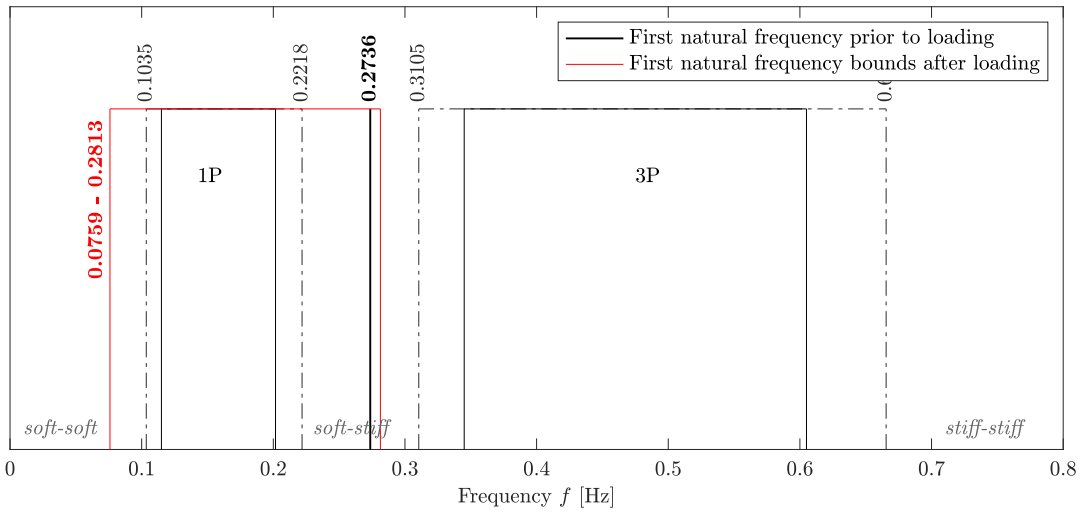

Figure 5.31: *The first natural frequency maximum-minimum range of the soil-structure system for the recorded earthquake, with the nonlinear inelastic series hysteretic-viscous damping soil-structure interaction model under shutdown conditions.*

Figure 5.33 overall shows the same correlation between response behaviour, ground motion, external forces, soil response and natural frequency as in Figure 5.29; the observations are similar.

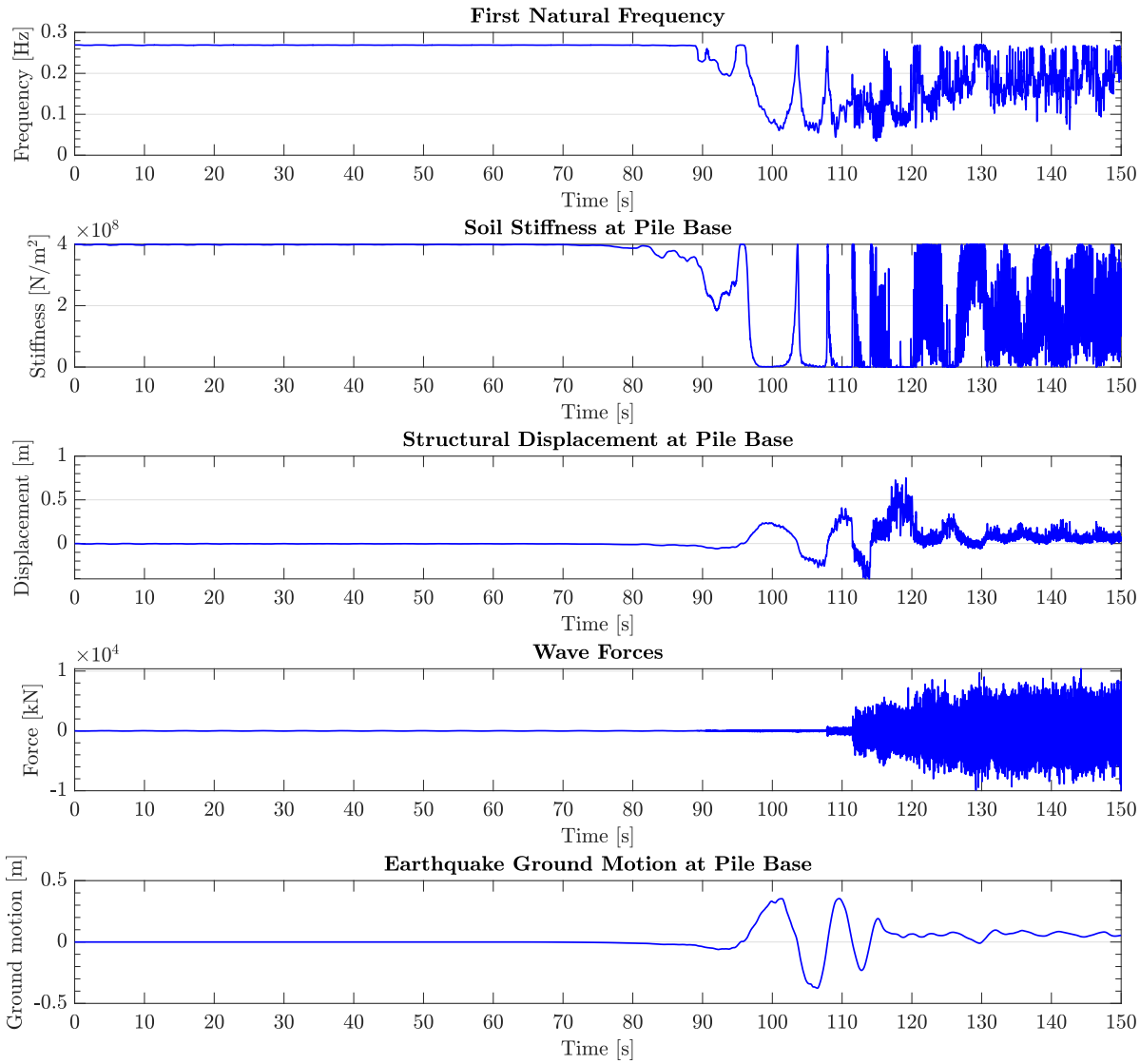

Figure 5.32: *Change in first natural frequency over time, in comparison to the change in soil stiffness, change in pile base deflection and wave forcing, for the nonlinear elastic soil-structure interaction model to wind, waves and the earthquake, after the turbine performed an emergency break.*

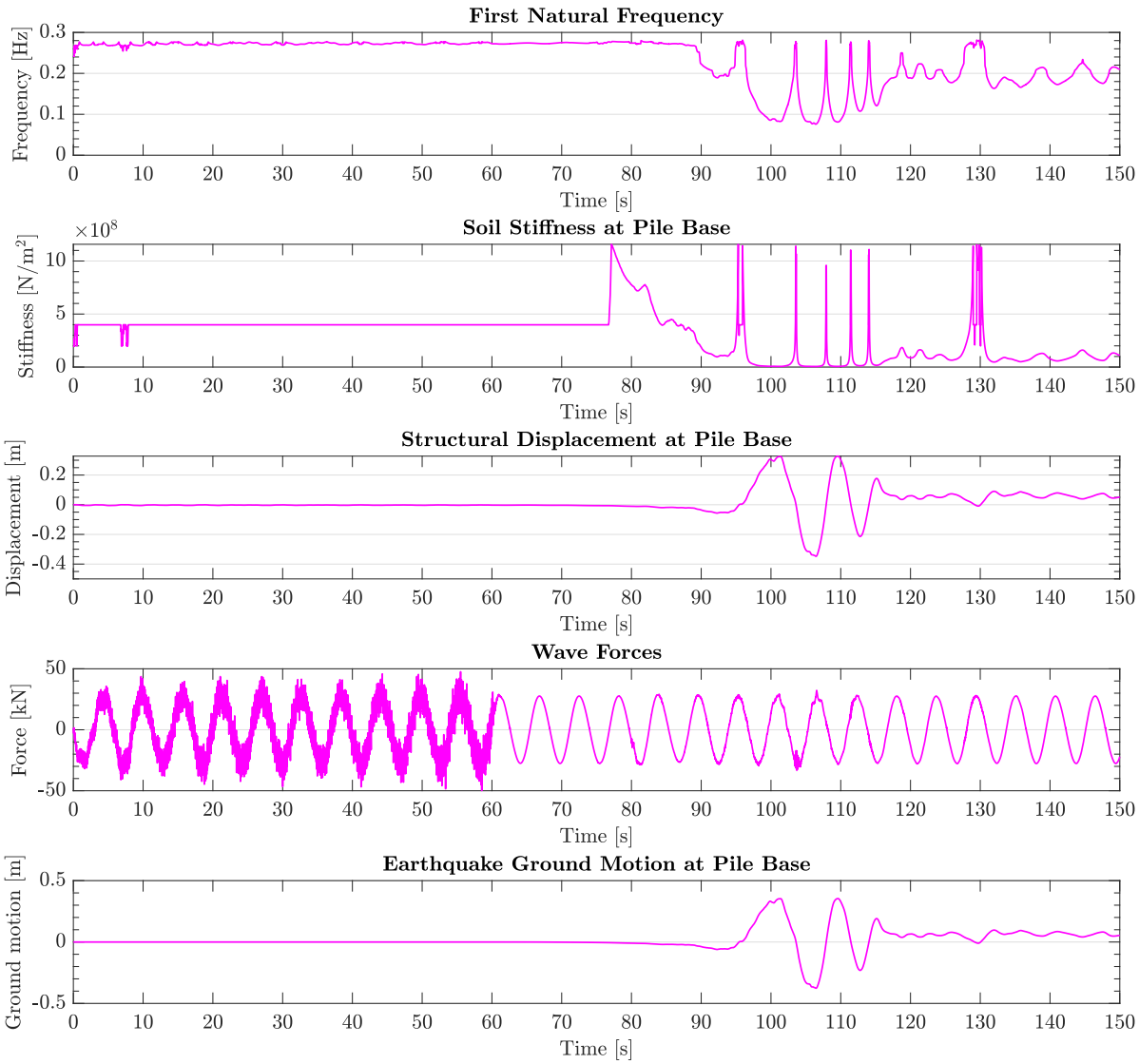

Figure 5.33: *Change in first natural frequency over time, in comparison to the change in soil stiffness, change in pile base deflection and wave forcing, for the nonlinear inelastic series hysteretic-viscous damping soil-structure interaction model to wind, waves and the earthquake, after the turbine performed an emergency break.*

5.4.3. Structural Tilt Behaviour

Operational Mode

Figure 5.34 shows the largest deflected state of the offshore wind support structure in Fig. 5.34a and 5.34c, and the associated tilt angle in Fig. 5.34b and 5.34d.

The figures clearly show that the motion predicted by the nonlinear elastic model does not comply with the SLS requirements to keep the tilt of the turbine below 0.5°. The response of the nonlinear inelastic model does stay within the tilt limit.

The Nonlinear Elastic Soil-Structure Interaction Model For the nonlinear elastic SSI1 model, the largest deflection of the system is reached during earthquake ground motion. That is why the new balance reference lays at approximately +0.38 m, which is the ground motion displacement at the time of the largest deflected state. I.e., the entire structure system is moved by the lateral movement of the soil.

Additionally, it explains the somewhat unexpected pile deformation at this ultimate deflection state. It does not seem to bend as rigid beam anymore. This could be explained from the minimal soil stiffness, and resulting dynamic instability of the system at PGD; as the soil stiffness matrix becomes minimal, the compressive action by the weight of the RNA and the cylindrical structure (summarized in the geometric stiffness matrix) creates an almost negative system stiffness (reflected in the near zero natural frequency in Fig. 5.27). Below mudline, the structure starts to bend in multiple directions due to the instability by absent soil stiffness.

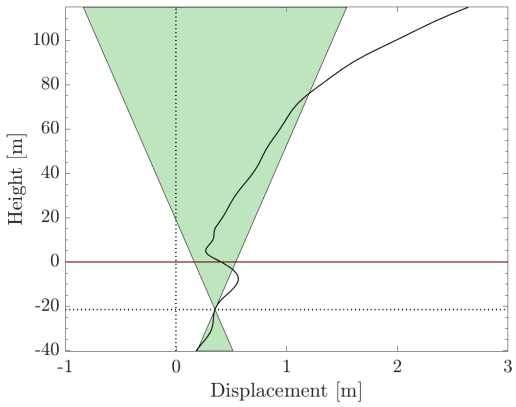

(a) *Ultimate tilt displacement versus limit - SSI1.*

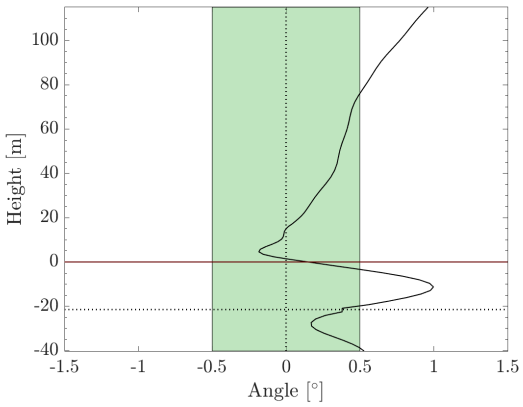

(b) *Ultimate tilt angle versus limit - SSI1.*

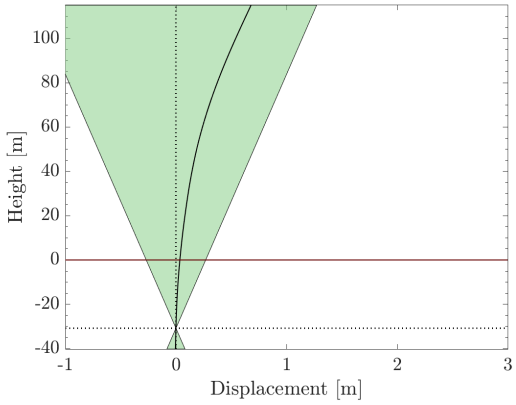

(c) *Ultimate tilt displacement versus limit - SSI2.*

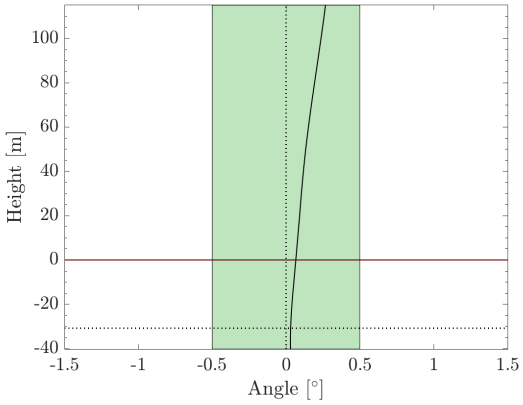

(d) *Ultimate tilt angle versus limit - SSI2.*

Figure 5.34: *Tilt limit check for the nonlinear elastic soil-structure interaction model (SSI1, 5.34a and 5.34b) and the nonlinear inelastic series hysteretic-viscous damping model (SSI2, 5.34c and 5.34d) under wind, wave and earthquake loads, when the turbine is in normal operation mode.*

The Nonlinear Series Hysteretic-Viscous Damping Soil-Structure Interaction Model For the nonlinear inelastic SSI2 model, the maximum deflected state occurs during startup of the rotor, and is hence identical to the tilt behaviour for the NSS simulation (see Fig. 5.14). By the radiation damping effect and absence of excessive wave forces as in SSI1, the amplitude of the displacement during earthquake ground motion is not larger than the motions during NSS. That is why (1) the balance point is still at zero, and not at a new soil position due to the earthquake ground motion, and (2) the tilt is within SLS limits.

Emergency Shutdown Mode

Figure 5.35 indicates that a shutdown strategy is not beneficial to reduce the response amplitude in case the soil-structure is modeled as a nonlinear elastic interaction. The tilt of SSI1 is completely out of bounds.

The Nonlinear Elastic Soil-Structure Interaction Model The response of the nonlinear elastic model reaches it maximum deflection at $t = 120$ s (see Fig. 5.24). At this time, the ground motion is actually minimal, as can also be seen by the balance point in Figure 5.35a. The large deflection at that time is forced by the wave inertia loads. The soil stiffness is slightly larger than at PGD of the ground, hence the more stable response of the pile compared to Figure 5.34a; all soil layers do still have some stiffness against the lateral pile deflection.

The Nonlinear Series Hysteretic-Viscous Damping Soil-Structure Interaction Model For the nonlinear inelastic model, the shutdown operation has no adversary effect on the response of the structure during earthquake motion. Although the amplitude of the motion is larger by the absence of the rotor aerodynamic damping, the maximum pile deflection is not. This still occurs during startup of the rotor, in the transient response of the system. Hence, the tilt state of the nonlinear inelastic SSI2 system is equal to the situation during operation of the rotor (see Figure 5.34c).

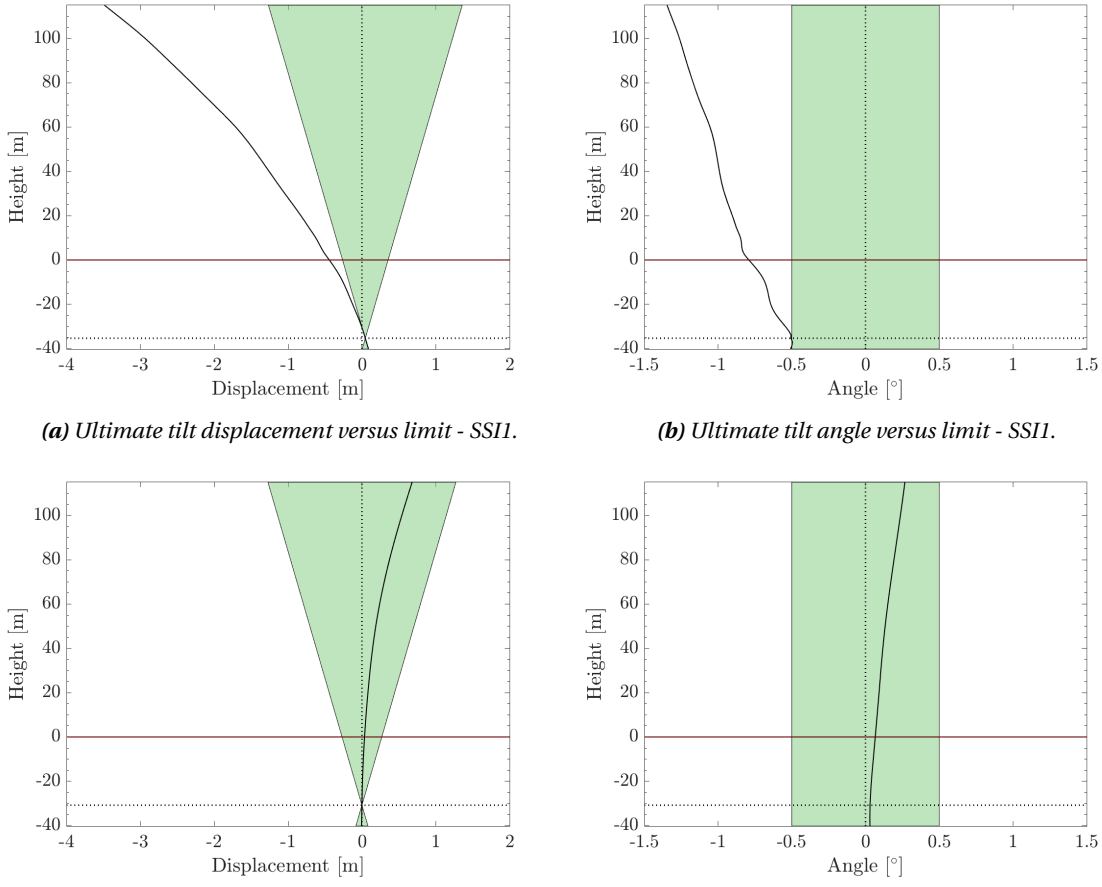

(a) *Ultimate tilt displacement versus limit - SSI1.*

(b) *Ultimate tilt angle versus limit - SSI1.*

(c) *Ultimate tilt displacement versus limit - SSI2.*

(d) *Ultimate tilt angle versus limit - SSI2.*

Figure 5.35: *Tilt limit check for the nonlinear elastic soil-structure interaction model (SSI1, 5.35a and 5.35b) and the nonlinear inelastic series hysteretic-viscous damping model (SSI2, 5.35c and 5.35d) under wind, wave and earthquake loads, after the turbine performed an emergency shutdown.*

5.4.4. Structural Capacity Behaviour

Operational Mode

Figure 5.36 visualizes the structural demand of the structure, for both SSI1 and SSI2. For the linear elastic model (SSI1) the structure clearly fails in yield below the mudline. For the nonlinear inelastic model (SSI2) more of the structural capacity is mobilized compared to DLC-1 (NSS simulation), but it remains within the ULS requirements.

The Nonlinear Elastic Soil-Structure Interaction Model Although the soil resistance to lateral motion by the pile is comparable for both SSI1 and SSI2 during PGD, the structural demand in the former nonlinear elastic model is much higher in Figure 5.36b. The difference in yield stress in the structure between both models starts right below mean sea level, thereby indicating that the excessive inertia wave forces are the cause of the vast capacity demand in SSI1. The structure is not able to meet the yield criterion by the large wave action. The ultimate soil resistance in the sand and gravel layer is mobilized, but is not the driving factor behind the yield failure.

Figure 5.37a shows a comparable difference between SSI1 and SSI2. The monopile is estimated to buckle near the pile base. Starting right below mean sea level, the buckling ratio between both models starts to differ, again hinting at the large influence of the wave loads.

The Nonlinear Series Hysteretic-Viscous Damping Soil-Structure Interaction Model The monopile is able to fulfill the yield criterion in the nonlinear inelastic model with radiation damping. In this model too the ultimate soil resistance is mobilized in the sand and gravel layer, and soil resistance forces in all layers are similar in magnitude. But the pile does not yield below mudline as the nonlinear elastic model does. Hence, the capacity usage in Figure 5.36c supports the conclusion that the inertia wave force creates the large structural demand in SSI1.

The buckling ratio in Figure 5.37b stays well within bounds. The structure is not expected to buckle for the as-recorded earthquake intensity.

Emergency Shutdown Mode

The Nonlinear Elastic Soil-Structure Interaction Model During shutdown, the amplitude of the response in the nonlinear elastic motion becomes larger than in an operational simulation of the response, as a consequence of even larger inertia wave action. As such, the structural demand in SSI1 is higher than during operation, as can be seen in Figure 5.38 versus Figure 5.36. The buckling ratio in Figure 5.39 grows accordingly.

The Nonlinear Series Hysteretic-Viscous Damping Soil-Structure Interaction Model The ultimate response behaviour during shutdown for SSI2 is not so different from the response behaviour during operation, except for some slightly larger deflections below mudline. These slightly larger deflections mobilize a bit more soil spring resistance forces, and as a result the capacity demand during shutdown is minimally larger than during operation in case of earthquake ground motion, as shown in Figure 5.38c and 5.39b.

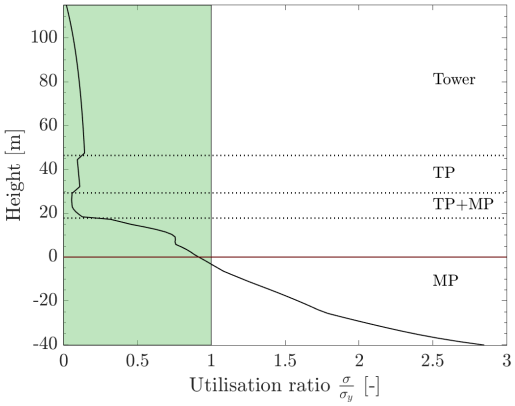

(a) *Yield utilization ratio - SSI1.*

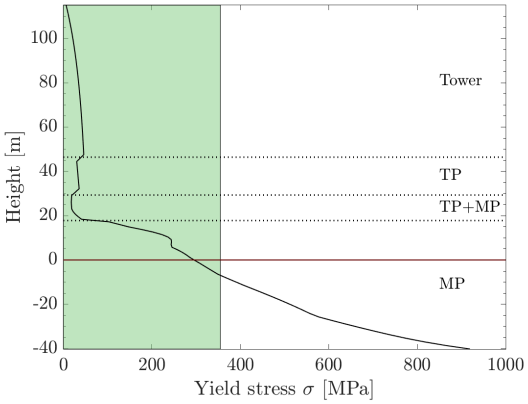

(b) *Yield stress versus material yield strength - SSI1.*

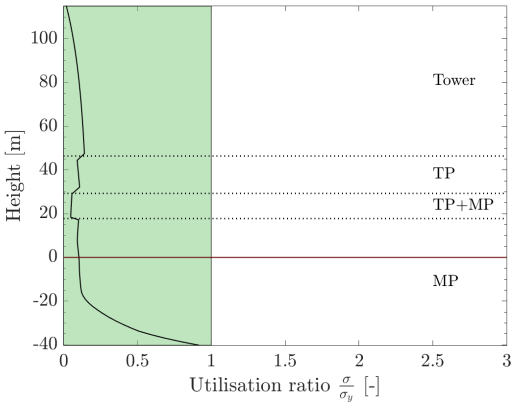

(c) *Yield utilization ratio - SSI2.*

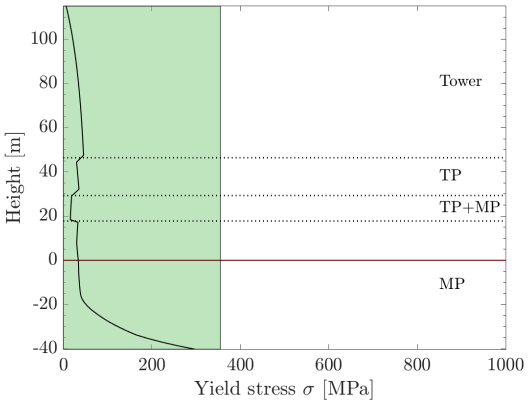

(d) *Yield stress versus material yield strength - SSI2.*

Figure 5.36: *Global yield limit check for the nonlinear elastic soil-structure interaction model (SSI1, 5.36a and 5.36b) and the nonlinear inelastic series hysteretic-viscous damping model (SSI2, 5.36c and 5.36d) under wind, wave and earthquake loads, when the turbine is in normal operation mode.*

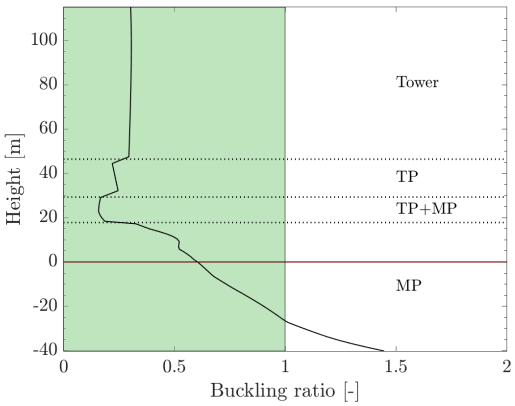

(a) *Buckling ratio versus limit - SSI1.*

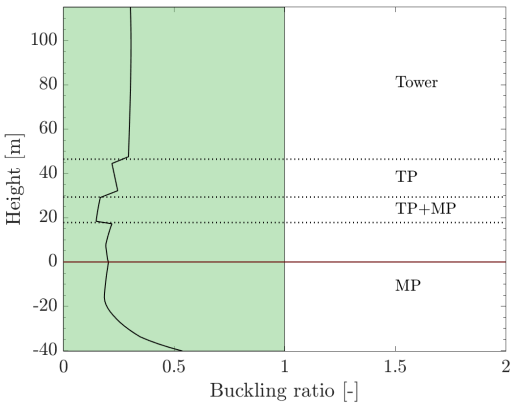

(b) *Buckling ratio versus limit - SSI2.*

Figure 5.37: *Global buckling limit check for the nonlinear elastic soil-structure interaction model (SSI1, 5.37a) and the nonlinear inelastic series hysteretic-viscous damping model (SSI2, 5.37b) under wind, wave and earthquake loads, when the turbine is in normal operation mode.*

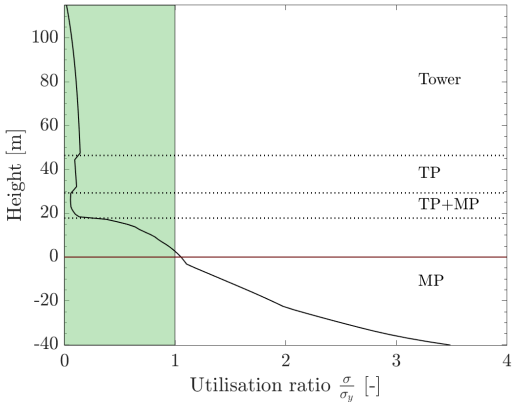

(a) *Yield utilization ratio - SSI1.*

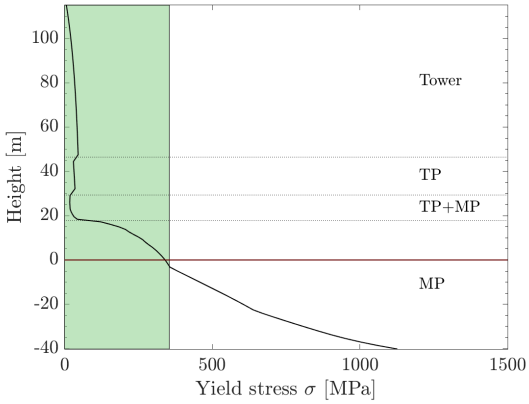

(b) *Yield stress versus material yield strength - SSI1.*

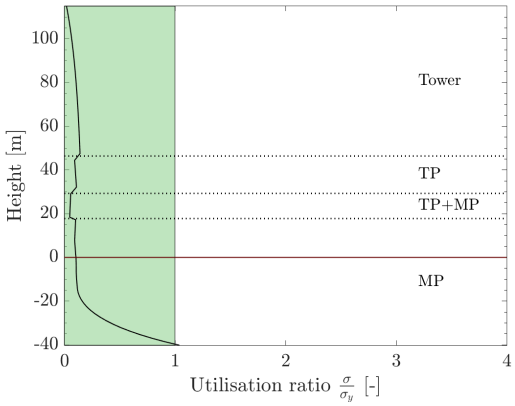

(c) *Yield utilization ratio - SSI2.*

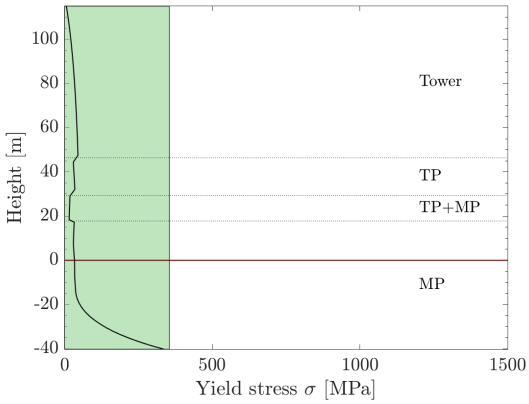

(d) *Yield stress versus material yield strength - SSI2.*

Figure 5.38: *Global yield limit check for the nonlinear elastic soil-structure interaction model (SSI1, 5.38a and 5.38b) and the nonlinear inelastic series hysteretic-viscous damping model (SSI2, 5.38c and 5.38d) under wind, wave and earthquake loads, when the turbine is in emergency shutdown mode.*

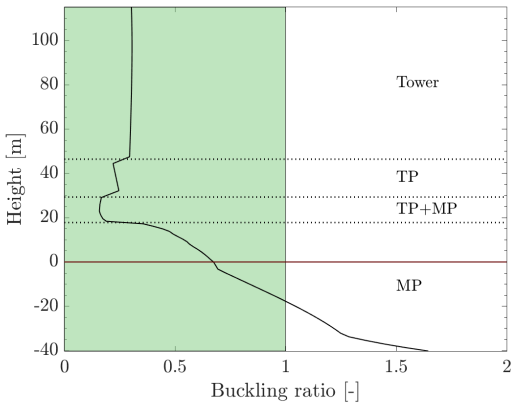

(a) *Buckling ratio versus limit - SSI1.*

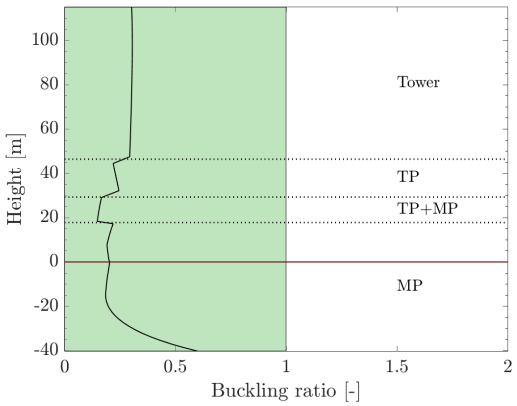

(b) *Buckling ratio versus limit - SSI2.*

Figure 5.39: *Global buckling limit check for the nonlinear elastic soil-structure interaction model (SSI1, 5.39a) and the nonlinear inelastic series hysteretic-viscous damping model (SSI2, 5.39b) under wind, wave and earthquake loads, when the turbine is in emergency shutdown mode.*

5.5. Response Behaviour Under Increasing Seismic Loading - ELE

The amplitude of the recorded earthquake signal was scaled to meet the PGA associated with the Extreme Level Earthquake as defined by ISO19901-2 [49]. The site response analyses results of the acceleration, velocity and displacement at each node in the finite-element model are shown in Chapter 4.5.2. In this chapter, the influence of the increased ground motion on the structural response is investigated.

5.5.1. Pile Displacement Behaviour

The lateral pile displacement response of the structure interacting nonlinearly elastic with the soil is compared to a nonlinear inelastic interaction, this for the Extreme Earthquake Level under both operational and shutdown conditions.

Operational Mode

Just as for the recorded earthquake ground motion, the nonlinear elastic SSI1 model predicts a far larger response than the nonlinear inelastic SSI2 model to the Extreme Level Earthquake, shown in Figure 5.40

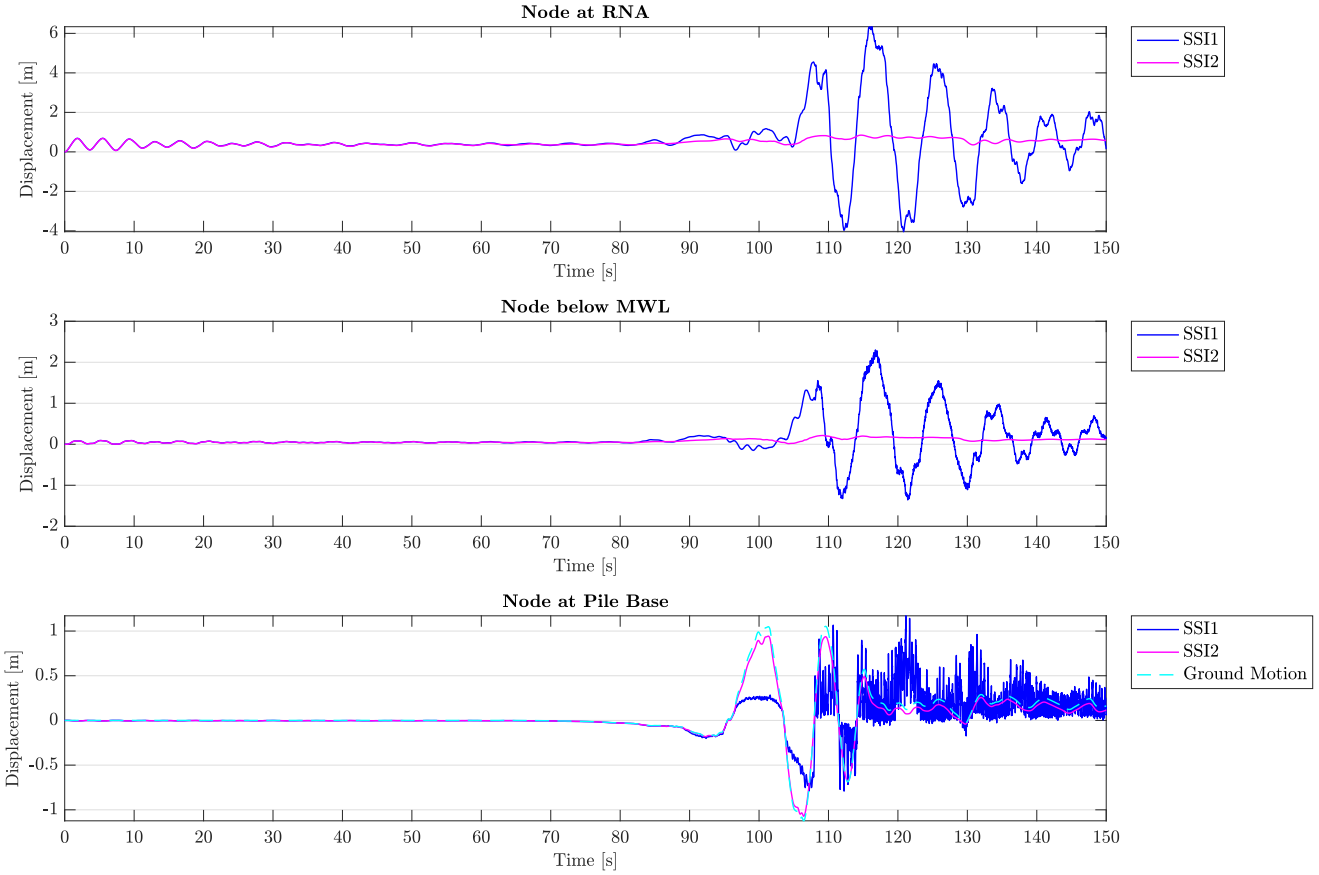

Figure 5.40: *Lateral pile displacement time history for SSI1 and the simplified SSI2 models, for co-directional loading by wind, waves and the Extreme Level Earthquake, under operational conditions (DLC 3-N). Time history depicted for the RNA node, the node directly below maximum water level, and the node at the pile base below mudline. As a reference, the ground motion is shown versus the pile displacement below mudline.*

The Nonlinear Elastic Soil-Structure Interaction Model Figure 5.40 and 5.41 show that the nonlinear elastic soil-structure interaction model predicts an increase in maximum pile deflection to +6.2 m at RNA for the Extreme Level Earthquake with respect to a maximum deflection of +2.7 m at RNA for the as-recorded earthquake motion.

The maximum pile response happens during the extreme earthquake ground motion at $t = 118$ s, just as during the recorded earthquake simulation. But at that time the ground motion due to the earthquake returns to a minimum after PGD, and one would expect the response of the structure to follow a same decrease in motion amplitude. However, just as for load case DLC-2 with the recorded motion, the wave inertia loads are suspected to govern this maximum response.

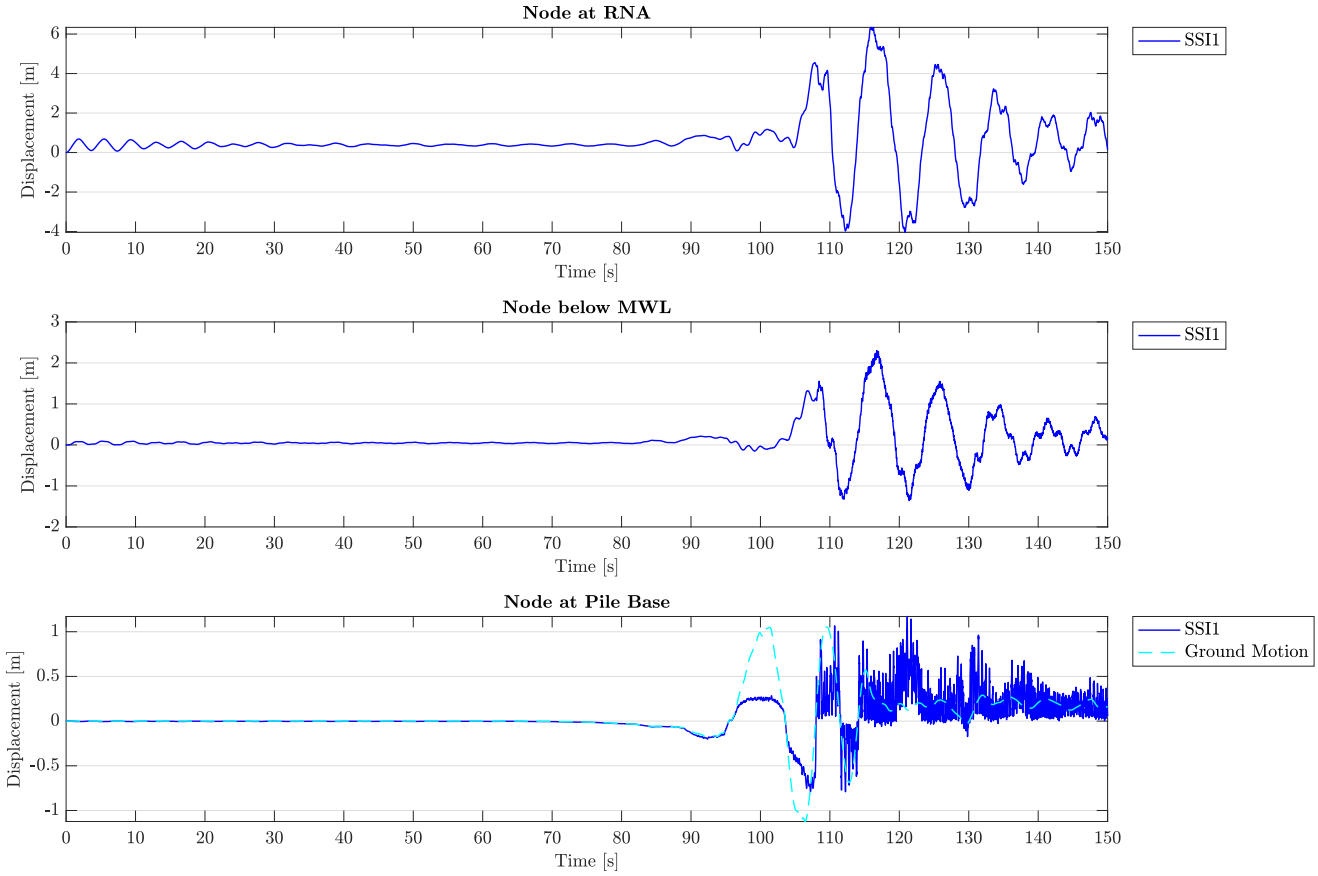

Figure 5.41: *Lateral pile displacement time history for the nonlinear elastic soil-structure interaction model (SSI1), for co-directional loading by wind, waves and the Extreme Level Earthquake, under operational conditions (DLC 3-N). Time history depicted for the RNA node, the node directly below maximum water level, and the node at the pile base below mudline. As a reference, the ground motion is shown versus the pile displacement below mudline.*

The Nonlinear Series Hysteretic-Viscous Damping Soil-Structure Interaction Model The response predicted by the nonlinear inelastic soil-structure model in Figure 5.40 and 5.42 are far below the response predicted by the elastic model; the RNA is maximally displaced by +0.83 m at 115 s. For the recorded earthquake motion in DLC-2 of Chapter 5.4, the maximum displacement was +0.62 m at $t = 5.48$ s.

The time instance of maximum deflection tells that the largest response now occurs during ground motion, more specifically at the last major peak of the motion, and no longer in the transient response. Starting from $t = 90$ s, the pile is forced in more positive direction by the moving soil, thereby shifting the equilibrium position at +0.38 m due to thrust, wind and waves only to 0.55 m following the first ground motion peak. The subsequent soil motion in negative direction (i.e. the dip in the ground motion time history) forces the pile response back to a slightly less positively displaced equilibrium. The trend of the soil motion and pile response is thus similar.

The pile above mudline is however not deflected to the same extend as the pile below mudline. This result may be hinting at the viscous dashpot modeling radiation damping – the only major difference with the elastic model – being overdesigned. Or it may be that the motion is adequately damped by the water body and the operational rotor, although this does not seem to be the case given the results from the elastic model which only differs from the inelastic model by the viscous dashpot.

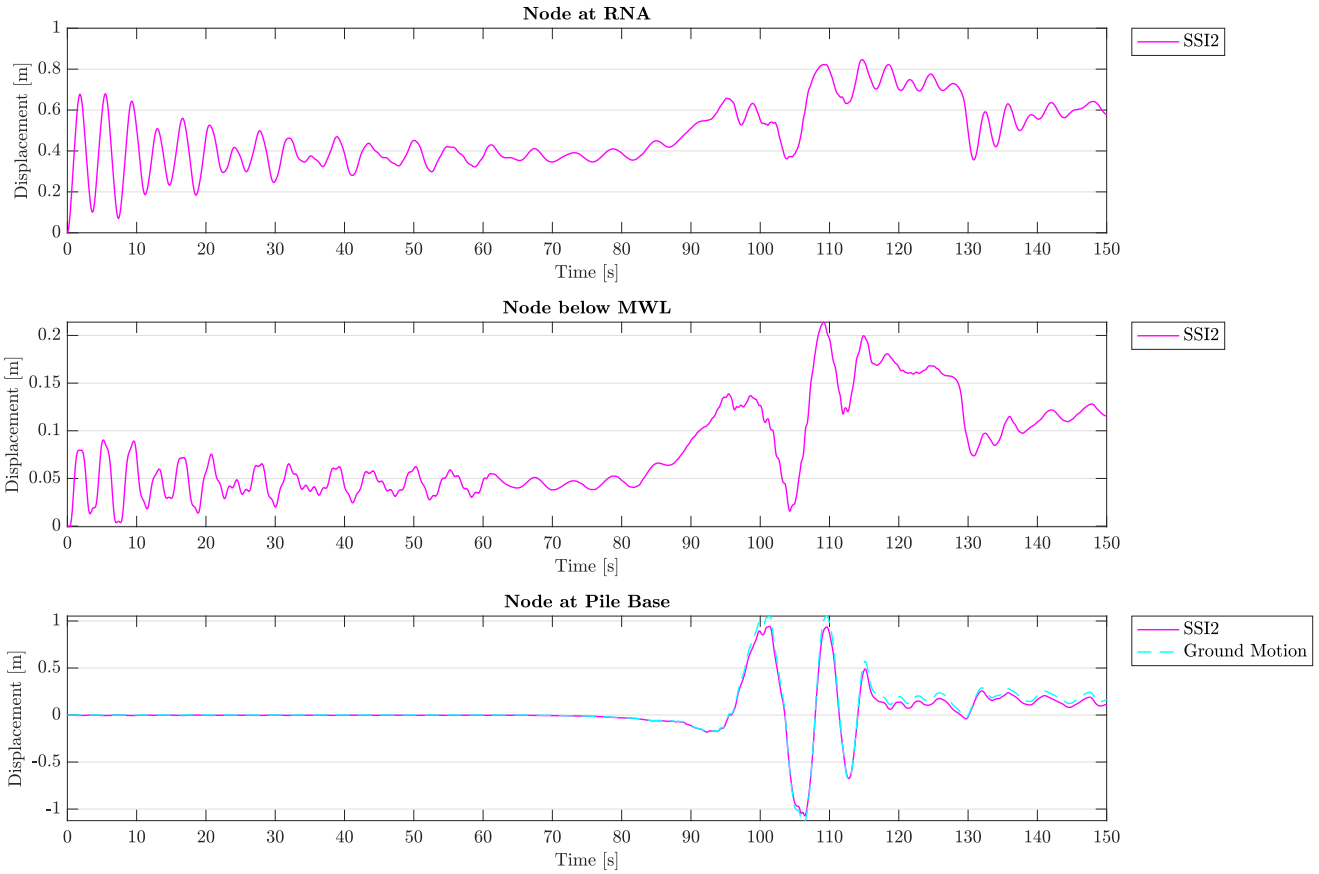

Figure 5.42: *Lateral pile displacement time history for the nonlinear inelastic series hysteretic-viscous damping soil-structure interaction model (SSI2), for co-directional loading by wind, waves and the Extreme Level Earthquake, under operational conditions (DLC 3-N). Time history depicted for the RNA node, the node directly below maximum water level, and the node at the pile base below mudline. As a reference, the ground motion is shown versus the pile displacement below mudline.*

Emergency Shutdown Mode

Figure 5.43 shows the situation for both SSI models in case the turbine performs an emergency stop after perceiving the first ground motion tremors.

The Nonlinear Elastic Soil-Structure Interaction Model From Figure 5.44 it can be seen that the pile response amplitude increases due to shutdown with respect to operational mode of the rotor (Fig. 5.41), and reaches a staggering -7.5 m maximum deflection following the extreme ground motion.

The response of the pile above and below mudline does not seem to follow the soil displacement, but rather follows the wave inertia loads by the pile motion. That is why at times where the ground motion is nearly zero, the pile still deflects at very large amplitudes. The cause of the excessive wave forces is the same as for the recorded earthquake motion, please see Chapter 5.4. As the wave-induced motion is no longer damped by the active rotor, the displacement is more pronounced than for the operational mode of the Extreme Level Earthquake simulation on the nonlinear elastic model.

The Nonlinear Series Hysteretic-Viscous Damping Soil-Structure Interaction Model By nullification of the thrust force, the maximum displacement during ground motion is reduced from 0.83 m to -0.38 m at t = 105 s, as can be seen in Figure 5.4.

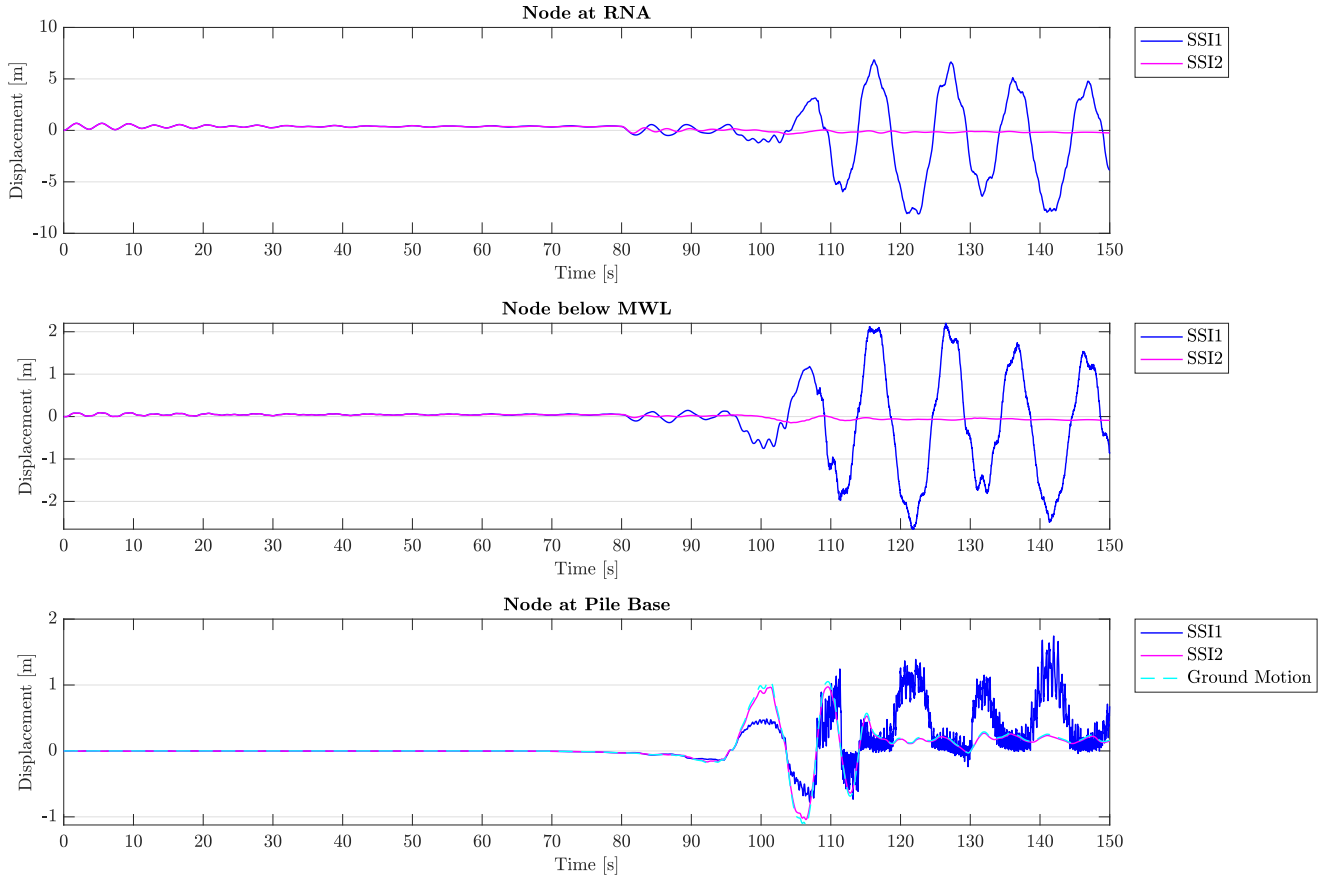

Figure 5.43: *Lateral pile displacement time history for SSI1 and the simplified SSI2 models, for co-directional loading by wind, waves and the Extreme Level Earthquake, under shutdown conditions (DLC 3-S). Time history depicted for the RNA node, the node directly below maximum water level, and the node at the pile base below mudline. As a reference, the ground motion is shown versus the pile displacement below mudline.*

The rotor damping is no longer active. The only sources of damping left are hydro- and aerodynamic drag damping, and radiation damping. Comparing the responses of SSI1 and SSI2 by the Extreme Level Earthquake under shutdown conditions, it is suspected that the radiation damping is responsible for the motion damping of the transient following cancellation of the thrust force at $t = 80$ s. It is also expected that it is this radiation damping that keeps the pile deflections during ground motion and inactivity of the rotor at so much smaller levels than for the nonlinear elastic model, when comparing the responses of Figure 5.45 with Figure 5.44.

The displacement above mudline is smaller than the pile displacement in the soil column, leaving to suspect that the radiation damping may be overestimated as this behaviour is counter-intuitive; for large ground motion, up to 1 m, one would expect for the structure to reach at least equally large deflection states at RNA.

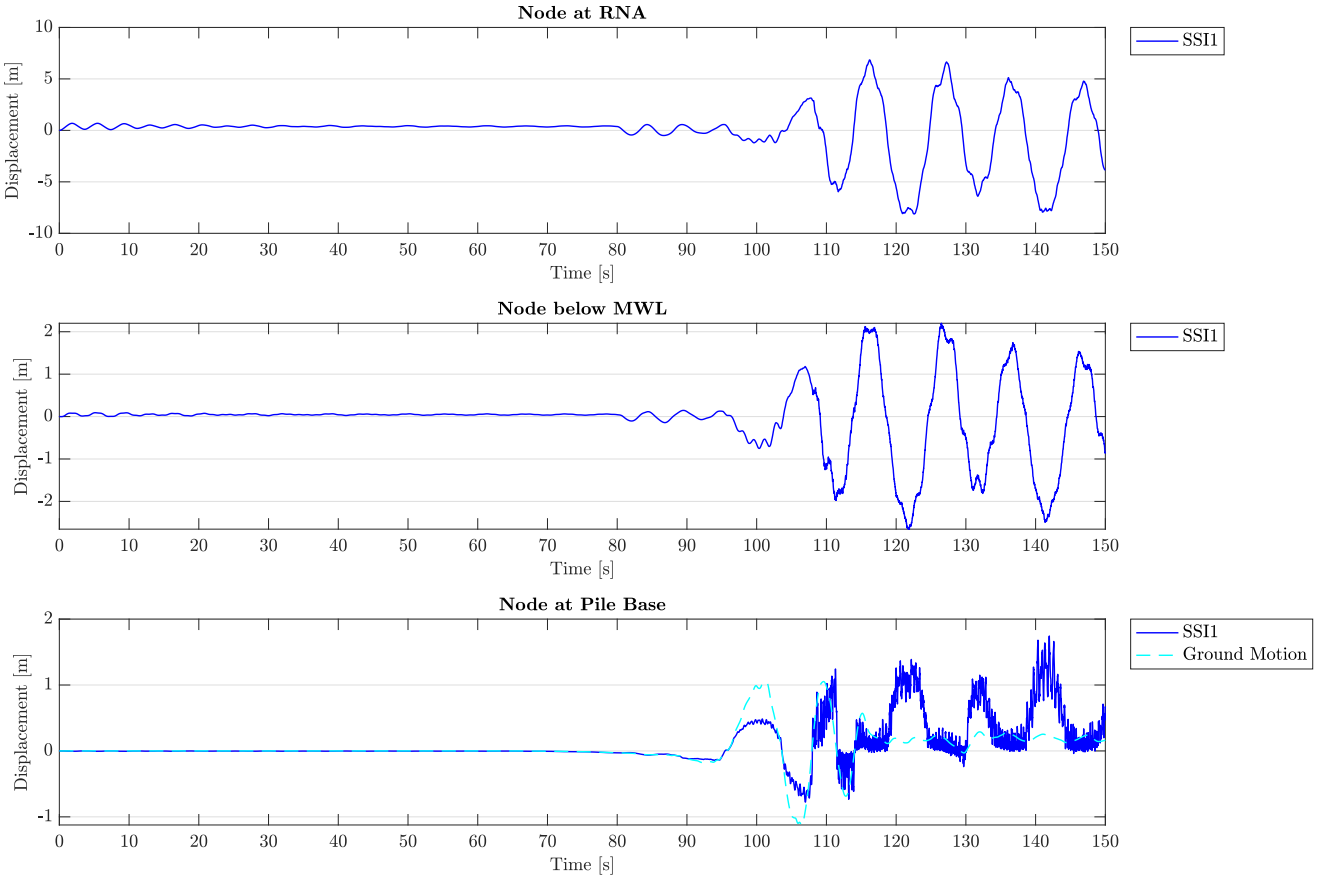

Figure 5.44: *Lateral pile displacement time history for the nonlinear elastic soil-structure interaction model (SSI1), for co-directional loading by wind, waves and the Extreme Level Earthquake, under shutdown conditions (DLC 3-S). Time history depicted for the RNA node, the node directly below maximum water level, and the node at the pile base below mudline. As a reference, the ground motion is shown versus the pile displacement below mudline.*

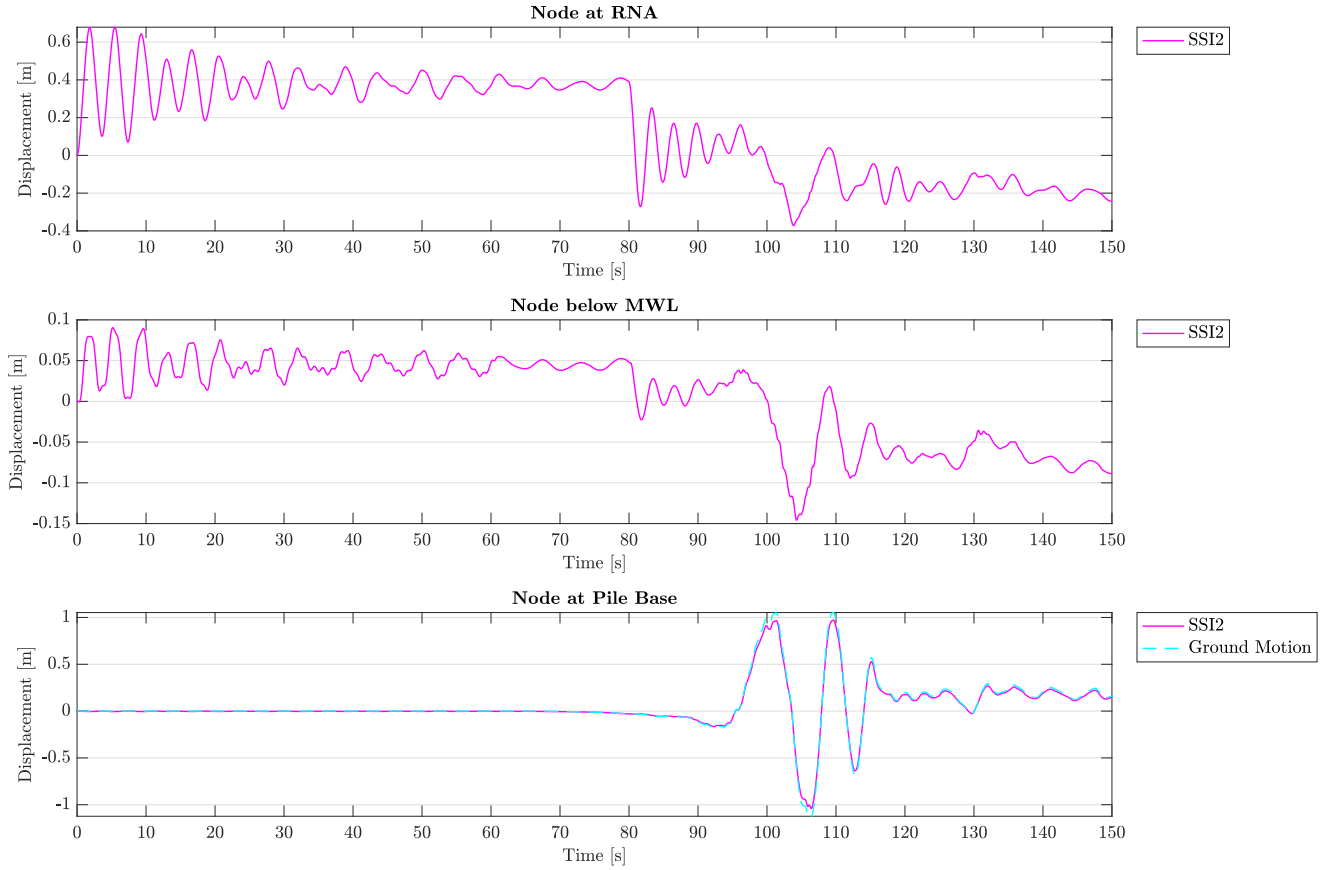

Figure 5.45: *Lateral pile displacement time history for the nonlinear inelastic series hysteretic-viscous damping soil-structure interaction model (SSI2), for co-directional loading by wind, waves and the Extreme Level Earthquake, under shutdown conditions (DLC 3-S). Time history depicted for the RNA node, the node directly below maximum water level, and the node at the pile base below mudline. As a reference, the ground motion is shown versus the pile displacement below mudline.*

5.5.2. Natural Frequency Progression

Although not shown in Figures 5.46 to 5.53, the first eigenvalue of the system becomes negative at certain occasions in the time history. This is an indicator of dynamic instability. It shows that in both soil-structure interaction models the soil springs have reached their ultimate resistance (i.e. zero stiffness) to lateral motion, leaving the compressive action by the geometric stiffness matrix to render the system unstable.

Operational Mode

The Nonlinear Elastic Soil-Structure Interaction Model Figure 5.46 shows that the structure during the Extreme Level Earthquake not only risks resonance by the 1P rotor frequency and the wave loads as for the recorded earthquake level, but also risks to be rendered dynamically unstable due to the relative motion of the soil with respect to the structure. With 1 m ground motion due to the Extreme Level Earthquake, almost all soil springs have zero stiffness left to lateral motion (except for the clay layer, see Fig. 3.18), creating negative indices in the global stiffness matrix where the geometric matrix becomes larger than the structural stiffness matrices. As such, eigenvalues can become negative, and the system unstable.

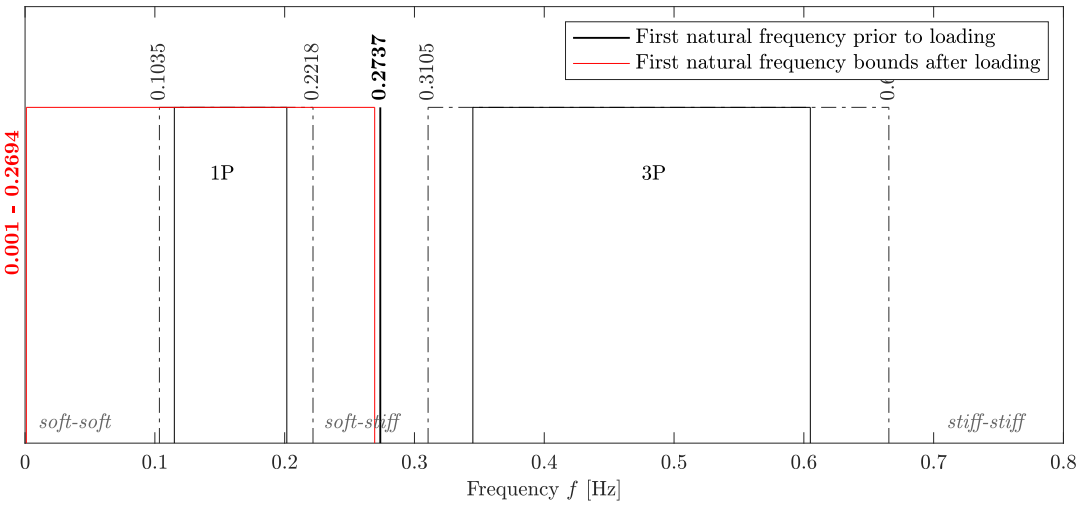

Figure 5.46: *The first natural frequency maximum-minimum range of the soil-structure system for the Extreme Level Earthquake, with the nonlinear elastic soil-structure interaction model under operational conditions.*

In Figure 5.47 the same observation with regard to the influence of the added inertia wave loads by the pile motion can be made as for the recorded earthquake motion. The large ground motion gives rise to nonphysically large pile accelerations as there exists no sufficient damping of the acceleration response in the elastic model. The added inertia wave loads consequently increase to equivalent nonphysical measures. For the Extreme Level Earthquake, with ground motions up to 1 m, the wave loads increase from 50 kN before seismic action to a staggering 20,000 kN following ground motion.

Due to this excessive wave forcing following PGD in the time history, the pile displacement later than PGD occurrence is forced by the wave loads. With forces and pile displacements during ELE being larger than for the earthquake recording, the soil stiffness is often reduced to zero and the natural frequency reaches zero or becomes imaginary.

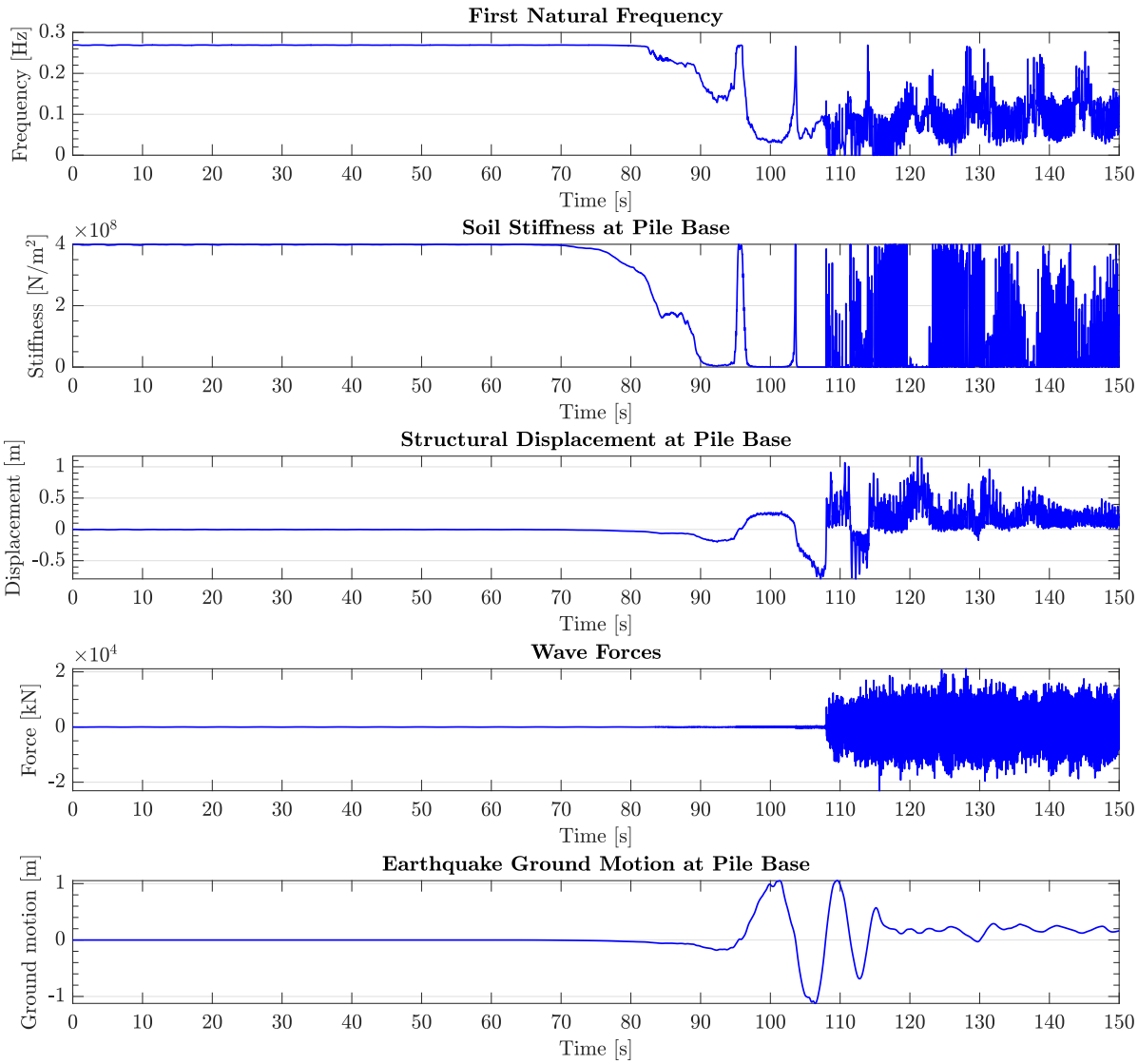

Figure 5.47: *Change in first natural frequency over time, in comparison to the change in soil stiffness, change in pile base deflection and wave forcing, for the nonlinear elastic soil-structure interaction model to wind, waves and the Extreme Level Earthquake, while the turbine is operational.*

The Nonlinear Series Hysteretic-Viscous Damping Soil-Structure Interaction Model Also Figure 5.48 for the nonlinear inelastic soil-structure interaction model shows that the eigenvalues of the first mode(s) may become unstable over time as the soil stiffness is further reduced to zero by increasing ground motion under the Extreme Level Earthquake.

Same as for the recorded earthquake motion, Figure 5.49 shows that the radiation damper must be providing adequate damping to the acceleration and velocity response of the pile to ground displacement. From the moment radiation damping exists at $t = 60$ s, the added inertia wave load that caused the erratic loading path in the wave load prior to ground motion is minimized.

Only during instances of large displacement gradients in the ground motion, as between $t = 95$ s and $t = 115$ s, does this added hydrodynamic inertia term cause obscurities in the steady wave loading trend; at these points, the acceleration due to the significant change in ground position needs more than one time step to be damped by the viscous dashpot.

Opposite to the recorded earthquake motion response (Fig. 5.29), the soil spring stiffness after the largest ground displacements have passed is still near zero for the sand and gravel layer; this is because the soil remains displaced at 0.1 m after the ground shock, where the p-y curves of the soil layers have (much) smaller gradients than for smaller spring displacements (see Figure 3.2 to 3.14). That is why after the Extreme Level Earthquake the first natural frequency is lower than for the recorded earthquake level, see Figure 5.47 versus 5.28.

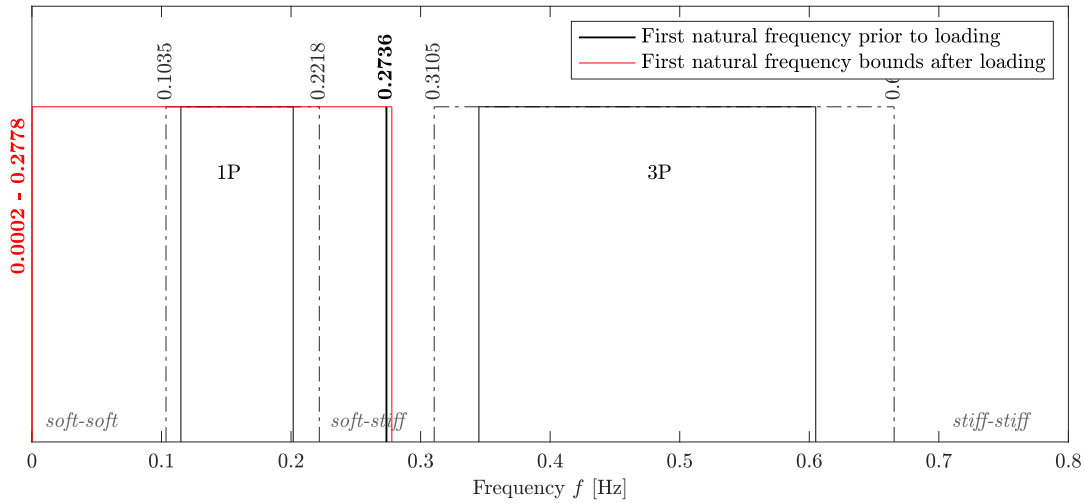

Figure 5.48: *The first natural frequency maximum-minimum range of the soil-structure system for the Extreme Level Earthquake, with the nonlinear inelastic series hysteretic-viscous damping soil-structure interaction model under operational conditions.*

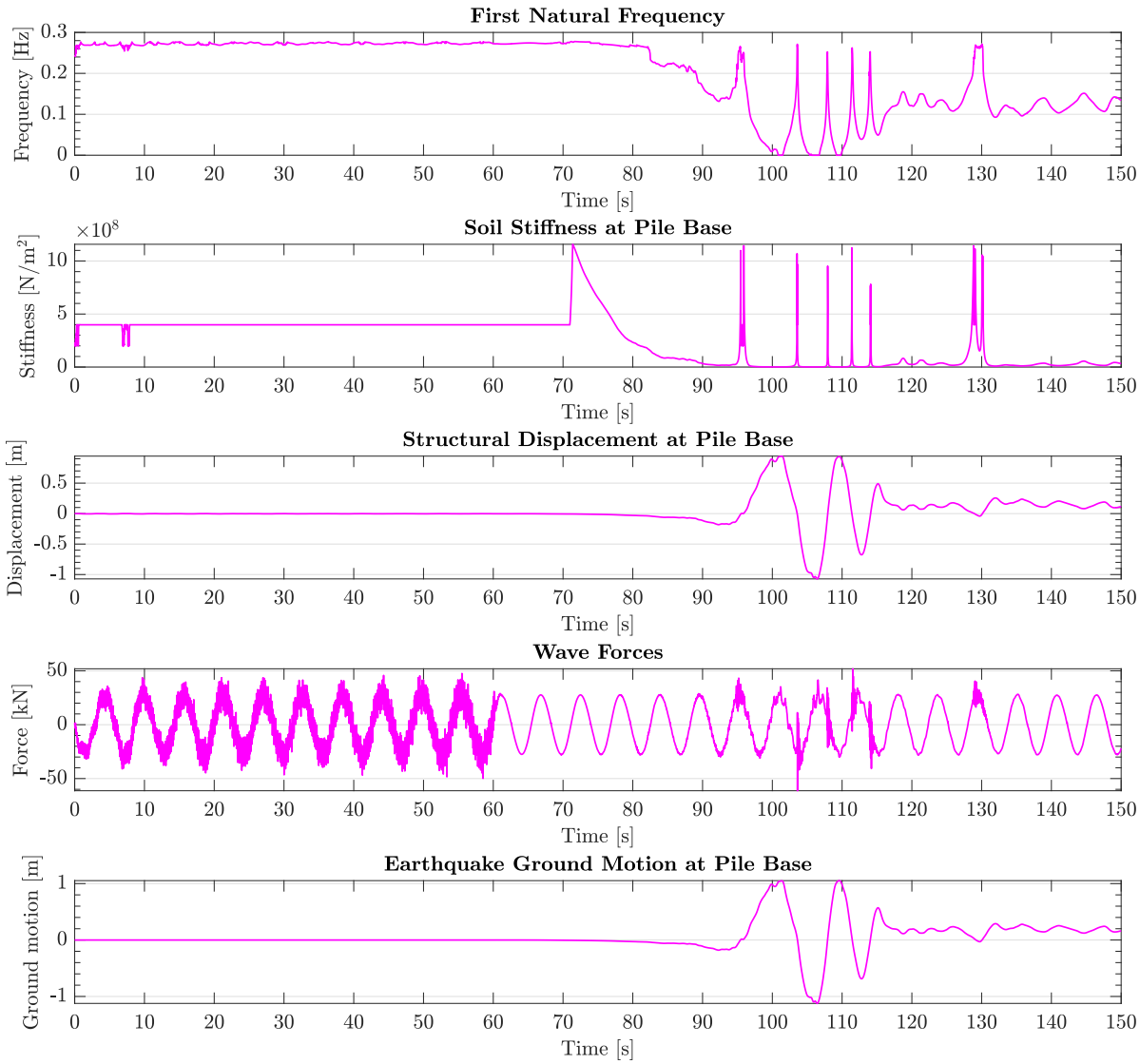

Figure 5.49: *Change in first natural frequency over time, in comparison to the change in soil stiffness, change in pile base deflection and wave forcing, for the nonlinear inelastic series hysteretic-viscous damping soil-structure interaction model to wind, waves and the Extreme Level Earthquake, while the turbine is operational.*

Emergency Shutdown Mode

The Nonlinear Elastic Soil-Structure Interaction Model Figure 5.52 shows that the pile tip displacement is far larger following emergency shutdown of the system than during operation; 1.2 m versus 1.9 m, see Figure 5.47. Consequently, the soil spring stiffness is reduced to zero at more locations in the soil column and over time, which in turn leads to a smaller foundation stiffness matrix of the system, and thus makes the eigenvalues more negative than during operational mode of the turbine (compare with Figure 5.46). The instability of the system is further provoked.

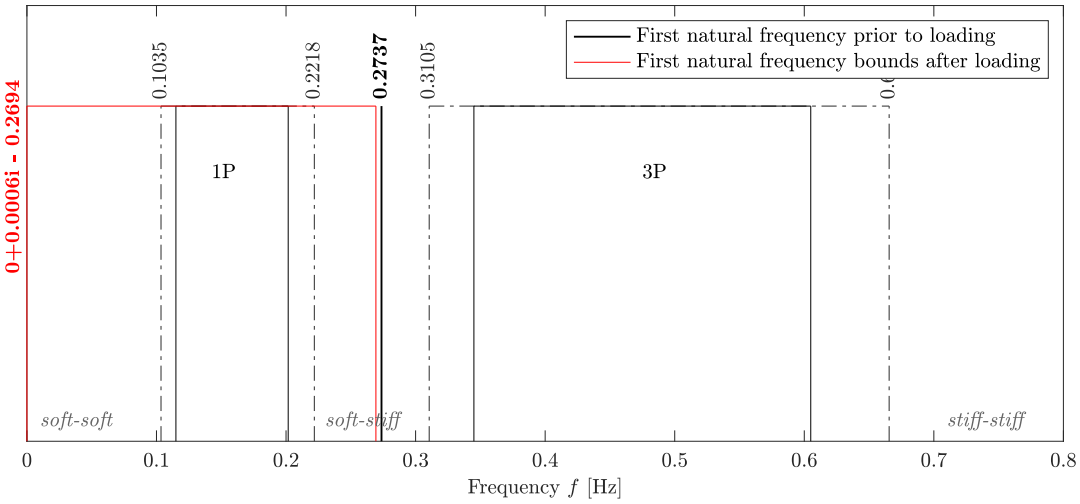

Figure 5.50: *The first natural frequency maximum-minimum range of the soil-structure system for the Extreme Level Earthquake, with the nonlinear elastic soil-structure interaction model under shutdown conditions.*

The Nonlinear Series Hysteretic-Viscous Damping Soil-Structure Interaction Model Figure 5.51 shows nearly identical frequency bounds over the loading history during shutdown as during operation of the rotor under ELE loading. That is because the displacement history of the pile in the soil column in nearly identical for the operational and stopped condition of the rotor, see Figure 5.53 versus Figure 5.49. Under the same ground motion (ELE) and nearly identical pile displacements in the soil, the soil springs are equally mobilized in operational and shutdown conditions, leading to comparable foundation stiffness matrices and consequently similar frequency progression.

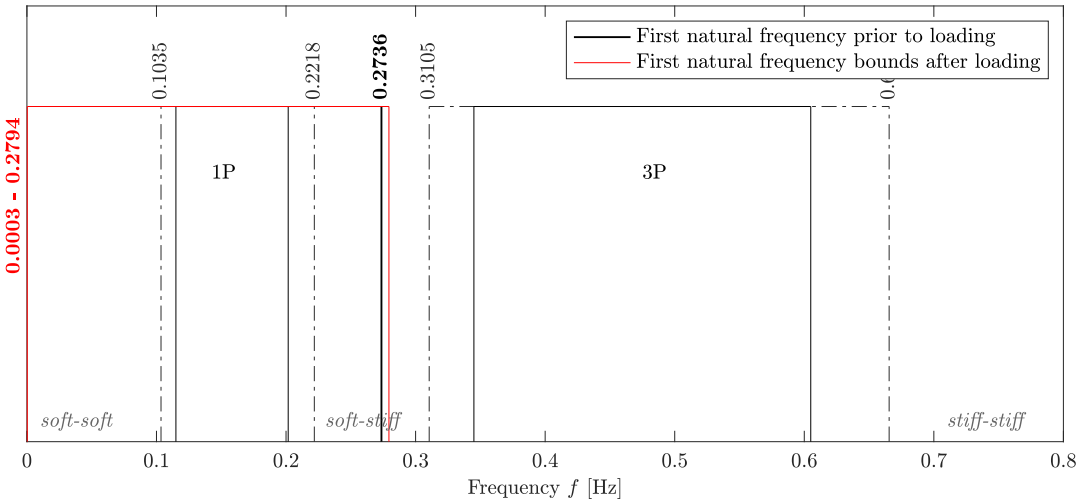

Figure 5.51: *The first natural frequency maximum-minimum range of the soil-structure system for the Extreme Level Earthquake, with the nonlinear inelastic series hysteretic-viscous damping soil-structure interaction model under shutdown conditions.*

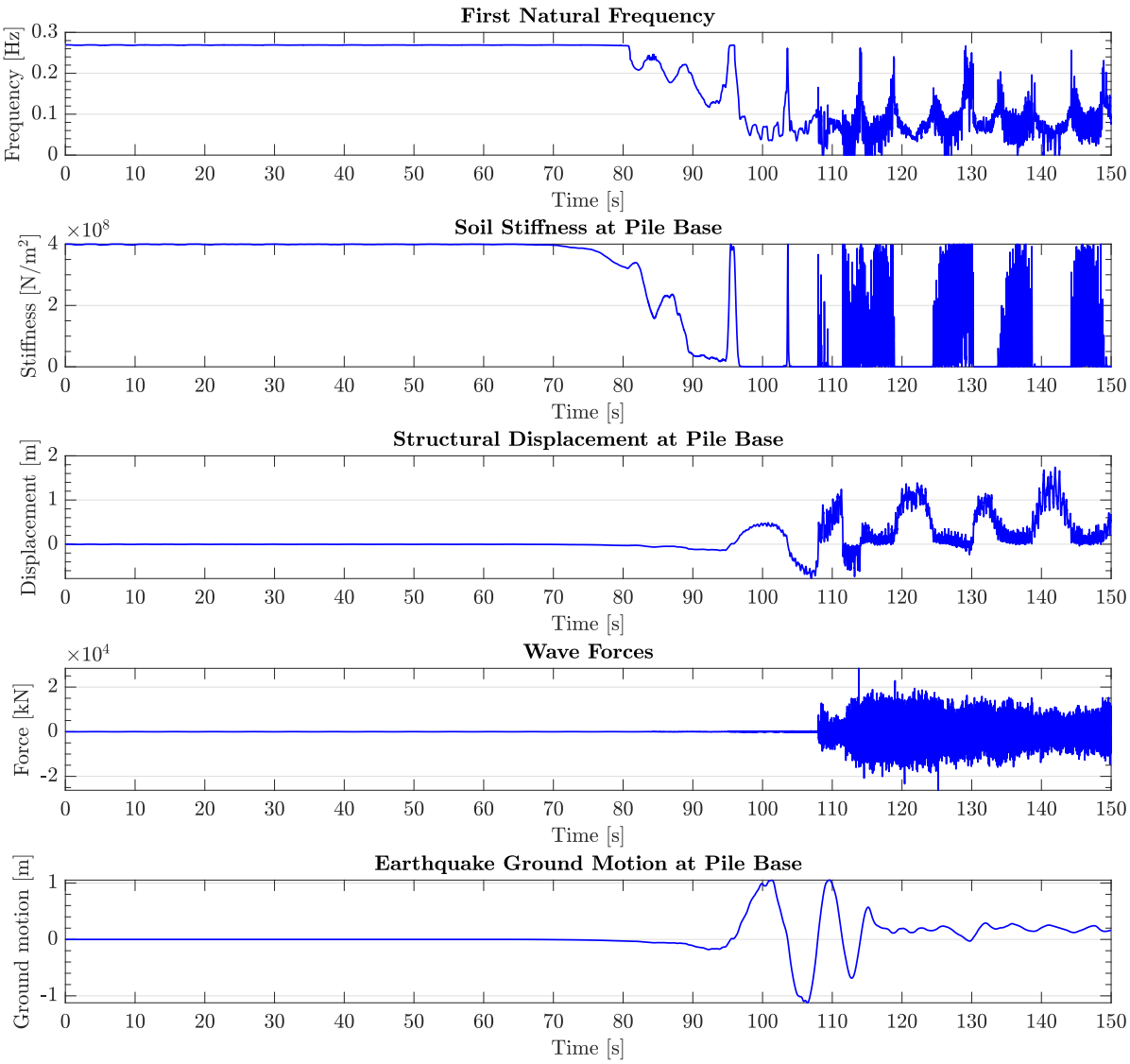

Figure 5.52: *Change in first natural frequency over time, in comparison to the change in soil stiffness, change in pile base deflection and wave forcing, for the nonlinear elastic soil-structure interaction model to wind, waves and the Extreme Level Earthquake, after the turbine performed an emergency break.*

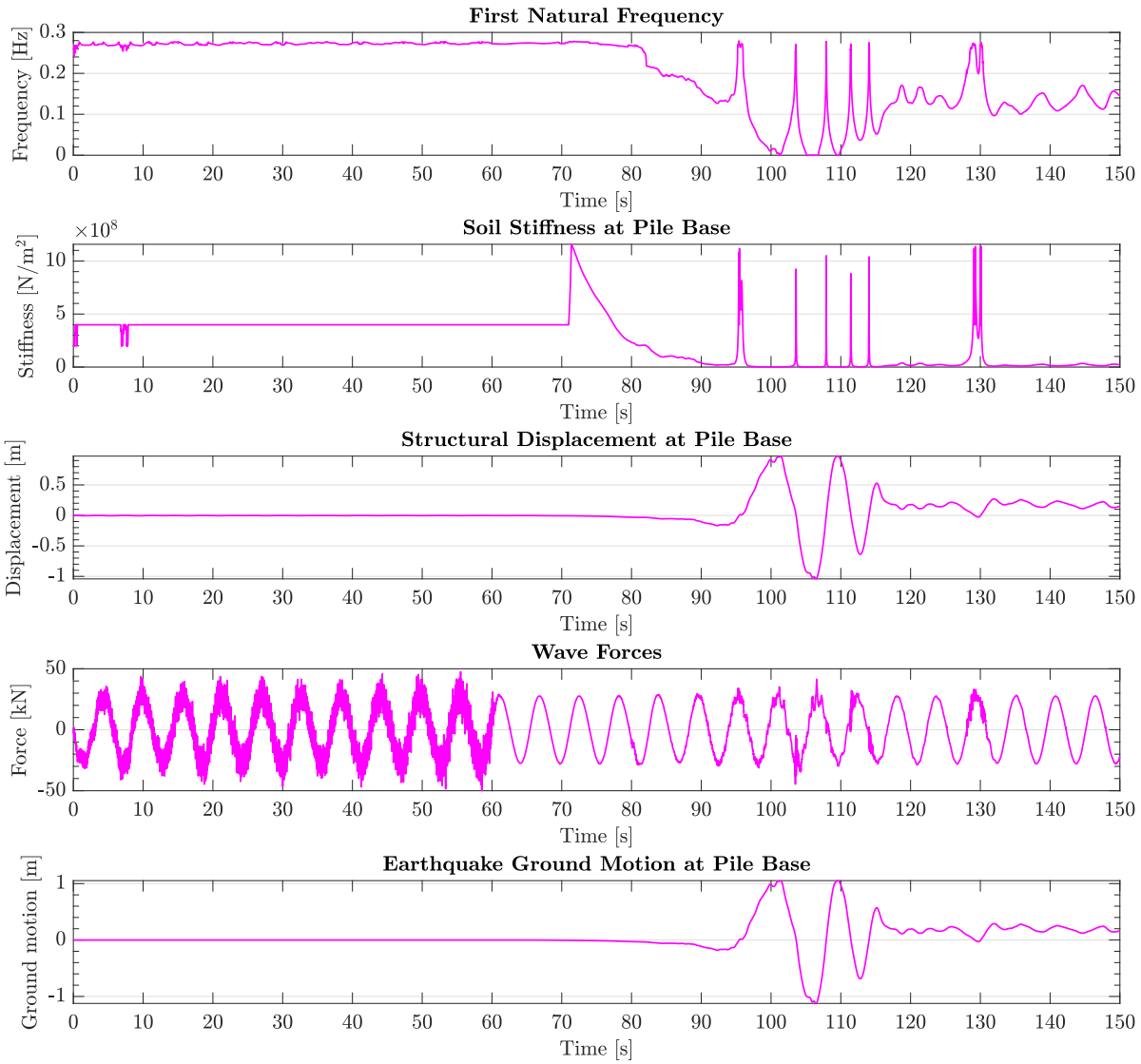

Figure 5.53: *Change in first natural frequency over time, in comparison to the change in soil stiffness, change in pile base deflection and wave forcing, for the nonlinear inelastic series hysteretic-viscous damping soil-structure interaction model to wind, waves and the Extreme Level Earthquake, after the turbine performed an emergency break.*

5.5.3. Structural Tilt Behaviour

Operational Mode

As previously shown in Chapter 5.5.2, the system becomes unstable as the soil spring stiffnesses are reduced to (nearly) zero by the extreme ground motion and relative pile deflection. Therefore, in Figure 5.54, the tilt of the pile in both the nonlinear elastic and the nonlinear inelastic model shows unexpected deformation behaviour. It does not show the anticipated bending motion of the pile under external forces.

From the balance points the occurrence of the maximum displacement in the time history of the response in Chapter 5.5.1 is confirmed. For SSI1, the largest deflection is caused by the excessive wave loads after ground motion, at $t = 118$, when the ground motion by the earthquake is minimal as in Figure 5.54a. For SSI2 under ELE with an operational rotor, the largest deflection is caused by the ground motion at $t = 115$ s, reflected in Figure 5.54c by the negative soil displacement by the earthquake at that time instance.

For none of the two soil-structure models under operational conditions to Extreme Level Earthquake loading does the tilt of the structure meet the serviceability requirement of the turbine manufacturers, i.e. 0.5°.

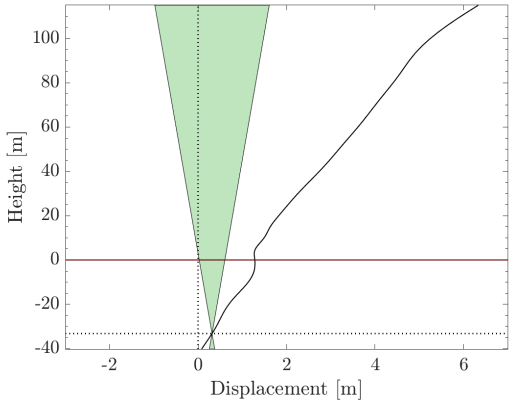

(a) *Ultimate tilt displacement versus limit - SSI1.*

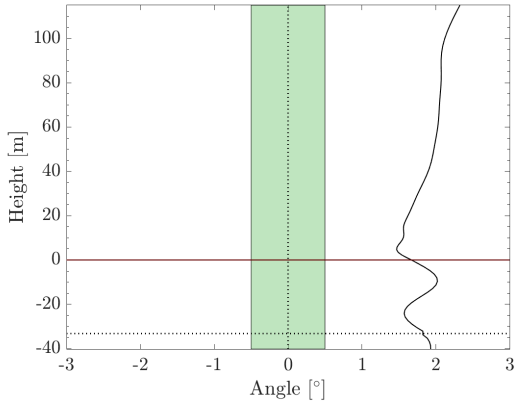

(b) *Ultimate tilt angle versus limit - SSI1.*

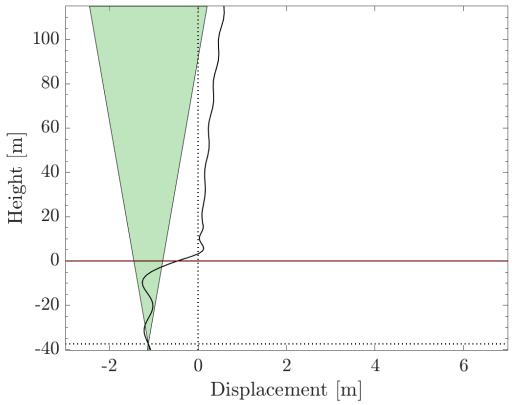

(c) *Ultimate tilt displacement versus limit - SSI2.*

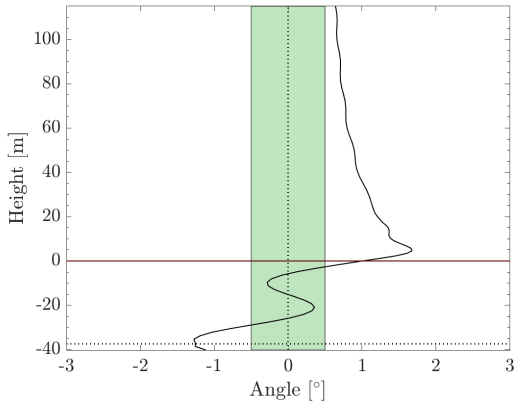

(d) *Ultimate tilt angle versus limit - SSI2.*

Figure 5.54: *Tilt limit check for the nonlinear elastic soil-structure interaction model (SSI1, 5.54a and 5.54b) and the nonlinear inelastic series hysteretic-viscous damping model (SSI2, 5.54c and 5.54d) under wind, wave and Extreme Level Earthquake loads, when the turbine is in normal operation mode.*

Emergency Shutdown Mode

To shut down the rotor in case of earthquake motion proved adversary for the amplitude response of the nonlinear elastic model, where the pile displacement reached a new maximum (Fig. 5.41). Hence Fig. 5.55a shows an even worse tilted state of the RNA, at -8 m, than for when the turbine would be kept operational.

The maximum displacement of the nonlinear inelastic model was brought back by shutting down the rotor, from +0.83 m to -0.4 m, which causes the RNA to be just within tilt bounds again. However, the dynamic instability of the beam still exists as the large relative motion between pile and ground reduced the soil spring stiffnesses to nearly null, which is visualized in the erratic deformation mode of the pile.

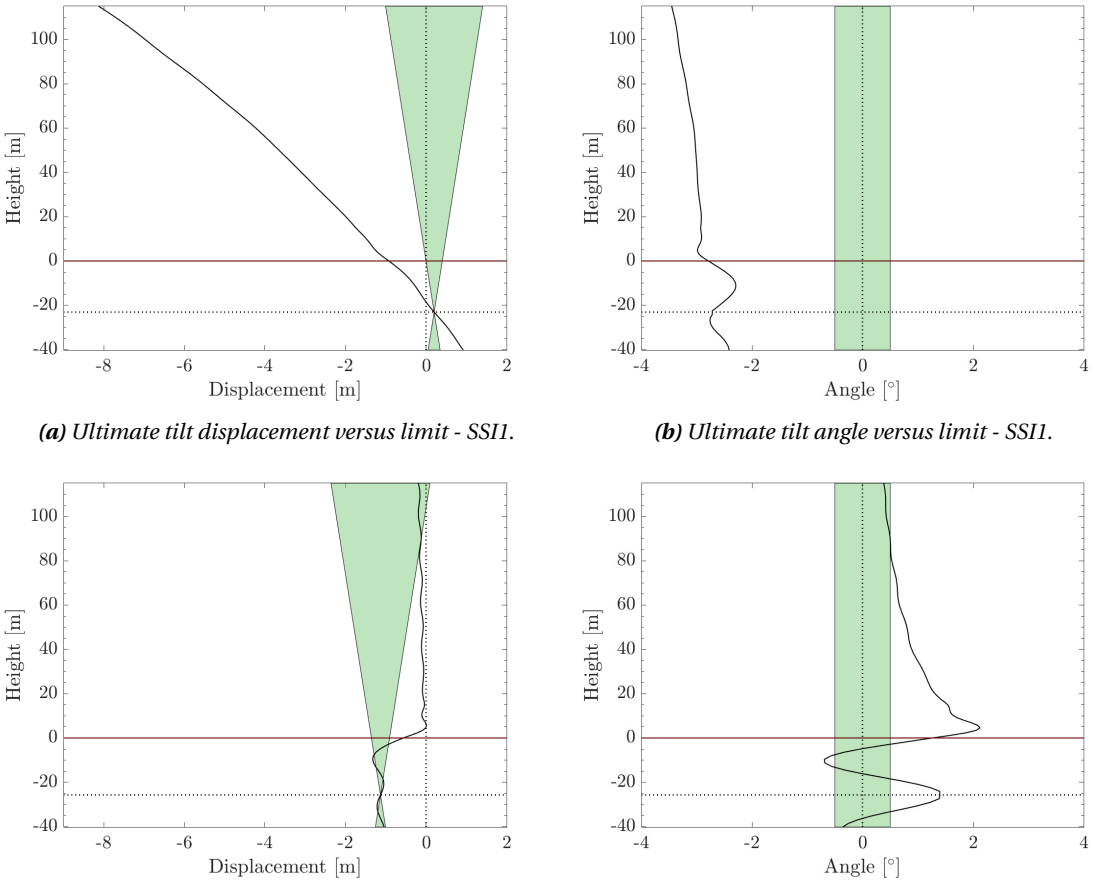

(a) *Ultimate tilt displacement versus limit - SSI1.*

(b) *Ultimate tilt angle versus limit - SSI1.*

(c) *Ultimate tilt displacement versus limit - SSI2.*

(d) *Ultimate tilt angle versus limit - SSI2.*

Figure 5.55: *Tilt limit check for the nonlinear elastic soil-structure interaction model (SSI1, 5.55a and 5.55b) and the nonlinear inelastic series hysteretic-viscous damping model (SSI2, 5.55c and 5.55d) under wind, wave and Extreme Level Earthquake loads, after the turbine performed an emergency shutdown.*

5.5.4. Structural Capacity Behaviour

For the recorded earthquake level, the structural demand in the elastic SSI model proved to be a lot bigger than in the inelastic SSI model; the elastic model did not meet the yield and buckling criterion, the inelastic model did. Here, the structural capacity behaviour for the Extreme Level Earthquake is investigated.

Operational Mode

Figure 5.56 displays the yield ratio and yield stress for both the nonlinear elastic SSI1 model and the nonlinear inelastic SSI2 model. For Extreme Level Earthquake ground motion, the already excessive structural demand in SSI1 due to the free-field gound motion in Chapter 5.4.4 rises even more; at pile base, the yield stress surpasses the limit by almost six times. The demand in the inelastic SSI2 model remains within bounds of the yield criterion.

Figure 5.57 indicates if the structure is prone to buckling during the ELE. The elastic soil-structure system clearly is, for the inelastic system the global buckling ratio stays well within bounds.

Just as for the recorded earthquake motion in Chapter 5.4, the difference in capacity demand starts below Mean Sea Level (<20 m). From that height, the excessive inertia wave forces are active in the elastic model, while in the inelastic model they are not as the acceleration component of the lateral pile displacement driving this force is strongly damped by the radiation damper in the soil.

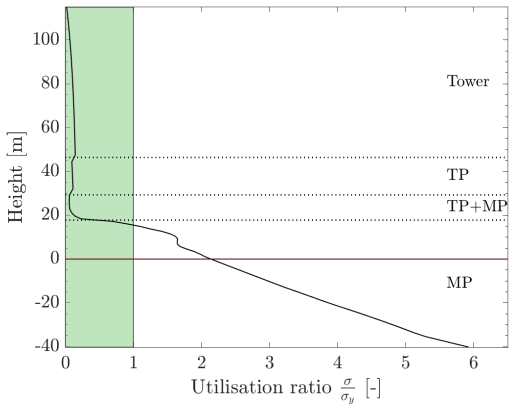

***(a)** Yield utilization ratio - SSI1.*

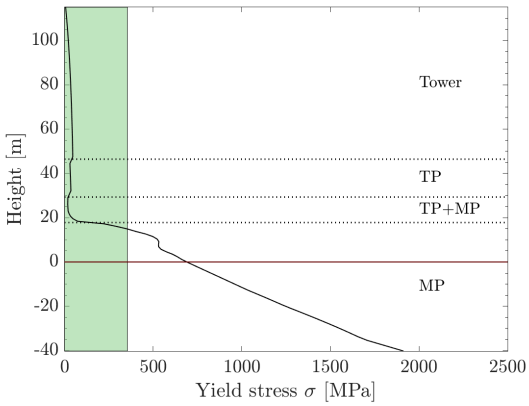

***(b)** Yield stress versus material yield strength - SSI1.*

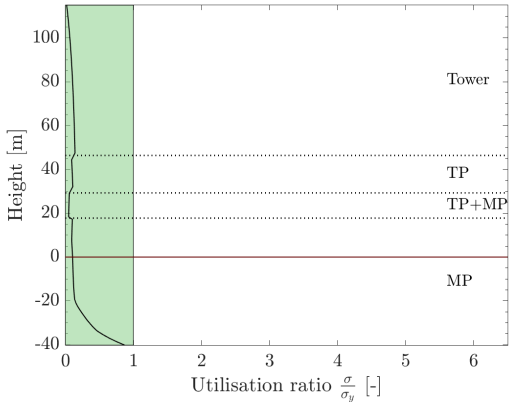

***(c)** Yield utilization ratio - SSI2.*

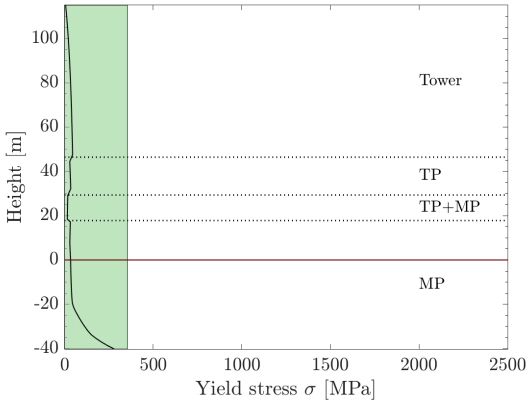

***(d)** Yield stress versus material yield strength - SSI2.*

***Figure 5.56:** Global yield limit check for the nonlinear elastic soil-structure interaction model (SSI1, 5.56a and 5.56b) and the nonlinear inelastic series hysteretic-viscous damping model (SSI2, 5.56c and 5.56d) under wind, wave and Extreme Level Earthquake loads, when the turbine is in normal operation mode.*

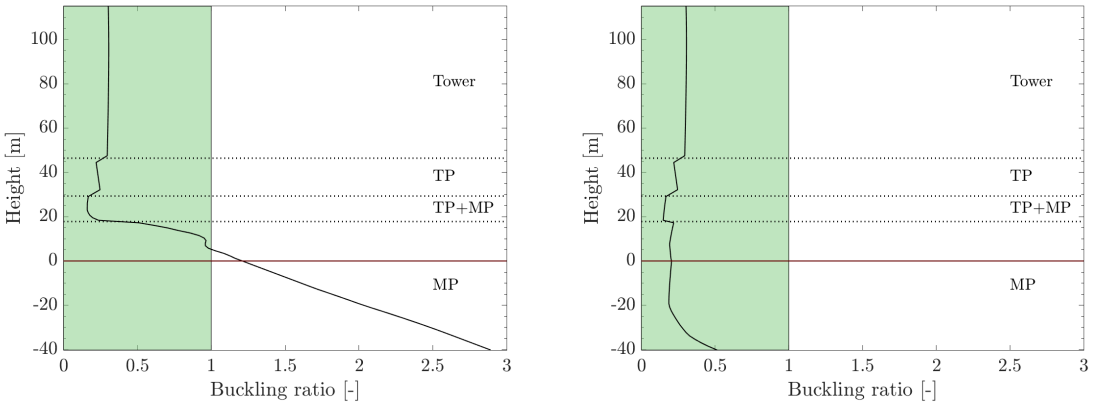

(a) *Buckling ratio versus limit - SSI1.*

(b) *Buckling ratio versus limit - SSI2.*

Figure 5.57: *Global buckling limit check for the nonlinear elastic soil-structure interaction model (SSI1, 5.57a) and the nonlinear inelastic series hysteretic-viscous damping model (SSI2, 5.57b) under wind, wave and Extreme Level Earthquake loads, when the turbine is in normal operation mode.*

Emergency Shutdown Mode

With shutting down the operation of the turbine, the displacement in the elastic system becomes even larger and the wave loads grow further as the motion is now no longer damped by the active rotor. That is why below MSL the yield of the elastic system almost immediately grows out of bounds in Figure 5.59. For the buckling ratio in Figure 5.58 the situation remains similar to operation of the rotor.

For the inelastic system, the yield and buckling values stay within bounds but are slightly higher for the shutdown condition than during operation below mudline (see Figure 5.59c versus Figure 5.56c. This is because the pile displacement below mudline is minimally larger in a shutdown simulation than during operation of the rotor, just as for NSS simulation DLC-2 (see Table 5.1 and Chapter 5.4). As a result the soil resistance forces are higher during ELE when the shutdown strategy is applied, but the yield and buckling limits are not exceeded.

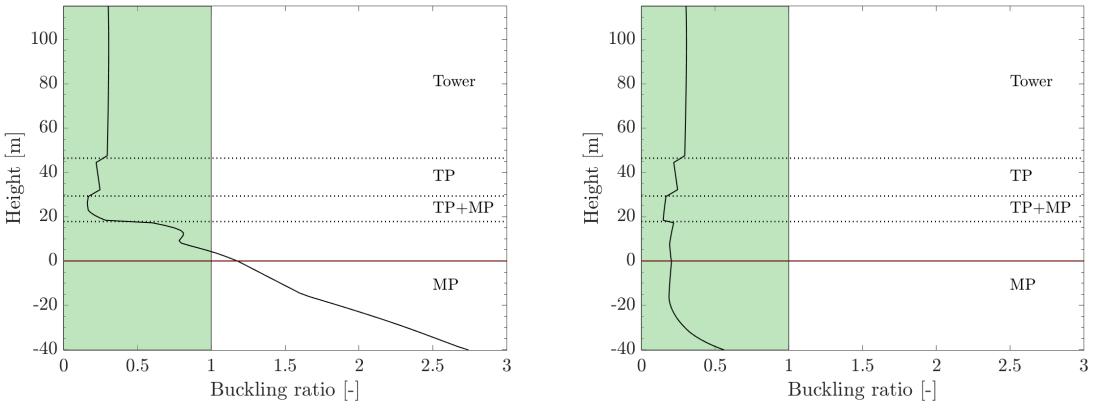

(a) *Buckling ratio versus limit - SSI1.*

(b) *Buckling ratio versus limit - SSI2.*

Figure 5.58: *Global buckling limit check for the nonlinear elastic soil-structure interaction model (SSI1, 5.58a) and the nonlinear inelastic series hysteretic-viscous damping model (SSI2, 5.58b) under wind, wave and Extreme Level Earthquake loads, when the turbine is in emergency shutdown mode.*

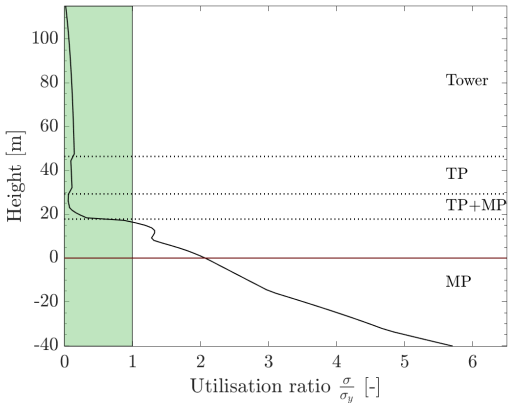

(a) *Yield utilization ratio - SSI1.*

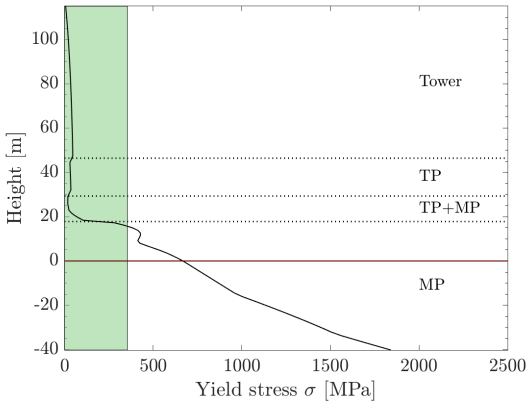

(b) *Yield stress versus material yield strength - SSI1.*

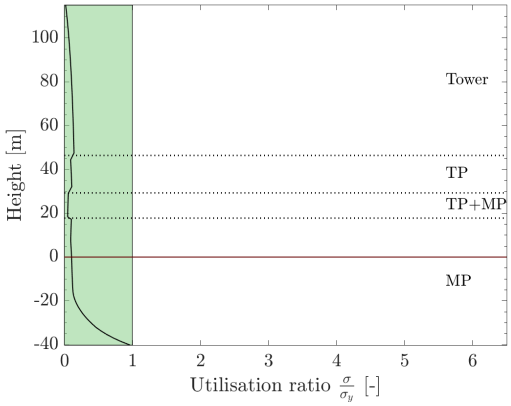

(c) *Yield utilization ratio - SSI2.*

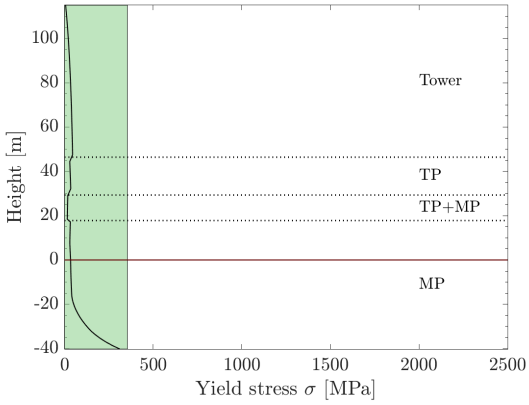

(d) *Yield stress versus material yield strength - SSI2.*

Figure 5.59: *Global yield limit check for the nonlinear elastic soil-structure interaction model (SSI1, 5.59a and 5.59b) and the nonlinear inelastic series hysteretic-viscous damping model (SSI2, 5.59c and 5.59d) under wind, wave and Extreme Level Earthquake loads, when the turbine is in emergency shutdown mode.*

5.6. Response Behaviour Under Increasing Seismic Loading - ALE

The Abnormal Level Earthquake is the earthquake level defined by ISO19901-2 [49] for which the structure may suffer irreparable damage but may not fully collapse (see Chapter 2.1). This chapter summarized the response and capacity behaviour of the monopile offshore wind foundation to the aforementioned earthquake level.

5.6.1. Pile Displacement Behaviour

Operational Mode

Figure 5.60 compares the response behaviour over time of an assumed elastic soil-structure interaction and an assumed inelastic soil-structure interaction with radiation damping. Just as in Chapter 5.4 for the as-recorded earthquake level and in Chapter 5.5 for the Extreme Level Earthquake, the elastic system predicts far larger responses than the inelastic viscous damping model.

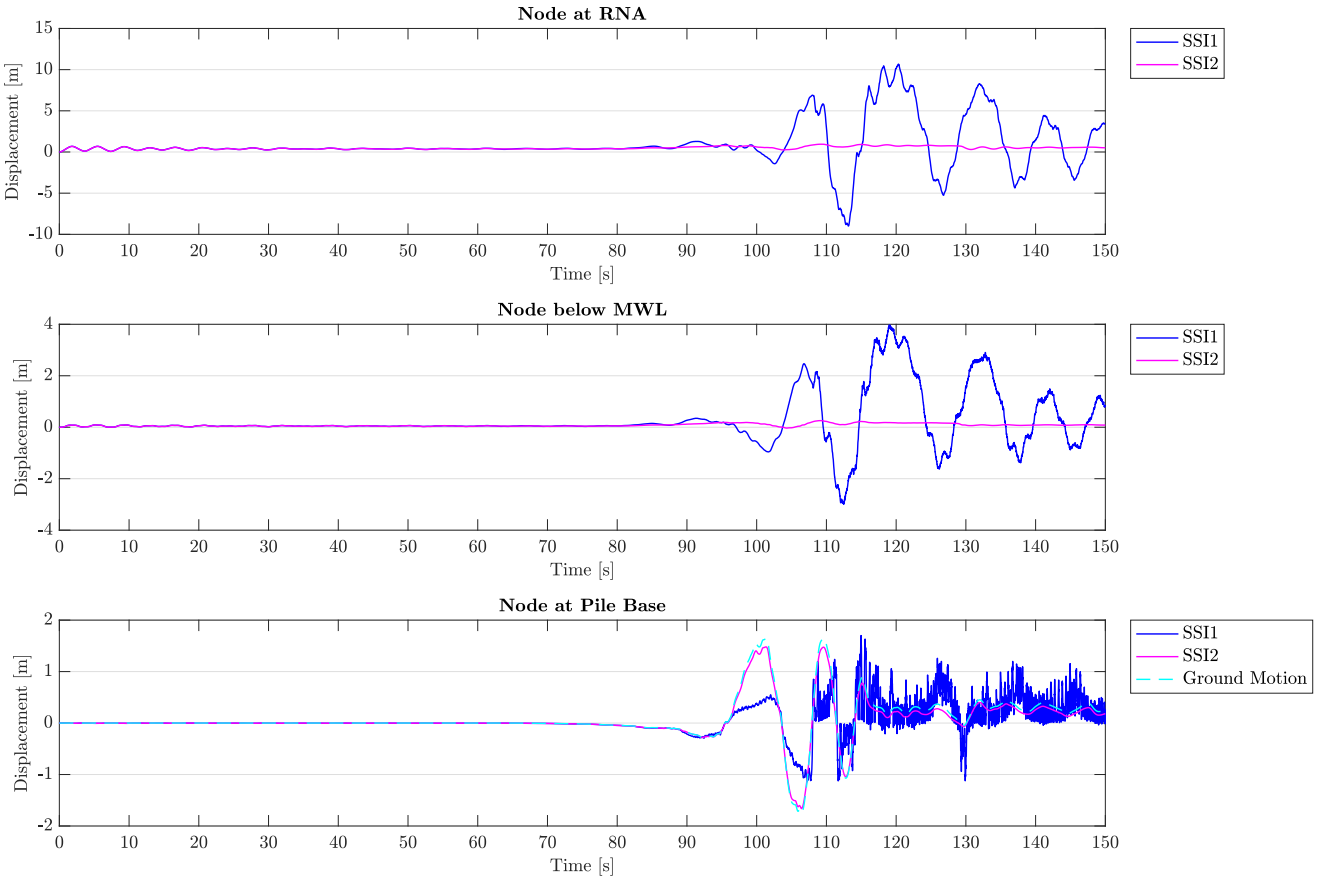

Figure 5.60: *Lateral pile displacement time history for SSI1 and the simplified SSI2 models, for co-directional loading by wind, waves and the Abnormal Level Earthquake, under operational conditions (DLC 4-N). Time history depicted for the RNA node, the node directly below maximum water level, and the node at the pile base below mudline. As a reference, the ground motion is shown versus the pile displacement below mudline.*

The Nonlinear Elastic Soil-Structure Interaction Model For the elastic system the wave forces clearly dominate the displacement behaviour following the first peak ground motion in Figure 5.61, as the pile becomes maximally deflected at times where the ground motion is in fact near zero. This behaviour is similar to the pile response under ELE, see Chapter 5.5. The displacement from ELE to ALE grows from +6.2 m at RNA to a massive +10.8 m at t = 120 s.

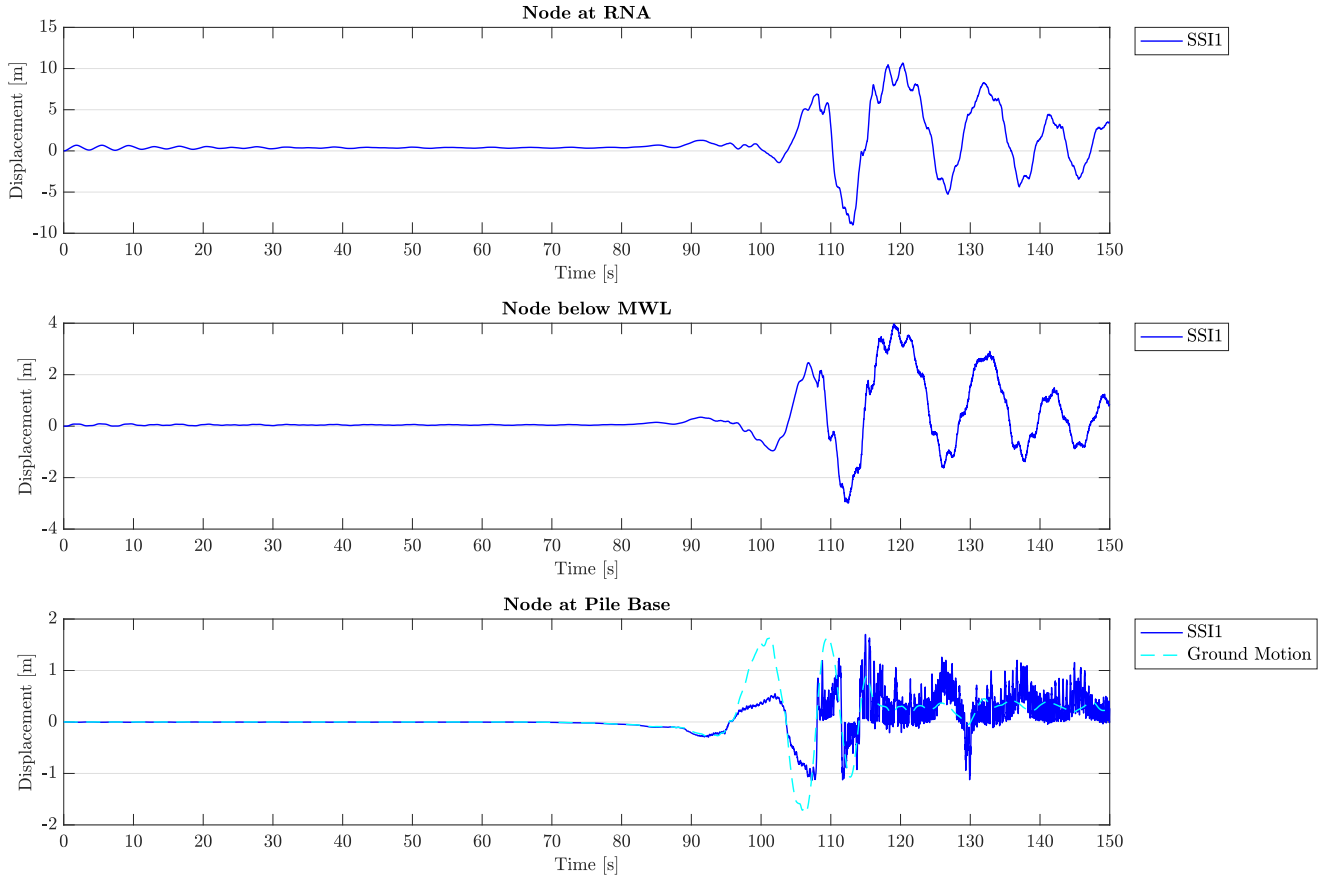

Figure 5.61: *Lateral pile displacement time history for the nonlinear elastic soil-structure interaction model (SSI1), for co-directional loading by wind, waves and the Abnormal Level Earthquake, under operational conditions (DLC 4-N). Time history depicted for the RNA node, the node directly below maximum water level, and the node at the pile base below mudline. As a reference, the ground motion is shown versus the pile displacement below mudline.*

The Nonlinear Series Hysteretic-Viscous Damping Soil-Structure Interaction Model For the inelastic model with radiation damping, the pile response clearly follows the characteristic ground motion. The maximum pile displacement reaches +0.96 m at RNA under ALE, at time t = 109 s; for ELE, this was +0.83 m.

The maximum pile deflection thus does not occur at PGD, which is -1.76 m at t =106.5 s (see Figure 4.26). That is because a negative ground displacement decreases the positive displacement position by the thrust (which happens at t =106.5 s of the PGD), while a positive ground motion further enhances the already positive position (which happens at t = 109 s of the peak pile displacement).

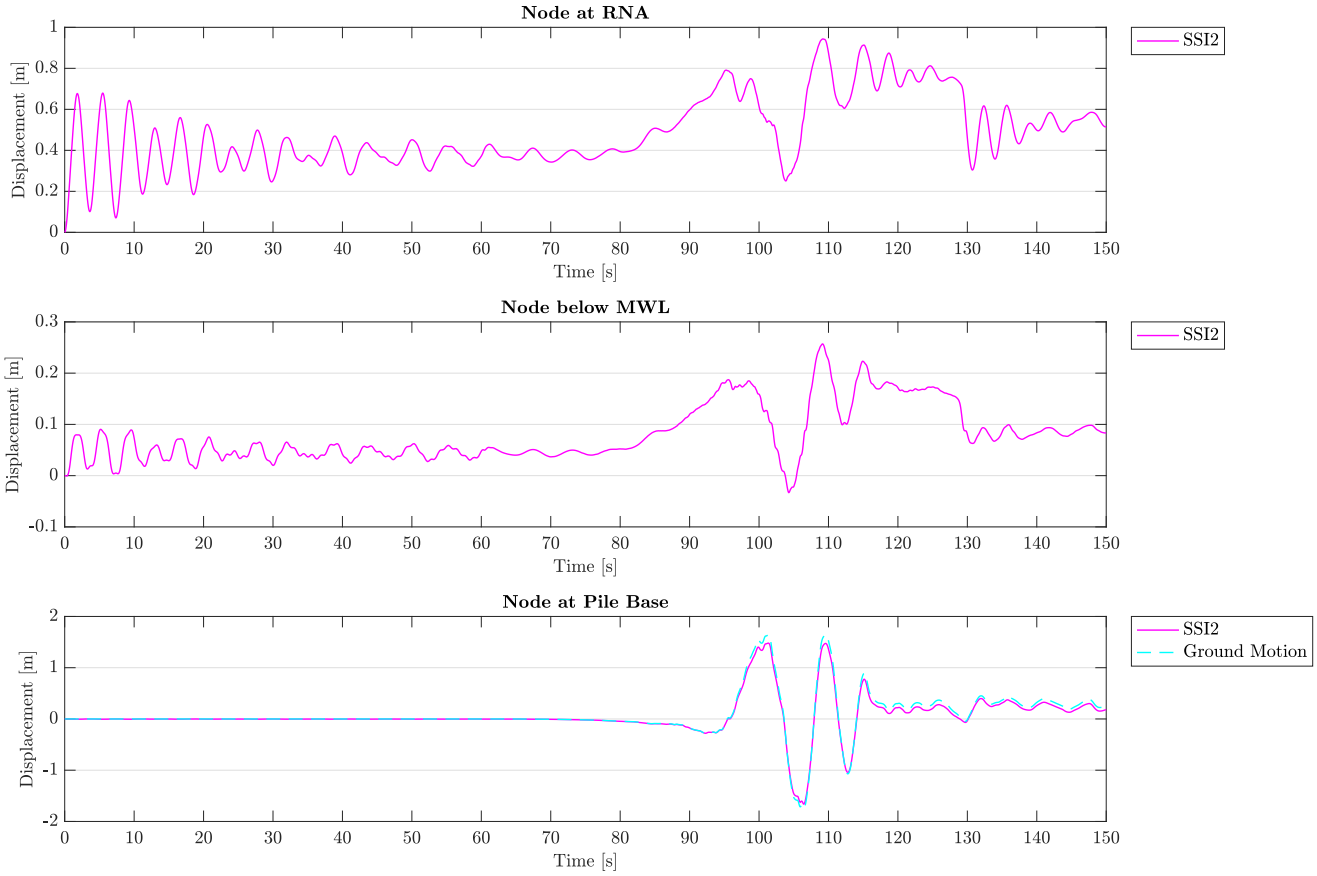

Figure 5.62: *Lateral pile displacement time history for the nonlinear inelastic series hysteretic-viscous damping soil-structure interaction model (SSI2), for co-directional loading by wind, waves and the Abnormal Level Earthquake, under operational conditions (DLC 4-N). Time history depicted for the RNA node, the node directly below maximum water level, and the node at the pile tip. As a reference, the ground motion is shown versus the pile displacement below mudline.*

Emergency Shutdown Mode

Figure 5.63 shows the responses of both soil-structure interaction models to a shutdown-strategy.

The Nonlinear Elastic Soil-Structure Interaction Model It is clear when comparing Fig. 5.64 with Fig. 5.61 that shutdown is not a good strategy when the earthquake, wind, wave and thrust forces are co-directional. The maximum pile displacement at RNA grows further from +10.8 m at t = 120 s to -15 m at t = 112.5 s.

At the time of maximum pile displacement, the combination of negative ground motion and the largely negative acting excessive wave forces make the structure deflect largely in negative direction to -15 m. Where the thrust force previously provided counterbalance to this large negative combination of forces, it is now non-existent during shutdown.

The Nonlinear Series Hysteretic-Viscous Damping Soil-Structure Interaction Model The pile motion below mudline has decreased in Figure 5.75c compared to Figure 5.74c, indicating the shutdown-strategy would be beneficial in reducing the response of the structure to Abnormal Earthquake ground motion.

Above mudline, the pile motion becomes mainly negatively displaced by the increasing positive directed ground motion; no thrust force exists to provide positive counterbalance. The combination of negative ground motion and negative wave loads at time t = 105 s cause the structure to reach a maximum negative deflection at that time, again because there is far more little positive directed forcing by the wind load on the tower.

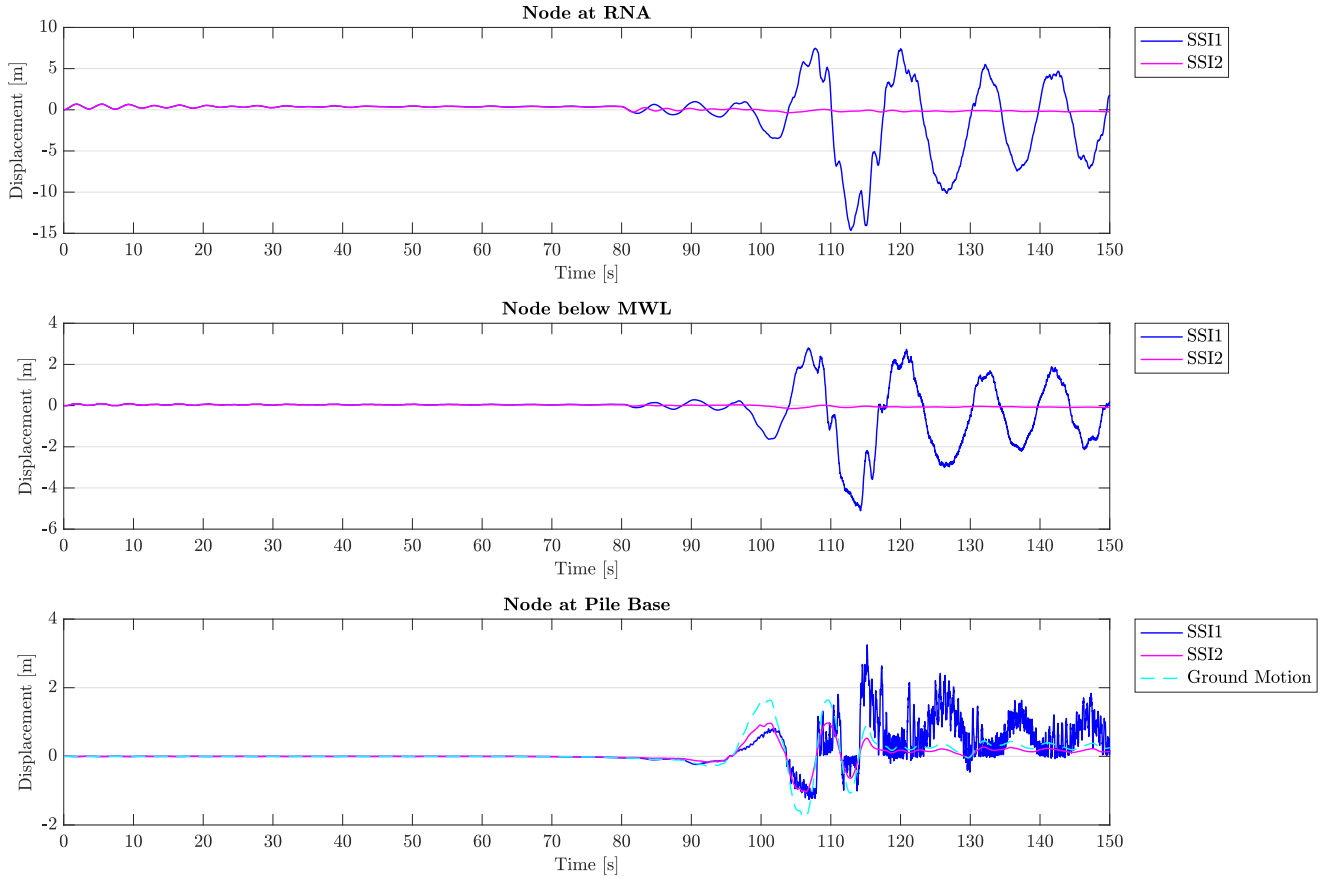

Figure 5.63: *Lateral pile displacement time history for SSI1 and the simplified SSI2 models, for co-directional loading by wind, waves and the Abnormal Level Earthquake, under shutdown conditions (DLC 4-S). Time history depicted for the RNA node, the node directly below maximum water level, and the node at the pile base below mudline. As a reference, the ground motion is shown versus the pile displacement below mudline.*

The radiation damper seems to be overly active, causing the earthquake-induced motion above mudline to be much smaller than the ground motion. Also, the maximum displacement occurs during the transient response due to rotor startup, and not due to the abnormally large earthquake motion, which is not in line with expectations. Lastly, the amplitude motion introduced by the existence of earthquake ground motion is quickly damped, indicating an overdamped system.

Also below mudline the motion by the pile is smaller than the ground motion. The soil springs have barely any stiffness left for ground displacements of 1.76 m (except for the clay layer), thus one would expect the soil and pile motion to be nearly identical, and not as different as in Figure 5.65. There must be another mechanisms providing resistance against the pile motion. As was found in Wallace et al. [97], the parallel set-up of the spring-dashpot element may have led to excessive dashpot forces to resist pile motion that actually exceed the ultimate resistance by the soil springs, which is reflected here in the smaller displacement of the pile with respect to the soil.

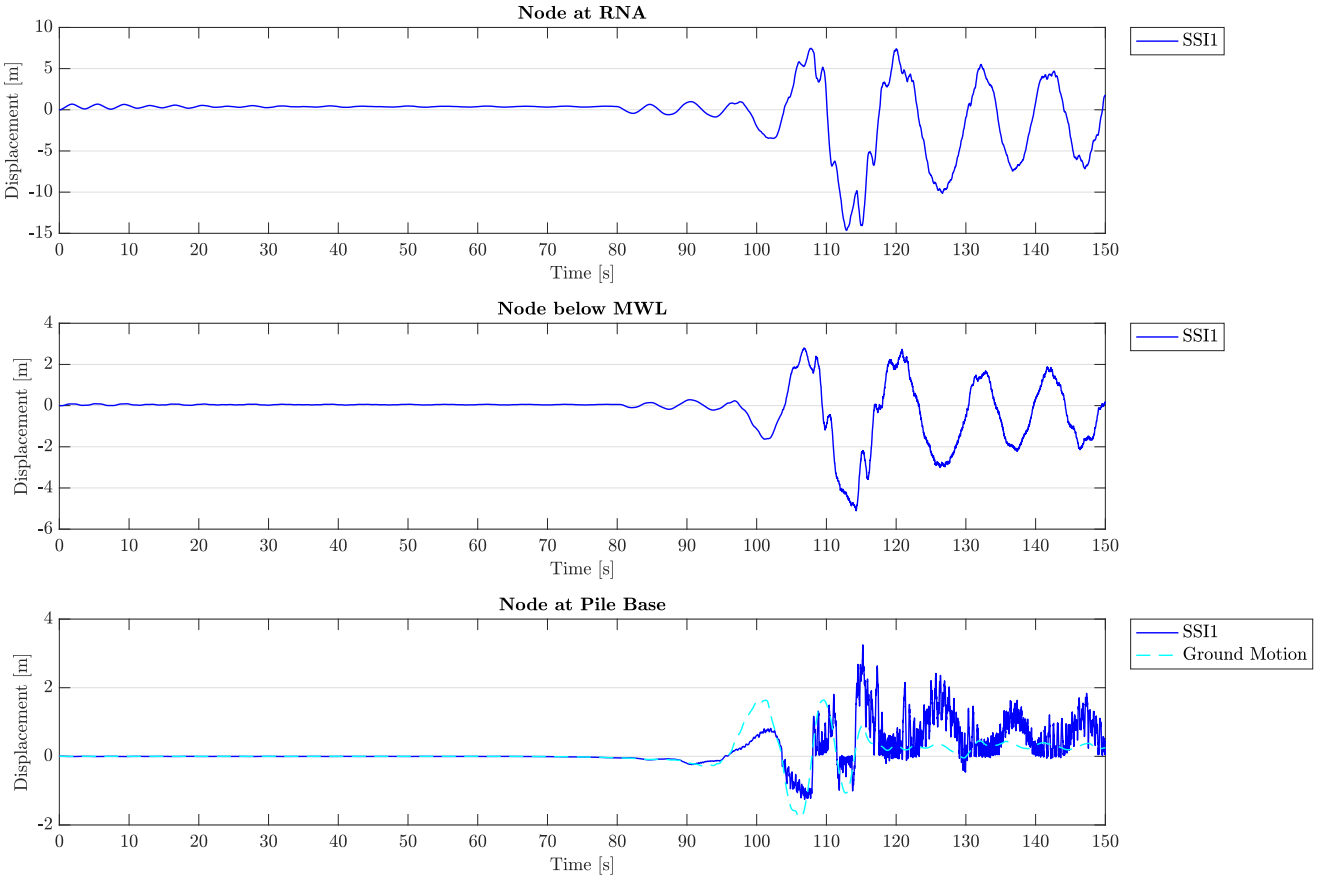

Figure 5.64: *Lateral pile displacement time history for the nonlinear elastic soil-structure interaction model (SSI1), for co-directional loading by wind, waves and the Abnormal Level Earthquake, under shutdown conditions (DLC 4-S). Time history depicted for the RNA node, the node directly below maximum water level, and the node at the pile base below mudline. As a reference, the ground motion is shown versus the pile displacement below mudline.*

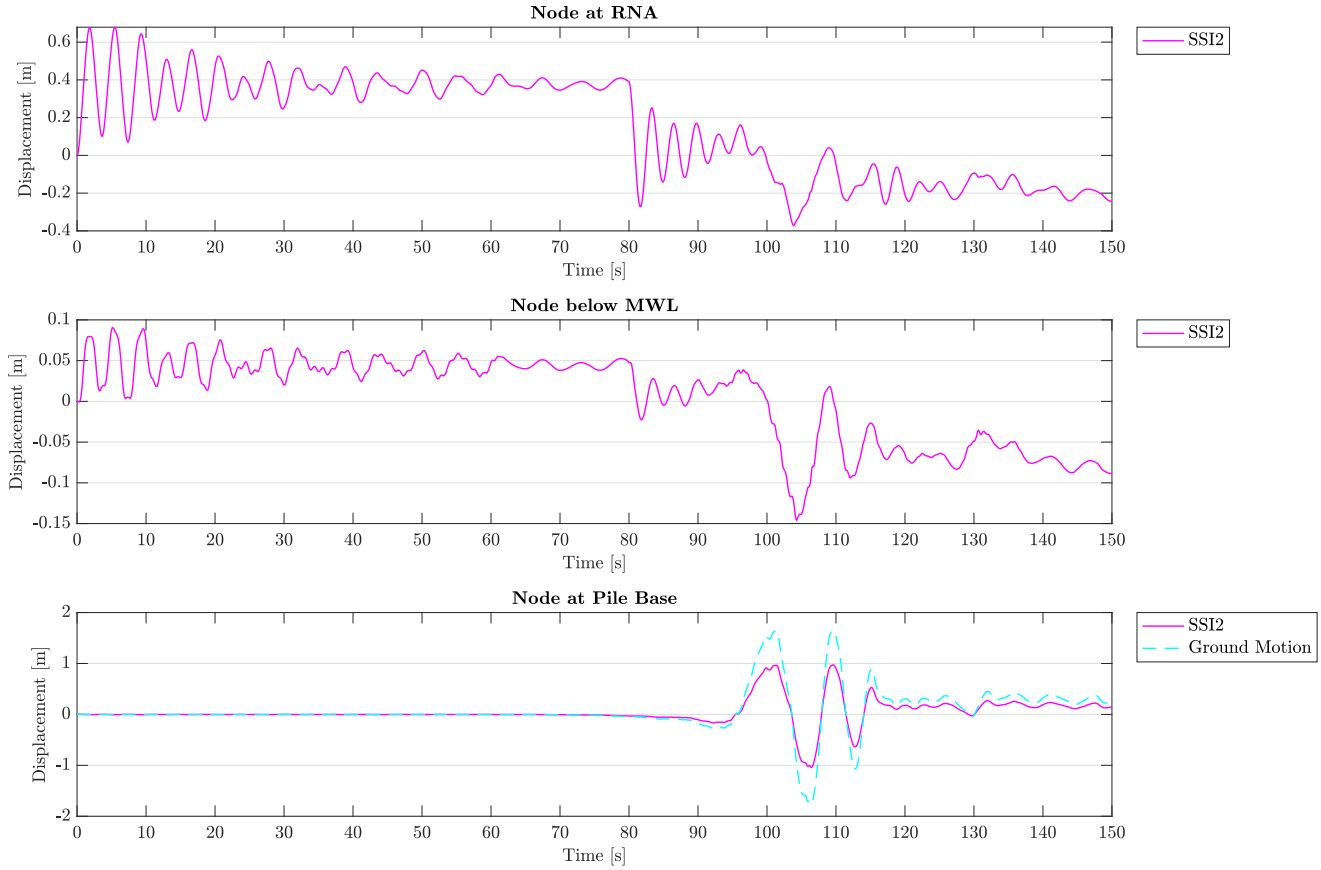

Figure 5.65: *Lateral pile displacement time history for the nonlinear inelastic series hysteretic-viscous damping soil-structure interaction model (SSI2), for co-directional loading by wind, waves and the Abnormal Level Earthquake, under shutdown conditions (DLC 4-S). Time history depicted for the RNA node, the node directly below maximum water level, and the node at the pile base below mudline. As a reference, the ground motion is shown versus the pile displacement below mudline.*

5.6.2. Natural Frequency Progression

The natural frequency progression for the Abnormal Level Earthquake, and its correlation with the soil stiffness, pile displacement, wave inertia loads and ground motion, is not much different from the Extreme Level Earthquake in Chapter 5.5.2.

Operational Mode

For the offshore wind structure at operation under Abnormal Earthquake ground motion, the displacements for both soil-structure interaction models grew larger. This is reflected in the stability of the system, discussed hereafter.

The Nonlinear Elastic Soil-Structure Interaction Model Figure 5.66 and Figure 5.67 show behaviour that is very similar to the Extreme Level Earthquake in Chapter 5.5.2. At more and more instances in the time history does the first eigenvalue become negative, leading to imaginary natural frequencies which indicate an unstable state of the system.

Due to the massive increases in the system's acceleration by the non-dissipated energy transfer of the seismic waves to the structure, the inertia wave loads grow out of bounds. For the Abnormal Level Earthquake, they become as high as 40,000 kN. Pile displacement, soil stiffness and hence frequency progression are dominated by the excessive wave loads and not directly by the ground motion anymore.

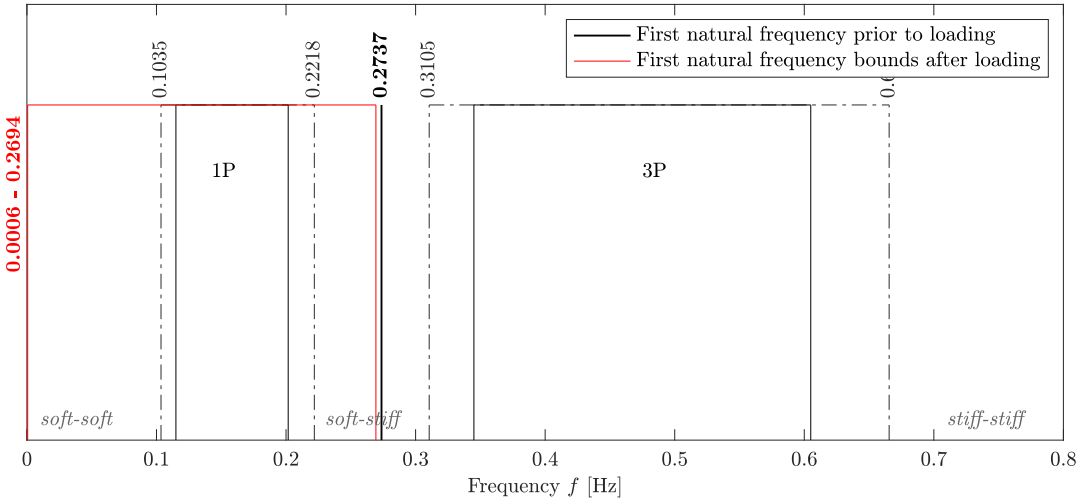

Figure 5.66: *The first natural frequency maximum-minimum range of the soil-structure system for the Abnormal Level Earthquake, with the nonlinear elastic soil-structure interaction model under operational conditions.*

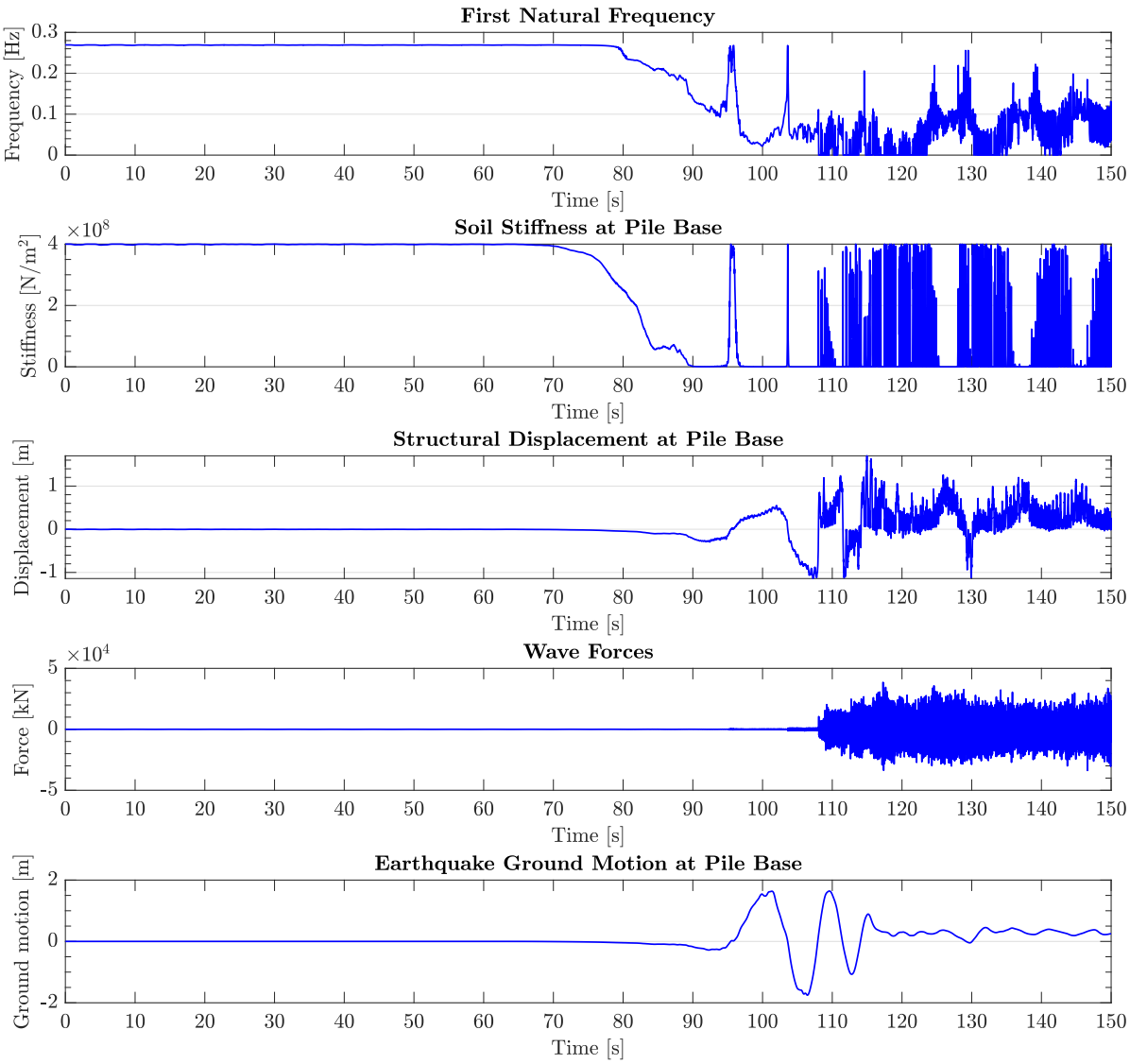

Figure 5.67: *Change in first natural frequency over time, in comparison to the change in soil stiffness, change in pile base deflection and wave forcing, for the nonlinear elastic soil-structure interaction model to wind, waves and the Abnormal Level Earthquake, while the turbine is operational.*

The Nonlinear Series Hysteretic-Viscous Damping Soil-Structure Interaction Model Also for the nonlinear inelastic damping model in Figure 5.68 and Figure 5.69 does the natural frequency become imaginary from time to time. The system which includes energy dissipation of the seismic shear waves hence becomes dynamically unstable at certain times too.

However, opposite to the nonlinear elastic system, by the viscous radiation dashpot not all energy of the seismic waves is conveyed to the structure which led to far lower and more damped pile accelerations. These in turn did not create the large inertia wave forces as for the other elastic model.

In the inelastic model, the zero soil spring stiffness is due to the ground motion and not the wave forces, and the amplitude of the response is damped/smaller than for the elastic model by energy dissipation through the radiation damper.

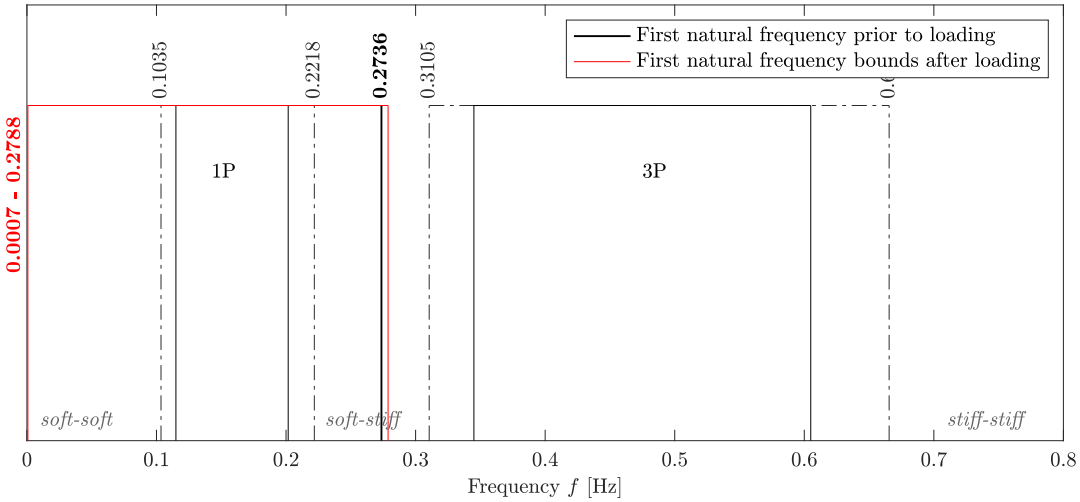

Figure 5.68: *The first natural frequency maximum-minimum range of the soil-structure system for the Abnormal Level Earthquake, with the nonlinear inelastic series hysteretic-viscous damping soil-structure interaction model under operational conditions.*

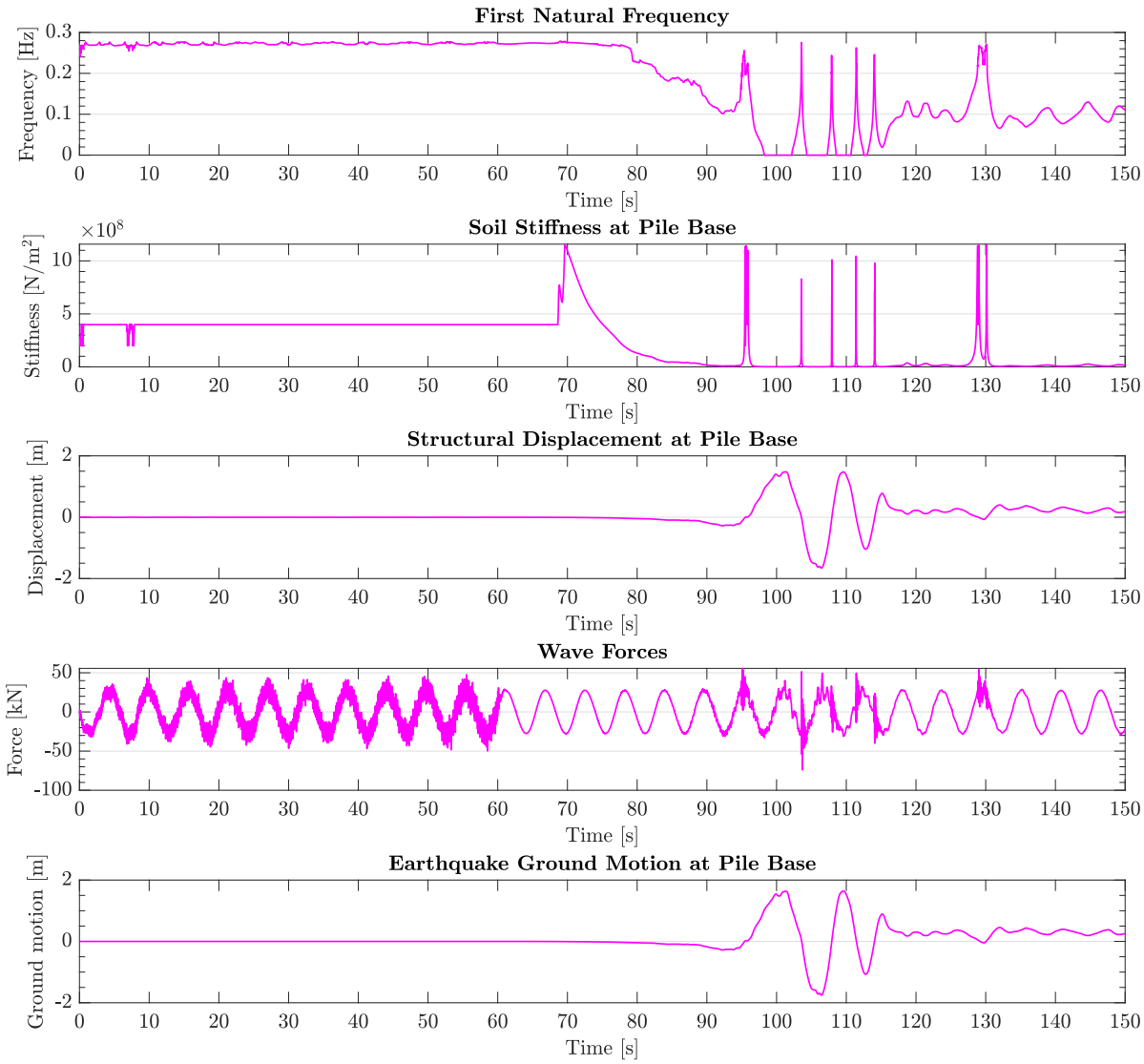

Figure 5.69: *Change in first natural frequency over time, in comparison to the change in soil stiffness, change in pile base deflection and wave forcing, for the nonlinear inelastic series hysteretic-viscous damping soil-structure interaction model to wind, waves and the Abnormal Level Earthquake, while the turbine is operational.*

Emergency Shutdown Mode

The observations with regard to the nonlinear elastic soil-structure model and the nonlinear inelastic soil-structure model under shutdown mode during the Abnormal Level Earthquake are no different from the Extreme Level Earthquake in Chapter 5.5.

Due to the the full mobilization of the soil springs, and the tangent definition used to express the soil spring stiffness, both models are left with zero stiffness from the soil in the sand and gravel layer. Consulting the p-y curves of these soil layers in Figures 3.17 and 3.20, it becomes clear that at ground displacements exceeding 0.2 m in the aftermath of the ground motion, the soil spring stiffness is zero. This zero soil stiffness in Figures 5.71 and 5.73 make the natural frequencies become imaginary in Figures 5.70 and 5.72.

The Nonlinear Elastic Soil-Structure Interaction Model Figure 5.71 also makes clear that the elastic model results in nonphysical response and load demand on the structure. This is partly caused by the absence of hysteresis damping, which could have been reflected in a different loading versus unloading path of the soil; the unloading curve stiffness should perhaps better have been represented by a secant definition, through which the difference in stiffness during loading and unloading for the same pile displacements would have modeled hysteresis damping. Hysteresis damping is known to govern the response under large amplitude loading, when nonlinear responses of the soil occur, or in other words when the secant and tangent gradient of the curve become different.

On the other hand the unrealistic demand on the structure is caused by the absence of radiation damping during linear elastic response of the structure, when loading amplitudes are small as during the P-wave tremors preceding the large shear wave ground motion.

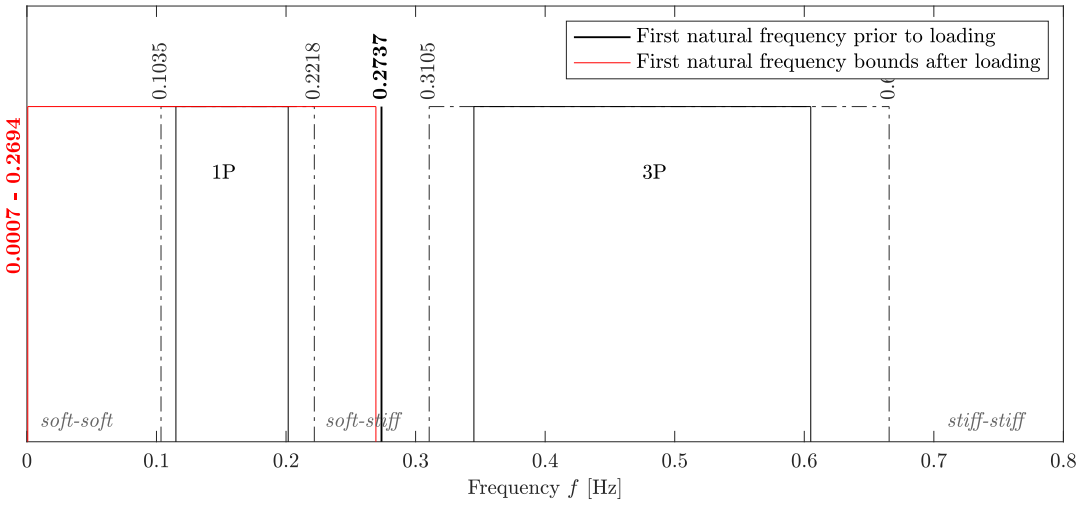

Figure 5.70: *The first natural frequency maximum-minimum range of the soil-structure system for the Abnormal Level Earthquake, with the nonlinear elastic soil-structure interaction model under shutdown conditions.*

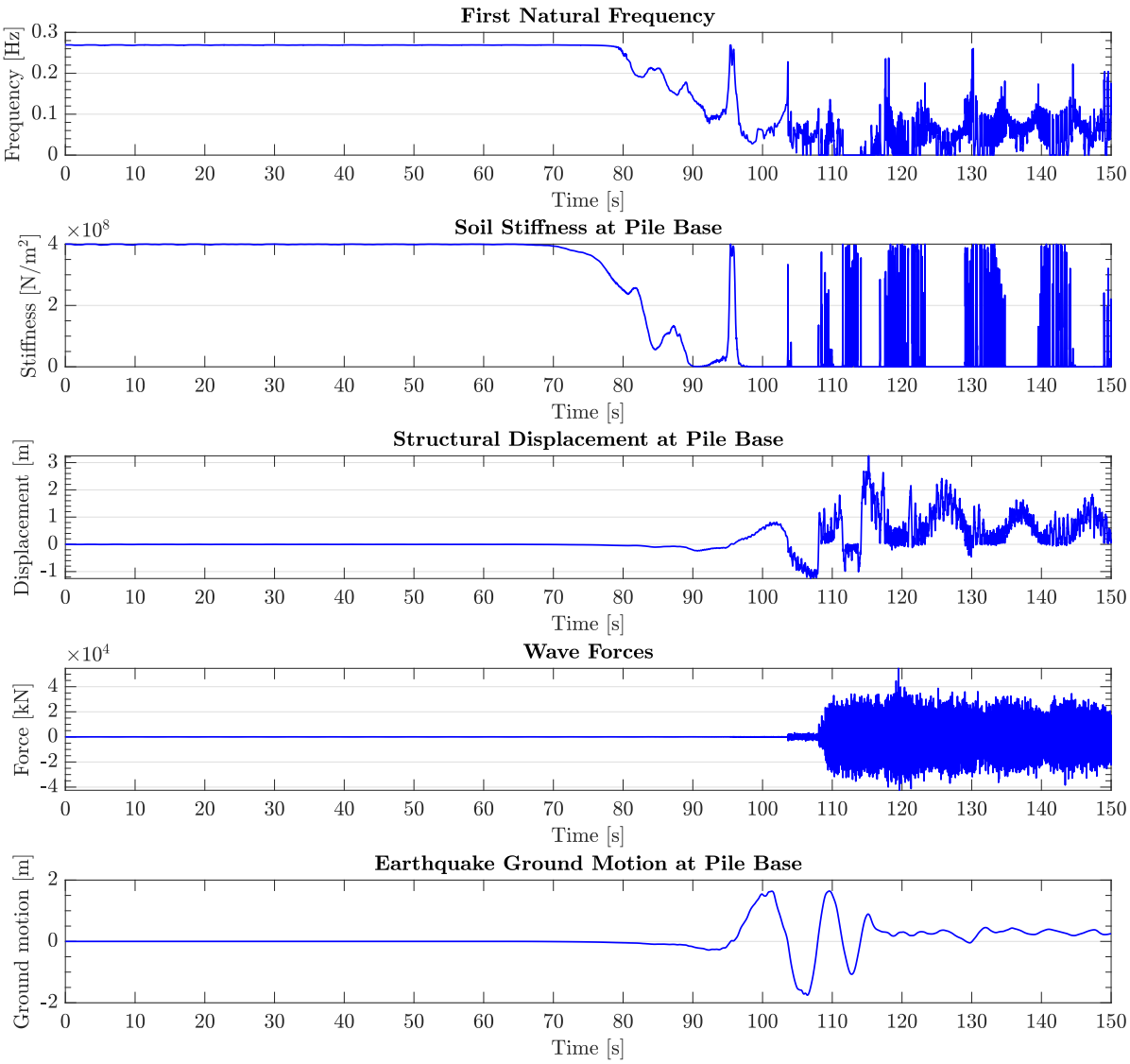

Figure 5.71: *Change in first natural frequency over time, in comparison to the change in soil stiffness, change in pile base deflection and wave forcing, for the nonlinear elastic soil-structure interaction model to wind, waves and the Abnormal Level Earthquake, after the turbine performed an emergency break.*

The Nonlinear Series Hysteretic-Viscous Damping Soil-Structure Interaction Model Figure 5.72 shows that the soil foundation has lost nearly all stiffness with increasing ground motion, as the natural frequencies becomes imaginary just as for the elastic model.

Figure 5.73 on the other hand shows that this model does not suffer from excessive loads on the structure by undamped motion as for the elastic model, this by the activity from the radiation damper. It should however be emphasized that the radiation damper seems to be overdesigned from the results in Figure 5.65, where the pile response in the soil body is larger than at RNA. This was explained to be caused by the parallel setup of the viscous radiation dashpot with both the elastic and plastic spring of the simplified nonlinear inelastic element presented in Figure 4.34. Radiation damping would in reality only be significant at low amplitude loading, meaning at linear elastic response of the soil-structure. At large ground motion, this radiation damping effect should have been minimal, but the opposite is the case in the current nonlinear inelastic model presented here. The parallel connection of the radiation dashpot with the plastic spring must have caused excessive dashpot forces in the model that in fact surpass the ultimate soil resistance of the soil column. The response of the inelastic system is overly damped.

Hysteresis damping should have been included, by the method explained before in the ALE shutdown analysis of the elastic model. And it should have been this damping that should have governed the response at PGD, not the excessive radiation damping.

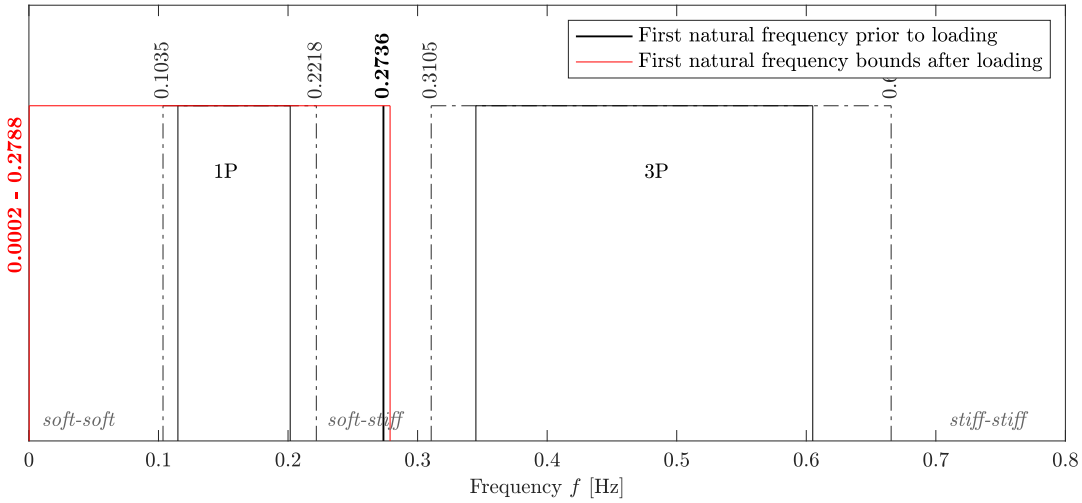

Figure 5.72: *The first natural frequency maximum-minimum range of the soil-structure system for the Abnormal Level Earthquake, with the nonlinear inelastic series hysteretic-viscous damping soil-structure interaction model under shutdown conditions.*

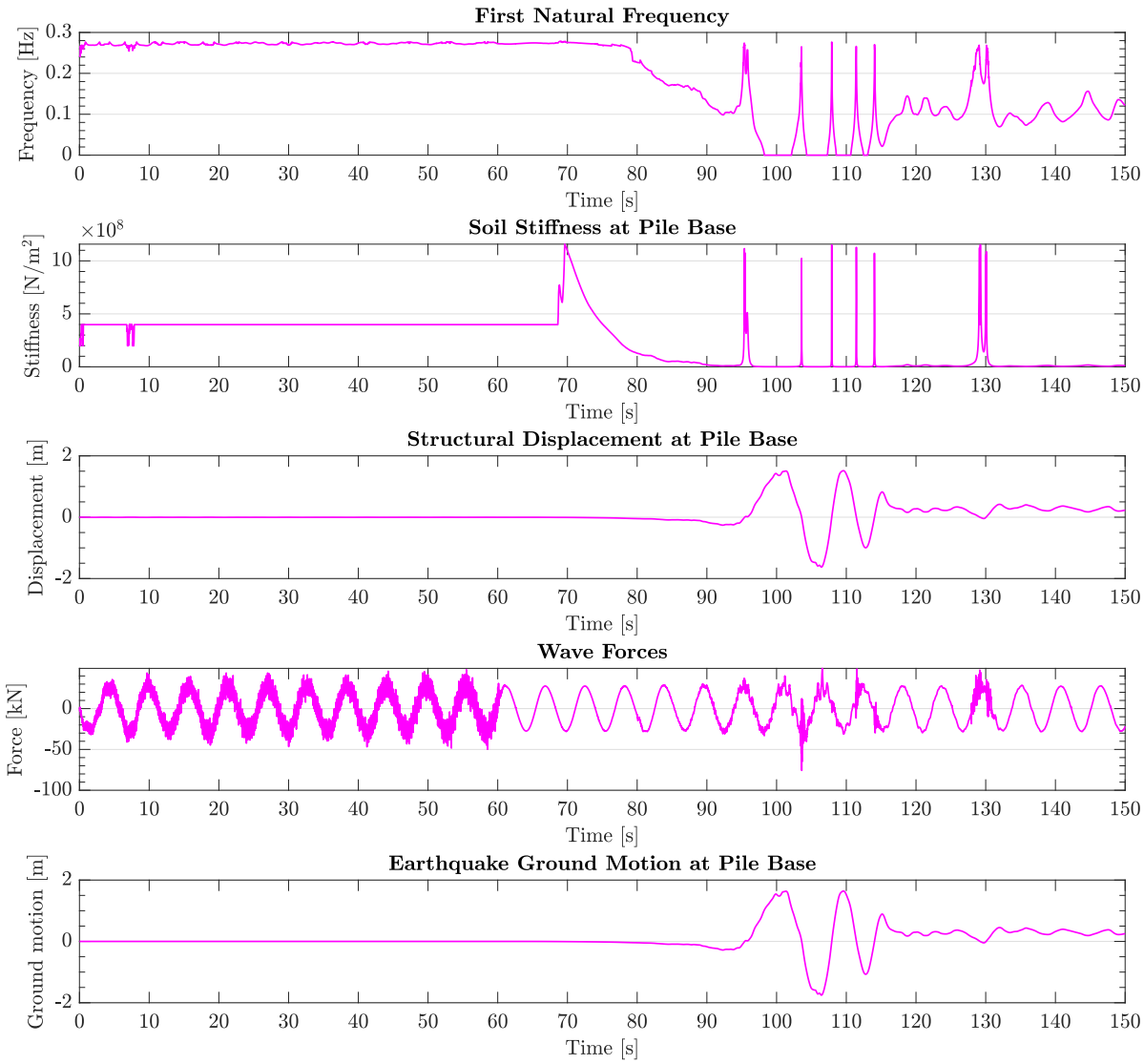

Figure 5.73: *Change in first natural frequency over time, in comparison to the change in soil stiffness, change in pile base deflection and wave forcing, for the nonlinear inelastic series hysteretic-viscous damping soil-structure interaction model to wind, waves and the Abnormal Level Earthquake, after the turbine performed an emergency break.*

5.6.3. Structural Tilt Behaviour

Opposite to the Extreme Earthquake Level simulations, both the nonlinear elastic and nonlinear inelastic model fail in tilt. This was explained in Chapter 5.6.2 to be caused by the dynamic instability of the system by the absence of soil foundation stiffness at Abnormal Level ground motion in both models.

Operational Mode

Figure 5.74 shows that with operation of the rotor under Abnormal Level Earthquake ground motion, the largest tilt occurs in the time following the major ground motion for the elastic model and during PGD for the inelastic model; this can be derived from the balance points with respect to the y-axis, and is confirmed by the time history displacement graphs in Figures 5.61 and Figures 5.62.

For both the elastic and inelastic model the RNA reaches a tilt angle exceeding the required 0.5° maximum angle, and both models show unstable deformation behaviour.

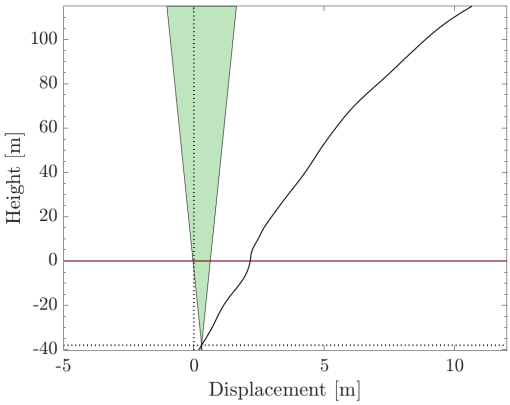

(a) *Ultimate tilt displacement versus limit - SSI1.*

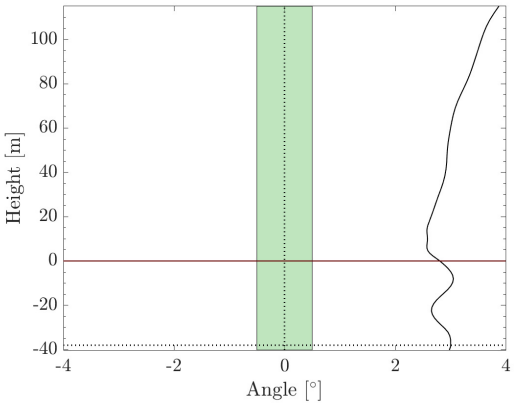

(b) *Ultimate tilt angle versus limit - SSI1.*

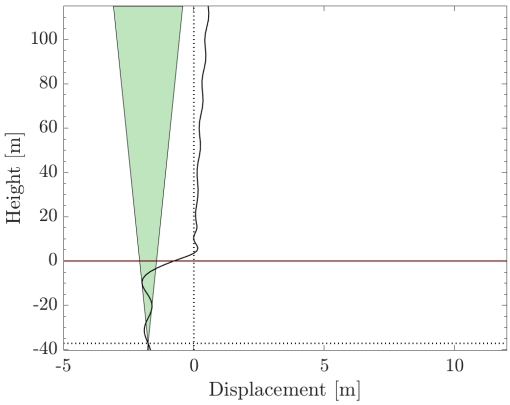

(c) *Ultimate tilt displacement versus limit - SSI2.*

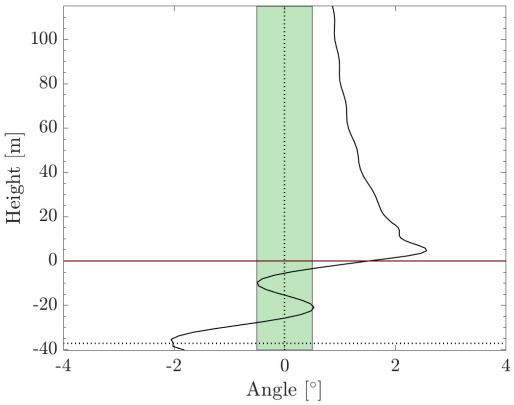

(d) *Ultimate tilt angle versus limit - SSI2.*

Figure 5.74: *Tilt limit check for the nonlinear elastic soil-structure interaction model (SSI1, 5.74a and 5.74b) and the nonlinear inelastic series hysteretic-viscous damping model (SSI2, 5.74c and 5.74d) under wind, wave and Abnormal Level Earthquake loads, when the turbine is in normal operation mode.*

Emergency Shutdown Mode

Again, the shutdown strategy seems to be beneficial to reduce the deflected state of the inelastic model, but worsens the elastic response; this can be concluded by comparing Figure 5.75 with Figure 5.74. However, both models fail to meet the tilt limit state criterion.

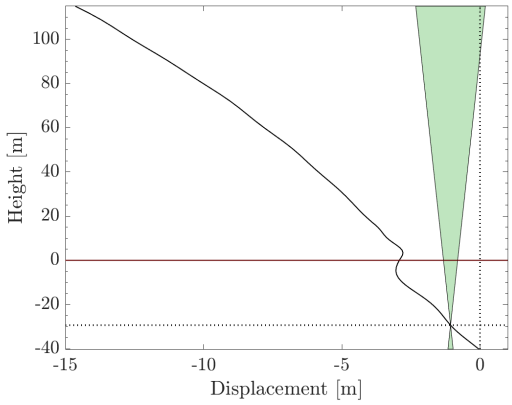

(a) *Ultimate tilt displacement versus limit - SSI1.*

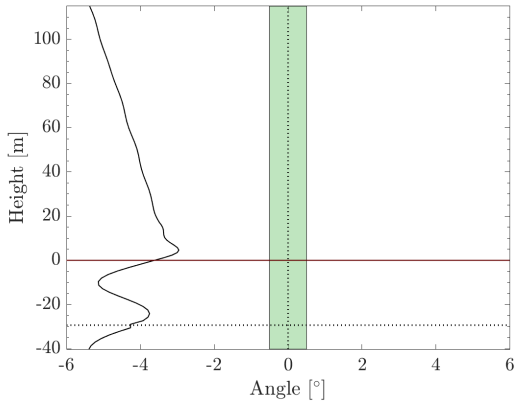

(b) *Ultimate tilt angle versus limit - SSI1.*

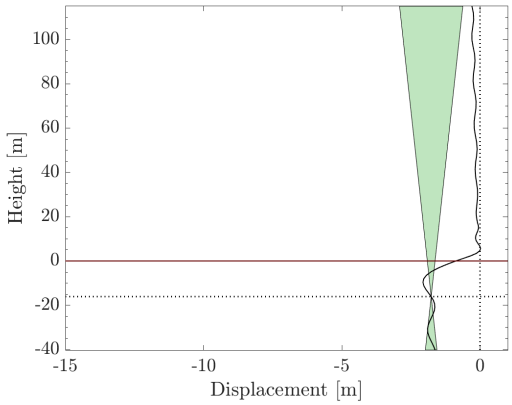

(c) *Ultimate tilt displacement versus limit - SSI2.*

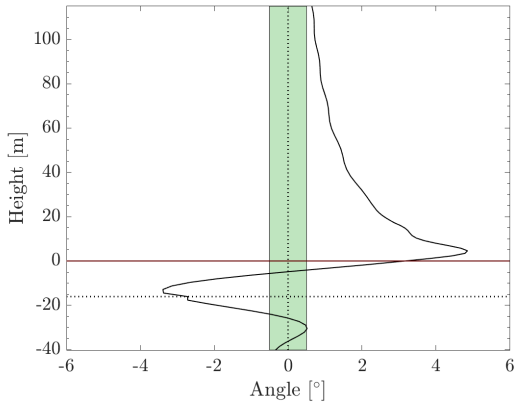

(d) *Ultimate tilt angle versus limit - SSI2.*

Figure 5.75: *Tilt limit check for the nonlinear elastic soil-structure interaction model (SSI1, 5.75a and 5.75b) and the nonlinear inelastic series hysteretic-viscous damping model (SSI2, 5.75c and 5.75d) under wind, wave and Abnormal Level Earthquake loads, after the turbine performed an emergency shutdown.*

5.6.4. Structural Capacity Behaviour

The structure already failed under recorded earthquake and Extreme Level motion for the elastic model (see Chapter 5.4.4 and 5.5.4). For the inelastic model, the Extreme Level earthquake pushed the structure to its yield limit after shutdown of the rotor, but it still remained within ULS bounds for both buckling and yield. For the Abnormal Level Earthquake, the capacity behaviour is discussed hereafter.

Operational Mode

Figure 5.76 and Figure 5.77 show the yield and buckling of the structure for both an elastic and an inelastic soil-structure interaction assumption.

The elastic model fails further in yield and buckling following even larger ground motion than during ELE, where it already failed due to excessive wave loads. The absence of hysteresis and radiation damping in the elastic model led to unrealistic accelerations of the pile response, which created nonphysical wave loads that exceed the structural capacity.

For the inelastic model, the yield is pushed to its limit. The increasing ground motion causes the soil springs to exert a slightly larger soil resistance to lateral motion than during ELE. Contrary to the elastic model, the p-y curves never obtain a zero gradient in the nonlinear response past yielding of the soil; the soil layers always keep some residual resistance. That is why below the mudline the capacity demand of the structure in both yield and buckling grows in Figure 5.76c with respect to 5.56c (or Figure 5.77b with respect to 5.57b).
It is food for thought how the inelastic model's capacity behaviour would have evolved when the excessive dashpot forces – by the parallel action with the plastic spring – would not have existed. Even with unrealistically high radiation damping, the monopile reaches its yield limit state. With reduced radiation damping, the structure may have failed in yield to the Abnormal Level Earthquake. But then in the end, hysteresis damping was not considered in the inelastic model, which could have relieved the seismic demand on the structure during strong ground motion.

Emergency Shutdown Mode

The pile motion grows significantly after shutdown for the elastic model, hence the further increase in yield and buckling exceedance in Figures 5.78a and 5.79a. For the inelastic model, the pile motion below mudline minimally increases, leading to a slight increase in structural yield and buckling in Figures 5.78c and 5.79b. The structure is pushed to the yield limit, but remains within bounds.

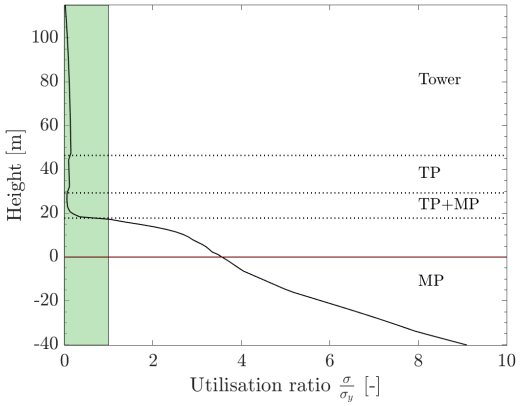

(a) *Yield utilization ratio - SSI1.*

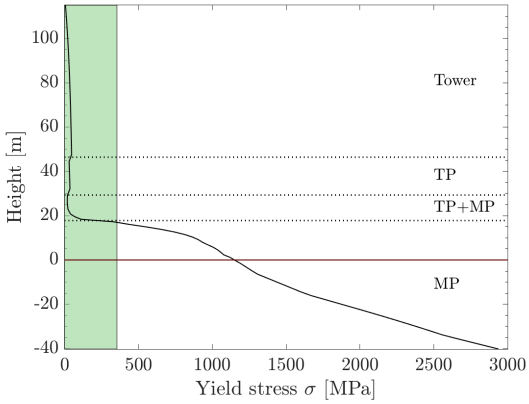

(b) *Yield stress versus material yield strength - SSI1.*

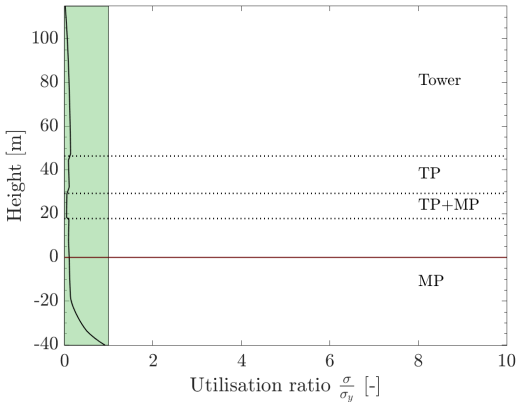

(c) *Yield utilization ratio - SSI2.*

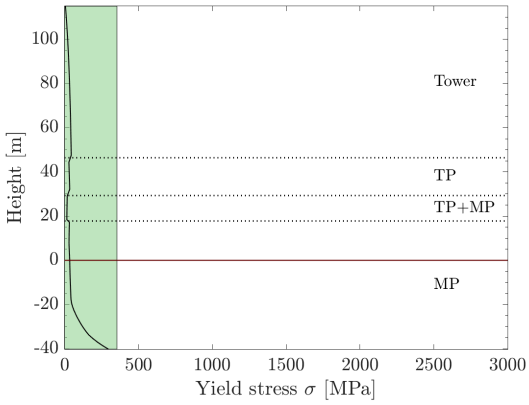

(d) *Yield stress versus material yield strength - SSI2.*

Figure 5.76: *Global yield limit check for the nonlinear elastic soil-structure interaction model (SSI1, 5.76a and 5.76b) and the nonlinear inelastic series hysteretic-viscous damping model (SSI2, 5.76c and 5.76d) under wind, wave and Abnormal Level Earthquake loads, when the turbine is in normal operation mode.*

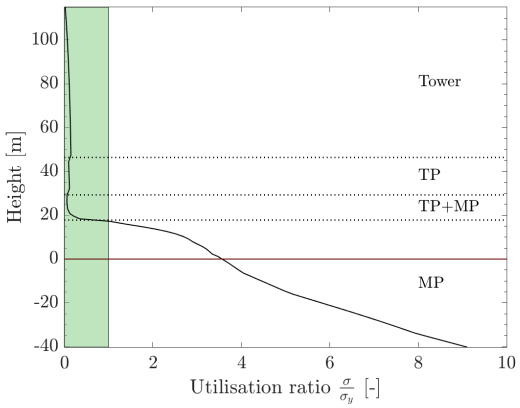

(a) *Buckling ratio versus limit - SSI1.*

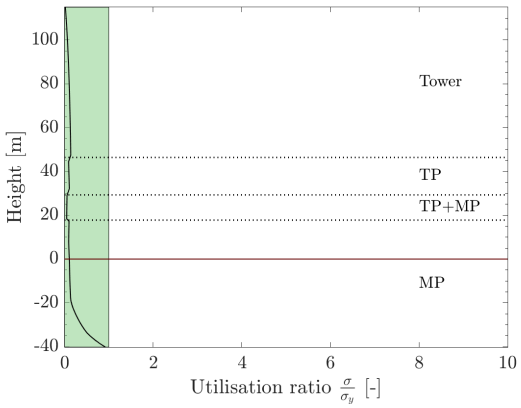

(b) *Buckling ratio versus limit - SSI2.*

Figure 5.77: *Global buckling limit check for the nonlinear elastic soil-structure interaction model (SSI1, 5.77a) and the nonlinear inelastic series hysteretic-viscous damping model (SSI2, 5.77b) under wind, wave and Abnormal Level Earthquake loads, when the turbine is in normal operation mode.*

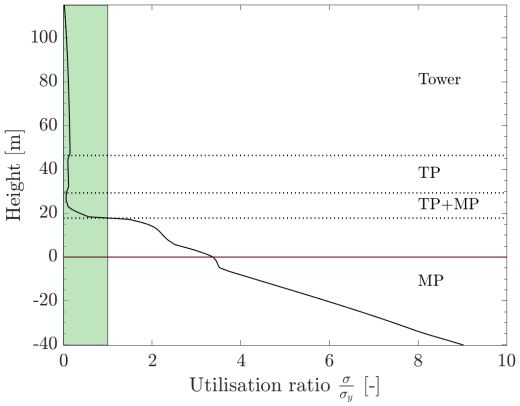

(a) *Yield utilization ratio - SSI1.*

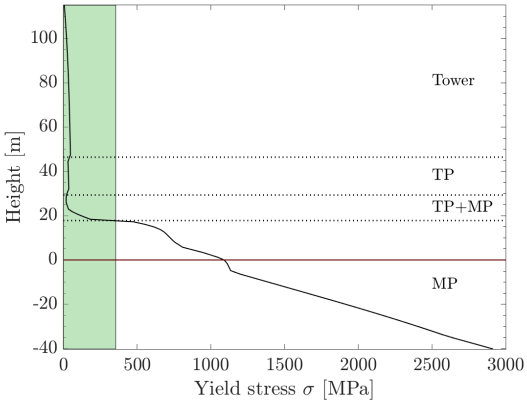

(b) *Yield stress versus material yield strength - SSI1.*

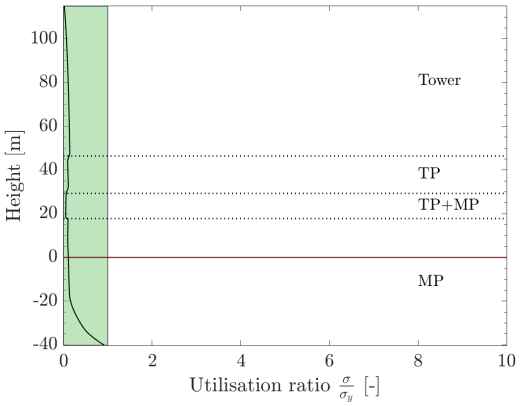

(c) *Yield utilization ratio - SSI2.*

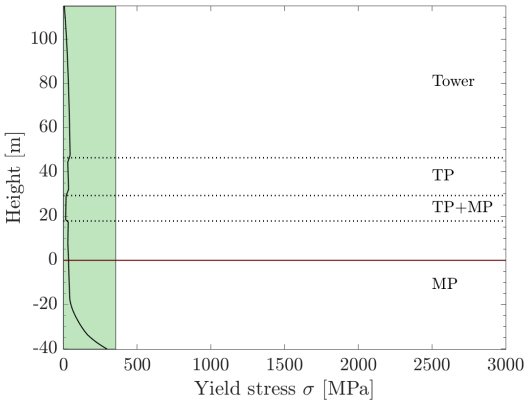

(d) *Yield stress versus material yield strength - SSI2.*

Figure 5.78: *Global yield limit check for the nonlinear elastic soil-structure interaction model (SSI1, 5.78a and 5.78b) and the nonlinear inelastic series hysteretic-viscous damping model (SSI2, 5.78c and 5.78d) under wind, wave and Abnormal Level Earthquake loads, when the turbine is in emergency shutdown mode.*

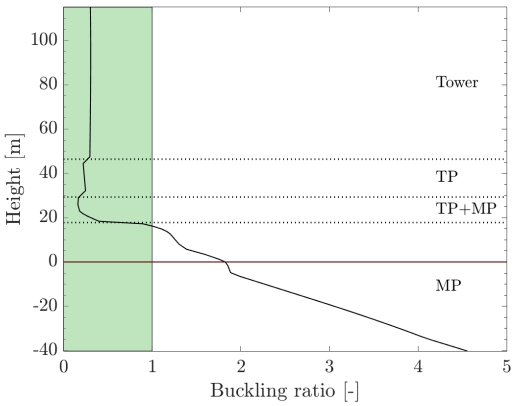

(a) *Buckling ratio versus limit - SSI1.*

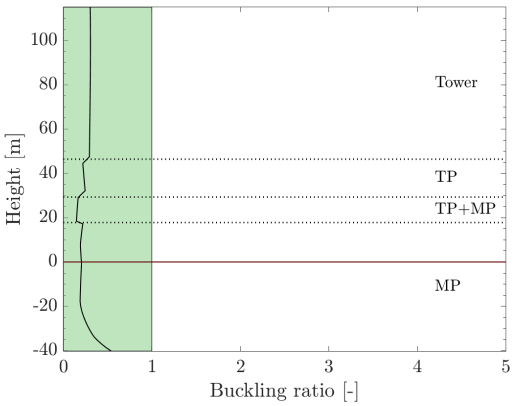

(b) *Buckling ratio versus limit - SSI2.*

Figure 5.79: *Global buckling limit check for the nonlinear elastic soil-structure interaction model (SSI1, 5.79a) and the nonlinear inelastic series hysteretic-viscous damping model (SSI2, 5.79b) under wind, wave and Abnormal Level Earthquake loads, when the turbine is in emergency shutdown mode.*

6

Conclusions

In this thesis study, the lateral response to horizontal earthquake ground motion of a monopile offshore wind foundation supporting an NREL 5 MW turbine was investigated. The structure is located offshore the coast of Taiwan, and is assumed to be embedded in a soft layered soil profile of sand overlying clay, mud- and sandstone, and gravel.

The earthquake ground motion was assumed to act co-planar and co-directional with the constant thrust, steady wind and regular wave loads. The wind and wave conditions represent a Normal Sea State. The earthquake motion, recorded to have a PGA of 0.253 g near the location of the foundation, was scaled for IDA to the ELE (0.75 g) and ALE (1.17 g) level according to ISO19901-2 [49].

Prior to soil-structure interaction analyses, the free-field motion record was extrapolated to all soil layers by linear equivalent SRA in DEEPSOIL. This procedure is necessary as the ground motion amplitude is known to vary over distinct soil layers with the largest amplitude motion in the soft layers.

The soil-structure system was modeled as a beam on a nonlinear Winkler spring foundation. The soil spring foundation, modeling the soil resistance against lateral motion, was conceptualized in two ways:

1. **A nonlinear elastic model**, which neglects any energy dissipation. The soil resistance p-y curves are according to API recommended practice [2][28]. The stiffness of the soil springs in the loading path is equal to the stiffness in the unloading path, that is the tangent modulus.
2. **A nonlinear inelastic simplified viscous damping model**, which incorporates radiation damping of the seismic shear wave by a viscous dashpot. The p-y curves are expressed as hyperbolic elastoplastic curves according to Boulanger et al. [13]. The loading and unloading path is different due to the energy dissipation, and tangent stiffness is used for the spring stiffness in loading and unloading.

The structure was modeled as a two-node Timoshenko beam with cubic displacement functions, and was suspended on either foundation (1) or (2). The two resulting soil-structure interaction models were exposed to NSS loading (DLC-1), as-recorded earthquake loading (DLC-2) and incremental earthquake loading by the ELE (DLC-3) and ALE (DLC-4), this to investigate the progression in response and capacity behaviour.

The problem definition and analysis set-up as above were established to answer the research question ***"whether elastic soil-structure interaction can be assumed for a monopile foundation under seismic loads"***, by answering the subquestions:

(a) How do an assumed elastic and as assumed inelastic SSI model's responses compare? What are the differences and what is the cause?

(b) At what level of earthquake ground motion do nonlinear or inelastic effects become governing?

(c) Does the elastic assumption lead to an economically feasible and safe monopile design?

(d) How does a shutdown strategy influence the structural demand?

From the seismic analyses it became clear that the absence of of energy dissipation in the nonlinear **elastic** SSI model by hysteresis or radiation damping led to unrealistic structural capacity demands. The motion predicted by the nonlinear elastic model was far larger than for the nonlinear inelastic model, already at recorded earthquake level. It is not physical that no energy dissipation would exist in the system, which caused unrealistically large displacements, velocities and acceleration of the entire structure. The nonphysical accelerations in turn created excessive wave loads that further amplified the response. Hysteresis damping should have been implemented to damp the large amplitude motions during strong ground motion (when the soil responds nonlinear elastoplastic), and radiation damping should have been active during low amplitude motion anticipating the large amplitude shear wave motion (when the soil still responds linear elastic to ground motion).

In the simplified nonlinear **inelastic** radiation damping SSI model, the predicted responses of the system to seismic action were significantly smaller. Radiation damping proved to have a too large influence, causing the responses to be smaller than would have been expected in reality. The parallel action of the viscous damper to the plastic soil spring generated excessive dashpot forces in the model that exceeded the ultimate soil resistance. The radiation damping should only have significant influence during low amplitude loading, and hence should not have affected the largely nonlinear soil-structure response during ground motion. During these large amplitude ground motions, hysteresis damping – which was omitted in the model – could have delivered a more realistic response.

Nonlinear effects in the soil proved to be mobilized at relatively small pile versus ground motion displacements (starting from 7 to 10 cm). In the analyses, the stiffness of the soil springs started to decrease for small pile displacements. The consequential large changes in first natural frequency proved nonlinearity to be present at the recorded earthquake intensity level already. So concluding, for small ground motions below 10 cm, when the soil behaves mainly linear elastic, radiation damping should have been the driving energy dissipation mechanism. For larger ground motion – such as the PGD during the recorded, Extreme and Abnormal earthquake –, hysteresis damping should be the driving energy dissipation mechanism. **Inelastic effects** by damping were concluded to become present at small ground motions by radiation damping.

Nonlinearity in the response advocates for the use of full time history analysis of the coupled nonlinear equations of motion. Modal reduction as implemented in this study, which uses the mode shapes based on the initial linear state of the soil foundation, will introduce an accuracy error to the computation as the mode shapes are not recomputed to the nonlinear decrease in soil stiffness.

The **elastic assumption**, causing the loading path of the soil to be identical to the unloading path and to neglect any form of soil-structure damping, leads to largely overestimating the seismic structural demand. This in turn would lead to an overdesigned, economically unfeasible monopile foundation.

No clear assessment on the usefulness of a **shutdown strategy** could be performed by the unrealistic energy dissipation in the models, although the inelastic SSI model's responses to emergency shutdown of the rotor indicate there might be potential in the strategy to reduce structural loads.

Given the results of this study, it is not recommended to assume elastic soil-structure interaction under seismic action on a monopile. The responses and structural demands become nonphysically high. Adequate implementation of radiation and hysteresis damping is of paramount importance to predict realistic responses.

7

Recommendations

Based on the results of this study, some recommendations can be made with regard to:

- the definition of the p-y curves and their validity in BNWF modeling for large diameter piles in highly dynamic seismic environments,
- the analysis method and the implementation of the external forces in the model,
- the accuracy of equivalent linear site response analysis input to soil-structure interaction analyses,
- the selected foundation structure and the structural model.

All of these recommendations hereafter could improve the current computational model to deliver more realistic response estimates for a monopile structure under earthquake motion. They can be read as action points to ameliorate the predictive soil-structure interaction model, and are listed here in sequential order.

The P-y Curves and Soil Spring Foundation

1. **Missing damping and nonlinear elasticity**. The absence of hysteresis and drag damping in the nonlinear elastic spring foundation leads to unrealistic demands on the structure. Assuming equal loading and unloading paths of the soil, thereby neglecting energy dissipation under seismic loading, largely overestimates the response. The result is an overdesigned and economically unfeasible monopile. It is a key recommendation to investigate the response of a hysteretic-radiation damping model for earthquake-resistant design of monopiles, as it is expected that such a model would provide more realistic predictions of the earthquake response of the offshore structure. Hysteresis damping could be implemented by a dissimilar definition of the soil spring stiffness in loading (tangent) and unloading (secant). Radiation damping can be implemented by a dashpot in parallel to an elastic spring as in Boulanger et al. [13].

2. **The radiation dashpot**. The parallel configuration of the radiation dashpot with the elastic ánd plastic spring caused excessive radiation damping in the current inelastic model in this study. It is advised to only allow action of a radiation viscous dashpot in parallel to a linear elastic spring in the element, as this spring represents the linear elastic low amplitude response which in reality is damped by radiation energy dissipation.

3. **Computation of radiation damping**. The definition by Wang et al. [99] was used to define the constant value of the viscous dashpot at each node. It is recommended to investigate the sensitivity of the soil-structure response to changes in the damping parameters, especially with regard to large diameter effects and the estimated shear wave velocity. It is advised to compare how the definition by Wang et al. compares to other definitions of shear wave radiation damping.

4. **Omitted inelastic effects by earthquakes**. Hysteresis and radiation were already identified to be of significant influence in seismic response analysis, and are important inelastic effects that should be (more correctly) implemented in the model. Of other hysteresis effects, such as drag friction damping by gap formation, the influence should be assessed; this hysteresis gap-drag damping proved important for small cylinder piles in unsaturated soil [13][97][31][1], and its influence for large diameter monopiles is

saturated soil is recommended to be investigated. In this study, gap formation and drag participation around a subaqueous soil-pile contact were assumed insignificant, but no definite assessment on the matter was made.

5. **Large diameter effect**. The p-y curves in the recommended practice by API [2] and DNV-GL [28] were empirically derived for slender piles. The empirical equations and coefficients should be validated for large diameter monopiles.

6. **High amplitude loading**. The empirical equations were derived from low cycle amplitude loading tests. It should be validated how these p-y curves represent true soil resistance such as under high amplitude seismic loading.

7. **Liquefaction**. In loose sand such as in this study, the sand layer is expected to compact. The excessive build of pore water pressure in highly dynamic loading such as earthquakes is likely to make the sand particles lose contact. The loss of soil structure, called liquefaction, is of major concern in earthquake-resistant design of bottom-fixed structures in soft saturated soils. Liquefaction was not simulated in this study, but investigation of the onset of liquefaction through IDA and the influence of liquefaction on the response of a monopile foundation is highly recommended.

8. **Vertical resistance and three-dimensional effect**. The model was simplified to a one-plane, one-dimensional contact problem in lateral direction with p-y curves expressing the soil resistance to lateral motion of the pile. However, in reality, external forces may act in all possible directions and angles to the structure, and true responses will be three-dimensional. It is recommended to add soil resistance to vertical motion of the pile (by t-z and q-z curves [2]), as under earthquake motion the structure will also be forced in vertical direction. The implementation of independent p-y springs neglects interaction between soil layers, radial and three-dimensional effects. An assessment of the influence of the independent spring formulation compared to more complex three-dimensional FEM is recommended.

The Analysis Method and External Forces

1. **Time history analysis**. Considering the already high degree of nonlinearity in the soil-structure response for moderate ground motion, it is recommended to prefer time history analysis over spectral analysis of piled structures to earthquake loading. This because nonlinear responses of the soil-structure system not only depend on the amplitude of the motion, but also on the frequency and duration.

2. **Modal reduction**. Modal reduction was applied in this study to reduce the computation time of the coupled nonlinear equations of motion, as time history analysis of the full coupled system proved too computationally expensive. However, modal reduction is a linear reduction technique, where changes in the mode shape due to changes in the soil foundation stiffness by its nonlinear behaviour to pile motion are not accounted for. The mode shapes during large earthquake ground motion may be significantly different due to the weakened stiffness of the foundation. Assuming constant mode shapes over the time history is thus a simplification of the true nonlinear response of the system, of which the impact on that response should be investigated.

3. **Loading direction**. All forces were assumed to act co-planar and co-directional. This is however just one of many possible loading combinations that may exist. The response to wind, waves, earthquakes and thrust acting in different directions should be investigated. It should also be assessed how much influence the rotor damping has if it is not aligned with the wind, wave and earthquake loading direction.

4. **Use of only one earthquake record**. It was already assessed in the literature review prior to this study [95] that no two earthquake records are the same, and consequently one earthquake record cannot capture all possible seismic response behaviour of a structure. Statistical approaches such as incremental dynamic analysis where the amplitude of one earthquake record is scaled to all probable intensity levels, is able to capture the variability in amplitude of earthquake ground motion. However, it does not account for variation in frequency and duration of the signal, which are the two other factors of large influence to the expected nonlinear inelastic responses of the system. Therefore it is advised to perform IDA with multiple distinct earthquake records, preferably from different earthquake events of comparable or different magnitude.

5. **Consideration of only one earthquake direction of action**. In this study, the earthquake was assumed to have only a horizontal motion component in one plane. However, in reality, the earthquake motion is recorded in one more horizontal and one vertical direction. Improvement to the current model could be achieved by implementing the earthquake motion in all three directions.

6. **Steady wind and regular waves**. In reality, the wind is turbulent and the waves irregular. It is recommended to implement a turbulence model for the wind (e.g. Kaimal spectrum) and an irregular wave spectrum (e.g. JONSWAP).

7. **Source-to-site effects**. In further detailed studies, it would be worthwhile to investigate the attenuation of the recorded earthquake signal by distance and site effects. In this study, the recordings of an onshore seismographic station were used. It leads to question how this signal would be altered by the saturated soft soil between the onshore station and the offshore location.

8. **The governing design load case**. Now, only the combination of earthquake ground motion with Normal Sea State conditions was assessed, under operational and shutdown mode of the rotor. It is however possible that combinations with other sea or wind states (e.g. ESS, ETM [46] or tsunamis) may be the response driving load case. Also other operation modes of the rotor, such as parked or fault, should be assessed.

9. **Fatigue analysis**. Only ultimate analysis was conducted in the study. From the change in natural frequency over time with weakening of the soil, it became clear that not only fatigue in the higher modes of the structure is likely by earthquake ground motion. Also more signification short duration fatigue damage may be sustained when the frequency progresses to resonance with the 1P rotor frequency and wave loads. It is hence advised to perform fatigue analysis studies when a reliable model for ultimate analysis has been established.

The Site Response Analysis Method

1. **Sensitivity of the soil-structure response**. A sensitivity study should be conducted to investigate the influence of variation in the site response analysis parameters on the soil-structure response. Other studies have identified the poor correlation between SRA computed results and borehole data, and the large impact of inaccurate SRA input to the soil-structure response [13][31][1]. Also in this thesis research it was encountered that SRA results do not always match realistic expectations. It is recommended to use borehole data as input to the SSI model (if this is available), or to invest in validation studies of the current SRA models as they introduce to much uncertainty in seismic soil-structure analyses as it is now.

2. **Linear versus nonlinear SRA**. Based on literature [1][31][13][42][41][89], nonlinear site response analysis should have been used in this study as the ground motions were considered moderate to strong. However, the poor results from NERA and DEEPSOIL software [8][37] forced the author to use equivalent linear software (EERA [7] and linear DEEPSOIL [37]). It is recommended to investigate the numerical sensitivity of the nonlinear site response analysis software, to assess the sensitivity of nonlinear results to the computation input, and to validate the nonlinear SRA output with borehole data. This to arrive at a reliable nonlinear SRA computation method for moderate and strong ground motion. But by the high degree of uncertainty in modeling the soil characteristics, it is reckoned that this will be an extensive task involving quantification of source and source-to-site effects as identified in the literature study preceding this thesis research [95].

The Structure and Structural Model

1. **Material damping**. Material damping was ignored in the model. It is advised to include mass- and stiffness-proportional damping, and to assess the influence on the response of the SSI system under earthquake loads. This can give an indication of the importance of material damping in seismic design.

2. **Other foundation options**. Considering the long list of uncertainties and improvement points in the seismic design of bottom-fixed monopile foundations for offshore wind in earthquake zones, it may be advisable to assess the feasibility of other foundation concepts that would be largely unaffected by ground motion or would not have such a high elastic demand, e.g. floating solutions or jacket structures.

Bibliography

[1] Allotey, N. and El Naggar, M.H. Generalized Dynamic Winkler Model for Nonlinear Soil–Structure Interaction Analysis. *Canadian Geotechnical Journal*, 45(4):560–573, April 2008.

[2] American Petroleum Institute. *Recommended Practice for Planning, Designing and Constructing Fixed Offshore Platforms - Working Stress Design*. API, Washington D.C. (USA), 21st edition, December 2000. Offshore Recommended Practice 2A-WSD.

[3] American Petroleum Institute. *Recommended Practice for Geotechnical and Foundation Design Considerations*. API, Washington D.C. (USA), 1st edition, April 2011. Offshore Recommended Practice 2GEO.

[4] Arslan, H. and Siyahi, B. A Comparative Study on Linear and Nonlinear Site Response Analysis. *Environmental Geology - International Journal of Geosciences*, 50(8):1193–1200, September 2006.

[5] Assareh, M.A. and Asgarian, B. Nonlinear Behavior of Single Piles in Jacket Type Offshore Platforms Using Incremental Dynamic Analysis. *American Journal of Applied Sciences*, 5(12):1793–1803, December 2008.

[6] Azrbakht, A. and Dolšek, M. Progressive Incremental Dynamic Analysisfor First-Mode Dominated Structures. *Journal of Structural Engineering*, 137(3):445–455, March 2011. American Society of Civil Engineers.

[7] Bardet, J.P., Ichii, K., and Lin, C.H. *EERA - A Computer Program for Equivalent-linear Earthquake site Response Analyses of Layered Soil Deposits*. University of Southern California Department of Civil Engineering, Los Angeles, California (USA), August 2000.

[8] Bardet, J.P. and Tobita, T. *NERA - A Computer Program for Nonlinear Earthquake site Response Analyses of Layered Soil Deposits*. University of Southern California Department of Civil Engineering, Los Angeles, California (USA), April 2001.

[9] Basu, D. and Salgado, R. Elastic Analysis of Laterally Loaded Pile in Multi-Layered Soil. *Geomechanics and Geoengineering*, 2(3):183–196, September 2007.

[10] Basu, D., Salgado, R., and Prezzi, M. Analysis of Laterally Loaded Piles in Multilayered Soil Deposits. Research Report FHWA/IN/JTRP-2007/23, Department of Civil Engineering, Purdue University, West Lafayette, Indiana (USA), May 2008. Joint Transportation Research Program.

[11] BMT Argoss. WaveClimate Wind and Wave Database. `waveclimate.com`, June 2018. Data granted without expense for research purposes.

[12] Boulanger, R. *The PySimple1 Material*. University of California at Davis, Davis, California (USA), 2010 edition, March 2010. OpenSees Command Manual.

[13] Boulanger, R.W., Curras, C.J., Kutter, B.L., Wilson, D.W., and Abghari, A. Seismic Soil-Pile-Structure Interaction Experiments and Analyses. *Journal of Geotechnical and Geoenvironmental Engineering*, 125(9):750–759, September 1999.

[14] Boulanger, R.W., Kutter, B.L., S.J., Brandenberg, Singh, P., and Chang, D. Pile Foundations in Liquefied and Laterally Spreading Ground During Earthquakes: Centrifuge Experiments and Analyses. Research Report UCD/CGM-03/01, Center for Geotechnical Modeling, Department of Civil and Environmental Engineering, College of Engineering, University of California at Davis, Davis, California (USA), September 2003. Research supported by the California Department of Transportation under contract 59A0162.

[15] Brandenberg, S.J., Zhao, M., Boulanger, R.W., and Wilson, D. P-y Plasticity Model for Nonlinear Dynamic Analysis of Piles in Liquefiable Soil. *Journal of Geotechnical and Geoenvironmental Engineering*, 139(8):847–863, August 2013.

[16] Burton, T., Jenkins, N., Sharpe, D., and Bossanyi, E. *Wind Energy Handbook*. John Wiley & Sons, Ltd., West Sussex (UK), 2nd edition, 2011.

[17] Central Weather Bureau. Geophysical Database Management System. `http://gdms.cwb.gov.tw/index.php`, 2008.

[18] Central Weather Bureau Seismology Center. Earthquakes. `https://www.cwb.gov.tw/V7e/earthquake/`, 2018.

[19] Chehouri, Younes R., A., Ilinca, A., and Perron, J. Review of Performance Optimization Techniques Applied to Wind Turbines. *Journal of Applied Energy*, 142:361–388, March 2015. American Society of Civil Engineers.

[20] Choobbasti, A.J. and Zahmatkesh, A. Computation of Degradation Factors of p-y Curves in Liquefiable Soils for Analysis of Piles Using Three-Dimensional Finite-Element Model. *Soil Dynamics and Earthquake Engineering*, 89:61–74, July 2016.

[21] Clough, R.W. and Penzien, J. *Part V - Earthquake Engineering*. Dynamics of Structures. Computers and Structures Inc., Berkeley, California (USA), 3rd edition, 2003.

[22] Construction and Planning Agency. *Seismic Design Code and Commentary for Buildings*. Ministry of Interior Affairs, Taipei (Taiwan), 2011 edition, 2011. Only available in Chinese.

[23] Council, Global Wind Energy. Global Cumulative Offshore Wind Capacity in 2017. `http://gwec.net/global-figures/global-offshore/`, 2017.

[24] Dash, S., Rouholamin, M., Lombardi, D., and Bhattacharya, S. A Practical Method for Construction of p-y Curves for Liquefiable Soils. *Soil Dynamics and Earthquake Engineering*, 97:478–481, June 2017.

[25] Deep Foundations Institute. P-Y Curves: Definition. `http://www.findapile.com/p-y-curves/definition`, 2013. International Association of Foundation Drilling.

[26] Deere, D.U. and Deere, D.W. The Rock Quality Designation (RQD) Index in Practice. *Rock Classification Systems for Engineering Purposes*, pages 91–101, February 1988. ASTM STP 984.

[27] Det Norske Veritas AS - Germanischer Lloyd. *Design of Offshore Wind Turbine Structures*. DNV GL AS, Høvik (Norway), 2014 edition, May 2014. Offshore Standard DNV-OS-J101.

[28] Det Norske Veritas AS - Germanischer Lloyd. *Support Structures for Wind Turbines*. DNV GL AS, Høvik (Norway), 2016 edition, April 2016. Offshore Standard DNVGL-ST-0126.

[29] Dobry, R., Taboada, V., and Liu, L. Centrifuge modelling of liquefaction effects during earthquakes. In *1st International Conference on Earthquake Geotechnical Engineering*, pages 14–16. International Journal for Numerical and Analytical Methods in Geomechanics, January 1997.

[30] Effendi, M.K. and Uckan, E. True Nonlinear Seismic Response Analyses of Soil Deposits. *Procedia Engineering*, 54:387–400, 2013. The 2nd International Conference on Rehabilitation and Maintenance in Civil Engineering (ICRMCE).

[31] El Naggar, M.H., Shayanfar, M., Kimiaei, M., and Aghakouchak, A. Simplified BNWF Model for Nonlinear Seismic Response Analysis of Offshore Piles with Nonlinear Input Ground Motion Analysis. *Canadian Geotechnical Journal*, 42(2):365–380, April 2005.

[32] European Committee for Standardization. *Design of Structures for Earthquake Resistance - Part 5: Foundations, Retaining Structures and Geotechnical Aspects*. The European Union, Brussels (Belgium), 2004 edition, November 2004. Design Standard EN 1998-5.

[33] Gazetas, G. and Dobry, R. Horizontal Response of Piles in Layered Soils. *International Journal of Geotechnical Engineering*, 110(1):20–40, 1984.

[34] Georgiadis, M. Development of P-y Curves for Layered Soils. In *Geotechnical Practice in Offshore Engineering*, pages 536–545. ASCE, 1983.

[35] Goter, S.K. Map Showing Global Distribution of Seismicity 1977-1986. `https://pubs.er.usgs.gov/publication/gp989`, 1988. Prepared by National Earthquake Information Center, World Data Center A for Seismology - Geophysical Investigation Map 989.

[36] Hansen, M.L. The Classical Blade Element Momentum Method. In *Aerodynamics of Wind Turbines*, pages 45–62. Earthscan, 2008.

[37] Hashash, Y.M.A., Musgrove, M.I., Harmon, J.A., Ilhan, O., Groholski, D.R., Phillips, C.A., and Park, D. *DEEPSOIL - Nonlinear and Equivalent Linear Seismic Site Response of One-Dimensional Soil Columns*. Department of Civil and Environmental Engineering University of Illinois at Urbana-Champaign, Illinois (USA), 7 edition, Februari 2018.

[38] Heidari, M., El Naggar, H., Jahanandish, M., and Ghahramani, A. Generalized Cyclic P–y Curve Modeling for Analysis of Laterally Loaded Piles. *Soil Dynamics and Earthquake Engineering*, 63:138–149, August 2014.

[39] Hoek, E. *Practical Rock Engineering*. University of Toronto, Toronto, Ontario (Canada), 2006.

[40] Hoek, E. and Diederichs, M.S. Empirical Estimation of Rock Mass Modulus. *International Journal of Rock Mechanics and Mining Science*, 43(2):203–215, February 2006.

[41] Hosseini, S.M.M.M. and Pajouh, M.A. Comparative Study on the Equivalent Linear and Fully Nonlinear Site Response Analysis Approaches. *Arabian Journal of Geosciences*, 5(4):587–597, July 2012. Also appeared under the title "The Limitations of Equivalent Site Response Analysis Considering Soil Nonlinearity Properties" in the proceedings of the fifth International Conference on Recent Advances in Geotechnical Earthquake Engineering and Soil Dynamics (May 2010).

[42] Hosseini, S.M.M.M. and Pajouh, M.A. Comparative Study on the Equivalent Linear and Fully Nonlinear Site Response Analysis Approaches. *Arabian Journal of Geosciences*, 5(4):587–597, July 2012. Also appeared under the title Limitations of Equivalent Site Response Analysis Considering Soil Nonlinearity Properties in the proceedings of the fifth International Conference of Recent Advances in Geotechnical Earthquake Engineering and Soil Dynamics (May 2010).

[43] Hoving, J.S. Offshore Foundation Design Theory. Lecture slides course Bottom Founded Offshore Structures, December 2015. TU Delft, Delft (Netherlands).

[44] Hutchinson, J.R. Shear Coefficients for Timoshenko Beam Theory. *Journal of Applied Mechanics*, 68: 87–92, January 2001.

[45] IEC technical committee 88: Wind turbines. *Wind Turbines - Part 3: Design Requirements for Offshore Wind Turbines*. International Electrotechnical Commission, Geneva (Switzerland), 1st edition, Februari 2009.

[46] IEC technical committee 88: Wind turbines. *Wind Turbines - Part 1: Design Requirements*. International Electrotechnical Commission, Geneva (Switzerland), 3.1st edition, April 2014.

[47] Institute of Earth Sciences Academia Sinica. Strong Motion and Mobil Seismic Networks. `http://www.earth.sinica.edu.tw/~smdmc/`, 2016.

[48] International Organization for Standardization. *Petroleum and Natural Gas Industries - Fixed Steel Offshore Structures*. Technical Committee ISO/TC 67/SC 7, Offshore structures, Geneva (Switzerland), 1st edition, 2007.

[49] International Organization for Standardization. *Petroleum and Natural Gas Industries - Specific Requirements for Offshore Structures - Part 2: Seismic Design Procedures and Criteria*. Technical Committee ISO/TC 67, Materials, equipment and offshore structures for petroleum, petrochemical and natural gas industries, Subcommittee 7, Offshore structures, Geneva (Switzerland), 2nd edition, 2017.

[50] Jia, J. Lateral Force–Displacement of Piles—p-y Curve. In *Soil Dynamics and Foundation Modeling - Offshore and Earthquake Engineering*, chapter 16, pages 481–519. Springer, Cham (Switzerland), 2018.

[51] Jonkman, J., Butterfield, S., Musial, W., and Scott, G. Definition of a 5-MW Reference Wind Turbine for Offshore System Development. Technical Report NREL/TP-500-38060, National laboratory of the U.S. Department of Energy Office of Energy Efficiency and Renewable Energy Operated by the Alliance for Sustainable Energy, LLC, Golden, Colorado (USA), February 2009.

[52] Journée, J.M.J. and Massie, W.W. Rigid Body Dynamics. In *Offshore Hydromechanics*, chapter 6, pages 209–365. Delft University of Technology, Delft (Netherlands), 2001.

[53] Kaynia, A.M. Seismic Considerations in Design of Offshore Wind Turbines. *Soil Dynamics and Earthquake Engineering*, May 2018. Article in press.

[54] Lancellotta, R. *Geotechnical Engineering*. Taylor & Francis, 2nd edition, 2009. p. 172.

[55] Lasley, S.J., Green, R.A., and Rodriguez-Marek, A. Comparison of Equivalent-Linear Site Response Analysis Software. In *Proceedings of the 10th US National Conference on Earthquake Engineering*, Anchorage, Alaska (USA), July 2014. Earthquake Engineering Research Institute.

[56] Laszlo, A., Bhattacharya, S., Macdonald, J., and Hogan, S.J. Design of Monopiles for Offshore Wind Turbines in 10 Steps. *Soil Dynamics and Earthquake Engineering*, 92:126–152, January 2017.

[57] Lee, C.-T., Cheng, C.-T., Liao, C.-W., and Tsai, Y.-B. Site Classification of Taiwan Free-Field Strong-Motion Stations. *Bulletin of the Seismological Society of America*, 91(5):1283–1297, October 2004.

[58] Lee, C.-T. and Tsai, B.-R. Mapping Vs30 in Taiwan. *Terrestrial Atmospheric and Oceanic Sciences*, 19(6): 671–682, December 2008.

[59] Lee, W.H.K., Kanamori, H., Jennings, P.C., and Kisslinger, C. *International Handbook of Earthquake and Engineering Seismology*, volume 81B of *International Geophysics Series*. Academic Press, San Diego, California (USA), 1st edition, 2003.

[60] Liang, F., Chen, H., and Jia, Y. Quasi-Static P-y Hysteresis Loop for Cyclic Lateral Response of Pile Foundations in Offshore Platforms. *Ocean Engineering*, 148:62–74, January 2018.

[61] Lombardi, D. and Bhattacharya, S. Evaluation of Seismic Performance of Pile-supported Models in Liquefiable Soils. *Earthquake Engineering & Structural Dynamics*, 45(6):1019–1038, February 2016. International Association for Earthquake Engineering.

[62] Lu, T., Huo, J., and Rong, M. Nonlinear Response Analysis of Soil Layers Under Severe Earthquake. *Procedia Environmental Sciences*, 12(B):940–948, 2012. 2011 International Conference of Environmental Science and Engineering.

[63] MacCamy, R.C. and Fuchs, R.A. Wave Forces on Piles: A Diffraction Theory. Technical Memorandum 69, U.S. Army Corps of Engineers, Beach Erosion Board, December 1954.

[64] Martin, A.J. and Diehl, J.G. Practical Experience Using a Simplified Procedure to Measure Average Shear-Wave Velocity to a Depth of 30 Meters (Vs30). In *13th World Conference on Earthquake Engineering*, August 2004. Paper No. 952.

[65] Matlock, H. Correlation for Design of Laterally Loaded Piles in Soft Clay. In *Proceedings of the 2nd Annual Offshore Technology Conference*, pages 577–588, 1970. paper no. OTC 1204.

[66] McKenna, F. and Fenves, G.L. and Filippou, F.C. and Scott, M. and Elgamal, A. and Yang, Z. and Lu, J. and Arduino, P. and McKenzie, P. and Deierlein, G.G. and Law, K. Open System for Earthquake Engineering Simulation (OpenSees). `http://opensees.berkeley.edu/index.php`, 2006. University of California, Berkeley (USA).

[67] Meyer, B.J and Reese, L.C. Analysis of Single Piles Under Lateral Loading. Research Report 244-1, Center for Highway Research University of Texas, Austin, Texas (USA), December 1979.

[68] Newmark, N.M. and Rosenblueth, E. *Fundamentals of Earthquake Engineering*. Prentice-Hall Inc., Englewood Cliffs, New Jersey (USA), 1th edition, 1971.

[69] Ning, S.A. 5 MW Aerodynamic Files. https://github.com/WISDEM/CCBlade/tree/master/test/5MW_AFFiles, 2013.

[70] Nixon, J.B. Verification of the Weathered Rock Model for P-y Curves. Master's thesis, North Carolina State University, Faculty of Civil Engineering, Raleigh, North Carolina (USA), 2002.

[71] of Economic Affairs, Ministry. Energy Statistics. https://www.moea.gov.tw/MNS/english/content/ContentMenu.aspx?menu_id=1480, 2017.

[72] O'Neill, M.W. and Murchison, J.M. An Evaluation of P-y Relationships in Sands. Research Report GT-DF02-83, University of Houston, Department of Civil Engineering, Houston, Texas (USA), May 1983.

[73] Ordóñez, G.A. *SHAKE2000 - A Computer Program for the 1-D Analysis of Geotechnical Earthquake Engineering Problems*. GeoMotions LCC, Lacey, Washington (USA), 2005.

[74] Oñate, E. *Structural Analysis with the Finite Element Method - Linear Statics*, volume 2 - Beams, Plates and Shells of *Lecture Notes on Numerical Methods in Engineering and Sciences*. Springer, Technical University of Catalonia, Barcelona (Spain), 1st edition, 2013.

[75] Pineda, I. (ed.). *Offshore Wind in Europe - Key trends and statistics 2017*. WindEurope, Brussels (Belgium), 2017 edition, February 2018.

[76] Q.T. Convergent Boundary, Transform Boundary, Divergent Boundary. https://www.thinglink.com/scene/731240248696111105, 2015.

[77] Rahmani, A., Taiebat, M., Finn, W.D.L., and Ventura, C.E. Determination of dynamic p-y curves for pile foundations under seismic loading. In *15th World Conference on Earthquake Engineering*. WCEE, September 2012.

[78] Reese, L.C. Analysis of Laterally Loaded Piles in Weak Rock. *Journal of Geotechnical and Geoenvironmental Engineering*, 123(11):1010–1017, November 1997.

[79] Reese, L.C. and Van Impe, W.F. Models for Response of Soil and Weak Rock - Method of Georgiadis. In *Single Piles and Pile Groups Under Lateral Loading*, chapter 3. CRC Press Taylor & Francis Group, Boca Raton, Florida (USA), 2nd edition, 2011.

[80] Reuters. Earthquake in Taiwan: At least 14 dead in 6.4 magnitude quake, over 100 missing. Online archive Financial Express https://www.financialexpress.com/world-news/earthquake-in-taiwan-6-4-magnitude-quake-kills-at-least-12-destroys-17-storey-apartment-block/208317/, February 2016.

[81] Shin, T.C., Tsai, Y.B., Yeh, Y.T., Liu, C.C., and Wu, Y.M. Strong-Motion Instrumentation Programs in Taiwan. In Lee, W.H.K., Kanamori, H., Jennings, P.C., and Kisslinger, C., editors, *International Handbook of Earthquake and Engineering Seismology Part 81B*, pages 1057–1062. Academic Press, San Diego, 2003. International Geophysics Series.

[82] Shin, T.-C., Chang, C.-H., Pu, H.-C., Lin, H.-W., and Leu, P.-L. The Geophysical Database Management System in Taiwan. *Terrestrial Atmospheric and Oceanic Sciences*, 24(1):11–18, February 2013. Central Weather Bureau, Taipei, Taiwan.

[83] Su, D. and Yan, W.M. A Multidirectional p-y Model for Lateral Sand-Pile Interactions. *Soils and Foundations*, 53(2):199–214, February 2013.

[84] Sumer, B.M. and Fredsøe, J. *Hydrodynamics around Cylindrical Structures*, volume 26 of *Advanced Series on Ocean Engineering*. World Scientific, Technical University of Denmark, Lyngby (Denmark), revised edition, 2006.

[85] Suzuki, P.T., Maloney, D., and Hamre, L. Influence of Layered Soil Profiles on the Application of p-y Curves for Large Diameter Monopiles. In Randolph, M.F. et al., editor, *Proceedings of the 1st Vietnam Symposium on Advances in Offshore Engineering - Energy and Geotechnics*, pages 415–420. Springer, 2019.

[86] Tabesh, A. and Poulos, H.G. The Effects of Soil Yielding on Seismic Response of Single Piles. *Soils and Foundations*, 41(3):1–16, June 2001.

[87] Terzaghi, K., Peck, R.B., and Mesri, G. *Soil Mechanics in Engineering Practice*. John Wiley & Sons, Inc., 3rd edition, 1996. p. 22.

[88] T.L., Holzer., Borcherdt, R.D., and Eaton, G.P. The Loma Prieta, California, Earthquake of October 17, 1989 – Strong Ground Motion. Professional Paper 1551-A, United States Geological Survey, 1994.

[89] Tombari, A., El Naggar, M.H., and Dezi, F. Impact of Ground Motion Duration and Soil Non-linearity on the Seismic Performance of Single Piles. *Soil Dynamics and Earthquake Engineering*, 100:72–87, September 2017.

[90] Tsai, Y.-B. and Lee, C.-P. Strong Motion Instrumentation Programs in Taiwan - Past and Present. In Gülkan, P. and Anderson, J.G., editors, *Directions in Strong Motion Instrumentation*, pages 255–278. Springer, Dordrecht, 2005. Nato Science Series: IV: Earth and Environmental Sciences book series, vol. 58).

[91] U.S. Army Corps of Engineers. Water Wave Mechanics. In *Coastal Engineering Manual Part II – Coastal Hydrodynamics*, chapter 1, page 5. Coastal Hydraulics Laboratory Publication, 2008. Em 1110-2-1100.

[92] Valamanesh, V. and Myers, A.T. Aerodynamic Damping and Seismic Response of Horizontal Axis Wind Turbine Towers. *Journal of Structural Engineering*, 140(11), November 2014. American Society of Civil Engineers.

[93] Vamvatsikos, D. and Cornell, C.A. Incremental Dynamic Analysis. *Earthquake Engineering and Dynamic Analysis*, 31(3):491–514, March 2002.

[94] Van Buren, E. and Muskulus, M. Improving Pile Foundation Models for Use in Bottom-Fixed Offshore Wind Turbine Applications. In Tande, J.O.G., Kvamsdal, T., and Dahlhaug, O.G., editors, *Energy Procedia*, pages 363–370. Elsevier, January 2012. Selected papers from Deep Sea Offshore Wind R&D Conference, Trondheim, Norway, 19-20 January 2012.

[95] Van de Putte, V.C. Specialization Project - A Review of Earthquake Engineering with Regard to Offshore Wind Support Structure Design. Literature review, Norwegian University of Science and Technology, February 2018.

[96] van der Tempel, J. Design of Support Structures for Offshore Wind Turbines. Master's thesis, Delft University of Technology, Delft (Netherlands), 2006. DUWIND, report 2006.029.

[97] Wallace, J.W., Fox, P.J., Stewart, J.P., Janoyan, K., Qiu, T., and Lermitte, S.P. Cyclic Large Deflection Testing of Shaft Bridges Part II: Analytical Studies. Research report, University of California, Department of Civil and Environmental Engineering, Los Angeles, California (USA), March 2002. Research report for the California Department of Transportation (Caltrans).

[98] Wang, G. and Sitar, N. Nonlinear Analysis of a Soil-Drilled Pier System under Static and Dynamic Axial Loading. Report 2006/06, Pacific Earthquake Engineering Research Center, Berkeley, California (USA), November 2006.

[99] Wang, S., Kutter, B.L., Chacko, M.J., Wilson, D.W., Boulanger, R.W., and Abghari, A. Nonlinear Seismic Soil-Pile Structure Interaction. *Earthquake Spectra*, 14(2):377–396, May 1998.

[100] World Maps. Active Volcanoes in the US. `https://canyontxcountryclub.com/136610_active_volcanoes_in_the_us_map/`, 2018.

[101] Yang, M., Ge, B., Li, W., and Zhu, B. Dimension Effect on P-y Model Used for Design of Laterally Loaded Piles. *Procedia Engineering*, 143:598–606, June 2016.

[102] Yokoyama, T. Parametric Instability of Timoshenko Beams Resting on an Elastic Foundation. *Computers and Structures*, 28(2):207–216, 1988.

[103] Yokoyama, T. Vibrations of a Hanging Timoshenko Beam under Gravity. *Journal of Sound and Vibration*, 141(2):245–258, September 1990.

A

Summary of the Static P-y Curves

Table A.1 summarizes all used equations and assumed parameters in computing the ultimate soil resistance p_{ult} and soil resistance p per unit length for the static p-y curves in the nonlinear elastic soil-structure interaction model.

Table A.1: *Summary of the equations and parameters used to compute construct the nonlinear elastic seismic soil-structure interaction model.*

Layer	Behaves as	Equations	Parameters	Thickness	Loading	Corrections
Sand	Sand below the water table	O'Neill & Murchison [72]	$\rho' = 897\,\text{kg/m}^3$ $\phi = 25°$	5.7 m	Cyclic	Soil layering [34]
Clay	Soft clay below the water table	Matlock [65]	$\rho' = 958\,\text{kg/m}^3$ $\sigma_u = 55\,\text{kN/m}^2$ $\epsilon_{50} = 1.000$	7.3 m	Cyclic	Soil layering [34]
Mudstone	Weak rock	Reese [78]	$\rho' = 1009\,\text{kg/m}^3$ $\sigma_u = 150\,\text{kN/m}^2$ $\epsilon_{50} = 0.018$	20.3 m	–	Soil layering [34]
Gravel	Sand below the water table	O'Neill & Murchison [72]	$\rho' = 1019\,\text{kg/m}^3$ $\phi = 32°$	9.7 m	Cyclic	Soil layering [34]
Sandstone	Weak rock	Reese [78]	$\rho' = 1009\,\text{kg/m}^3$ $\sigma_u = 265\,\text{kN/m}^2$ $\epsilon_{50} = 0.018$	7 m	–	Soil layering [34]

B

Structural and Aerodynamic Blade Properties

The structural and aerodynamic properties of the NREL MW rotor blades are those as stated in the reference work by Jonkman et al. [51] of the National Renewables Energy Laboratory. These blade properties in Tables B.1 to B.3 are used together with the properties from Table 3.7 to compute the axial thrust force and aerodynamic damping by the operational rotor in the blade element momentum algorithm in MATLAB.

Table B.1: *NREL 5 MW blade structural properties [51].*

Structural properties	
Length	61.5 m
Overall mass	17,740 kg

Table B.2: *Distributed blade aerodynamic properties of the NREL 5 MW reference turbine [51]. The drag and lift coefficients associated with the airfoil for different angles of attack can be downloaded from [69].*

Node	**Radius**	**Twist**	**Chord**	**Airfoil**
1	2.8667 m	13.308°	3.542 m	Cylinder C_d =0.5
2	5.6000 m	13.308°	3.854 m	Cylinder C_d =0.5
3	8.3333 m	13.308°	4.167 m	Cylinder C_d =0.35
4	11.7500 m	13.308°	4.557 m	DU40-A17
5	15.8500 m	11.480°	4.652 m	DU35-A17
6	19.9500 m	10.162°	4.458 m	DU35-A17
7	24.0500 m	9.011°	4.249 m	DU30-A17
8	28.1500 m	7.795°	4.007 m	DU25-A17
9	32.2500 m	6.544°	3.748 m	DU25-A17
10	36.3500 m	5.361°	3.502 m	DU21-A17
11	40.4500 m	4.188°	3.256 m	DU21-A17
12	44.5500 m	3.125°	3.010 m	NACA64-A17
13	48.6500 m	2.319°	2.764 m	NACA64-A17
14	52.7500 m	1.526°	2.518 m	NACA64-A17
15	56.1667 m	0.863°	2.313 m	NACA64-A17
16	58.9000 m	0.370°	2.086 m	NACA64-A17
17	61.6333 m	0.106°	1.419 m	NACA64-A17

Table B.3: *Relation between pitch angle of the blades and incoming wind speed for the NREL 5 MW variable speed, collective pitch reference turbine [51].*

Pitch angle	**Wind speed**	**Rotor speed**
0.00°	11.4 m/s	12.1 rpm
3.83°	12.0 m/s	12.1 rpm
6.60°	13.0 m/s	12.1 rpm
8.70°	14.0 m/s	12.1 rpm
10.45°	15.0 m/s	12.1 rpm
12.06°	16.0 m/s	12.1 rpm
13.54°	17.0 m/s	12.1 rpm
14.92°	18.0 m/s	12.1 rpm
16.23°	19.0 m/s	12.1 rpm
17.47°	20.0 m/s	12.1 rpm
18.70°	21.0 m/s	12.1 rpm
19.94°	22.0 m/s	12.1 rpm
21.18°	23.0 m/s	12.1 rpm
22.35°	24.0 m/s	12.1 rpm
23.47°	25.0 m/s	12.1 rpm

C

Two-Node Timoshenko Beam Finite-Element Formulation

C.1. Derivation of Element Matrices

A two-node Timoshenko beam element rests on an elastic foundation and is subjected to axial loading. The potential energy of a beam element U^e of length l is [102]:

$$U^e = \frac{1}{2}\int_0^l EI\left(\frac{d\theta}{dz}\right)^2 dz + \frac{1}{2}\int_0^l kGA\left(\frac{dy}{dz}-\theta\right)^2 dz + \frac{1}{2}\int_0^l k_f y^2 dz - \frac{1}{2}\int_0^l P\left(\frac{dy}{dz}\right)^2 dz \tag{C.1}$$

where P is the axial force.

The kinetic energy of a beam element T^e of length l is [102]:

$$T^e = \frac{1}{2}\int_0^l \rho A\left(\frac{dy}{dt}\right)^2 dz + \frac{1}{2}\int_0^l \rho I\left(\frac{d\theta}{dt}\right)^2 dz \tag{C.2}$$

A cubic displacement distribution for y is assumed over the element [102]:

$$y = a_0 + a_1 z + a_2 z^2 + a_3 z^3 \tag{C.3}$$

By considering the beam element in static equilibrium under the axial and soil pressure forces, the lateral displacement y and rotation θ can be expressed in terms of the nodal displacement vector [102]:

$$y = \begin{bmatrix} N_{y,1} & N_{y,2} & N_{y,3} & N_{y,4}\end{bmatrix}\cdot\begin{bmatrix} y_1 & \theta_1 & y_2 & \theta_2\end{bmatrix}^T = \underline{\underline{\mathbf{N}}}_{\nu}\cdot\underline{q}^e \tag{C.4}$$

$$\theta = \begin{bmatrix} N_{\theta,1} & N_{\theta,2} & N_{\theta,3} & N_{\theta,4}\end{bmatrix}\cdot\begin{bmatrix} y_1 & \theta_1 & y_2 & \theta_2\end{bmatrix}^T = \underline{\underline{\mathbf{N}}}_{\theta}\cdot\underline{q}^e \tag{C.5}$$

where, with $z/l = \xi$ and $\Phi = 12EI/\left(kGAl^2\right)$ [102]:

$$N_{y,1} = \frac{1-3\xi^2+2\xi^3+(1-\xi)\Phi}{1+\Phi} \tag{C.6}$$

$$N_{y,2} = \frac{\xi l - 2\xi^2 l + \xi^3 l + \left(\xi-\xi^2\right)\frac{\Phi}{2} l}{1+\Phi} \tag{C.7}$$

$$N_{y,3} = \frac{3\xi^2 - 2\xi^3 + \xi\Phi}{1+\Phi} \tag{C.8}$$

$$N_{y,4} = \frac{-\xi^2 l + \xi^3 l - \left(\xi-\xi^2\right)\frac{\Phi}{2} l}{1+\Phi} \tag{C.9}$$

$$N_{\theta,1} = \frac{-6\xi+6\xi^2}{l(1+\Phi)} \tag{C.10}$$

$$N_{\theta,2} = \frac{1-4\xi+3\xi^2+(1-\xi)\Phi}{1+\Phi} \tag{C.11}$$

$$N_{\theta,3} = \frac{6(\xi-\xi^2)}{l(1+\Phi)} \tag{C.12}$$

$$N_{y,1} = \frac{-2\xi+3\xi^2+\xi\Phi}{1+\Phi} \tag{C.13}$$

The flexural strain and shear strain within the element are [102]:

$$\kappa = \frac{d\theta}{dz} = \underline{\underline{\mathbf{B}}}_b \cdot \underline{q}^e \tag{C.14}$$

$$\psi = \frac{dy}{dz} - \theta = \underline{\underline{\mathbf{B}}}_s \cdot \underline{q}^e \tag{C.15}$$

with [102]:

$$\underline{\underline{\mathbf{B}}}_b = \frac{d}{dz}\underline{\underline{\mathbf{N}}}_\theta \tag{C.16}$$

$$\underline{\underline{\mathbf{B}}}_s = \frac{d}{dz}\underline{\underline{\mathbf{N}}}_y - \underline{\underline{\mathbf{N}}}_\theta = \underline{\underline{\mathbf{B}}}_y - \underline{\underline{\mathbf{N}}}_\theta \tag{C.17}$$

Equation C.1 and C.2 can be rewritten in terms of the nodal displacement vector $\underline{q}^e$ as [102]:

$$U^e = \frac{1}{2}\underline{q}^{e,T}\underline{\underline{\mathbf{K}}}_b^e\underline{q}^e + \frac{1}{2}\underline{q}^{e,T}\underline{\underline{\mathbf{K}}}_s^e\underline{q}^e + \frac{1}{2}\underline{q}^{e,T}\underline{\underline{\mathbf{K}}}_f^e\underline{q}^e - \frac{1}{2}\underline{q}^{e,T}\underline{\underline{\mathbf{K}}}_g^e\underline{q}^e \tag{C.18}$$

$$T^e = \frac{1}{2}\underline{\dot{q}}^{e,T}\underline{\underline{\mathbf{M}}}_t^e\underline{\dot{q}}^e + \frac{1}{2}\underline{\dot{q}}^{e,T}\underline{\underline{\mathbf{M}}}_r^e\underline{\dot{q}}^e \tag{C.19}$$

with the element bending stiffness matrix:

$$\underline{\underline{\mathbf{K}}}_b^e = \int_0^l \underline{\underline{\mathbf{B}}}_b^T EI\underline{\underline{\mathbf{B}}}_b\, dz \tag{C.20}$$

the element shear stiffness matrix:

$$\underline{\underline{\mathbf{K}}}_s^e = \int_0^l \underline{\underline{\mathbf{B}}}_s^T kGA\underline{\underline{\mathbf{B}}}_s\, dz \tag{C.21}$$

the element soil foundation stiffness matrix:

$$\underline{\underline{\mathbf{K}}}_f^e = \int_0^l \underline{\underline{\mathbf{N}}}_y^T k_f\underline{\underline{\mathbf{N}}}_y\, dz \tag{C.22}$$

the element geometric stiffness matrix:

$$\underline{\underline{\mathbf{K}}}_g^e = \int_0^l P\underline{\underline{\mathbf{B}}}_y^T\underline{\underline{\mathbf{B}}}_y\, dz \tag{C.23}$$

the element translational mass matrix:

$$\underline{\underline{\mathbf{M}}}_t^e = \int_0^l \underline{\underline{\mathbf{N}}}_y^T \rho A\underline{\underline{\mathbf{N}}}_y\, dz \tag{C.24}$$

and lastly, the element rotary inertia mass matrix:

$$\underline{\underline{\mathbf{M}}}_r^e = \int_0^l \underline{\underline{\mathbf{N}}}_\theta^T \rho I\underline{\underline{\mathbf{N}}}_\theta\, dz \tag{C.25}$$

The explicit expressions for the element bending and element shear stiffness matrix of the structural element are respectively [102][103]:

$$\underline{\underline{\mathbf{K}}}_b^e = \frac{EI}{l^2(1+\Phi)^2}\begin{bmatrix} 12 & 6l & -12 & 6l \\ 6l & \left(4+2\Phi+\Phi^2\right)l^2 & -6l & \left(2-2\Phi-\Phi^2\right)l^2 \\ -12 & -6l & 12 & -6l \\ 6l & \left(2-2\Phi-\Phi^2\right)l^2 & -6l & \left(4+2\Phi+\Phi^2\right)l^2 \end{bmatrix} \tag{C.26}$$

$$\underline{\underline{\mathbf{K}}}_s^e = \frac{kGA\Phi^2}{4l(1+\Phi)^2}\begin{bmatrix} 4 & 2l & -4 & 2l \\ 2l & l^2 & -2l & l^2 \\ -4 & -2l & 4 & -2l \\ 2l & l^2 & -2l & l^2 \end{bmatrix} \tag{C.27}$$

where Φ is the shear deformation parameter [102]:

$$\Phi = \frac{12EI}{kGAl^2} \tag{C.28}$$

The soil, here modeled as an elastic foundation, delivers stiffness to the system as well. The element foundation stiffness matrix becomes:

$$\underline{\underline{\mathbf{K}}}_f^e = \frac{k_f l}{(1+\Phi)^2}\begin{bmatrix} \frac{13}{35}+\frac{7\Phi}{10}+\frac{\Phi^2}{3} & \left(\frac{11}{210}+\frac{11\Phi}{120}+\frac{\Phi^2}{24}\right)l & \frac{9}{70}+\frac{3\Phi}{10}+\frac{\Phi^2}{6} & -\left(\frac{13}{420}+\frac{3\Phi}{40}+\frac{\Phi^2}{24}\right)l \\ \left(\frac{11}{210}+\frac{11\Phi}{120}+\frac{\Phi^2}{24}\right)l & \left(\frac{1}{105}+\frac{\Phi}{60}+\frac{\Phi^2}{120}\right)l^2 & \left(\frac{13}{420}+\frac{3\Phi}{40}+\frac{\Phi^2}{24}\right)l & -\left(\frac{1}{140}+\frac{\Phi}{60}+\frac{\Phi^2}{120}\right)l^2 \\ \frac{9}{70}+\frac{3\Phi}{10}+\frac{\Phi^2}{6} & \left(\frac{13}{420}+\frac{3\Phi}{40}+\frac{\Phi^2}{24}\right)l & \frac{13}{35}+\frac{7\Phi}{10}+\frac{\Phi^2}{3} & -\left(\frac{11}{210}+\frac{11\Phi}{120}+\frac{\Phi^2}{24}\right)l \\ -\left(\frac{13}{420}+\frac{3\Phi}{40}+\frac{\Phi^2}{24}\right)l & -\left(\frac{1}{140}+\frac{\Phi}{60}+\frac{\Phi^2}{120}\right)l^2 & -\left(\frac{11}{210}+\frac{11\Phi}{120}+\frac{\Phi^2}{24}\right)l & \left(\frac{1}{105}+\frac{\Phi}{60}+\frac{\Phi^2}{120}\right)l^2 \end{bmatrix} \tag{C.29}$$

where k_f is the soil spring stiffness, derived from the load-displacement relation of the p-y curves in Chapters 3.1.2 and 3.1.3, with the procedure explained in Chapter 4.6.

The axial load of the RNA and the self-weight of the structure will deliver geometric stiffness to the system, which reduces the overall stiffness of the system. The element geometric stiffness due to all overlying elements and due to the element itself are [103]:

$$\underline{\underline{\mathbf{K}}}^e_{g,0} = \frac{\sum_{e=1}^{E} W^{e-1} + W^{RNA}}{l\,(1+\Phi)^2} \begin{bmatrix} \frac{6}{5}+2\Phi+\Phi^2 & \frac{1}{10}l & -\left(\frac{6}{5}+2\Phi+\Phi^2\right) & \frac{1}{10}l \\ \frac{1}{10}l & \left(\frac{2}{15}+\frac{\Phi}{6}+\frac{\Phi^2}{12}\right)l^2 & -\frac{1}{10}l & -\left(\frac{1}{30}+\frac{\Phi}{6}+\frac{\Phi^2}{12}\right)l^2 \\ -\left(\frac{6}{5}+2\Phi+\Phi^2\right) & -\frac{1}{10}l & \frac{6}{5}+2\Phi+\Phi^2 & -\frac{1}{10}l \\ \frac{1}{10}l & -\left(\frac{1}{30}+\frac{\Phi}{6}+\frac{\Phi^2}{12}\right)l^2 & -\frac{1}{10}l & \left(\frac{2}{15}+\frac{\Phi}{6}+\frac{\Phi^2}{12}\right)l^2 \end{bmatrix} \tag{C.30}$$

$$\underline{\underline{\mathbf{K}}}^e_{g} = \frac{W^e}{l\,(1+\Phi)^2} \begin{bmatrix} \frac{3}{5}+\Phi+\frac{\Phi^2}{2} & \left(\frac{1}{10}+\frac{2\Phi}{15}+\frac{\Phi^2}{12}\right)l & -\left(\frac{3}{5}+\Phi+\frac{\Phi^2}{2}\right) & -\left(\frac{2\Phi}{15}+\frac{\Phi^2}{12}\right)l \\ \left(\frac{1}{10}+\frac{2\Phi}{15}+\frac{\Phi^2}{12}\right)l & \left(\frac{1}{30}+\frac{\Phi}{20}+\frac{\Phi^2}{24}\right)l^2 & -\left(\frac{1}{10}+\frac{2\Phi}{15}+\frac{\Phi^2}{12}\right)l & -\left(\frac{1}{60}+\frac{\Phi}{12}+\frac{\Phi^2}{24}\right)l^2 \\ -\left(\frac{3}{5}+\Phi+\frac{\Phi^2}{2}\right) & -\left(\frac{1}{10}+\frac{2\Phi}{15}+\frac{\Phi^2}{12}\right)l & \frac{3}{5}+\Phi+\frac{\Phi^2}{2} & \left(\frac{2\Phi}{15}+\frac{\Phi^2}{12}\right)l \\ -\left(\frac{2\Phi}{15}+\frac{\Phi^2}{12}\right)l & -\left(\frac{1}{60}+\frac{\Phi}{12}+\frac{\Phi^2}{24}\right)l^2 & \left(\frac{2\Phi}{15}+\frac{\Phi^2}{12}\right)l & \left(\frac{1}{10}+\frac{7\Phi}{60}+\frac{\Phi^2}{24}\right)l^2 \end{bmatrix} \tag{C.31}$$

where W^{RNA} is the weight of the rotor-nacelle assembly, equal to its mass time the gravitational acceleration constant, and W^e is the weight of one element, equal to:

$$W^e = \rho^e \cdot A^e \cdot l^e \cdot g \tag{C.32}$$

Lastly, the element mass matrix of respectively translational and rotational inertia are [102]:

$$\underline{\underline{\mathbf{M}}}^e_{t} = \frac{\rho A l}{(1+\Phi)^2} \begin{bmatrix} \frac{13}{35}+\frac{7\Phi}{10}+\frac{\Phi^2}{3} & \left(\frac{11}{210}+\frac{11\Phi}{120}+\frac{\Phi^2}{24}\right)l & \frac{9}{70}+\frac{3\Phi}{10}+\frac{\Phi^2}{6} & -\left(\frac{13}{420}+\frac{3\Phi}{40}+\frac{\Phi^2}{24}\right)l \\ \left(\frac{11}{210}+\frac{11\Phi}{120}+\frac{\Phi^2}{24}\right)l & \left(\frac{1}{105}+\frac{\Phi}{60}+\frac{\Phi^2}{120}\right)l^2 & \left(\frac{13}{420}+\frac{3\Phi}{40}+\frac{\Phi^2}{24}\right)l & -\left(\frac{1}{140}+\frac{\Phi}{60}+\frac{\Phi^2}{120}\right)l^2 \\ \frac{9}{70}+\frac{3\Phi}{10}+\frac{\Phi^2}{6} & \left(\frac{13}{420}+\frac{3\Phi}{40}+\frac{\Phi^2}{24}\right)l & \frac{13}{35}+\frac{7\Phi}{10}+\frac{\Phi^2}{3} & -\left(\frac{11}{210}+\frac{11\Phi}{120}+\frac{\Phi^2}{24}\right)l \\ -\left(\frac{13}{420}+\frac{3\Phi}{40}+\frac{\Phi^2}{24}\right)l & -\left(\frac{1}{140}+\frac{\Phi}{60}+\frac{\Phi^2}{120}\right)l^2 & -\left(\frac{11}{210}+\frac{11\Phi}{120}+\frac{\Phi^2}{24}\right)l & \left(\frac{1}{105}+\frac{\Phi}{60}+\frac{\Phi^2}{120}\right)l^2 \end{bmatrix} \tag{C.33}$$

$$\underline{\underline{\mathbf{M}}}^e_{r} = \frac{\rho A l}{(1+\Phi)^2}\left(\frac{r_g}{l}\right)^2 \begin{bmatrix} \frac{6}{5} & \left(\frac{1}{10}-\frac{\Phi}{2}\right)l & -\frac{6}{5} & \left(\frac{1}{10}-\frac{\Phi}{2}\right)l \\ \left(\frac{1}{10}-\frac{\Phi}{2}\right)l & \left(\frac{2}{15}+\frac{\Phi}{6}+\frac{\Phi^2}{3}\right)l^2 & -\left(\frac{1}{10}-\frac{\Phi}{2}\right)l & -\left(\frac{1}{30}+\frac{\Phi}{6}+\frac{\Phi^2}{6}\right)l^2 \\ -\frac{6}{5} & -\left(\frac{1}{10}-\frac{\Phi}{2}\right)l & \frac{6}{5} & -\left(\frac{1}{10}-\frac{\Phi}{2}\right)l \\ \left(\frac{1}{10}-\frac{\Phi}{2}\right)l & -\left(\frac{1}{30}+\frac{\Phi}{6}+\frac{\Phi^2}{6}\right)l^2 & -\left(\frac{1}{10}-\frac{\Phi}{2}\right)l & \left(\frac{2}{15}+\frac{\Phi}{6}+\frac{\Phi^2}{3}\right)l^2 \end{bmatrix} \tag{C.34}$$

C.2. Derivation of the Governing Equation

The Langrangian functional of the potential and kinetic energy, or the total dynamic energy, is:

$$\mathscr{L} = \sum_{e=1}^{E} \left(U^e - T^e\right) \tag{C.35}$$

Using Hamilton's principle of least action, stating that the true evolution of a physical system is a solution of the functional equation of the Lagrangian, the governing equation of the Timoshenko beam on an elastic foundation under axial loads becomes:

$$\delta \int_{t_1}^{t_2} \mathscr{L}\, dt = \delta \int_{t_1}^{t_2} \sum_{e=1}^{E} \left(U^e - T^e\right) dt = 0 \tag{C.36}$$

$$\sum_{e}^{E} \left(\underline{\underline{\mathbf{K}}}^e_b + \underline{\underline{\mathbf{K}}}^e_s + \underline{\underline{\mathbf{K}}}^e_f - \underline{\underline{\mathbf{K}}}^e_g\right)\underline{q} + \sum_{e}^{E} \left(\underline{\underline{\mathbf{M}}}^e_t + \underline{\underline{\mathbf{M}}}^e_r\right)\underline{\ddot{q}} = 0 \tag{C.37}$$

$$\underline{\underline{\mathbf{M}}}\,\underline{\ddot{q}} + \underline{\underline{\mathbf{K}}}\,\underline{q} = 0 \tag{C.38}$$

Assuming a harmonic solution to the governing equation $\underline{q} = \underline{Q}e^{iwt}$, the eigenvalue problem, – from which the eigenfrequencies and mode shapes of the system can be determine –, is found:

$$\left(\underline{\underline{\mathbf{K}}}\,\underline{q} - \omega^2 \underline{\underline{\mathbf{M}}}\right)\underline{\ddot{Q}} = 0 \tag{C.39}$$

D

Equivalent Linear Site Response Analysis

Equivalent linear site response analysis is the most widely used approach to approximate the soil column response [4]. The soil response is approximated by a piecewise-linear solution, where the soil properties are adjusted iteratively to be consistent with an effective level of shear strain [4]; the dynamic properties are approximated by an equivalent shear modulus and equivalent damping ratio compatible with the effective level of shear strain. The equivalent system is most commonly modeled by an equivalent linear Kelvin-Voigt soil model (Figure 4.12) [41][7].

The equivalent shear modulus and damping ratio vary with shear strain amplitude, and are found to be compatible with an effective level of shear strain by iteration [7]. The effective shear strain in a layer is:

$$\gamma_{\text{eff}}^{j} = R_\gamma \cdot \gamma_{\text{max}}^{j} \quad \text{, with strain reduction factor depending on earthquake magnitude:} \quad R_\gamma = \frac{M-1}{10} \tag{D.1}$$

The iterative nature of the equivalent shear modulus and equivalent damping ratio is visualized in Figure D.1. The result of the iteration is a strain-compatible equivalent shear modulus and damping ratio; equivalent SRA uses the $G-\gamma$ and $\xi-\gamma$ curves to approximate the cyclic soil behaviour of actual soils that exhibit strength degradation and energy dissipation under strong ground motion.

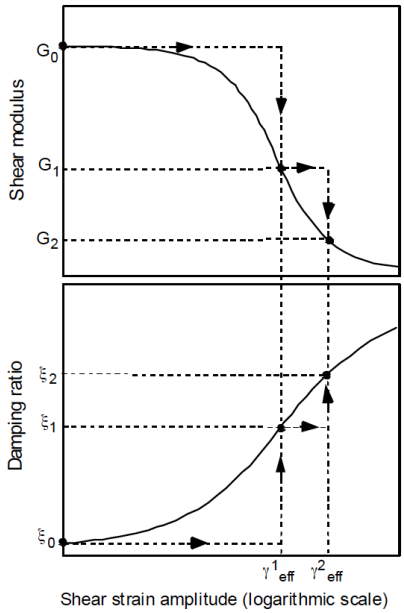

Figure D.1: *Iteration of equivalent shear modulus and equivalent damping ratio in equivalent linear site response analysis.*

According to the Kelvin-Voigt model, the stress-strain relation is [7]:

$$\tau = G \cdot \gamma + \eta \cdot \dot{\gamma} \tag{D.2}$$

where τ is the shear stress, G the shear modulus, η the soil damping, γ the shear strain and $\dot{\gamma}$ the strain rate. The one-dimensional equation of motion for vertically propagating shear waves is [7]:

$$\rho \cdot \frac{\delta^2 u}{\delta t^2} = \frac{\delta \tau}{\delta z} \tag{D.3}$$

with ρ the density of the soil – equal to the unit weight γ ($\neq$ shear strain) divided by the acceleration constant g –, u the soil displacement, t the time instance and z the depth.

Substituting the Kelvin-Voigt stress-strain relation of Equation D.2, the EOM becomes:

$$\rho \cdot \frac{\delta^2 u}{\delta t^2} = G \cdot \frac{\delta^2 u}{\delta z^2} + \eta \cdot \frac{\delta^3 u}{\delta z^2 \delta t} \tag{D.4}$$

For harmonic waves, the soil response of a layer u_j has the general solution [7]:

$$u_j(z,t) = \left(A_j \cdot \mathrm{e}^{i \cdot k_j^* \cdot z_j} + B_j \cdot \mathrm{e}^{-i \cdot k_j^* \cdot z_j} \right) \cdot \mathrm{e}^{i \cdot \omega \cdot t} \tag{D.5}$$

with k_j^* the complex wave number of the harmonic wave in soil layer j, z_j the depth of the soil layer with respect to surface level, ω the frequency of the harmonic wave, and A_j and B_j constants that need to be determined from the boundary conditions. The complex wave number k^* is equal to [7]:

$$k^* = \sqrt{\frac{\rho \cdot \omega^2}{G + i \cdot \omega \cdot \eta}} = \sqrt{\frac{\rho \cdot \omega^2}{G^*}} \tag{D.6}$$

with G^* the complex shear modulus, which is – by introducing the critical damping ratio $\xi = \frac{\omega \cdot \eta}{2G}$ – equal to:

$$G^* = G + i \cdot \omega \cdot \eta = G(1 + 2 \cdot i \cdot \xi) \tag{D.7}$$

The shear stress is, according to Eq. D.3 and D.5, expressed as [7]:

$$\tau_j(z,t) = i \cdot k_j^* \cdot G_j^* \cdot \left(A_j \cdot \mathrm{e}^{i \cdot k_j^* \cdot z_j} - B_j \cdot \mathrm{e}^{-i \cdot k_j^* \cdot z_j} \right) \cdot \mathrm{e}^{i \cdot \omega \cdot t} \tag{D.8}$$

Compatibility of displacements at adjacent boundary layers dictate that (using Equation D.5) [7]:

$$\left(A_{j+1} + B_{j+1} \right) = \left(A_j \cdot \mathrm{e}^{i \cdot k_j^* \cdot h_j} + B_j \cdot \mathrm{e}^{-i \cdot k_j^* \cdot h_j} \right) \tag{D.9}$$

and compatibility of shear stresses that (using Equation D.8) [7]:

$$\left(A_{j+1} - B_{j+1} \right) = \frac{k_j^* \cdot G_j^*}{k_{j+1}^* \cdot G_{j+1}^*} \left(A_j \cdot \mathrm{e}^{i \cdot k_j^* \cdot h_j} - B_j \cdot \mathrm{e}^{-i \cdot k_j^* \cdot h_j} \right) \tag{D.10}$$

From these two conditions, the unknown constants A and B can be determined in each layer.

The recursive algorithm to determine the soil response in each layer is started at the bedrock, where it is assumed that the shear stress is zero:

$$\tau_1(0,t) = 0 = i \cdot k_1^* \cdot G_1^* \cdot (A_1 - B_1) \cdot \mathrm{e}^{i \omega t} \longrightarrow A_1 = B_1 \tag{D.11}$$

The transfer function relating the displacements at the layer boundaries is, derived from Eq. D.9, [7]:

$$H(\omega) = \frac{u_j}{u_{j+1}} = \frac{A_j + B_j}{A_{j+1} + B_{j+1}} \tag{D.12}$$

from which the displacements at each layer can be computed fast in the frequency domain.

The velocity and acceleration are related to the displacement by (using Eq. D.5):

$$\dot{u}_j(z,t) = \frac{\delta u_j}{\delta t} = i\omega u_j(z,t) \quad \text{and} \quad \ddot{u}_j(z,t) = \frac{\delta^2 u_j}{\delta t^2} = -\omega^2 u_j(z,t) \tag{D.13}$$

Consequently, the transfer function from Eq. D.12 relates the displacements, the velocities and accelerations.

The shear strain at depth z in layer j is [7]:

$$\gamma_j(z,t) = \frac{\delta u_j}{\delta z} = i k_j^* \left(A_j e^{i k_j^* z} - B_j e^{-i k_j^* z} \right) e^{i\omega t} \tag{D.14}$$

The shear stress at that depth in the same layer is [7]:

$$\tau_j(z,t) = G_j^* \gamma_j(z,t) \tag{D.15}$$

Equivalent response analysis is an iterative approach, that assumes that the shear modulus and damping ratio are function of shear strain amplitude; the values of G and ξ are determined by iterations so that they become consistent with the level of strain induced in each layer. This approach is implemented in commercial software such as SHAKE [73], EERA [7] and DEEPSOIL [37].

The **iteration procedure** for the equivalent linear approach in each layer is as follows [7]:

1. *"Initialize the values of G^i and ξ^i at their small strain values."*
2. *"Compute the ground response, and get the amplitudes of maximum shear strain γ_{max} from the time histories of shear strain in each layer."*
3. *"Determine the effective shear strain γ_{eff} from γ_{max}"* according to Eq. D.1. R_γ, the strain reduction factor, has the same value for all layers of soil as it only depends on the earthquake magnitude.
4. *"Calculate the new equivalent linear values G^{i+1} and ξ^{i+1} corresponding to the effective shear strain γ_{eff}."*
5. *" Repeat steps 2 to 4 until the differences between the computed values of shear modulus and damping ratio in two successive iterations fall below some predetermined value in all layers."*

E

Linear Airy Wave Theory - Regular Waves

The wave elevation η, horizontal velocity u and acceleration $\dot{u}$ at some depth beneath SWL are depicted in Figures E.1 to E.3. These graphs are the result for a regular, sinusoidal wave for a normal sea state with peak period 5.69 s and significant wave height of 1.14 m. Use was made of the linear airy wave theory as explained in Chapter 4.3.

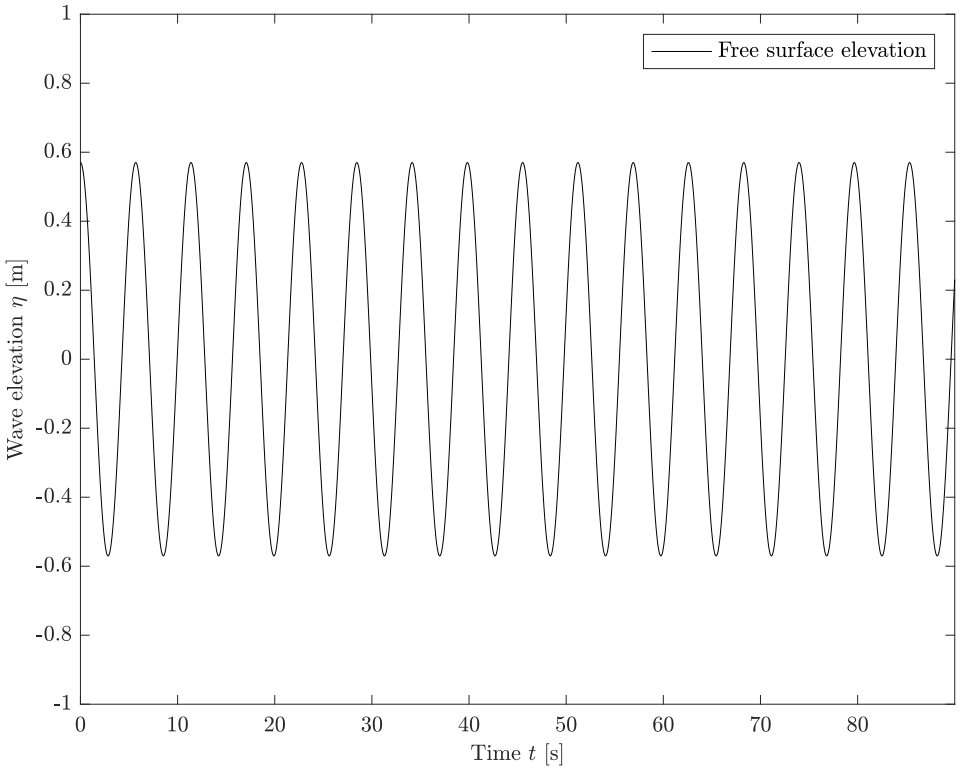

Figure E.1: *Wave elevation for a regular sinusoidal wave with T_p 5.69 s and H_s 1.14 m.*

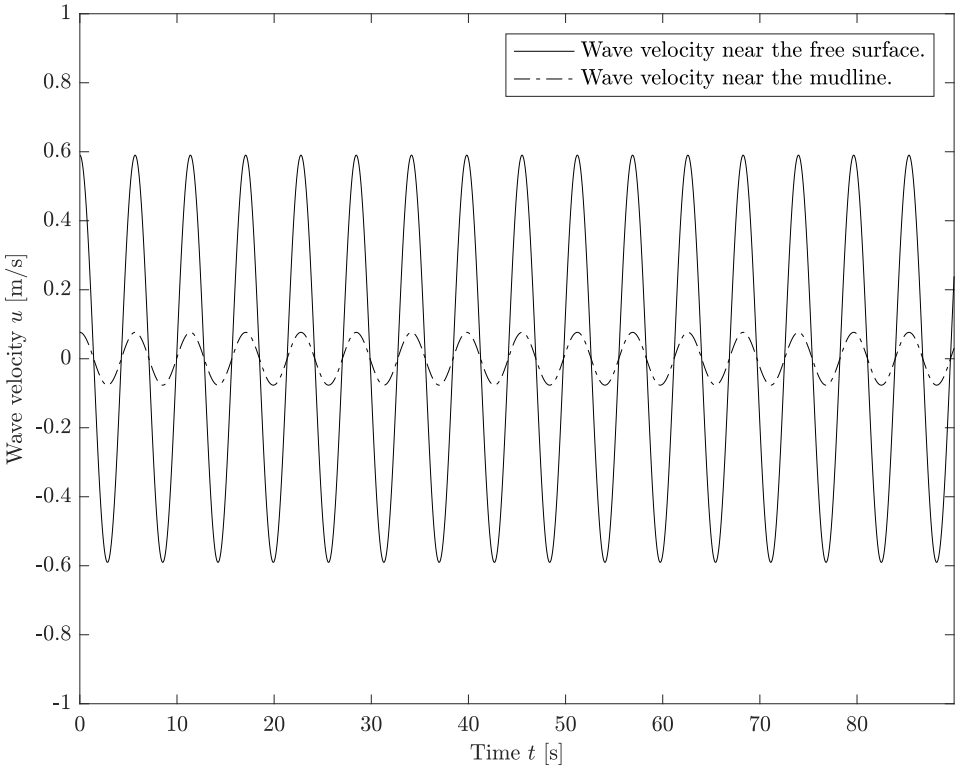

Figure E.2: *Wave velocity for a regular sinusoidal wave with T_p 5.69 s and H_s 1.14 m.*

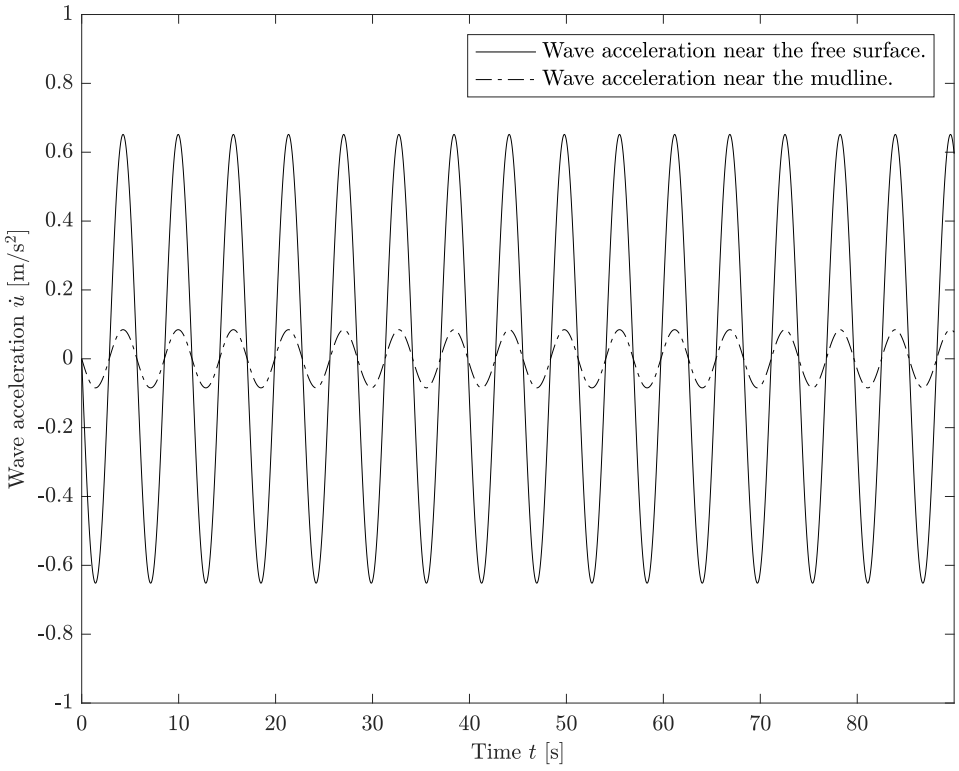

Figure E.3: *Wave acceleration for a regular sinusoidal wave with T_p 5.69 s and H_s 1.14 m.*

F

Global Yield and Global Buckling Check

The yield check was performed according to equation:

$$\sigma_z = \frac{N}{A} + \frac{M}{W_y} \leq \frac{\sigma_y}{\text{SF}} \tag{F.1}$$

with σ_z the yield stress along the longitudinal axis of the structure, N the force normal to the cross-section A, M the internal moment, W_y the elastic section modulus, σ_y the yield strength of the material, and SF the material safety factor.

The buckling check was performed with equation:

$$\frac{N}{\kappa N_p} + \frac{\beta_m M}{M_p} + \Delta n \leq \frac{1}{\text{SF}} \tag{F.2}$$

with N and M the normal force and moment due to the external loads. The plastic moment M_p is:

$$M_p = \frac{W_p \sigma_y}{\gamma_m} \tag{F.3}$$

with W_p the plastic section modulus and γ_m a material factor depending on the reduced slenderness:

$$\gamma_m = \begin{cases} 1.10 & \bar{\lambda} \leq 0.5 \\ 0.8 + 0.6 \cdot \bar{\lambda} & 0.5 < \bar{\lambda} < 1 \\ 1.40 & \bar{\lambda} \geq 1 \end{cases} \tag{F.4}$$

where $\bar{\lambda}$ is the reduced slenderness:

$$\bar{\lambda} = \sqrt{\frac{A \cdot \sigma_y}{N_e}} \tag{F.5}$$

The elastic load N_e is:

$$N_e = \frac{\pi^2 \cdot E \cdot I}{1.1 \cdot (\beta \cdot L)^2} \tag{F.6}$$

with β =2.1 for a clamped-free beam and L the length of the full structure. The plastic load N_p is:

$$N_p = \frac{A \cdot \sigma_y}{\gamma_m} \tag{F.7}$$

Δn is a function of κ and the reduced slenderness $\bar{\lambda}$:

$$\kappa = \begin{cases} \frac{1}{\Phi + \sqrt{\Phi^2 - \bar{\lambda}^2}} & \bar{\lambda} > 0.2 \\ 1 & \bar{\lambda} \leq 0.2 \end{cases} \tag{F.8}$$

with Φ equal to:

$$\Phi = 0.5 \cdot \left(1 + \alpha \cdot \left(\bar{\lambda} - 0.2\right) + \bar{\lambda}^2\right) \tag{F.9}$$

and lastly Δn equal to:

$$0.25 \cdot \kappa \cdot \bar{\lambda}^2 \leq 0.1 \tag{F.10}$$